Impact Analysis of Motor Faults on the DC Bus in Electric Vehicle Drivetrains

Prepared by:

Name: **Devon Pugin**

Student Number: **PGNDEV001**

Supervisor: **Paul Barendse**

Thesis submitted to the Department of Electrical Engineering, University of Cape Town, in complete fulfilment of the requirements for the degree of Master's in Science.

December 2024

Department of Electrical Engineering

Faculty of Engineering and the Built Environment

University of Cape Town

DECLARATION

This dissertation is submitted to the Department of Electrical Engineering in the Faculty of Engineering and the Built Environment, University of Cape Town, in fulfilment of the requirements for the degree of Master of Science.

I know the meaning of plagiarism and declare that all the work in the document, save for that which is properly acknowledged is my own. This thesis has been submitted to the Turnitin module (or equivalent similarity and originality checking software), and I confirm that my supervisor has seen my report and any concerns revealed by such has been resolved with my supervisor.

Signed by candidate

Devon Jordan Pugin

TERMS OF REFERENCE

To fulfil the requirements for a master's degree in the science of engineering in Electrical Engineering, students are required to write a 180 credit dissertation. To this end, the author approached Professor Paul Barendse for assistance in finding a suitable topic.

After consulting with Professor Barendse, it was agreed that the author would conduct research on fault analyses within electric vehicle drivetrains, with emphasis on how faults in the motor may affect the powertrain's battery. The brief was to use a test rig developed by previous students to research known faults within a motor and use appropriate methods for fault analysis on both the machine and the DC bus.

It was agreed that existing techniques could be used to validate faults in the motor in grid-connected and inverter-fed scenarios. The faults were also assessed through different control algorithms within the inverter using the same switching scheme throughout the algorithms. Finally, the potential impact of the faults on the motor will be studied in terms of their impact on the battery within an electric vehicle powertrain and an overview of how different complexities of control algorithms may mitigate the effect will be provided.

ACKNOWLEDGEMENTS

This thesis would not have been possible without the incredible assistance provided by Professor Barendse; his unwavering support and enthusiasm for the research was a refreshing presence in this long endeavour.

Maysam Soltanian, thank you for the countless hours that you provided in the lab and with the test rig, as well as being a great sounding board for ideas to tackle the problems we faced. To the Lab assistant Riyaad Hoosain, your efforts in aligning the motors and changing parts on the test rig made my efforts all easier.

To Professor Jayalath, your knowledge of filters was an immense help in the design stage of my setup.

To my mother, for whom none of this would be possible without you. Your unwavering support has made this achievable, and I am forever grateful.

Finally, to my Fiancé Paige, who was by my side at the toughest moments, thank you for your patience and love during this achievement.

ETHICS APPLICATION FORM

Please Note:
Any person planning to undertake research in the Faculty of Engineering and the Built Environment (EBE) at the University of Cape Town is required to complete this form **before** collecting or analysing data. The objective of submitting this application *prior* to embarking on research is to ensure that the highest ethical standards in research, conducted under the auspices of the EBE Faculty, are met. Please ensure that you have read, and understood the **EBE Ethics in Research Handbook** (available from the UCT EBE, Research Ethics website) prior to completing this application form: http://www.ebe.uct.ac.za/ebe/research/ethics1

APPLICANT'S DETAILS		
Name of principal researcher, student or external applicant		Devon Jordan Pugin
Department		Electrical Engineering
Preferred email address of applicant:		pgndev001@myuct.ac.za
If Student	Your Degree: e.g., MSc, PhD, etc.	MSc
	Credit Value of Research: e.g., 60/120/180/360 etc.	180
	Name of Supervisor (if supervised):	Paul Barendse
If this is a researchcontract, indicate the source of funding/sponsorship		
Project Title		Investigating the effects on the battery when faults occur in a motor of an EV Drivetrain

I hereby undertake to carry out my research in such a way that:

- there is no apparent legal objection to the nature or the method of research; and
- the research will not compromise staff or students or the other responsibilities of the University;
- the stated objective will be achieved, and the findings will have a high degree of validity;
- limitations and alternative interpretations will be considered;
- the findings could be subject to peer review and publicly available; and
- I will comply with the conventions of copyright and avoid any practice that would constitute plagiarism.

APPLICATION BY	Full name	ature	Date
Principal Researcher/ Student/External applicant	Devon Jordan Pugin		10/06/2021
SUPPORTED BY	Full name	ure	Date
Supervisor (where applicable)	Paul Barendse		11 June 2021

APPROVED BY	Full name	Signature	Date
HOD (or delegated nominee) Final authority for all applicants who have answered NO to all questions in Section 1; and for all Undergraduate research (Including Honours).	AMIT MISHRA		22/9/21
Chair: Faculty EIR Committee For applicants other than undergraduate students who have answered YES to any of the questions in Section 1.			

ABSTRACT

This study investigated the analysis of electric vehicle drivetrains in the presence of a motor fault within a powertrain. The investigation was conducted utilising a test rig that facilitated the controlled implementation of known faults in induction motors connected to an electric vehicle powertrain configuration, thus enabling the application of various control methodologies. The induction motors employed in this study comprised a healthy baseline motor without faults, a motor with known inter-turn short faults of two distinct severities, and a motor with a known broken rotor bar fault. The motors were connected to a grid source to establish a baseline for comparison. In each scenario, the faults were analysed using motor current signature analysis (MCSA), Park's Vector Approach (PVA), Extended Park's Vector Approach (EVPA), and DC bus current analysis. The objective of this study was to analyse the effects of various faults and their manifestation on the DC bus of powertrains, specifically under transient speed conditions.

The analysis of the results presented in this study indicates that the DC bus analysis demonstrates the presence of a fault in the case of an inter-turn fault in the motor in a significantly more consistent manner. This method, along with the EPVA, proved to be the most effective approach for identifying the presence of a fault within the powertrain across multiple control methodologies and motor load levels. It has been demonstrated that an inter-turn fault introduces additional harmonics at twice the fundamental frequency of the system on the DC bus current. This harmonic can serve as a fault indicator and may produce additional stress on the DC bus of the system for the inter-turn fault. The selected EVPA and DC bus analysis methods proved less conclusive when applied to a broken rotor bar fault; however, these techniques were utilised with a focus on specific harmonics based on the literature that emphasised the imbalance introduced through an inter-turn fault. These two techniques help illuminate the propagation throughout the powertrain as they are applied to different currents throughout the powertrain, with the EVPA being applied to the motor line current.

The most significant finding was that the DC bus analysis indicated the presence of a fault through a substantial increase in the harmonic at twice the fundamental frequency of the DC bus current, irrespective of the complexity of the control method employed. Although more sophisticated algorithms can address errors within a system, they are unable to conceal the presence of errors in the DC bus fully, particularly in the case of short inter-turn faults. Consequently, further research should be directed towards this methodology, as it may prove valuable in identifying a broader range of faults and providing essential information for mitigating the impact of these faults on the DC bus of electric vehicle powertrains.

TABLE OF CONTENTS

LIST OF FIGURES

LIST OF TABLES

1. INTRODUCTION

1.1 BACKGROUND TO THE STUDY

If engineers do not design a battery with performance and protection in mind, the entire vehicle becomes susceptible to expensive damage or complete failure [1]. This is especially true today, as electric vehicles have grown in popularity in recent years as a viable option for combating greenhouse gas emissions during transportation [2]. As of 2023, more than 10 million electric vehicles (EVs) have been sold worldwide, and it is expected that more than 40 million EVs will be circulating by 2030 [3]. With the growing demand, there has also emerged a necessity for drivetrains to be optimised for efficiency and cost-effectiveness. As such, particular attention must be directed towards maintaining the battery pack under optimal conditions, as this component represents one of the most substantial costs in a vehicle [4].

Induction motors are a viable option for EV use, as other options typically require natural magnetic materials, such as synchronous machines [5]. Induction motors are susceptible to faults, with the main faults related to the stator winding [6]. This fault produces an imbalance in the load, especially if the stator winding is shorted, which in turn produces additional unwanted harmonics. In EVs, these additional harmonics propagate through the powertrain of the vehicle and present themselves on the DC bus at approximately twice the fundamental frequency, particularly when there is an imbalance in the motor [7]. Significant research is being conducted to focus on battery fault diagnosis within EVs, as can be seen in papers such as [8, 9,10]. While the focus is important, especially in monitoring the state of health of the battery, so that thermal runaway, which can become a safety hazard, such as a fire and eventually an explosion [8], does not occur the focus is not on analysing potential causes for the degradation on the battery health. Methods such as spatial-temporal transformer networks [8], neural networks [9] and segmented regression are utilised in these studies, but rarely focus on faults within the motor causing the impact on the battery. Moradi et al. [7] is one of the few researchers who aim to quantify what a fault on the motor results in on the DC bus, along with Pei et al [11]. This is done using harmonic analysis with good correlation between simulation and experimentation. This research is, however, limited as it was focused on grid-tied inverters rather than being applied to EV applications.

This research aims to build on Moradi et al. work by utilising known fault detection methods on motors, such as MCSA [12], Park's Vector [13, 14], Extended Park's Vector approach [15, 16], and DC bus analysis [7, 11] can provide valuable insight into how various faults may present themselves on the DC bus of the EV powertrain. This research also aims to provide this information in the context of EVs. Although Gundeware et al [17] and Alsharif et al. [18] do focus on the EV context, it is more so on the motor diagnosis when referring to [17], and modelling the battery health with machine learning, not focusing on specific harmonics and how they propagate throughout the drivetrain. This research aims to introduce more complex control schemes compared to the existing literature mentioned earlier. Moradi et al [7] and Pei et al [11] show how the imbalance effect of an inter-turn short can add additional harmonics on the DC bus and as the battery is the costliest part of an electric vehicle it is beneficial to quantify and identify the additional harmonics introduced onto the DC bus, as they place additional strain on the battery pack and can increase ageing of the cell [19, 20]. Because of the limited research with a focus on EV-specific conditions, this study can form a springboard into areas of focus in terms of research in this area and help provide valuable insights into what could have a significant benefit in maintaining the health of EV drivetrains.

1.2 PROBLEM STATEMENT

Preventing issues from occurring within the battery in an EV is a critical consideration in the design process due to the high cost of these components. One important aspect involves protecting the DC bus from faults originating on the load side of the inverter. Such faults can stem from the motor, including imbalances, which are amongst the most common faults within induction motors [21].

Motor Current Signature Analysis [12] have been used in the past to detect faults within the motor. However, this approach has primarily been applied to grid-connected machines and does not account for additional noise that can be produced when connected to an inverter. Consequently, alternative methods need to be explored, assessed, and validated to address this challenge effectively.

Techniques such as the Park's Vector Approach and the Extended Park's Vector Approach have been utilised for effectively detecting asymmetrical faults [22]. These techniques are cost-effective and non-invasive towards the machine, making them an excellent starting point for analysing the drivetrain. The issue arises from translating the fault from the AC side of the inverter to the DC side. Any additional harmonics or faults that could propagate their way through need to be identified effectively to avoid any potential harm to the battery pack.

This serves as the main engineering problem, in which the analysis of a fault within an electric drivetrain is to be measured on the DC bus. Thus, there is a need to develop and apply a method for identifying the presence of a fault in the DC bus, to deepen the understanding of how this interaction occurs, specifically with more complex control algorithms applied to the motor of the powertrain. This would provide a stepping stone to understand the stress the DC bus undergoes, and provide a springboard for the safety design of the DC bus on an electric vehicle. This would eventually aid in prolonging the life of the battery as well as give more specific design targets to achieve when designing filters for the DC bus of the vehicle.

1.3 RESEARCH QUESTIONS

There are well-documented use cases of condition monitoring techniques on the motor side, such as the MCSA and IPSA [23]; however, little is known about identifying it from the DC bus. This can provide a cost-effective and novel approach for fault identification, particularly as it will help provide an understanding of what occurs in the DC bus and, in turn, the battery. With a view to faults within an Electric Vehicle drivetrain, the following research questions will be addressed:

1. What techniques can remotely detect an inter-turn short fault that occurs within an induction motor connected to an inverter in an EV drivetrain at low load?
2. What techniques can be used to detect these faults on the DC bus?
3. How robust are the techniques in detecting the faults through load variations?
4. What is the impact of different control techniques in determining the presence of the fault within the system?

1.4 OBJECTIVES OF THIS STUDY

This study aims to provide deeper insight into the behaviour of an EV drivetrain's induction motor faults. However, for this to be accomplished, the following objectives have been set out.

1. To successfully design and simulate an EV powertrain including the LCL filter, and perform V/Hz open loop, V/Hz closed loop and FOC control of an induction motor.
2. To verify the simulated setup through an experimental setup.
3. To gather data from this experimental setup using appropriate data acquisition tools.
4. To perform data analysis on the gathered data and asses the effectiveness of the chosen fault analysis techniques.
5. To draw conclusions and provide the findings on the chosen techniques.

In achieving these objectives, the study aims to develop an understanding of how faults that are present on the induction motor present themselves on the DC bus of an EV drivetrain.

1.5 METHODOLOGY

To complete this thesis, a literature review was conducted to gather the core knowledge forming its foundation. Following this, theoretical development was required to deepen the understanding of the key principles necessary for controlling the motors, designing the required filter, and applying various analysis techniques to detect the presence of the faults within the system.

Using this understanding, the design and simulation phase could begin. The overall implementation was tested through simulations to assess aspects such as load response, filtering performance, and overall system behaviour. Any unsatisfactory performance was addressed and re-simulated until acceptable results were achieved.

Once obtained, the implementation into the experimental setup can begin, with the simulated results providing a blueprint for configuring the experiments. These experiments will serve as the basis for data collection, so data acquisition tools and methods must also be determined at this stage. The key data to be collected includes line-to-line voltage, line current, load torque and speed of the shaft of the motor, which will guide the choice of data acquisition equipment. Once confirmed, the experiments can be conducted, during which the required data will be gathered for subsequent fault analysis. Finally, analysis of this data can be completed in order to provide conclusions on the techniques applied throughout the thesis. A visual flowchart of the overall methodology can be found in Figure 1.1 below.

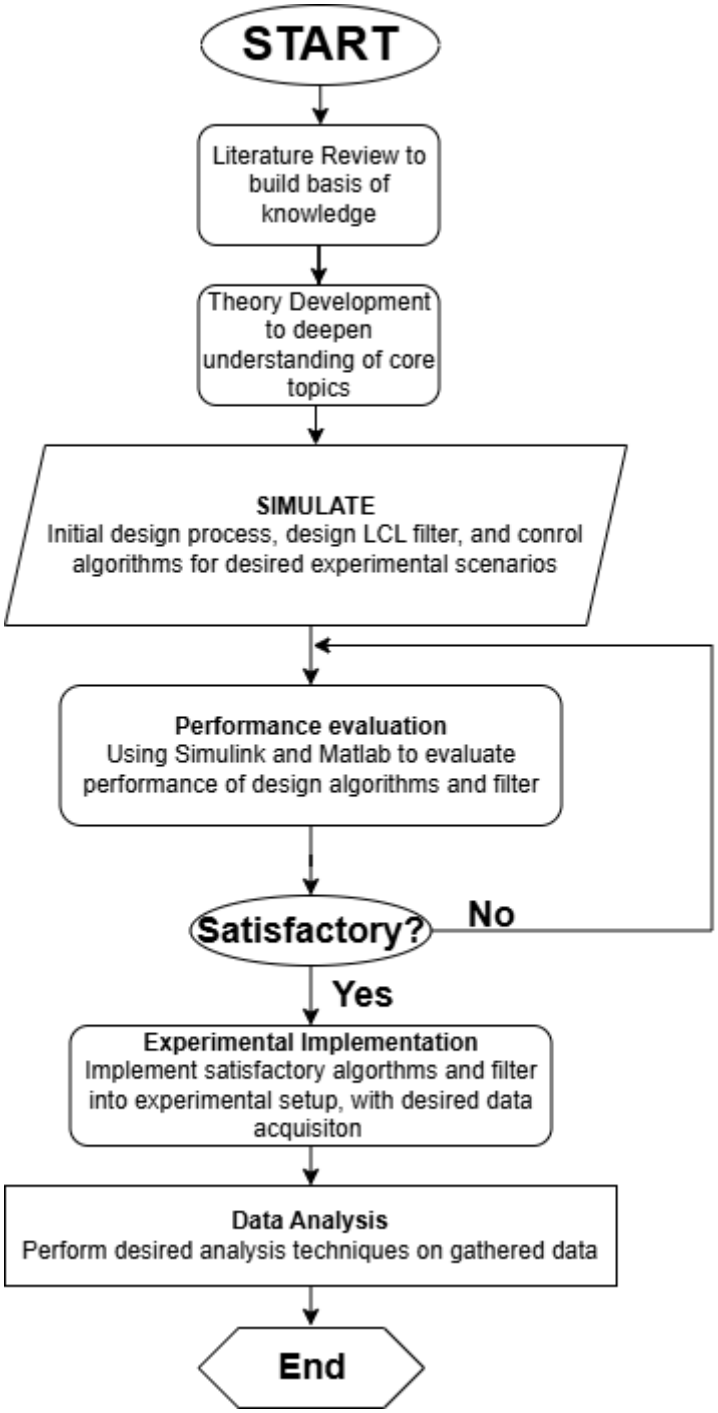

Figure 1.1: Visual flowchart of the methodology used to conduct this thesis.

1.6 SCOPE AND LIMITATIONS

This dissertation focuses on the behaviour of squirrel-cage induction machines operating in motor mode. This study examined two of the most common faults in such machines: winding faults and broken rotor bar faults. For a baseline comparison, the motors were initially connected to the grid; however, the primary investigation focused on an inverter-fed system utilising a space vector pulse-width modulation (SVPWM) switching scheme. This scheme was further compared against various control methods, including V/Hz open-loop, V/Hz

closed-loop, and field-oriented control (FOC). The FOC algorithm is also strictly indirect FOC, where there is no direct torque input into the algorithm.

The machines were connected to a servo mechanism to apply loads according to specific test requirements. The quality of the laboratory power supply was evaluated for balance and total harmonic distortion (THD) and deemed suitable for the experiments. To meet the objectives of this study, the key parameters measured included the DC current and voltage, AC current and voltage, shaft speed, and torque.

1.7 PLAN OF DEVELOPMENT

The remainder of this thesis is structured as follows:

Chapter 2 presents a comprehensive literature review on induction machines and their common faults. It also provides an overview of electric vehicles (EVs) and highlights the importance of maintenance and monitoring in the industry. In addition, this chapter elaborates on the various monitoring techniques currently employed and their applicability to both induction motors and EVs.

Chapter 3 outlines the theoretical foundation for spectral analysis, which is a widely used signal-processing tool in condition-monitoring applications. It details the concepts behind Motor Current Signature Analysis (MCSA), Park's Vector approach, Extended Park's Vector approach, and spectral signatures associated with various faults. Furthermore, the theory underlying the DC fault harmonic analysis is introduced, including the spectral signatures expected in the presence of a fault.

Chapter 4 provides a detailed overview of the experimental test setup and the equipment used throughout the study, as well as all necessary design steps to ensure the test bench was suited to conduct this experiment.

Chapter 5 describes the design of control algorithms as well as the methodology that will be followed to conduct the experiment.

Chapter 6 presents an extensive account of the experimental results.

Chapter 7 summarises the findings of the study and offers a thorough analysis of the results presented in Chapter 6. It also provides a conclusive discussion on how the research questions are addressed. Recommendations are made regarding the application and enhancement of the explored techniques, along with suggested directions for future research.

2 LITERATURE REVIEW

2.1 INTRODUCTION

Induction motors are widely used in various industries, including the Electric Vehicle (EVs) sector and are used in car models such as the Tesla Model S and the Mercedes EQC. It offers a simple and robust solution that can easily be implemented in EV applications [24]. Compared to alternatives such as permanent magnet synchronous machines (PMSMs) and switched reluctance machines, the induction motor stands out as one of the most cost-effective and low-maintenance options [23].

2.2 INDUCTION MACHINES

2.2.1 Construction and Features

The induction machine is one of the most rugged and widely used machines in the industry. Its primary components include a stator and a rotor, which are separated by an air gap [25]. Functionally, the induction machine operates similarly to a transformer, as it transfers electrical energy into mechanical energy. This similarity is evident in the equivalent circuits of both devices.

The stator typically consists of a three-phase winding embedded within laminations of sheet steel. These windings are placed in slots distributed around the air gap of the stator and can be wound in either a short-pitch or full-pitch configuration, depending on the specific motor's application requirements.

The rotor can be of two types: the wound rotor or the squirrel cage rotor. In the squirrel cage construction, bars made of aluminium or copper are embedded in rotor slots and short-circuited on either side by end rings [26]. The bars are often skewed to reduce humming, improve torque uniformity as the rotor position changes, and mitigate the rotor's locking tendency [27]. The wound rotor, on the other hand, features windings like those of the stator, embedded within laminations surrounding the rotor. The three-phase windings are connected to slip rings on one end of the rotor, allowing contact with carbon brushes for connection to external circuits [25]. These external circuits, often resistive, can be used for basic speed control of the machine.

To provide cooling, a fan is typically mounted on the non-drive end of the rotor, ensuring effective heat dissipation for both the stator and rotor (illustrated in Figure 1). The rotor itself is supported by two bearings, which may be either anti-friction or babbitt-type, depending on the motor's size and operational requirements [28]. The entire assembly is enclosed within a cast or fabricated body, chosen based on the motor's size and application needs.

This simple, robust, and cost-effective design has been employed in a variety of applications, ranging from small city vehicles to high-performance cars [29].

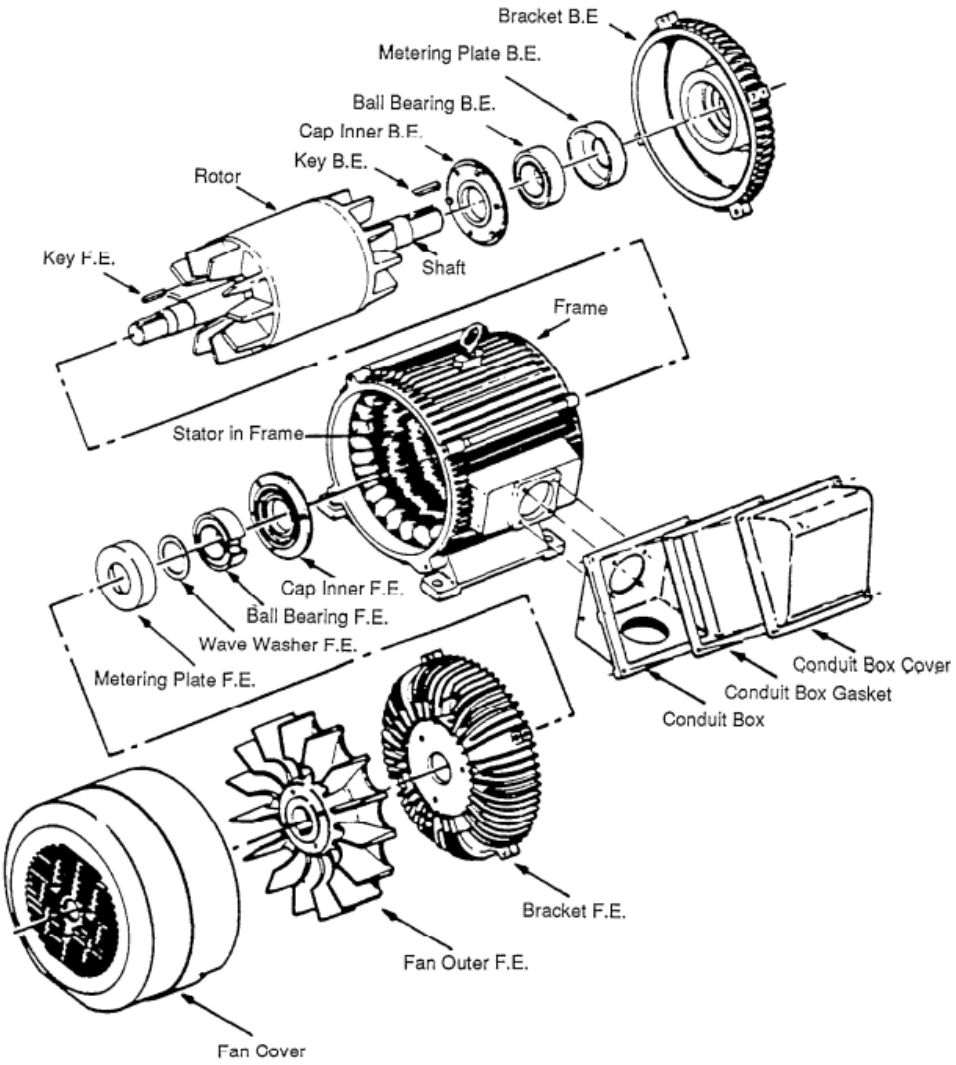

Figure 2.1: Exploded view of a typical construction of an Induction Motor [28].

2.2.2 Methods of Control

There are various methods of control for induction machines, depending on the desired level of control and the specific operation of the machine. These methods vary in complexity and hardware requirements. The simplest way to use an AC motor is to supply the machine with a three-phase voltage from the grid. However, since this method does not allow control over the frequency or voltage of the supply, it is rarely used in practical applications.

The most efficient method of controlling an induction machine is by connecting it to an inverter [26]. This configuration can be achieved either by rectifying a three-phase supply, which is commonly done in industrial settings, or by connecting it to a battery pack, as is the case in electric vehicles. Configurations of both types are illustrated in Figures 2.2 and 2.3.

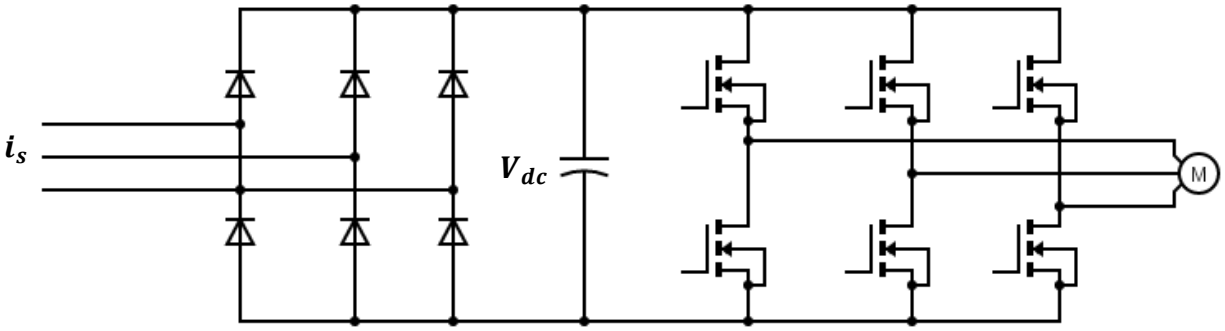

Figure 2.2: Simplified diagram of an Induction motor connected to an inverter and rectifier, where i_s is the supply current.

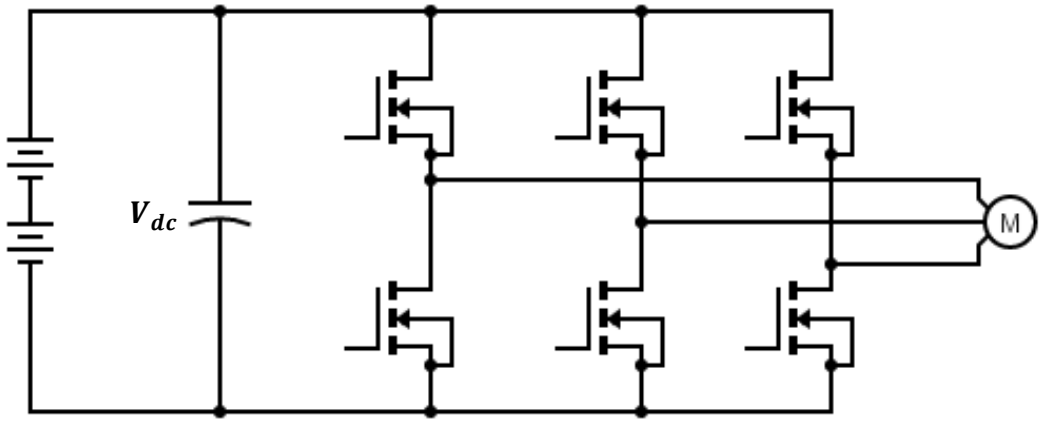

Figure 2.3: Simplified diagram of an induction motor connected to an inverter and battery.

Two main classifications of control methods are used to control the induction machine: scalar control and vector control [26].

2.2.2.1 Scalar Control

Scalar control refers to a control method where only the magnitude of the control variable is adjusted and regulated. This approach is simple and easy to implement; however, it often results in inferior performance due to its simplistic nature [30]. The most common mode of control within this category is open-loop V/Hz control. This method assumes that the desired speed is dependent on the frequency of the supply, with the voltage ($\mathrm{V_s}$) needing to be proportional to the frequency (ω) to maintain a constant stator flux (Φ_s).

$$\Phi_s = \frac{\mathrm{V_s}}{\omega} \tag{2.1}$$

A block diagram of the algorithm can be shown below in Figure 2.4.

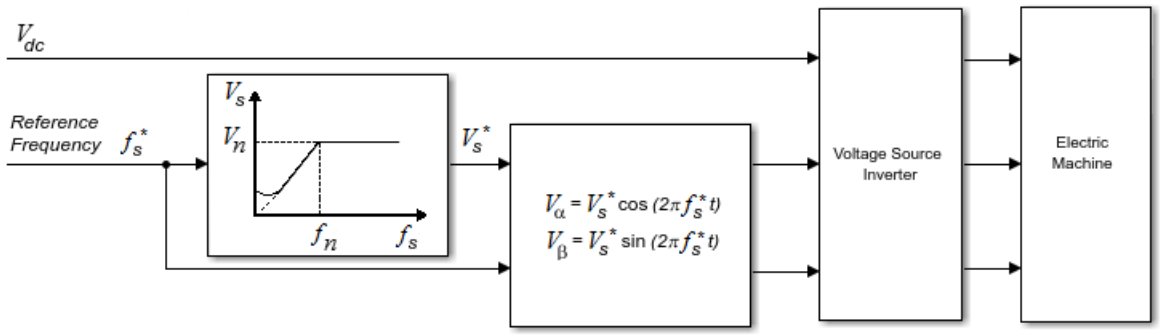

Figure 2.4: Simplified block diagram of V/Hz control of an induction machine [31].

This method calculates the appropriate voltage based on the desired frequency for the stator and provides this information to a controller, using V_α and V_β to act as the space vector for the switching scheme, which in turn adjusts the inverter's switching accordingly. The details of this switching process will be explained later in the chapter.

However, this control scheme has limitations, as it does not measure the speed of the rotor. Therefore, any errors that occur cannot be corrected, and the speed may become inaccurate since slip is not accounted for [30]. Despite this, for constant-speed applications such as fans, this control method is advantageous due to its simplicity and cost-effective implementation [32].

The performance of this control scheme can be improved by implementing it in a closed-loop configuration. While this increases complexity and cost, it allows for the correction of any speed errors using a PI controller. A general block diagram of this setup is shown below in Figure 2.5.

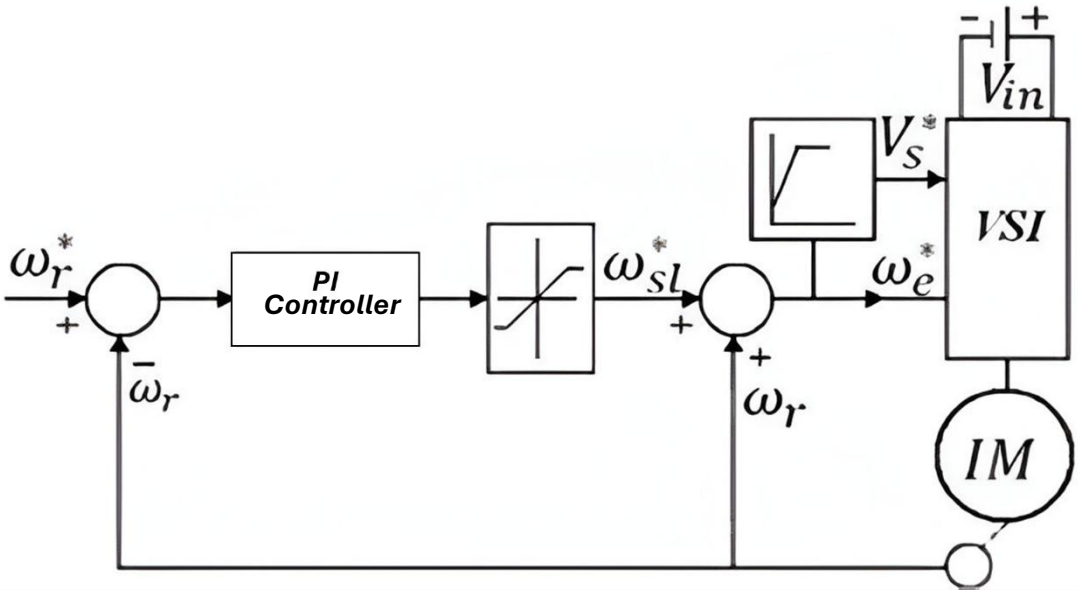

Figure 2.5: Generalised block diagram of V/Hz closed-loop control of Induction motor [33].

Figure 2.5 above provides a visual representation of various V/Hz closed-loop control scheme variables, where $\boldsymbol{\omega_r^*}$ is the desired angular frequency of the motor, $\boldsymbol{\omega_r}$ is the actual angular frequency of the motor, $\boldsymbol{\omega_{sl}^*}$ is the calculated slip angular frequency of the motor, all in rad/s. This information all gets supplied to a controller that controls the VSI, or the voltage source inverter, that in turn controls the induction motor. This configuration enables the desired speed to be achieved by measuring the actual speed of the motor and allowing the PI controller to correct any discrepancies between the actual and desired speeds. While this improves the performance of the control scheme, it still only controls one variable. Nevertheless, it provides significant benefits for applications where precise speed control is essential, particularly for speed-dependent loads.

2.2.2.2 Vector Control

Vector control is the most efficient method for controlling induction motors. Several types of vector control exist, including the Computed Charges Acceleration Method, Direct Torque Control, and Field-Oriented Control (FOC) [26]. This section will focus solely on Field-Oriented Control (FOC), as it offers a more convenient and effective way of directly controlling torque and current compared to other speed control methods [34]. Additionally, FOC is particularly suitable for the powertrain of an electric vehicle, which is a primary focus of this research.

FOC relies on the control of stator currents, which are represented in vector form. This method transforms the three-phase, time-dependent system into a two-coordinate system that is independent of time [35]. This transformation is accomplished using the Clarke (equation 2.2) and Park (equation 2.3) transformations, which are represented by the following formulas:

$$\begin{bmatrix} i_\alpha \\ i_\beta \\ i_0 \end{bmatrix} = \begin{bmatrix} 1 & 0 & 1 \\ -\frac{1}{2} & \frac{\sqrt{3}}{2} & 1 \\ -\frac{1}{2} & -\frac{\sqrt{3}}{2} & \frac{1}{2} \end{bmatrix} \begin{bmatrix} i_a \\ i_b \\ i_c \end{bmatrix} \tag{2.2}$$

$$\begin{bmatrix} i_d \\ i_q \end{bmatrix} = \begin{bmatrix} \cos(\theta) & \sin(\theta) \\ -\sin(\theta) & \cos(\theta) \end{bmatrix} \begin{bmatrix} i_\alpha \\ i_\beta \end{bmatrix} \tag{2.3}$$

In the case of this study, these transformations were made with reference to a rotating frame. The currents i_a, i_b, i_c, represent the three-phase currents of the machine. A graphical representation of how this transform occurs from the stator current vector to the two coordinate systems is shown below in Figure 2.6:

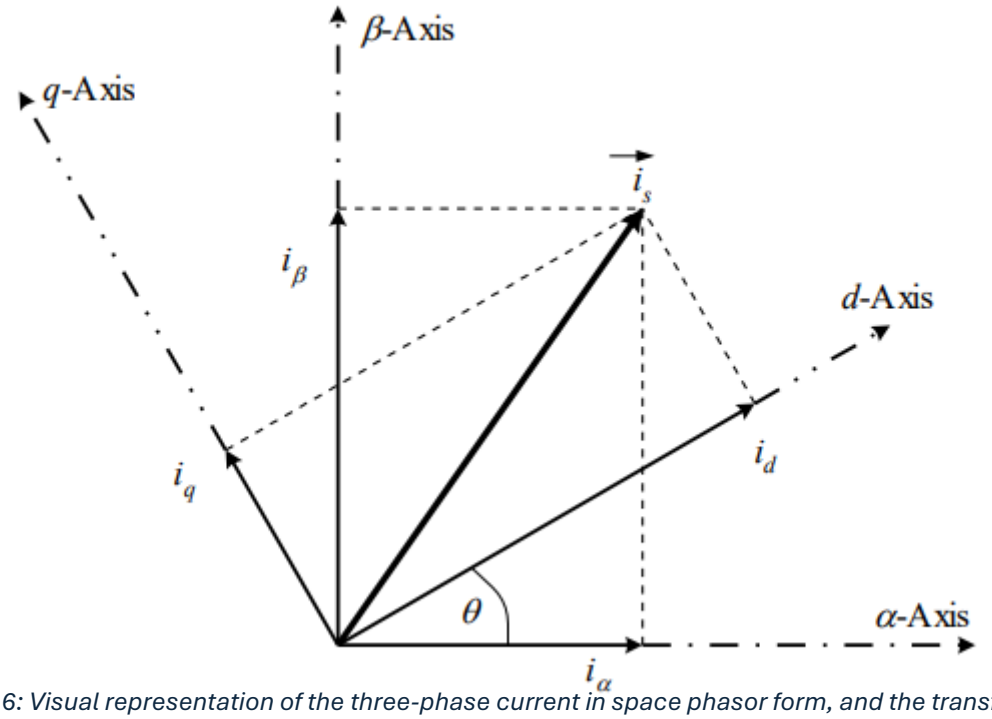

Figure 2.6: Visual representation of the three-phase current in space phasor form, and the transformation in the alpha-beta and d-q coordinate systems [36].

This is because the torque component of the stator space vector lies on the q-axis, while the flux component is aligned with the d-axis. This relationship can be expressed using the simplified formulas below, where T_e is the electromagnetic torque produced by the machine, p is the pole pairs, L_m is the mutual inductance, L_r is the rotor inductance, λ_r is the rotor flux linkage and i_q is the q-axis current of the machine.

$$T_e = \frac{3}{2} p \frac{L_m}{L_r} \lambda_r i_q \tag{2.4}$$

And

$$\lambda_r = \frac{L_m}{(1 + s\tau_r)} i_d \tag{2.5}$$

Where τ_r is the rotor time constant, and r_r is the rotor resistance, finally:

$$\tau_r = \frac{L_r}{r_r} \tag{2.6}$$

This allows for the two main factors of the induction motor to be controlled in this algorithm, whose standard block diagram can be seen below in Figure 2.7:

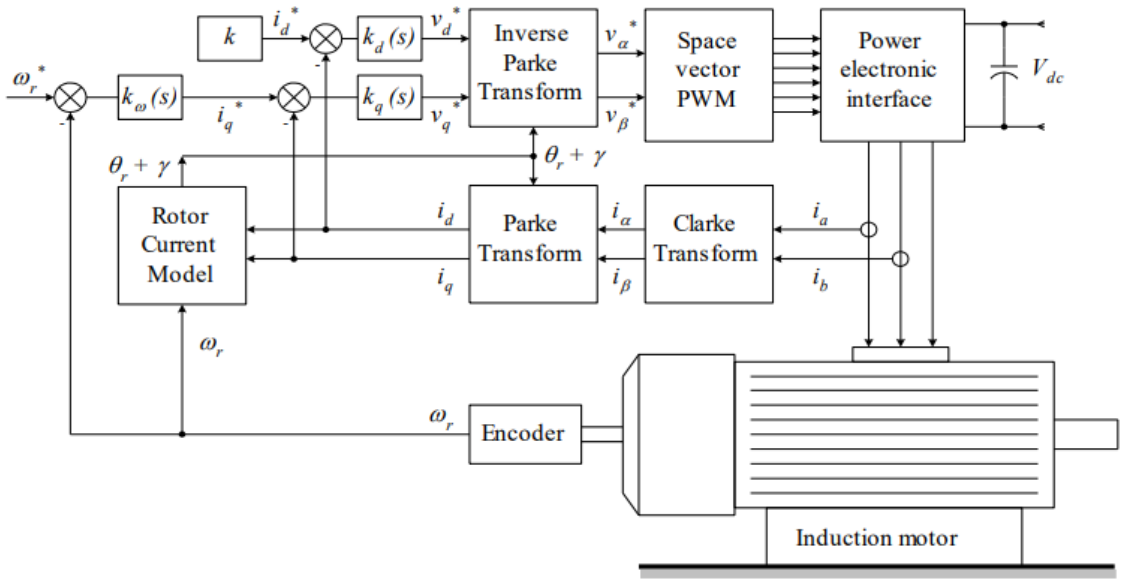

Figure 2.7: Practical implementation of FOC on an induction motor [36].

This control loop introduces some complexities, as it must account for the slip of the motor to accurately determine the rotor angle θ or, as is shown in the above diagram, $\theta_r + \gamma$. However, this approach enables precise control of the motor's speed. With PI controllers in both the speed and current loops of the algorithm, minimal errors are achieved, especially when torque is required at the motor's output. For electric vehicles (EVs), this control scheme is particularly beneficial due to the constant variation in speed and torque demands. Vector control is more suited to this dynamic behaviour, whereas scalar control methods, as discussed earlier, are better suited for steady-state conditions [34]. The scalar control methods are included in this research to analyse the effect of control complexity on the fault analysis techniques, although not applicable to EVs, it provides a base to compare the techniques to.

2.2.3 Overview of Induction Machine Faults

Although induction motors are known for their ruggedness and simplicity, faults can still occur, whether mechanical or electrical. These faults can arise due to numerous factors, including design flaws, manufacturing defects, loading conditions, insufficient maintenance, or adverse environmental conditions. Electrical faults may include voltage imbalance, stator inter-turn faults, overvoltage, undervoltage, overcurrent, and undercurrent, among others. Mechanical faults can involve bearing failure, airgap eccentricity, broken rotor bars, and end ring faults, to name a few [37]. These are some examples and are by no means an exhaustive list. The most common faults in an induction machine are summarised in the table below, which was adapted from a study conducted by the Electric Power Research Institute (EPRI) [21].

Table 2-1: Failure percentages related to each component type within the induction machine [21].

Major component	**Percentage Failures**
Bearing related	41%
Stator related	36%
Rotor related	9%
Other	14%

Table 2.1 demonstrates that while mechanical faults, such as bearing failures, account for most faults, electrical issues in the stator and rotor still contribute significantly to faults observed in the industry. Since the focus of this study is on electrical faults and the harmonics they may cause, the focus will be on two specific types of electrical faults: stator faults and broken rotor bar faults.

2.2.4 Types of Faults

2.2.4.1 Stator faults

Stator faults are typically associated with the failure of the insulation material on the stator windings. Over time, the degradation and ageing of the insulation can result in a turn-to-turn fault [38]. A turn-to-turn fault occurs when the windings within a coil of a motor phase short together, leading to an increase in current draw compared to normal operating conditions. This higher current causes the coil's temperature to rise, potentially leading to further insulation damage or even damage to the coil wire itself if the issue persists. Approximately 80% of all electrical faults within the stator are attributed to turn-to-turn insulation problems, which, if left unaddressed, can escalate into more severe faults [38]. A diagram illustrating a turn-to-turn (or inter-turn) fault is shown below in Figure 2.8.

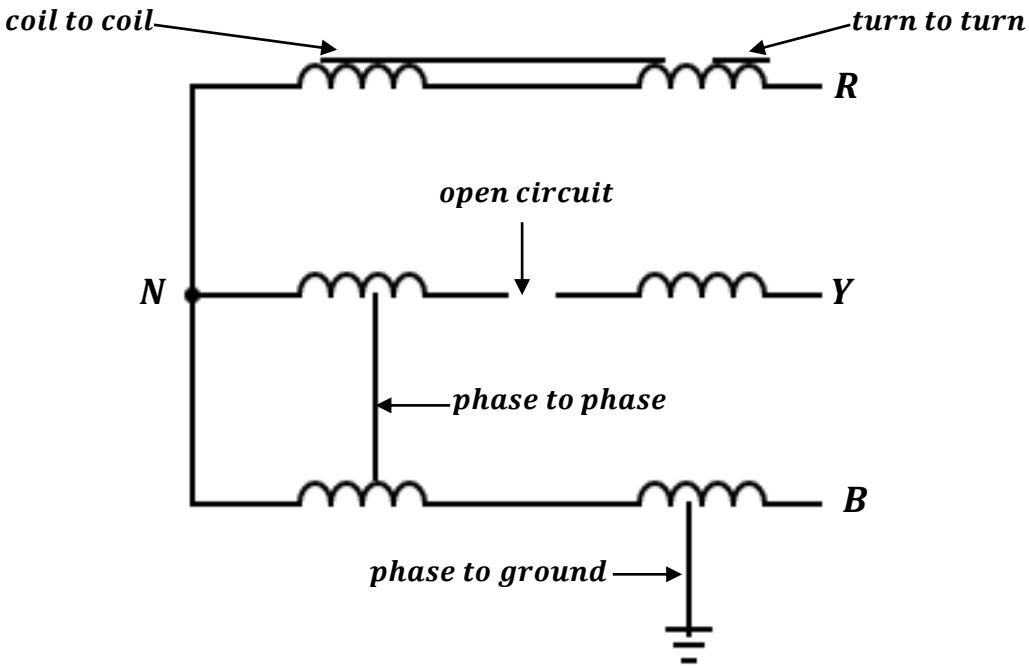

Figure 2.8: Diagram showing the different types of stator electrical faults.

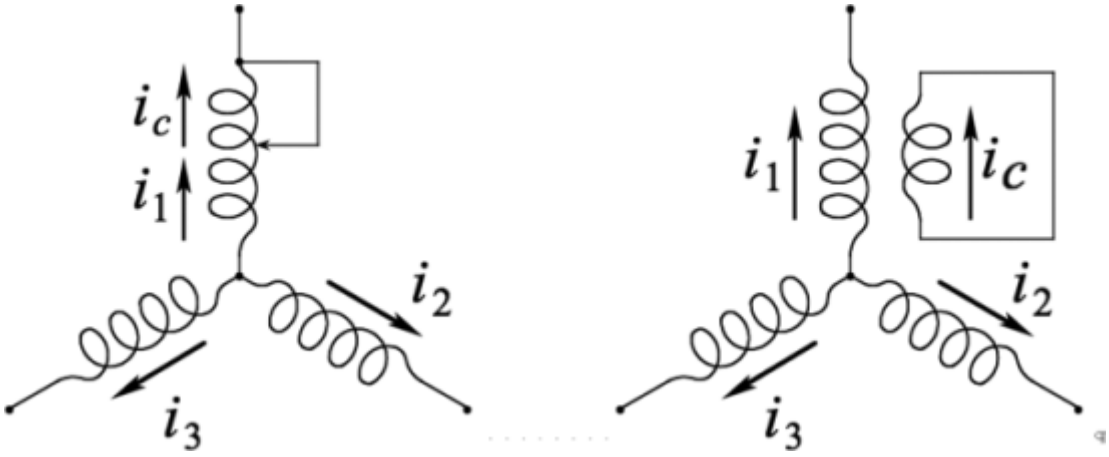

Figure 2.9: stator inter-turn short fault (left) and phase short circuit (right).

As shown in Figure 2.9, several additional issues can arise from an inter-turn fault. As the heat increases and the insulation degrades, coil-to-coil shorts, phase open circuits, phase-to-phase shorts, and coil-to-ground faults may develop, leading to significant operational problems, as discussed earlier in this chapter. However, inter-turn faults are difficult to detect, and if left unaddressed, they can cause severe damage, as previously mentioned. Therefore, early detection of this fault is crucial to reduce the operational and maintenance costs of the machine [38].

These types of faults create a voltage imbalance within the machine, which is a key point of interest in this study. Specifically, this study will explore how such imbalances can propagate through a powertrain topology.

2.2.4.2 Broken rotor bar

Broken rotor bars are exactly as the name of the fault suggests, one or more of the rotor bars within the squirrel cage rotor are broken. This can be illustrated in Figure 2.10 below.

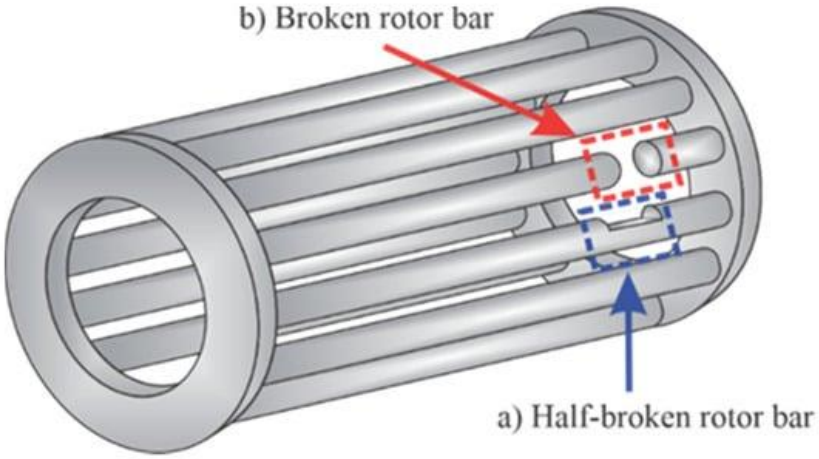

Figure 2.10: Illustration of what a broken and half-broken rotor bar means in an induction motor [39].

Rotor cages are typically manufactured in two ways: cast and fabricated. Cast rotor cages are used in motors up to 3000 kW, while fabricated rotor cages are used for motors exceeding this power rating. Cast rotors are more durable and rugged compared to their fabricated counterparts, but once damaged, they are impossible to repair [40].Since 90% of induction motors are squirrel-cage induction motors [41], the detection of broken rotor bars is highly relevant across various industries. A broken rotor bar can cause the adjacent bars to carry up to 50% more than the rated current, which can lead to further complications in the motor [41].

The primary causes of rotor cage failure include manufacturing defects, thermal stress on the bars, mechanical stress on the rotor, magnetic stress caused by unbalanced magnetic vibrations and pull, and dynamic stresses due to pulsating torques and mechanical loads.

Induction machines are highly symmetrical electric systems due to the rotating magnetic field. As such, any fault that occurs within the machine will disrupt this symmetry, which can affect the overall performance [41].

2.2.5 Condition monitoring methods for induction motors

Condition monitoring of induction machines has garnered substantial research interest in recent years, due to its significant impact on ensuring the continuous operation of these machines in industry [42]. Early and accurate fault detection can lead to prompt maintenance, reducing the need for regular inspections and minimising downtime by allowing maintenance to be focused directly on the identified issues.

There are various condition monitoring techniques, with ongoing research exploring new methods, particularly with the rise of AI, which may prove to be a valuable tool in this field. This section will focus on three prominent methods of condition monitoring for induction motors: Motor Current Signature Analysis (MCSA), Park's Vector Approach, and the Extended Park's Vector Approach.

2.2.5.1 MCSA

Motor Current Signature Analysis (MCSA) is a diagnostic technique that involves measuring and analysing the stator currents of an induction motor to detect faults. The process typically requires transducers, such as precise current transformers, to monitor the stator current and identify any variations caused by faults within the motor [12]. When a fault occurs, harmonics appear in the measured currents due to the interaction between the motor's flux in the airgap and the resulting backwards-rotating field [43].

MCSA offers several advantages, particularly because it does not require direct access to the motor's internal components. Instead, it relies on measuring currents at the connecting terminals supplying the motor. This is especially beneficial in the context of electric vehicles (EVs), where phase current measurements are already necessary for control algorithms, such as Field-Oriented Control (FOC) [44].

The stator current measured during Motor Current Signature Analysis (MCSA) can be transformed into the frequency domain using the Fast Fourier Transform (FFT) algorithm. This allows users to examine the current in its frequency spectrum, where specific components can be linked to mechanical or electrical faults [45]. Further elaboration on this technique will be provided later in the thesis.

However, MCSA is most effective under steady-state conditions, and its accuracy can be compromised by the averaging of spectral amplitudes over the sampling time, leading to potential errors [46]. As such, this method has certain limitations, particularly in the context of electric vehicles (EVs), where the operating conditions are frequently dynamic and not always steady-state.

While MCSA provides a solid foundation for fault detection, the following methods aim to extend its capabilities and improve its accuracy.

2.2.5.2 Park's vector approach

When the two quantities, i_d and i_q are plotted together such that $f(i_d) = i_q$, a circular plot is generated. This plot has its centre at the origin and a diameter equal to the stator current, representing the healthy state of the motor [13]. This method is beneficial because, in the presence of a fault, the curve may alter in shape and thickness, deviating from the healthy baseline. This provides a clear visual indication of a fault in the motor.

As shown in [14], this method has been effective in detecting various faults, such as shorted turn faults, and, in [22], the change in the circular shape is distinctly observed when an inter-turn short was introduced in the motor. This study also demonstrates the method's utility in detecting faults in both asynchronous (induction motors) and synchronous machines (e.g., PMSMs), making it a versatile tool applicable to a broad range of motor types. Furthermore, Abitha et al. [47] highlight the robustness of this approach, illustrating its effectiveness in simultaneously detecting multiple faults, which, although rare, provides a comprehensive view for making accurate repairs.

2.2.5.3 Extended Park's Vector Approach

The Extended Park's Vector approach, as the name suggests, is an extension of the basic Park's Vector method. This enhanced approach improves the utility of the original method by combining its simplicity with the added insights provided by spectral analysis [15].

The standard Park's Vector transformation assumes that the three-phase currents in the system are balanced, i.e.

$$i_a + i_b + i_c = 0 \tag{2.7}$$

In this scenario, it can be said that there is no negative sequence component, as the system's phases are balanced. However, an asymmetrical system generates a negative sequence component [48]. Positive, negative, and zero sequence components have been widely used to assess the level of voltage imbalance within systems, as described in [49], and these components can also be applied to the current of the machine. The presence of a negative sequence component typically signals that the system is not operating under ideal conditions. If the magnitude of this negative component increases significantly, it can indicate a serious fault within the machine. The presence of the negative sequence component can lead to increased heating in the machine [50], and it also generates a rotating magnetic field in the air gap that moves in the opposite direction [51]. This can reduce the motor's torque and introduce additional resistance, further stressing the system. The Extended Park's Vector approach is built around this concept, as, in the ideal scenario, the alpha-beta components of a stationary rotating reference frame of the machine can be represented by:

$$i_\alpha = \frac{\sqrt{2}}{\sqrt{3}} i_a - \frac{1}{\sqrt{6}} i_b - \frac{1}{\sqrt{6}}\, i_c \tag{2.8}$$

$$i_\beta = \frac{1}{\sqrt{2}} i_b - \frac{1}{\sqrt{2}} i_c \tag{2.9}$$

Which is like what was mentioned earlier in the chapter. This can then be simplified to

$$i_\alpha = \frac{\sqrt{6}}{2} i_+ \sin(\omega t) \tag{2.10}$$

$$i_\beta = \frac{\sqrt{6}}{2} i_+ \sin\left(\omega t - \frac{\pi}{2}\right) \tag{2.11}$$

This can be done as the transformation from phase components to positive, negative and zero sequence components can be shown in the matrix below.

$$\begin{bmatrix} i_0 \\ i_+ \\ i_- \end{bmatrix} = \begin{bmatrix} 1 & 1 & 1 \\ 1 & a^2 & a \\ 1 & a & a^2 \end{bmatrix} \begin{bmatrix} i_a \\ i_b \\ i_c \end{bmatrix} \tag{2.12}$$

Where 0, +, and – mean zero, positive and negative, respectively, and $a = e^{\frac{j2\pi}{3}}$ or e^{j120° . This is done in the phasor notation so $i_a,\ i_b$ and i_c represent the phasor notation of the respective currents. To detect a fault, the magnitude of these currents is taken and can be represented by the following equation.

$$|I| = \sqrt{i_\alpha^2 + i_\beta^2} = \sqrt{i_+^2 + i_-^2 + 2 i_+ i_- \cos(2\omega t)} \tag{2.13}$$

Equation 2.13 indicates the additional presence of a harmonic at twice the fundamental frequency, which, in the Extended Park's Vector approach, is measured and can serve as an indicator of a fault. Under ideal conditions, where no faults are present, there would be no negative sequence component, and the magnitude of the current vector would align with the positive sequence component, as expected. The spectrum of this data is then analysed, and the variations in the harmonic content are used to assist in fault detection within the induction machine.

2.3 INVERTER OPERATION AND HARMONICS

An inverter is an electrical device that converts a DC voltage or current source into an AC source. These inverters are commonly used in AC motor drives, where they provide a sinusoidal output, with both magnitude and frequency controllable [52]. The basic structure of a single-phase inverter is illustrated below in Figure 2.11.

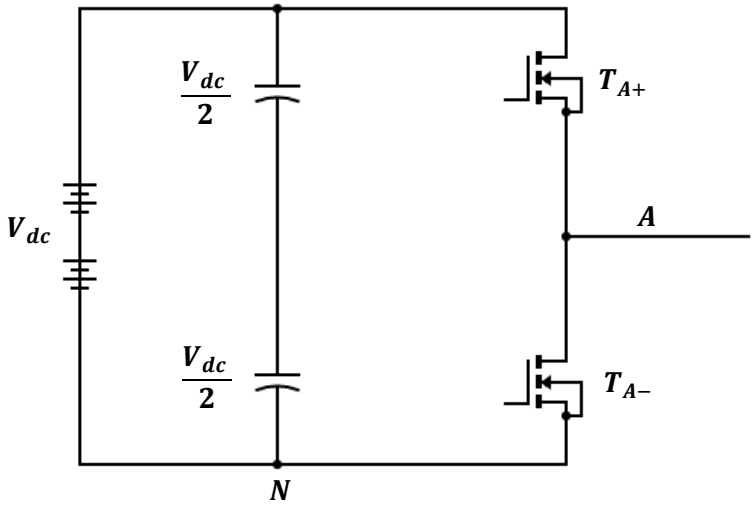

Figure 2.11: Basic Schematic of a single leg of an inverter.

An inverter typically operates using a pulse width modulation (PWM) scheme, where a sinusoidal control signal is compared to a triangular waveform. The frequency of the triangular waveform, known as the switching frequency f_s, is a critical factor to consider when designing a system that incorporates an inverter. This switching frequency is usually kept constant, along with its magnitude. The magnitude of the triangular waveform forms the basis for the modulation index, which is the ratio of the magnitude of the control signal to the magnitude of the triangular signal. This relationship is expressed in the formula below.

$$m = \frac{M_{control}}{M_{triangle}} \tag{2.14}$$

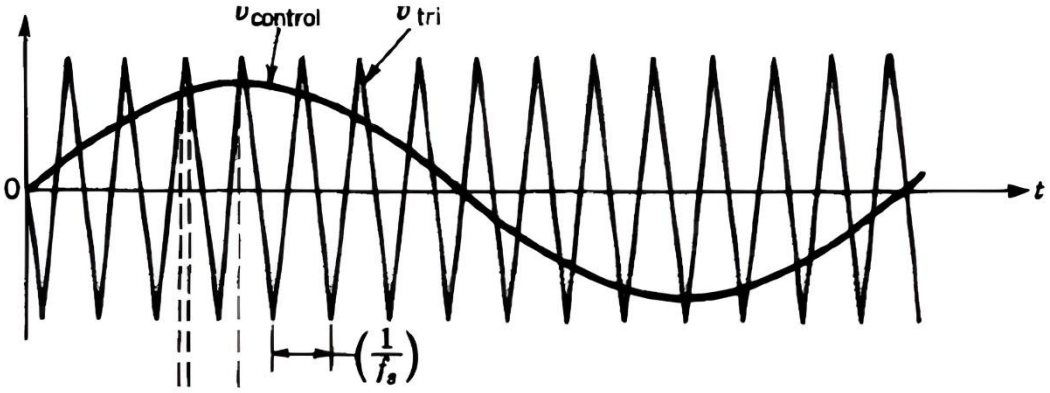

Figure 2.12: Visual representation of the control and triangular signal being compared when used in the PWM scheme [52].

This comparison can be shown visually above in Figure 2.12. This comparison is the basis for when to turn on and off the switches in each phase of the inverter, when $v_{control} > v_{triangle}$ then T_{A+}, as is Figure 2.12, is closed and current can flow through it, in the opposite case, T_{A-} is closed and $T_{A+}$is open, causing a different directional current flow to occur in that phase. A visual representation of this can be shown below in Figure 2.13.

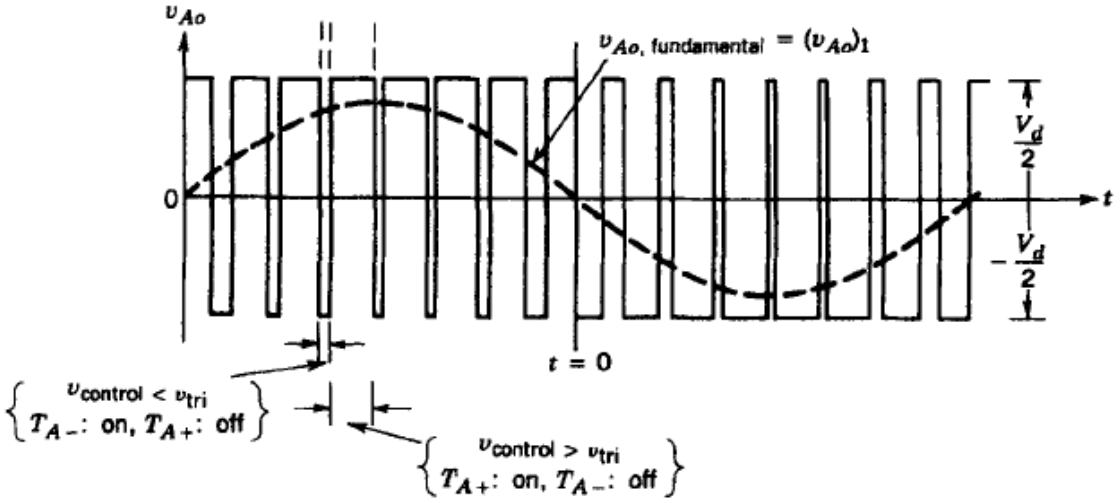

Figure 2.13: Visual representation of the output of a single phase of an inverter and when the switches are on and off [52].

This same principle is then applied to all three phases, with the control signals for phases B and C being 120 degrees offset from phase A, either in the positive or negative direction. As shown in Figure 2.13, an ideal sinusoidal output is not directly produced due to the generation of several harmonics during the process of converting DC power into AC power. The fundamental harmonic component can be expressed by the following equation:

$$(v)_1 = m \sin(\omega_1 t) \frac{V_d}{2} \tag{2.15}$$

where V_d is the DC voltage on the inverter. When focusing on the magnitude, it can work out to:

$$\widehat{V_1} = m \frac{V_d}{2} \tag{2.16}$$

As long as $m \leq 1$ [52]. The harmonics present often appear as sidebands centred around the switching frequency and around its multiples. This multiple can be defined as the frequency modulation ratio (m_f) which can be represented by:

$$m_f = \frac{f_s}{f_1} \tag{2.17}$$

where f_1 is the desired fundamental frequency of the output of the inverter. For sinusoidal PWM, the frequencies at which harmonics occur can be indicated by:

$$f_h = (jm_f \pm k) f_1 \tag{2.18}$$

where *h* is the harmonic order with the *kth* sideband of *j* times the frequency modulation ratio [52]. This can be best represented in Figure 2.14 below with calculations for a variety of modulation indices and the harmonics surrounding different multiples of the modulation frequency.

h \ m	0.2	0.4	0.6	0.8	1.0
1 Fundamental	0.2	0.4	0.6	0.8	1.0
m_f	1.242	1.15	1.006	0.818	0.601
$m_f \pm 2$	0.016	0.061	0.131	0.220	0.318
$m_f \pm 4$					0.018
$2m_f \pm 1$	0.190	0.326	0.370	0.314	0.181
$2m_f \pm 3$		0.024	0.071	0.139	0.212
$2m_f \pm 5$				0.013	0.033
$3m_f$	0.335	0.123	0.083	0.171	0.113
$3m_f \pm 2$	0.044	0.139	0.203	0.176	0.062
$3m_f \pm 4$		0.012	0.047	0.104	0.157
$3m_f \pm 6$				0.016	0.044
$4m_f \pm 1$	0.163	0.157	0.008	0.105	0.068
$4m_f \pm 3$	0.012	0.070	0.132	0.115	0.009
$4m_f \pm 5$			0.034	0.084	0.119
$4m_f \pm 7$				0.017	0.050

Note: $(\hat{V}_{Ao})_h/\frac{1}{2}V_d$ [$= (\hat{V}_{AN})_h/\frac{1}{2}V_d$] is tabulated as a function of m

Figure 2.14: Table of calculations for harmonics for SPWM for different values of m [52].

Finally, a visual representation of this type of spectrum can be seen below.

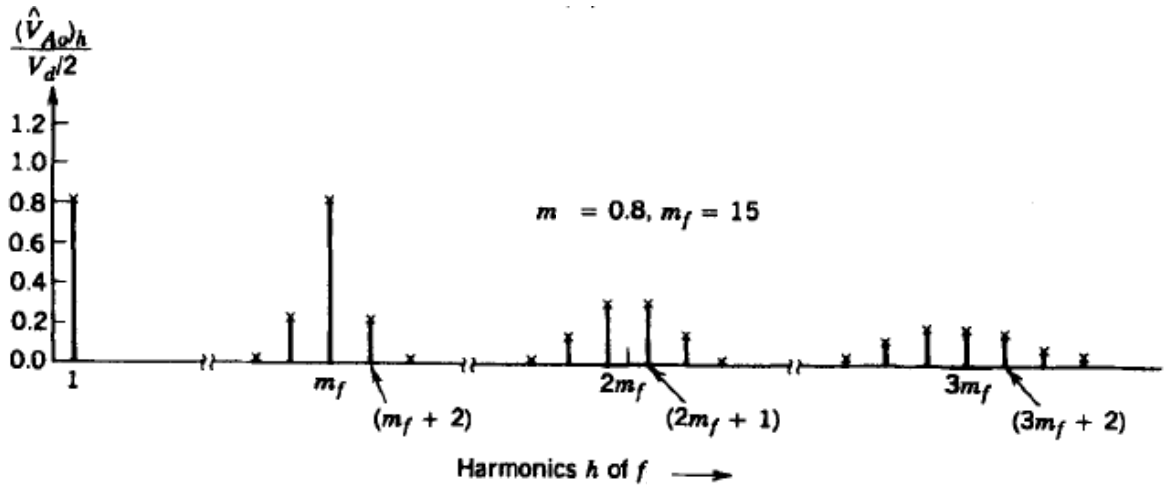

Figure 2.15: Theoretical Harmonic spectra of the output of an inverter [52].

2.3.1 DC Bus Harmonics

The harmonics on the input of the inverter are directly affected by the harmonics presented by the harmonics generated at the output of the inverter. This can be seen as:

$$\boldsymbol{i_{dc} = s_a i_a + s_b i_b + s_c i_c} \tag{2.19}$$

With s_x , $x \in a, b, c,$ being the switching function of each phase, respectively [9, 53]. These switching functions are specific to each pulse width modulation (PWM) scheme and, consequently, each scheme will produce varying spectral characteristics when analysing the DC bus current of the inverter. This current will exhibit both a DC value and harmonics resulting from the switching function. The presence of these current harmonics can negatively impact the lifetime of the DC-link capacitors [7] of the inverter, as well as the DC filter components.

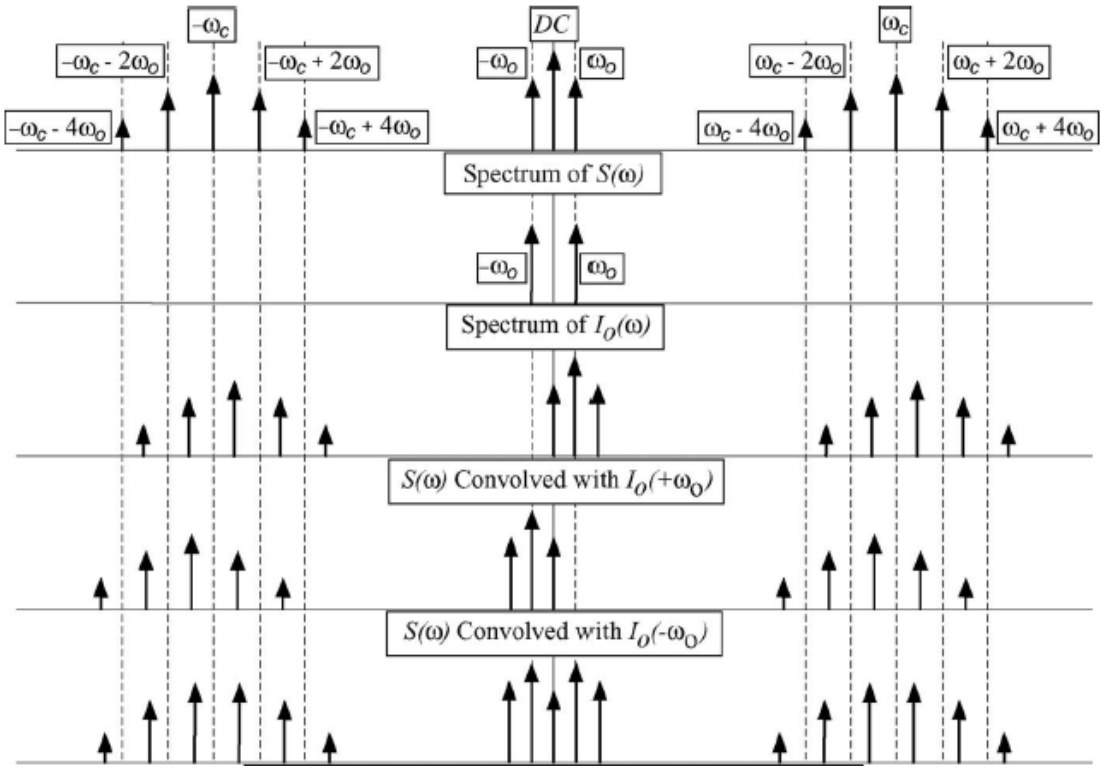

Figure 2.16: Visual representation of how the DC current spectrum is formed with the output current I0 and switching function S [54].

As can be seen in Figure 2.16, the DC current of an inverter contains many high-order harmonics due to the high-frequency switching signals within the inverter [55]. However, under certain undesirable conditions, lower-order harmonics can emerge. One such condition is a voltage unbalance at the output of the inverter, which can generate harmonics at lower frequencies, particularly around twice the fundamental frequency [7]. This will be further explored in the next chapter. It is important to highlight this, as it can significantly impact the DC-link capacitors of the inverter. These capacitors are typically electrolytic in type, and as such, they have a high equivalent series resistance (ESR), which increases notably at lower frequencies. These observations can prove useful in determining critical points on which to focus when designing an inverter, as well as point to issues that may be faced if components start to fail within the inverter's DC link, and what effect that may have on the battery.

2.4 APPLICATION IN EVS

2.4.1 Powertrain

Powertrains in electric vehicles (EVs) can vary in configuration, but the basic setup typically includes a battery and battery management system, a motor, and an inverter/motor drive unit. Additional components may also be included, such as a DC/DC converter to manage different voltage levels required throughout the vehicle, as well as systems for accurate battery charging.

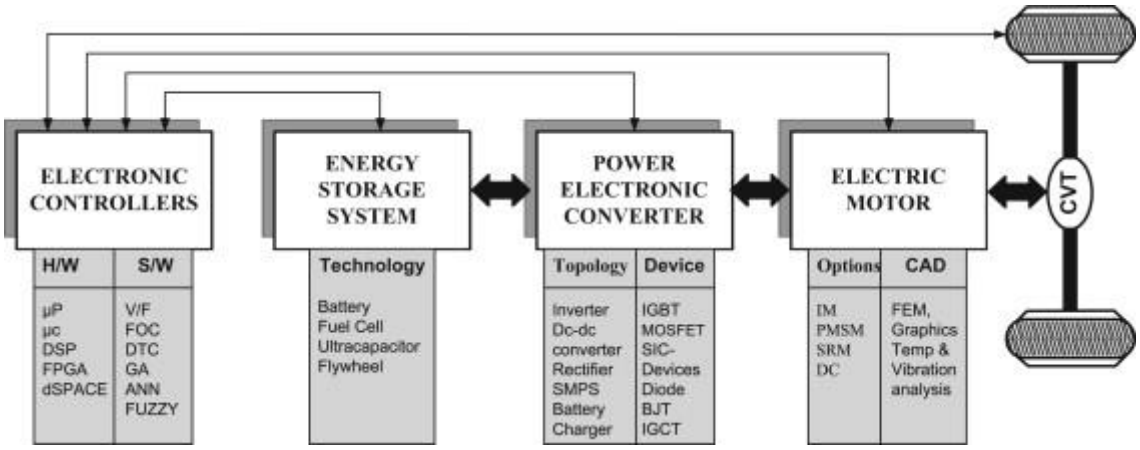

Figure 2.17: A functional block diagram of an electric powertrain [56].

Figure 2.17 illustrates this setup concisely, highlighting different options for selecting components such as the inverter devices, motor types, and the software used for modelling and analysing the powertrain.

Although electric vehicles (EVs) fall into four main categories: Battery Electric Vehicles (BEV), Hybrid Electric Vehicles (HEV), Plug-in Hybrid Electric Vehicles (PHEV), and Fuel Cell Electric Vehicles (FCEV). One might assume that their components would vary. However, they all require the same basic components, as shown in Figure 2.17 above. A comparison of these categories is provided below.

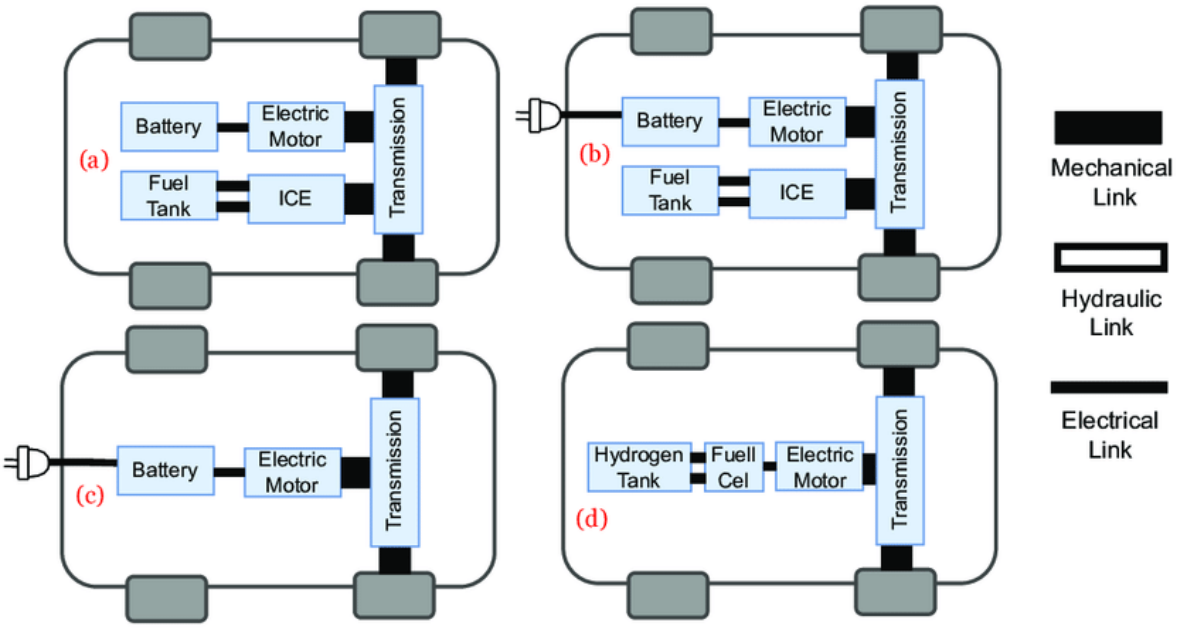

Figure 2.18: 4 different topologies of electric vehicles, a) hybrid EV (HEV), b) Plug-in Hybrid (PHEV), c) Battery EV (BEV), and d) Fuel cell EV (FCEV) [57].

2.4.2 Motor Control and Harmonic Analysis

As mentioned earlier, there are several ways to control an electric motor. However, electric vehicles (EVs) have unique performance demands. While typical industrial applications often require motors to run for extended periods at a constant speed, albeit with varying loads, EVs experience frequent start/stop operations along with high acceleration and deceleration requirements [58]. EVs also need to deliver high torque density and power across a wide range of operational speeds, with high starting torque and consistent power at steady-state speeds [59]. These demands necessitate more complex control algorithms than those needed for industrial motors that only deal with varying loads.

Several control methods can meet these requirements, including direct torque control and field-oriented control. However, as the level of intelligence and integration in control systems continues to improve, methods such as fuzzy control, sliding mode control, and neural networks have become areas of focus for development [60].

Harmonic analysis is critical for fault detection in electric motors, as mentioned earlier. Due to the nature of the electric powertrain, current and voltage harmonics are common, which can induce additional losses in cables and filters throughout the powertrain [61]. These losses can have a cascading effect, potentially accelerating the ageing of the battery system and causing malfunctions in the battery management system [62]. The importance and application of harmonic analysis in EVs will be discussed in the next section.

Harmonic analysis also plays a key role in ensuring that all components in the powertrain are operating as expected and can be used during the design phase of the powertrain. For instance, the minimum required DC-link capacitance in an EV powertrain is determined by the allowable voltage variation caused by load current harmonics [63]. In addition to the fault

diagnostic techniques discussed earlier, harmonic analysis can be applied to a range of strategies in the EV sector.

2.4.3 Implications for Battery System

The battery is a crucial component of an electric vehicle (EV), and ensuring its proper operation is vital when designing the vehicle's powertrain. Electrical faults and the harmonics they introduce can reduce the lifespan of various components, thereby decreasing the overall life expectancy of the EV [64]. Given that the battery pack is often one of the most expensive parts of the EV, preventing faults in the system is essential. Any faults or added harmonics can generate excess heat [65], which may affect the battery. As noted in [66], this can lead to an increase in the temperature of the battery cells, potentially causing a short circuit within the pack.

A key safeguard for the battery within EVs is the DC-link capacitor bank. The DC-link capacitor plays a vital role in several functions, such as providing reactive power, absorbing current ripple, attenuating electromagnetic interference (EMI), and suppressing surge voltage caused by leakage inductance and the switching operations of the inverter [67]. As mentioned earlier, faults in the powertrain can introduce additional harmonics onto the DC bus, particularly at lower frequencies. The equivalent series resistance (ESR) of the capacitor increases at these lower frequencies, causing higher temperatures within the capacitor and potentially leading to failure. This makes harmonic analysis critical, as it can help determine the stress levels on the DC-link capacitors and indicate when replacement is necessary.

This is particularly important because the DC-link capacitor is often the largest and heaviest component in the inverter [68]. The additional harmonics produced by faults can directly impact the capacitor, which in turn affects the battery. If the capacitor deteriorates, all the harmonics on the DC bus are transferred to the battery, potentially causing ripple currents on the DC bus. This increases the RMS (root mean square) value of the current and results in additional losses, which in turn raises the temperature of the battery [69]. Elevated temperatures are a major contributing factor to the ageing of lithium-ion battery cells.

Thus, unwanted harmonics play a significant role in reducing the lifespan of an EV, making harmonic analysis a crucial tool for fault monitoring and necessary for the design of DC filters to protect against faults in the system.

2.5 BATTERY SYSTEMS IN ELECTRIC VEHICLES

The battery system is becoming an increasingly vital component within a vehicle. This is because more car manufacturers move towards more electrification throughout their fleets for distinct reasons, such as meeting lower CO2 targets and catering to an increasing concern for environmental factors [86]. The batteries used are configured in such a way that it is called a battery pack. This battery pack consists of battery modules and battery management systems (BMS), amongst other smaller things that help it run efficiently and safely [70].

The modules themselves consist of many battery cells that are connected in a specific variation of series and parallel connections to achieve the desired Voltage ranges as well as the desired capacity for the specifications of the vehicle [70]. These cells consist of Lithium-ion batteries, as they have significant advantages in terms of the power, lifespan, and environmental impact that the cell has [71]. There are also disadvantages with these cells, as they do require battery cell protection circuits, and cell balancers, as well as being at a higher price compared to current alternative batteries [71]. This, along with the current cost of the battery pack coming out to about 60% of the total EV price [72], is a vital component to keep

in optimal health and extend its operation lifetime [73]. One aspect of this is the current discharge from the battery pack, which in turn affects the overall temperature of the cell if not done optimally. Thus, focus on additional harmonics on the DC bus current proves to be a vital focus of research in determining the effect of this on the life cycle of the battery.

There are, however, contradictory opinions surrounding the effects of harmonics and ripple currents on the lifespan of lithium-ion batteries. For instance, some studies, like Ghassemi et al. [74], suggest that ripple currents have a negligible negative impact on battery life, which has led to the oversizing of DC filter components in many designs. However, these studies did not report the temperature of the cells or the root mean square (RMS) currents, which could be critical in understanding the true impact of ripple currents. Moreover, their charging and discharging methods were highly controlled, which may not accurately reflect real-world EV usage. This discrepancy creates a gap in knowledge that this research aims to address.

Other studies, such as Barcellona et al. [74], emphasise the importance of considering both internal and external temperatures of the battery, arguing that previous research overlooked these factors in their conclusions. Temperature is a key element in the ageing process of lithium batteries, and a more nuanced approach to understanding how ripple currents and temperature interact is needed.

Another challenge is that much of the research on prolonging battery life focuses primarily on the charging process. Ruecker et al. [75], for example, present a charging algorithm designed to extend battery life, which is insightful but not directly applicable to discharging processes. While useful, this research underscores the need to monitor temperature, as it is a crucial factor in battery lifespan. Liu et al. [76] also provide valuable insights into the effects of harmonics on battery currents, particularly in grid-connected chargers. However, it concludes that eliminating these harmonics is critical for extending battery life, although this does not fully translate to EV applications.

While much of the research focuses on the charging phase or discharging with highly controlled ripple currents, there is little research on how these effects manifest within an EV drivetrain. This study aims to address these challenges and provide insights to fill the gaps in the existing literature, contributing to the advancement of research in this area.

2.6 CONCLUDING REMARKS

The preceding sections have explored the construction, operation, and control aspects of induction motors, highlighting common failure points and their potential causes. Various methods of condition monitoring were then discussed, focusing on how these techniques can be applied to detect faults within the motor. The discussion then shifted to how these concepts are relevant to electric vehicles (EVs), addressing the challenges and gaps in the current literature. Finally, the research focuses on bridging these gaps and contributing valuable insights to the field.

3 THEORY DEVELOPMENT

3.1 INTRODUCTION

The previous chapter reviewed the induction motor, its condition monitoring, and its application in electric vehicles. Spectral analysis of the motor current was discussed. This chapter will present the theoretical basis for this study.

3.2 PRINCIPLE OPERATION OF INDUCTION MOTOR

An induction machine operates by inducing a rotating magnetic field in the air gap between the stator and rotor. This magnetic field generates an induced voltage in both the stator and rotor. The machine has two modes of operation: in the generator mode, a rotating rotor induces a voltage in the stator. In motor mode, a three-phase voltage applied to the stator induces a voltage in the rotor, causing it to rotate.

The induced voltages in the stator and rotor are expressed by the following formula:

$$E = 4.44 f N_{ph} \Phi_p K_w \tag{3.1}$$

This formula is derived from Faraday's Law of Electromagnetic Induction, where:

f is the frequency of the applied voltage, N_{ph} is the number of turns in series per phase of the winding, $\Phi_p$is the flux per pole of the machine, and K_w is the winding factor [25].

The induced voltages generate currents that interact with the rotating magnetic field according to Lenz's Law. For motor operation, the rotor rotates in the direction of the magnetic field, reducing the relative speed between the rotor and the field. At a steady state, the rotor reaches a speed slightly less than the synchronous speed of the rotating magnetic field in the air gap. When $n = n_s$, no relative motion exists between the field and the rotor, resulting in no induced voltage, current, or torque. This characteristic classifies the machine as asynchronous.

The difference between the rotor speed and the speed of the rotating magnetic field is called slip, and is calculated by the formula below:

$$s = \frac{n_s - n}{n_s} \tag{3.2}$$

where n_s can be calculated using the following formula:

$$n_s = \frac{120 f_s}{p} \tag{3.3}$$

where p is the number of poles of the machine and f_s is the frequency of the supplied voltage to the stator. The above formula also describes the speed of the rotating field produced by the stator. The speed is measured in units of rpm.

The rotor's induced voltages also generate a rotating magnetic field, with its speed relative to the rotor, n_2 , expressed as:

$$n_2 = \frac{120sf_1}{p} \tag{3.4}$$

where f_1 is the frequency of the supplied voltages i.e. f_s, Substituting n_s from Equation 3.3, the formula simplifies to:

$$n_2 = sn_s \tag{3.5}$$

As the rotor rotates at a speed n and the rotating magnetic field moves at $n + n_2$ relative to the stator, simplifying and rearranging Equation 3.2 gives:

$$n + sn_s = (1 - s)n_s + n_s = n_s \tag{3.6}$$

This confirms that the field induced by the rotor rotates at the same speed as the field induced by the stator, relative to a stationary observer. The interaction of these fields generates torque [25].

3.2.1 Performance characteristics and efficiency

As previously discussed, an induction motor consists of a stator and a rotor, which can be viewed as the primary and secondary circuits of the machine, denoted by subscripts 1 and 2, respectively. This distinction is particularly useful because certain machine characteristics are determined by rotor parameters, while others depend on stator parameters, as will be demonstrated in this section.

An induction machine has several critical characteristics that must be considered, including power factor, current, starting, maximum torque, and efficiency. The power factor is expressed using the following formula:

$$PF = \cos(\theta) \tag{3.7}$$

The power factor is an important characteristic, as it determines the amount of useful power used for the supply and is something that can vary with the speed of the machine, as represented by the graph in Figure 3.1.

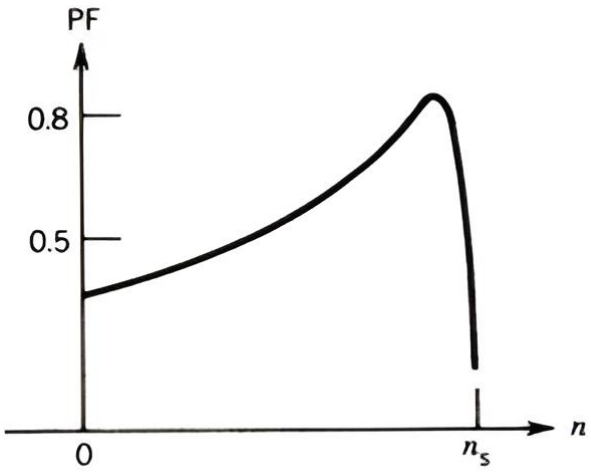

Figure 3.1: PF vs Speed of an induction motor [25].

Ideally, the power factor should be as high as possible to minimise losses and maximise the efficiency of the machine.

The mechanical torque and power produced by an induction machine can be represented by the following formula:

$$P_{mech} = T_{mech}\omega_{mech} = \frac{I_2^2 R_2}{s}(1 - s) \tag{3.8}$$

where $P_{mech}$is the mechanical power of the machine, T_{mech} is the mechanical torque of the machine, $\omega_{mech}$is the mechanical speed of the rotor of the machine, I_2 is the current present in the rotor, $R_2$is the resistance of the rotor, and s is the slip of the machine. Finally, the equation for rotational speed is

$$\omega_{mech} = \frac{2\pi n}{60} \tag{3.9}$$

which converts the speed from rpm to rad/s.

The equivalent circuit of the induction machine can be further analysed to show that the machine's mechanical torque is proportional to the square of the supply voltage [27]. This relationship is illustrated in Figure 3.2 below.

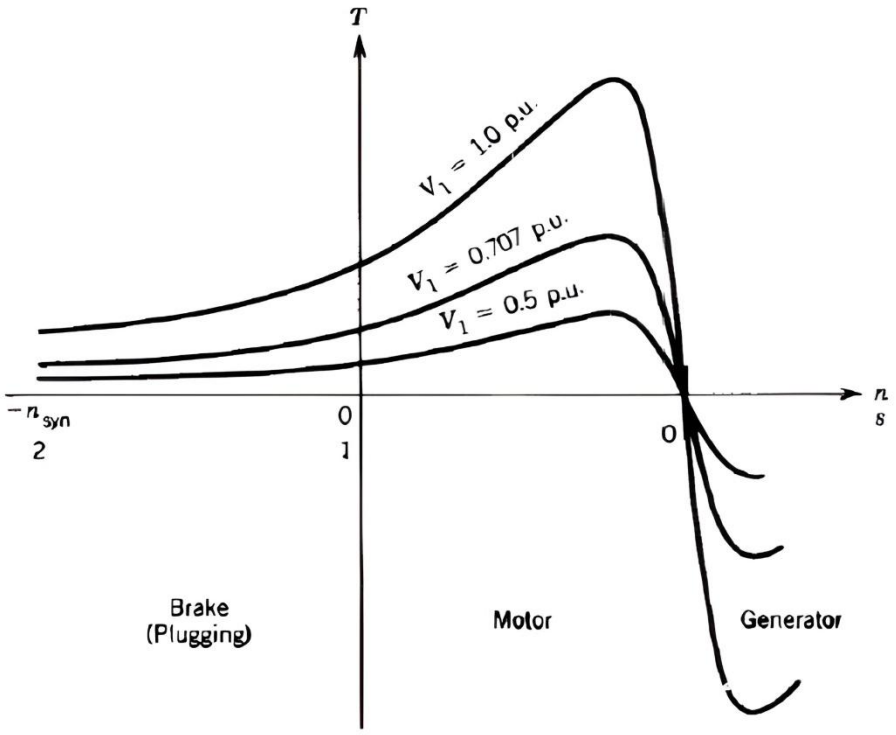

Figure 3.2: Torque vs speed graph of induction machine at varying voltages of the supply [25].

Further analysis reveals that the maximum torque produced by the machine is independent of the rotor resistance R_2. However, R_2 does influence the speed at which this maximum torque occurs [25], making it an important parameter to consider when designing an induction machine for different applications. This relationship is best illustrated in Figure 3.3 below.

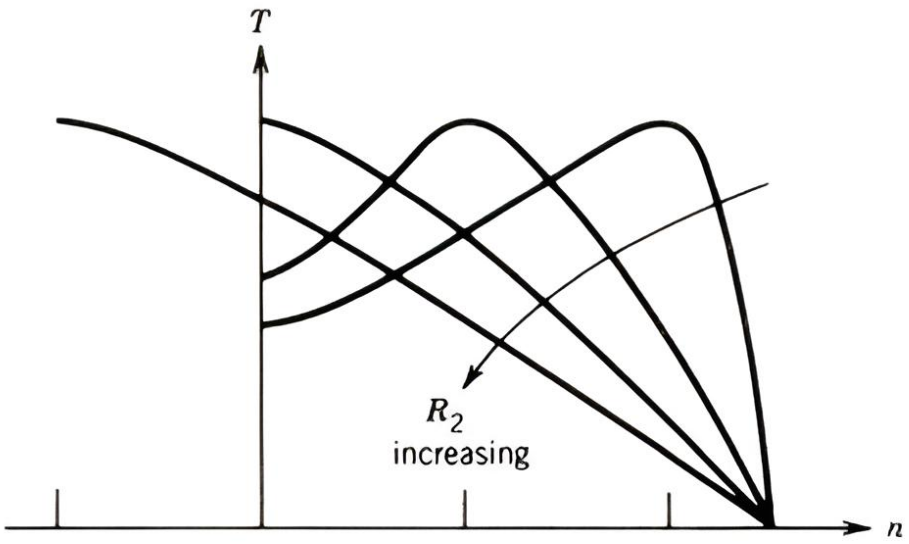

Figure 3.3: Torque vs Speed graph of an induction machine with varying values of R_2 [25].

The machine's efficiency is determined by analysing potential loss points, as illustrated in Figure 3.4 below.

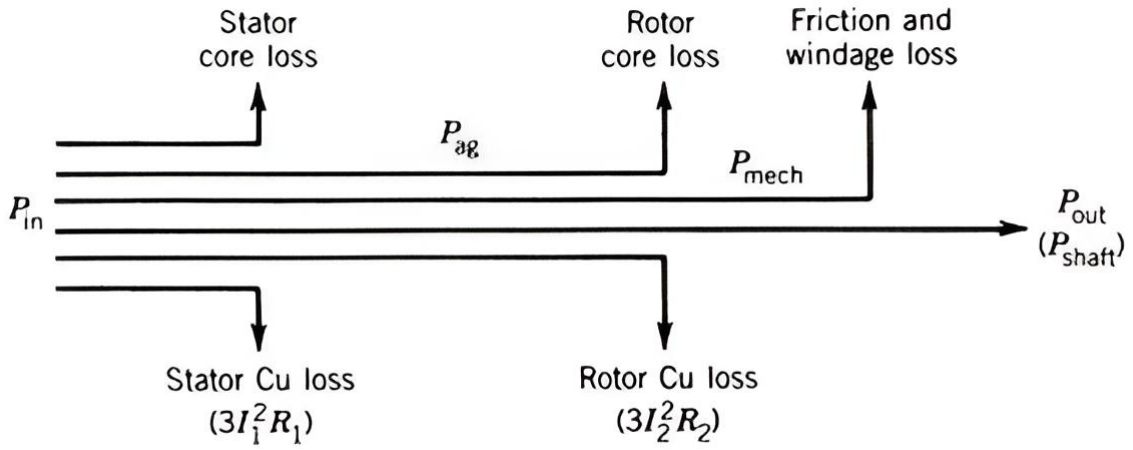

Figure 3.4: Diagram showing various points of power loss in an induction machine [25].

The input power of a three-phase machine can be determined using the following formula:

$$P_{in} = 3V_1 I_1 \cos(\theta_1) \tag{3.10}$$

with power losses in the stator and rotor being shown by the formula:

$$P_x = 3I_x^2 R_x \tag{3.11}$$

where $x = 1$ or 2 for stator and rotor, respectively. Other areas of potential loss in an induction machine include the stator core and rotor core, where power is lost as hysteresis and eddy current losses in the magnetic material of the cores [25]. However, more emphasis is typically

placed on the stator core, as these losses are frequency-dependent, and the frequency in the stator is higher than in the rotor. Additionally, friction from the bearings or the rotating shaft can result in further power losses, which are dependent on the machine's speed. The remaining power is then reflected as output power on the shaft. The efficiency of the machine can be calculated using the following formula:

$$Efficiency = \frac{P_{out}}{P_{in}} \tag{3.12}$$

This efficiency is highly dependent on the slip. If losses, other than those experienced in the rotor, are neglected, the ideal efficiency of the machine can be calculated using the following formula:

$$Efficiency_{ideal} = 1 - s \tag{3.13}$$

In this case, when stator losses are ignored, in which case $P_{in} = P_{ag}$, $P_2 = sP_{ag}$ and finally $P_{out} = (1 - s)P_{ag}$ [25]. In this equation P_{ag} is the power present in the air gap of the machine. This illustrates the significant impact that slip has on the machine's performance and highlights the importance of operating as close to synchronous speed as possible to achieve higher efficiency levels.

3.3 FAULT SIGNATURES

Faults present within an induction machine each present with their own signatures, and the motor faults covered in the study, together with the signatures associated with each technique, are now presented below.

3.3.1 Stator Faults

Of the faults that occur in induction machines, stator faults are the second most common, according to research [21]. Therefore, detecting stator faults, particularly inter-turn shorts, before they cause further damage, is critical. The fault detection techniques that aid in this endeavour are presented below.

3.3.1.1 Motor Current Signature Analysis

Analysis of the stator current of induction motors with inter-turn faults reveals harmonic frequencies that are produced by this fault. These harmonics can be determined by the following equation.

$$f_{st} = f_1 \left[\frac{n}{p}(1 - s) \pm k\right] \tag{3.14}$$

where f_{st} is the holder denoting the stator fault frequencies, f_1 is the fundamental frequency of the system, p is the pole pairs of the machine, s is the slip on the machine, $k = 1, 3, 5$ and $n = 1, 2 \ldots (2p - 1)$. A typical visual representation of the frequency spectrum of an induction motor, with the presence of a stator inter-turn fault, can be seen below in Figure 3.5.

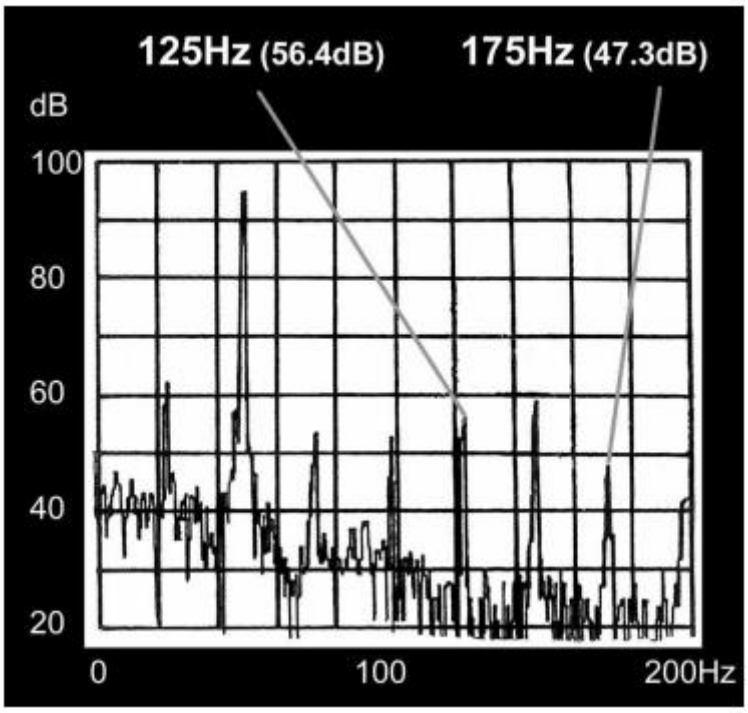

Figure 3.5: Frequency spectrum of stator current with inter-turn short [77].

3.3.1.2 Park's Vector Approach

The Park's Vector approach assists in visualising fault signatures. As mentioned earlier in Chapter 2, a circular plot can be plotted when plotting the d-q current values against each other, and a baseline can be derived when a motor is known to be running in a healthy state. Such a plot is shown below in Figure 3.6.

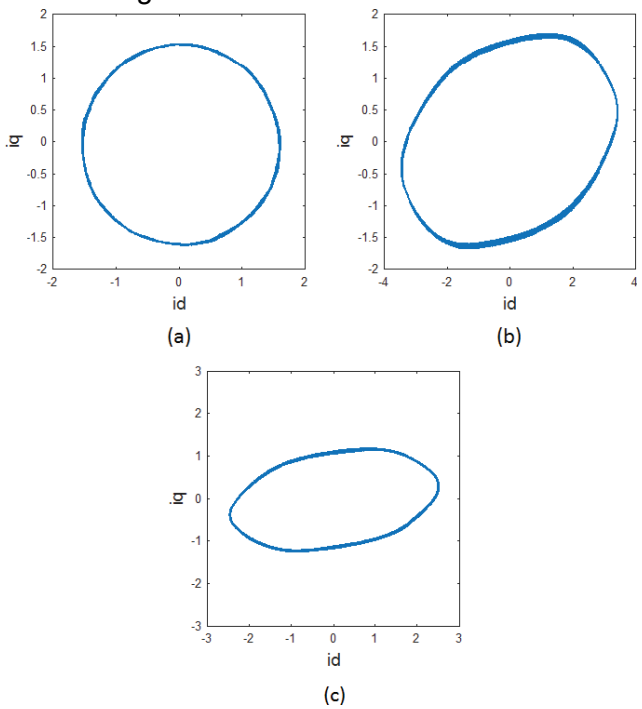

Figure 3.6: Park's Vector representation of a healthy motor (a) vs two cases of unhealthy motor (b) and (c) [78].

As can be seen in Figure 3.6, when a fault occurs in a motor, the normally circular Park's vector plot becomes a skewed ellipse due to the resulting three-phase unbalance. This provides a visual method for identifying the presence and severity of a stator short fault, with the elongation of the ellipse indicating the severity of the fault.

3.3.1.3 Extended Park's Vector Approach

The Extended Park's vector approach builds upon the techniques mentioned above by measuring the negative sequence component within the motor's three-phase system. As shown in Equation 2.13, the value of the harmonic at twice the fundamental frequency is measured and compared between healthy states and unhealthy states. A stator fault creates an unbalance in the three-phase system, thus increasing the value of the harmonic at twice the fundamental frequency. Thus, when the value of the harmonic increases above the baseline "healthy" value, the fault can be detected.

3.3.1.4 DC Bus

The DC bus is a crucial factor to monitor, as mentioned in the earlier chapter; however, it can also be used in aid of detecting faults through the drivetrain. The unbalanced system that occurs creates harmonics on the AC side, but as [7, 11] clarifies, there should also be the presence of this fault at a frequency of twice the fundamental on the DC bus. This can be shown by the following equation:

$$I_{dc} = \frac{3MI_{+}\cos\phi}{4} - \frac{3MI_{-}}{4}\cos(2\omega t - \theta) \tag{3.15}$$

where M is the modulation index on the inverter, ϕ is the positive sequence phase angle, and θ the negative sequence phase angle. This simplified formula indicates the magnitude of the DC current over one carrier period. However, it shows that an unbalanced load (i.e. presence of a negative sequence component) will produce a harmonic around twice the fundamental frequency in the DC currents' frequency spectrum. This mathematical understanding allows for analysis of the DC current, focusing on changes in the magnitude of the harmonic at twice the fundamental frequency to detect faults.

3.3.2 Broken Rotor Bars

Although less common than inter-turn short faults, broken rotor bar faults are a known issue in induction motors and can cause severe damage to equipment, making their detection a critical area of focus.

3.3.2.1 MCSA

A broken rotor bar within an induction motor will cause asymmetry within the system and produce a rotating airgap field in the opposite direction to the direction of the machine. This rotating field induces a current into the stator, which can result in both torque and speed

oscillations during the operation of the machine. This effect produces current components within the system, whose frequencies can be given by the equation below [79]:

$$f_b = f_1(1 \pm 2ks) \tag{3.16}$$

where f_1 is the fundamental frequency of the system, s is the slip of the induction motor and $k = 1, 2, 3$ etc. This results in a spectrum where additional harmonics will be present at $\pm 2 f_1 ks$ around the fundamental frequency. A comparison of the frequency spectrum of a machine with broken rotor bars and a healthy machine is shown below:

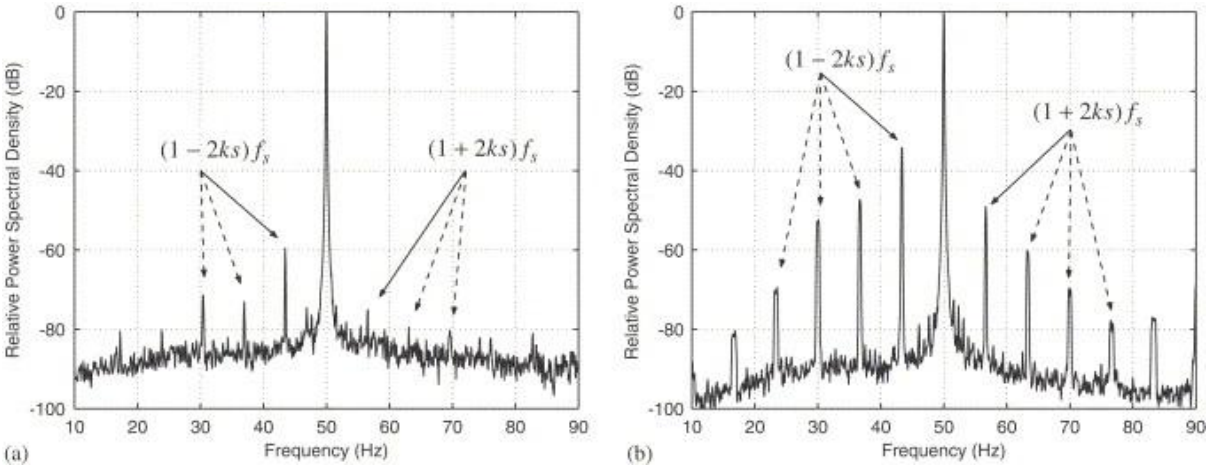

Figure 3.7: Line current frequency spectrum for a healthy motor (a) and a motor with a broken rotor bar (b) [80].

As can be seen in Figure 3.7, the frequency components of $\pm 2 f_1 ks$ around the fundamental, there is an increase in magnitude once there is the presence of a broken rotor, thus providing a useful metric to detect a broken rotor bar fault.

3.3.2.2 Park's Vector Approach

Park's vector approach applies to both broken rotor bar faults and inter-turn stator faults, but the results differ due to the nature of the faults. Unlike inter-turn faults, a broken rotor bar does not cause an imbalance in the system. However, Park's vector approach can still detect abnormal behaviour in the motor. In the case of a broken rotor bar, the key indicator is not the elongation of the plot, but rather the thickness of the circular plot. Increased thickness indicates a more severe broken rotor bar fault. A visual representation is shown in Figure 3.8.

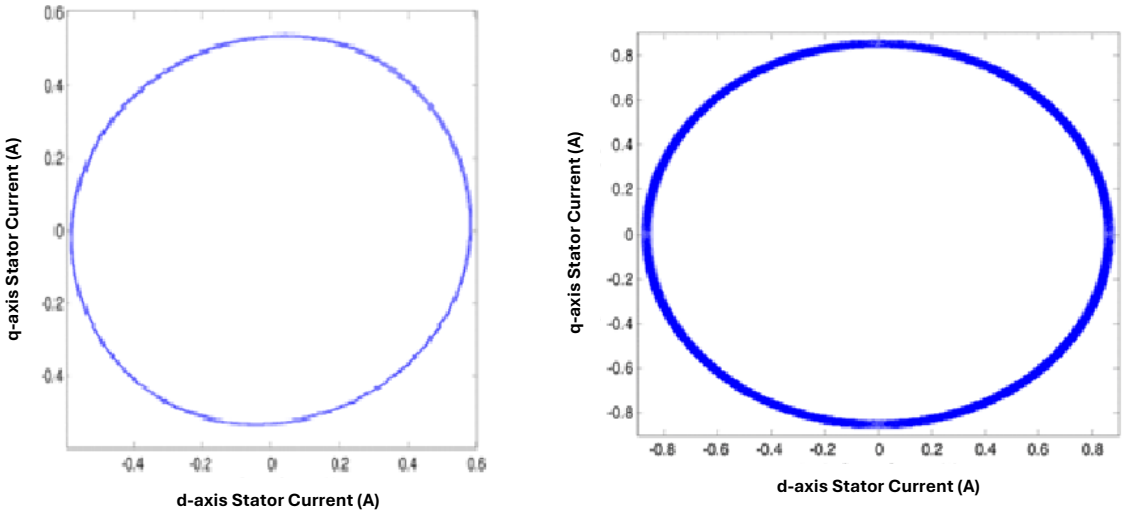

Figure 3.8 Park's vector approach with dq plot of healthy motor (left) and motor with 3 broken rotor bars (right) [81].

As can be seen above in Figure 3.8, in the presence of broken rotor bars, this method can provide useful information in detecting a broken rotor bar fault, as well as its severity within the motor.

3.3.2.3 Extended Park's Vector Approach

This approach is like the process used for detecting inter-turn faults, with a slight variation of the main formula. As was mentioned in the MCSA section, the presence of the broken rotor bars produces currents around the $(1 \pm 2ks)f_1$ frequencies, with $k = 1, 2, 3\ etc.$ Considering only the first sidebands of these harmonics, i.e. k = 1, the three-phase currents can be written as follows [82]:

$$i_x(t) = i_f \cos(\omega_s t - \alpha - \theta_x) + i_t \cos([1-2s]\omega_s t - \beta_t - \theta_x) + i_r \cos([1+2s]\omega_s t - \beta_r - \theta_x) \quad (3.17)$$

where i_f is the maximum value of the fundamental frequency current, i_t and i_r are maximum value of the lower and higher sideband currents, respectively. β_t and β_r are the phase angles of the lower and upper sideband, respectively. θ_x is the phase angle for each phase current, where $x = \{a, b, c\}$ and $\theta_x = \{0, \frac{2\pi}{3}, -\frac{2\pi}{3}\}$ for each of the three phases, and finally α is the phase angle of the supply phase current.

Assuming $\alpha, \beta_t, \beta_r = 0$, this information can then be used to manipulate equation (3.17) into becoming the following:

$$i_\alpha = i_f \cos(\omega_s t) + i_t \cos([1-2s]\omega_s t) + i_r \cos([1+2s]\omega_s t) \quad (3.18)$$

$$i_\beta = i_f \sin(\omega_s t) + i_t \sin([1-2s]\omega_s t) + i_r \sin([1+2s]\omega_s t) \quad (3.19)$$

The square of the modulus yields the following first four terms, which are

$$\left|i_\alpha + i_\beta\right|^2 = i_f^2 + i_r^2 + i_t^2 + i_f i_t \cos(2s\omega_s t) + i_f i_r \cos(2s\omega_s t) + i_r i_l \cos(4s\omega_s t) \quad (3.20)$$

As shown above, there is once again a presence of a term at twice the fundamental frequency as well as four times the fundamental frequency, suggesting useful frequencies to look at the Park's vector modulus to analyse if there is a presence of a fault. If the broken rotor bar is not present, then the only term left would be the fundamental frequency term.

3.3.2.4 DC Bus

To evaluate the effectiveness of monitoring the DC bus for the broken rotor bar fault, this analysis will also consider this scenario. While Equation 3.20, derived for inter-turn faults, does not strictly apply in this case, some imbalance is still present. Therefore, a fault harmonic around twice the fundamental frequency is expected, like what is shown in Equation 3.20. Given the limited existing research on this specific application, this study aims to establish a baseline for improving this fault detection method.

3.4 SIGNAL PROCESSING TECHNIQUES

Signal processing is essential for implementing the techniques discussed in this chapter. It allows the raw experimental data to be transformed into the various domains and forms necessary for the required analysis and drawing conclusions that further advance our understanding of this topic. All the data captured for this study were conducted under steady-state conditions of the motor, and the techniques chosen to be used for this study are presented below.

3.4.1.1 Fourier Transform

The Fourier transform mathematical technique that transforms a time-domain signal into the frequency domain [16]. The formula to complete this transformation is shown below:

$$X(\omega) = \int_{-\infty}^{\infty} x(t) e^{-j\omega t} dt \quad (3.21)$$

The inverse transformation is shown below:

$$x(t) = \frac{1}{2\pi} \int_{-\infty}^{\infty} X(\omega) e^{j\omega t} d\omega \quad (3.22)$$

However, since signals are captured digitally, the discrete Fourier transform (DFT) needs to be used as it can be defined for a finite number of signal values, n. The formula for this is shown below [83]:

$$X[k] = \sum_{n=0}^{N-1} x[n] e^{-\frac{jk2\pi n}{N}} \tag{3.23}$$

where $k = 0, 1, 2, \ldots . N - 1$. The inverse transformation is shown in Equation 3.24.

$$x[n] = \frac{1}{N} \sum_{n=0}^{N-1} X[k] e^{\frac{jk2\pi n}{N}} \tag{3.24}$$

The Fourier transform of the motor current signal is implemented using the fast Fourier transform (FFT) technique, which is the most common algorithm to use when processing data, as is done in this study [84].

3.4.1.2 Windowing and zero padding

Figure 3.9 shows the original data signal (top) and the windowed signal (bottom), with the applied window function overlaid in red [85].

The Fast Fourier Transform algorithm is extremely useful in processing data; however, it assumes that the data is periodic, or, at minimum, begins and ends at zero. Since this would rarely be the case, spectral leakage occurs, which causes the energy from the main frequencies to "leak" over the entire frequency spectrum of the signal [85]. While this cannot be eliminated, windowing can significantly mitigate its effects.

Windowing is achieved by applying a windowing function, which is a function that is of finite length and has an amplitude that varies smoothly and gradually toward zero at the edges of the window [86]. This waveform, when multiplied by the data waveform, ideally, causes the endpoints of the data to meet and result in a continuous waveform. This can be shown visually below, as well as the effect of several types of windows in the frequency domain.

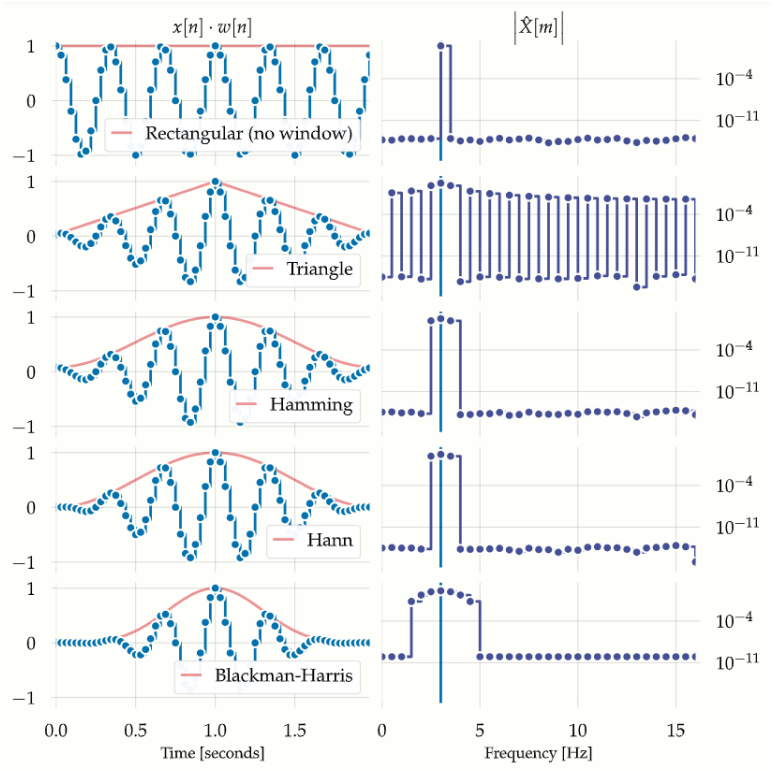

Figure 3.9: Figure showing the effect of different types of windows on a data signal [86].

Zero padding is the technique that would be employed to make the size of the input signal so that it is equal to a power of two [87]. This is done since the FFT algorithm is fastest when applied to a sample size that is a value that can be a power of two, i.e. 16. This aids in the speed of computation as well as enables you to gain more accurate amplitude estimates of the signals that you want to analyse [88].

3.5 CONCLUDING REMARKS

This chapter first explored the fundamental theory as it relates to the principal operation of induction machines, which established the foundation for understanding the behaviour in normal operation and in the presence of a fault. Furthermore, this chapter describes the theory of the selected techniques used in this study and provides a basis for analysing the relevant frequency components for fault detection. The techniques that are also typically applied for data capture were briefly explored, emphasising the role in accurate and effective fault detection.

4 MOTOR CONTROL DESIGN

4.1 INTRODUCTION

The previous chapter provided the theoretical basis for the study. This chapter outlines the connection setups for the test scenarios and the design choices made to establish the test rig for conducting the experiments. The details are outlined below.

4.2 DESIGN APPROACH

All the results from this chapter are obtained using MATLAB Simulink as the main tool for conducting the simulations. Since MATLAB Simulink would also be used to program the dSPACE controller for the laboratory tests, it was decided that this would provide a comparative set of results, as the source of programming is controlled. All control schemes and designs were derived using the literature review from this study as a basis for the setup of the simulation. Known values, such as rated values of the motor that would be used for the lab experiment, were used to tightly emulate real-world tests that would be conducted. The load torque was chosen based on preliminary lab tests and corresponds to the maximum torque the motor could handle on the test bench. The controller's proportional and integral values were chosen based on an empirical tuning method and trial and error to get satisfactory results in stability and response time. As the primary focus of this study was not controller optimisation, a more in-depth approach was not considered.

4.3 FILTER DESIGN

The filter design is a crucial aspect of this experiment as it will filter out unwanted high-frequency harmonics that are present in an inverter-connected system. Using the technique outlined in [89], the filter can be designed accordingly.

Since the measured motor parameters in Table 5.2 have been gathered, the design process can begin.

Firstly, the resonant frequency needs to be found and can be determined by the equation, taken from Mishra et al. [90], below.

To calculate the initial inductance value, L_i , the following formula for [91] can be used:

$$L_i = \frac{V_{dc}}{8 * f_{sw} * \Delta i_{inverter}} \tag{4.1}$$

where $\Delta i_{inverter}$ is the desired ripple current value of the inverter; in this case, it was chosen to be 10% of the max rating of the motor, being 1.85A. f_{sw} is the switching frequency and V_{dc} is the DC voltage of the system.

Filling in all the values, it equates to:

$$L_i = \frac{320}{8 * f_{sw} * 0.1 * 1.85} = 21.6mH \tag{4.2}$$

Since the nearest value to this in the lab was a 25.2mH this was used, since this would result in a smaller ripple current, which is desirable in this case. A larger inductor was also chosen firstly to have a lower ripple current, and secondly to decrease the size of the filter capacitor. Since the motor already has high inductance, it is best to use that to the advantage of the design of the filter.

The next step is to calculate the desired filter capacitance, and for this, the resonance frequency of the filter circuit needs to be decided. Now with the constraints of:

$$f_g \ll f_{res} < f_{switching} \tag{4.3}$$

where f_g is the grid frequency. The resonance frequency needs to be chosen such that it falls somewhere between these values. Since this experiment requires signal analysis on lower-order harmonics, a resonance frequency closer to the fundamental frequency was chosen. For this filter design, the exact value was 1000Hz, far enough away from either frequency so it would not interfere with either. The lower resonance frequency also aids in filtering out higher frequency components, which is essential for the low switching frequency used in this system.

Using the chosen resonance frequency, the formula below can be used to calculate the capacitor value.

$$f_{res} = \frac{1}{2\pi}\sqrt{\frac{L_i + L_g}{L_i L_g C}} \tag{4.4}$$

which once rearranged gets a value of : $C = 2.1791\mu F$ The nearest value component for this was 2.2μF capacitor, which once put into equation (4.4), gives us a resonant frequency of $f_{res} = 956.49Hz$ which is still close to the chosen resonance frequency. Next is the dampening resistor that needs to be calculated. Using the formula below, this can be calculated to help dampen the frequencies and aid the performance of the filter. This is calculated as follows:

$$R_f = \frac{1}{\omega_{res} C_f} = 75.6336\Omega \tag{4.5}$$

However, this value seems significantly too high to produce a highly efficient filter, as a larger resistor would have a larger power dissipation, thus a much more conservative number of 10Ω was chosen for this.

With all these values, the filter can now be implemented. However, the desired results were not what was expected. There were additional ripples on the output current waveform, as can be seen below in Figure 4.1.

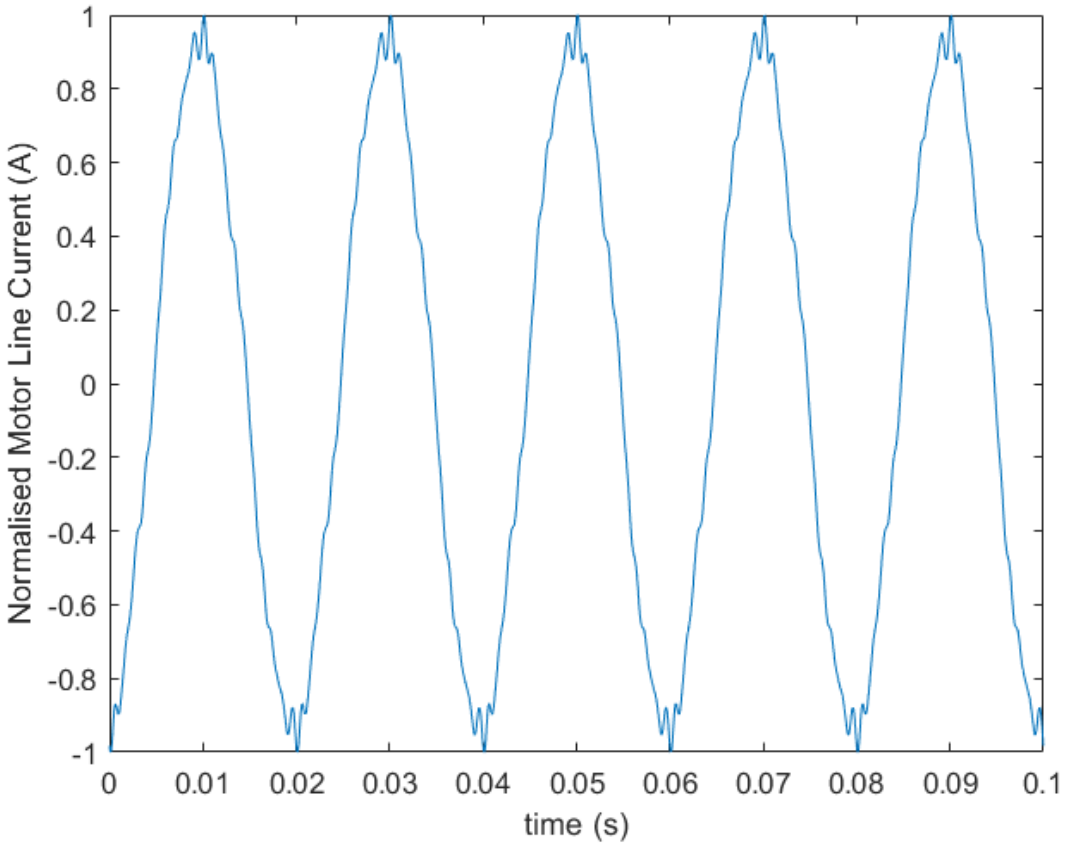

Figure 4.1: Motor line current utilised in the initial filter design.

The calculated Total Harmonic Distortion (THD) of the current was 5.21%, which is not good enough as set out by the guidelines in [89]. The main contributor to this THD was found at the 950Hz component, which is to be expected due to the resonance frequency. Thus, adjustments needed to be made. One would need to decrease the resonance frequency of the circuit so that the filter can attenuate the higher-frequency components more efficiently. The new target resonance frequency is 800Hz, and the same steps above follow.

This could be done by either increasing the capacitor value or by adding additional inductance to either the initial inductor or adding additional inductance after the capacitor. It was decided to add an inductor after the capacitance, as the initial performance choices were desirable in terms of the ripple current allowed. To achieve this frequency, the initial inductor value would need to be 62.9mH, which, as a single component, is a large and bulky component. Thus, the decision was taken to add it to the motor side of the filter, to have smaller components in size

but with more in number, and this can be achieved by using the already present inductance from the motor. Thus, the additional inductance would need to be:

$$L_g = L_{lr} + L_{ls} + L_{additional}$$

$$62.9mH = 12.57mH + 12.57mH + L_{additional}$$

$$L_{additional} = 37.7mH$$

which is about 50% larger than the initial inductance used, but still smaller than a single 62.9mH inductor. The closest component that was used was 37.5mH, which resulted in a resonance frequency of 800.44 Hz. This results in a much cleaner current signal, which is desirable and can be seen below in Figure 4.2.

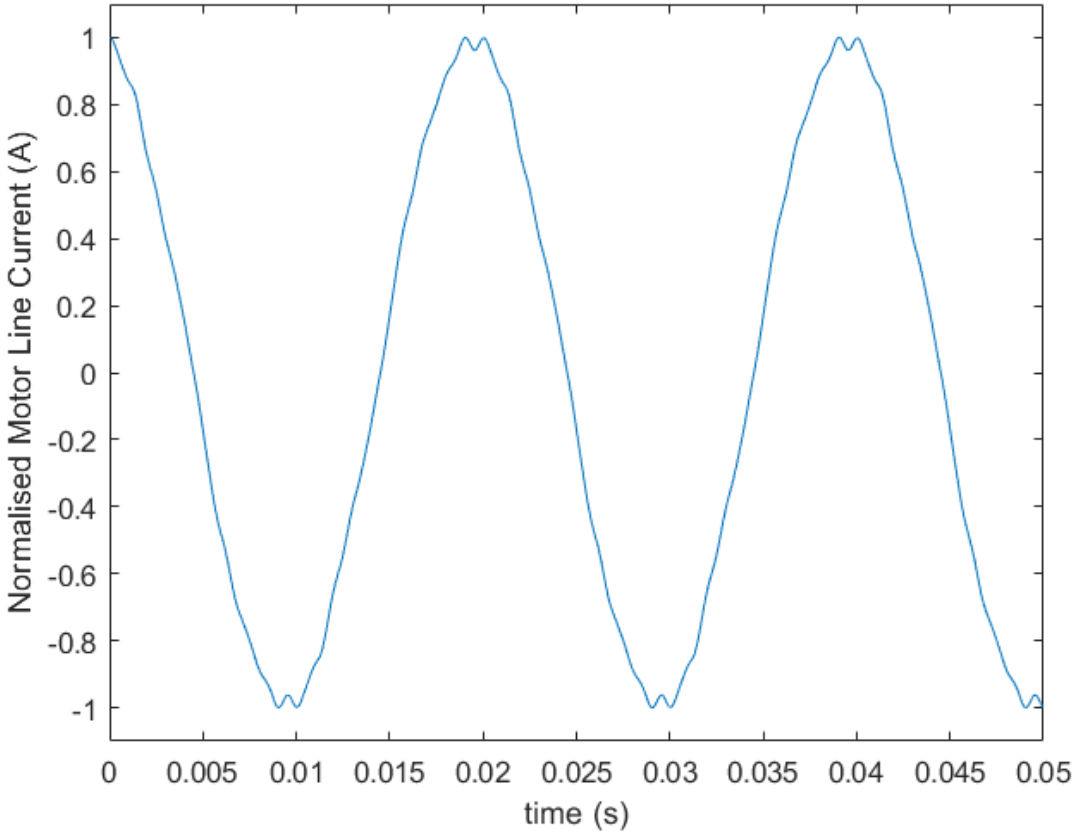

Figure 4.2: Motor line current simulation with additional inductance.

The THD calculated using this new filter design came out to be 2.54%, which fits into the guidelines set out by [89]. Thus, this is the finalised filter design that was used for these experiments, as shown in Table 4.1 below.

Table 4-1: Table of final filter values for the designed LCL filter.

Filter Components	Values
Initial Inductor	$25.2mH$
Filter Capacitor	$2.2\mu F$
Filter Dampening Resistor	10Ω
Secondary Inductor	37.5mH

4.4 CONNECTION SETUPS

The source connections and control methods for the motor need to be established. This was done to generate various test scenarios for this study's hypothesis. The block diagrams for the control strategies are shown in the following subsections, and the setups were done as follows.

4.5 MOTOR CONTROL CONFIGURATION

4.5.1 Load Conditions

The two load conditions chosen for the simulations and experiments, namely 0.8Nm and 0.2Nm, represent 100% and 25% load of the motor, respectively. The experiments were only conducted at 25% load torque.

These values are based on the following assumptions. Assuming an average speed of 100 km/h—typical for urban highway environments that frequently exhibit transient speed profiles—most electric vehicles (EVs) consume approximately 19 kWh of energy over the course of an hour [92]. Under the assumption of a constant speed of 100 km/h, this corresponds to an average power output of 19 kW. Given that EV motors typically have power ratings ranging from 100 kW to 300 kW, depending on the vehicle type [92], this results in an average power usage ranging from approximately 19% to 6.33% of the motor's rated capacity. While there is inherent variability in power demand due to acceleration, deceleration, and other dynamic factors, this range provides a reasonable baseline for the average power consumption of an EV motor during highway driving conditions.

It is also important to note that fault signature detection becomes increasingly challenging at low load conditions, primarily due to the reduced signal-to-noise ratio in the acquired data, particularly for current-based fault detection methods [93]. Consequently, faults that can be detected at low loads are generally more easily identified at higher load levels.

This is further highlighted in [94] where it is noted that fault signatures are difficult to detect at low slip levels, which does happen at lower load torques. Finally, the desire to conduct these tests at lower loads is that it serves as an earlier detection system, as well as potentially avoiding further damaging the motor at high loads [95].

4.5.2 V/Hz open-loop controlled inverter connected motor

V/Hz open-loop control is one of the simplest ways to control an induction motor, as can be seen by Figure 4.3 below, which outlines its general operation as well as its various variables and inputs.

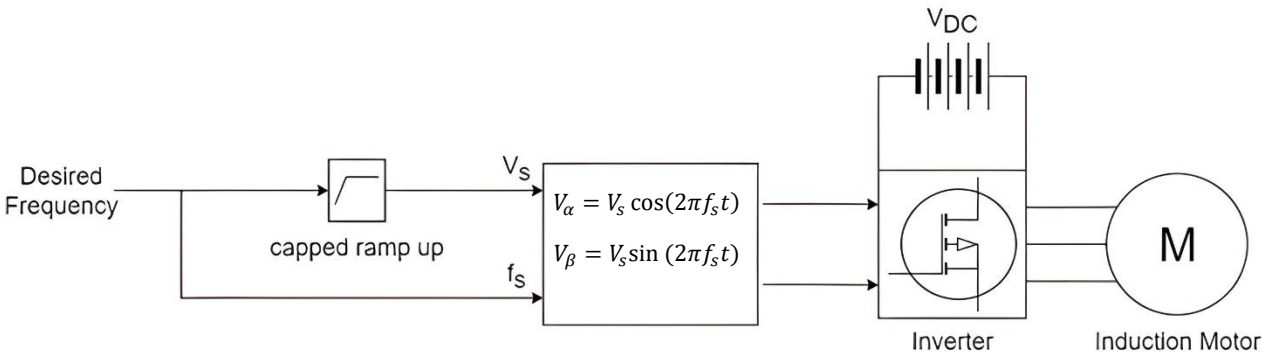

Figure 4.3: Block diagram showing the general operation of the V/Hz open-loop operation.

The above system in Figure 4.3 was implemented for the open-loop V/Hz tests, with the desired frequency set at 50Hz. The lookup table block acts as a gain, G, where the proportionality of it relates to the following formula.

$$G = \frac{V_{max} - V_{min}}{f_{max} - f_{min}} \tag{4.6}$$

With $V_{max} = 190, V_{min} = 0, f_{max} = 50$ and $f_{min} = 0$, with the upper and lower limits being constrained to 190 and 0, respectively. One could also set the desired frequency to be a ramp function to slowly speed up the motor; however, for this study, a set speed point is necessary, and so it shall be used. The results from a simulation with the desired frequency set to 50Hz are shown below.

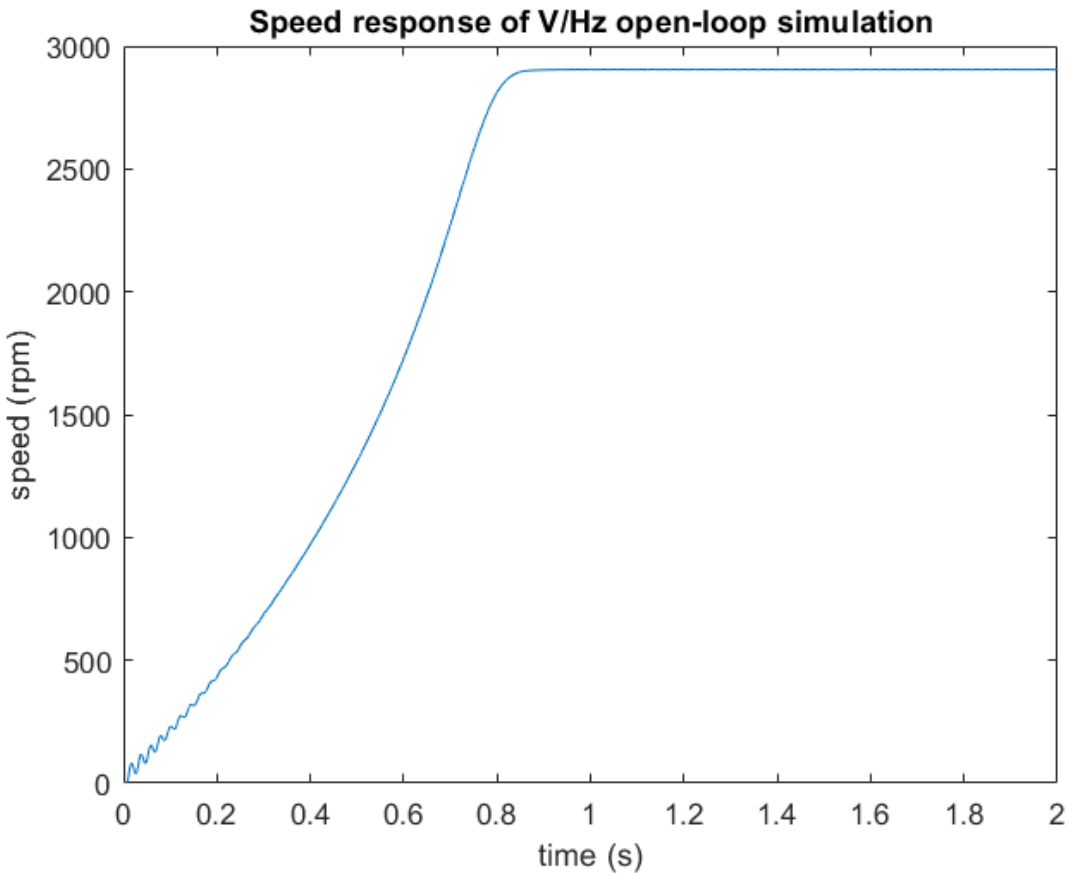

Figure 4.4: Simulation results of V/Hz open-loop connected induction motor.

As can be seen in Figure 4.4, the motor reaches the desired speed with a supply frequency of 50Hz; it does not reach the 3000 rpm, which is to be expected since it is an induction motor and there is slip that needs to be considered.

This setup does get the motor up to speed and will be the implementation that will be used in the tests.

4.5.3 V/Hz closed-loop controller inverter connected motor

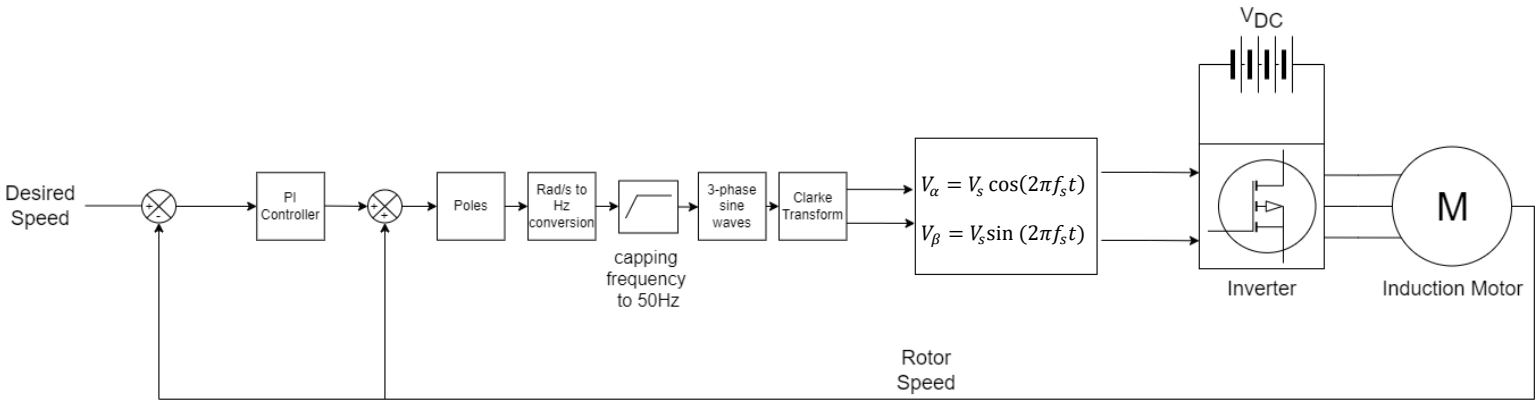

Figure 4.5: Block diagram including controller values for the closed-loop control loop.

For the V/Hz closed-loop control as shown in Figure 4.5, the following implementation was used. A controller was used in a closed-loop fashion, with the values of $P = 2,\ I = 0.05$. The desired speed in RPM was chosen as the desired setpoint input. The error in the rotor speed compared to the speed setpoint is the input to the controller, and then the output of that is then added to the current speed of the rotor to get the synchronous speed so that it can be equated to a frequency through multiplying it by the number of poles in the motor and then dividing by 120, which is the same as the inverse of the synchronous speed calculation for electric motors. This is then limited to 50 Hz as this is what the motor is rated for, and as such, do not want to exceed that to not damage the machine. Finally, this frequency is applied to generate a three-phase sinusoidal system, where the amplitude is modulated by the maximum frequency of the machine in the formula shown below.

$$m = \frac{f_{desired}}{f_{max}} \tag{4.7}$$

This will aid the SVPWM to be able to generate various speeds through the PWM generation scheme. The output speed of the motor is generated in a rad/s format, so it needs to be converted to rpm using the formula shown in the block diagram.

A simulation of the speed and torque of this system can be shown below with the following inputs. The speed setpoint is 0 until t = 1s, then it steps up to 3000 rpm. The torque load is 0 until t = 3s, where it changes to 0.8 N·m to simulate a full load test of a healthy motor, as will be conducted. The results are as follows:

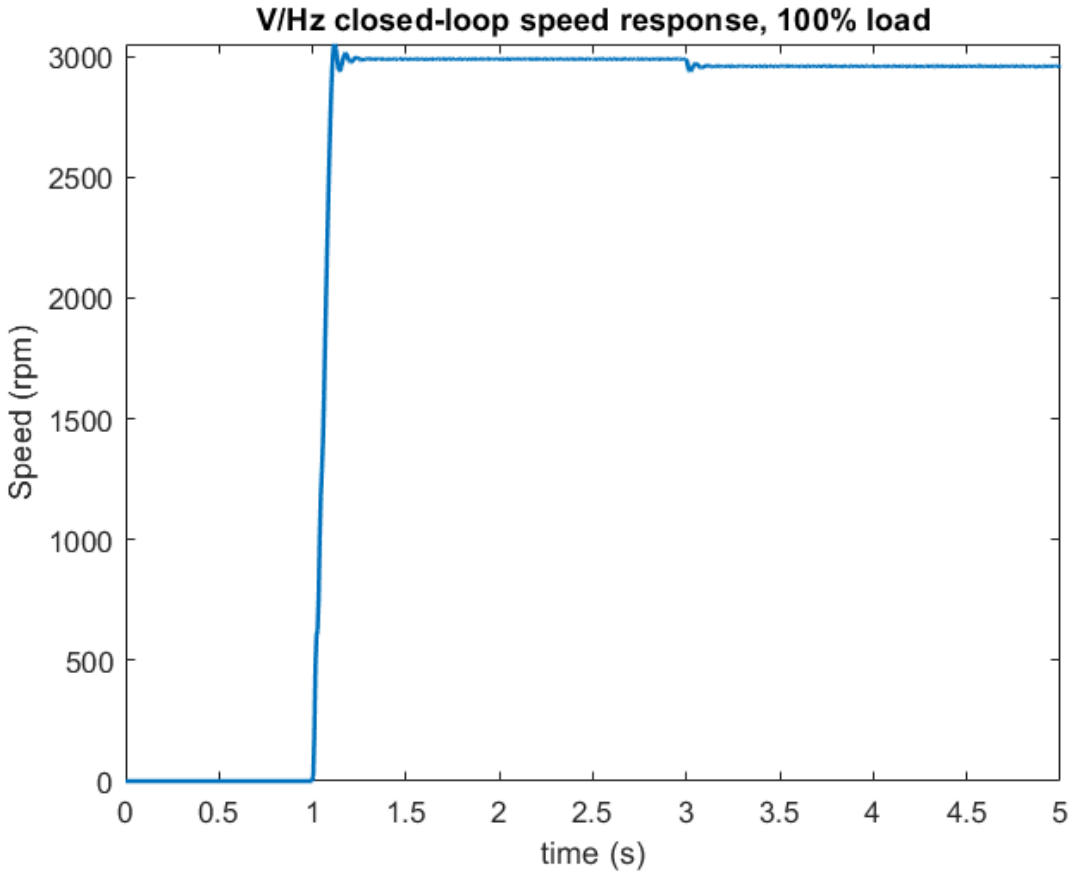

Figure 4.6: Speed response of V/Hz closed-loop simulation.

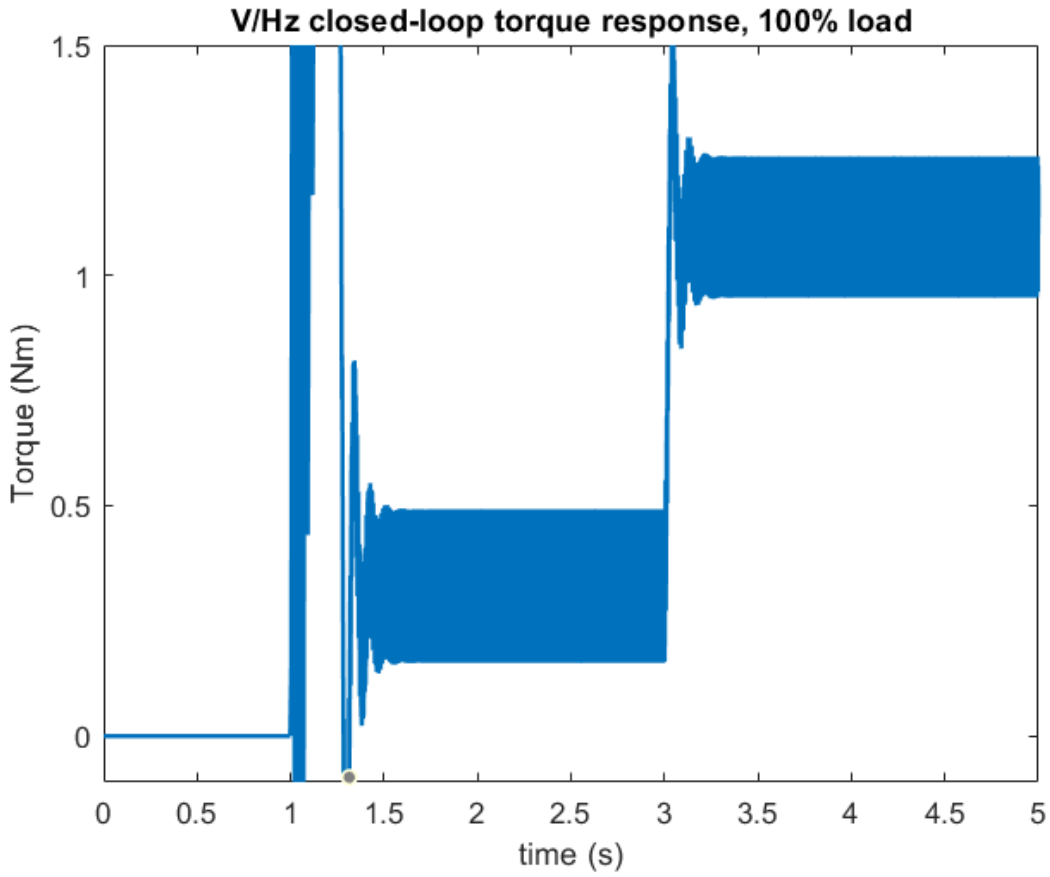

Figure 4.7: Torque response of V/Hz closed-loop simulation.

As can be seen from Figures 4.6 and 4.7, the speed follows a typical PI response of slight overshoots before finally settling at the desired speed. At t = 3s, the introduction of torque causes a slight disturbance, as expected, before settling to a transient value. There is a slight error in the final speed once the max torque is reached, but the transient response is steady, which is important for this study.

As can be observed, the speed response is smooth, but the torque is quite noisy. This points to the fact that the control could be further optimised to help with this situation; however, the controller is a speed controller, and since the speed response is stable at transient speeds, this is the most important outcome. As the tests will be run at 0.2N, the simulations for those results are shown below.

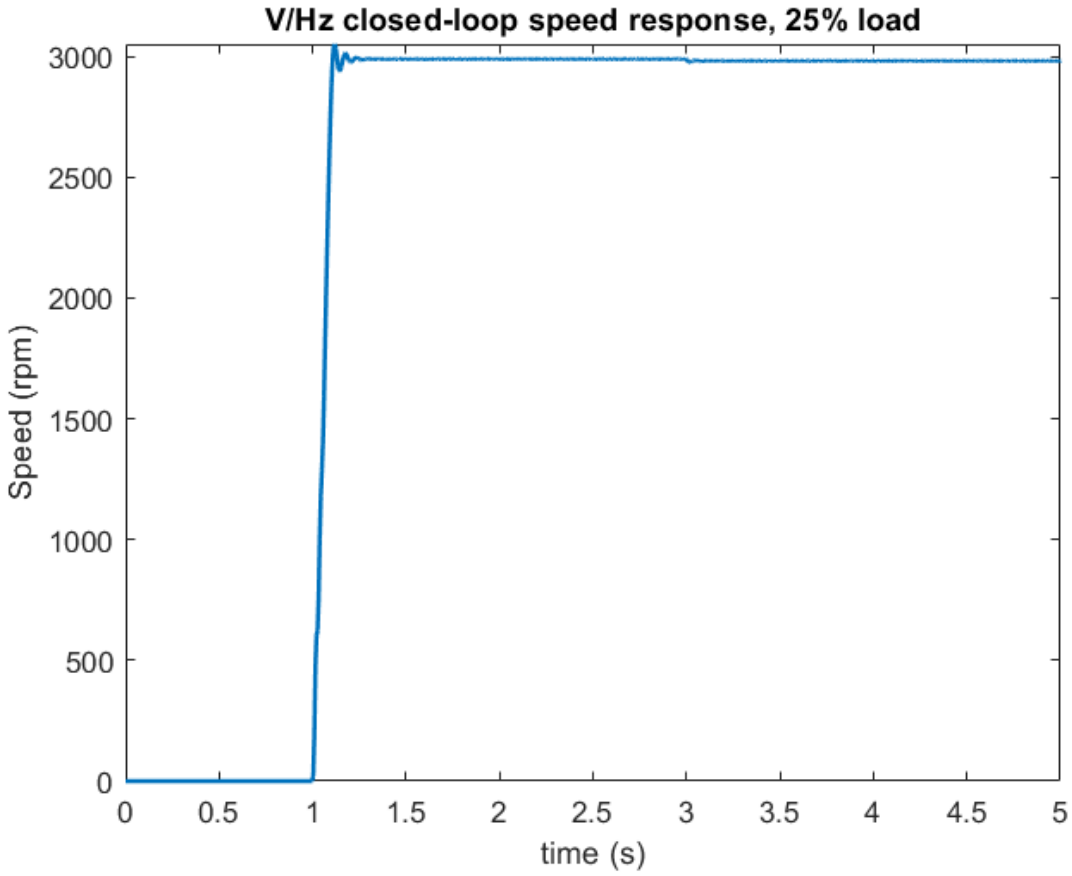

Figure 4.8: Speed response of V/Hz closed-loop simulation at 25% load.

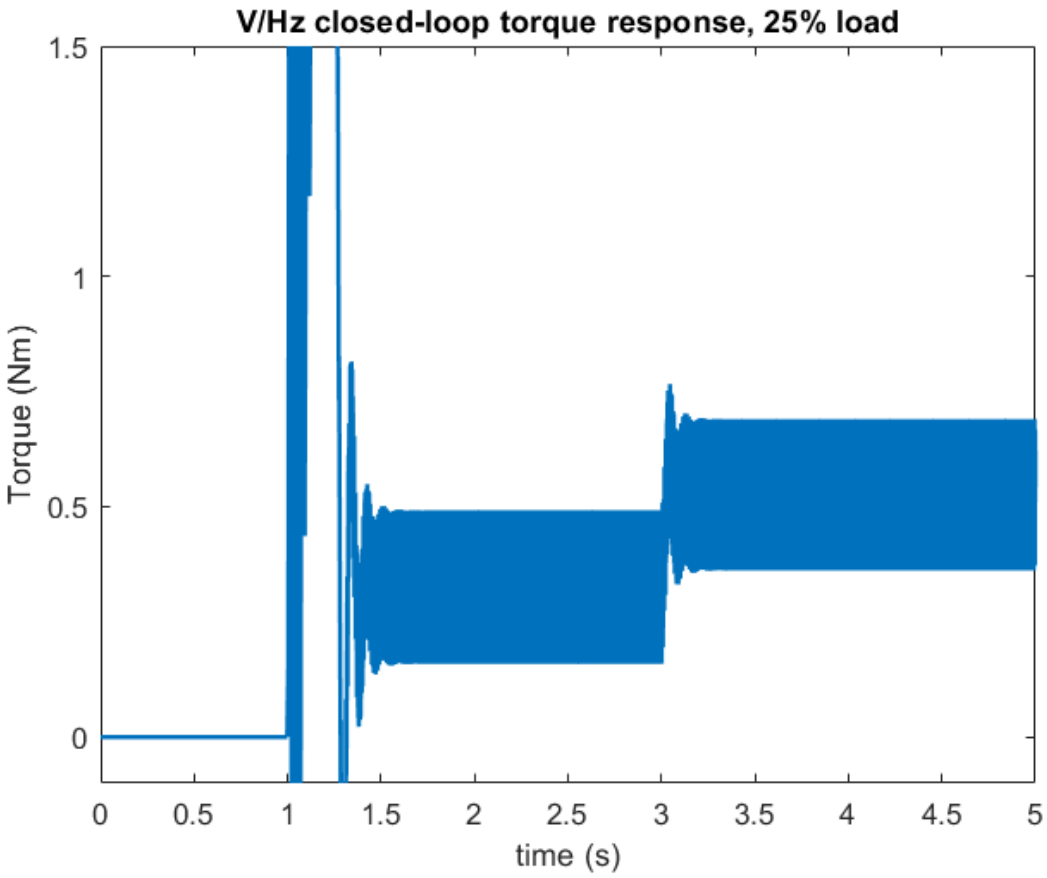

Figure 4.9: Torque response of V/Hz closed-loop simulation at 25% load.

As can be seen in Figures 4.8 and 4.9, similar traits are shown in both load conditions, with the transient response being stable after the load is introduced. It is to be noted that the torque in Figures 4.7 and 4.9 is electromagnetic torque, so there is a slight additional offset. However, once the load is applied, the additional increase from the torque can be seen to be the correct value of 0.8Nm and 0.2Nm, respectively. In both cases, the system is stable at the transient speed. This is the desired behaviour of the system, as it remains stable throughout the simulation and can manage the torque introduced. Thus, it proves to be a viable setup to run the desired tests throughout this study. This will be the exact setup that will be used in the laboratory experiments for this study.

4.5.4 FOC controlled inverter connected motor

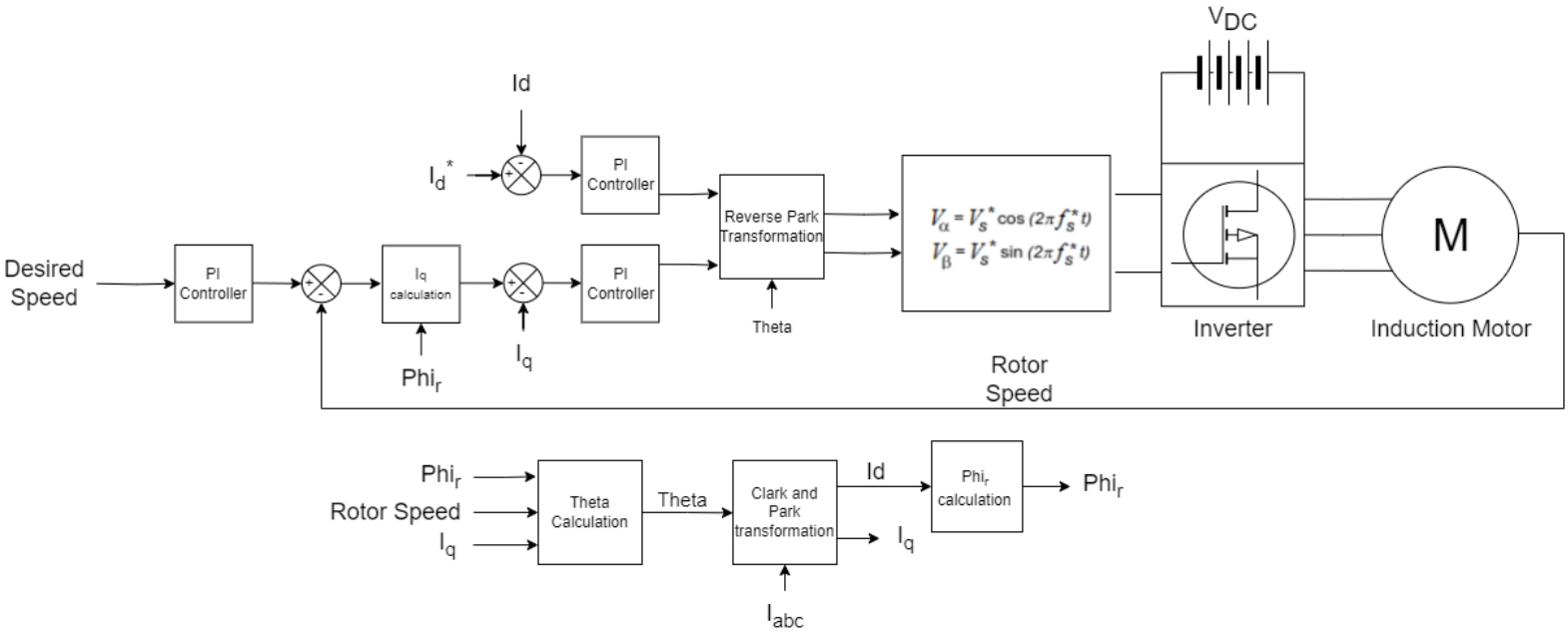

Figure 4.10: Block diagram including controller values FOC control loop.

As can be seen from Figure 4.10, the complexity of the FOC algorithm is significantly greater than the previous two control algorithms.

There are various conversions in terms of transformations used as well as additional calculations that need to be made, so that this type of control algorithm can be used with induction motors. It was implemented in the case used for this study, as will be outlined below.

Starting from the least complex step, the first transformation that needs to be implemented is a reverse Park transformation that can transform the output values from the current loop controller from the d-q plane to the alpha-beta plane. This is done using the following formula.

$$\begin{bmatrix} V_d \\ V_q \end{bmatrix} = \begin{bmatrix} \cos(\theta) & \sin(\theta) \\ -\sin(\theta) & \cos(\theta) \end{bmatrix} \begin{bmatrix} V_\alpha \\ V_\beta \end{bmatrix} \tag{4.8}$$

where θ is the angle of the rotating reference frame. V_α, V_β are necessary for the SVPWM and V_d, V_q are the outputs from the current loop controllers.

The next transformations necessary are Clarke and Park's transform to get the motor line currents to usable forms of the d-q plane values. The following formulae are used.

$$\begin{bmatrix} i_\alpha \\ i_\beta \\ i_0 \end{bmatrix} = \left(\frac{2}{3}\right) \times \begin{bmatrix} 1 & -\frac{1}{2} & -\frac{1}{2} \\ 0 & \frac{\sqrt{3}}{2} & -\frac{\sqrt{3}}{2} \\ \frac{1}{2} & \frac{1}{2} & \frac{1}{2} \end{bmatrix} \begin{bmatrix} i_a \\ i_b \\ i_c \end{bmatrix} \tag{4.9}$$

$$\begin{bmatrix} i_d \\ i_q \end{bmatrix} = \begin{bmatrix} \cos(\theta) & \sin(\theta) \\ -\sin(\theta) & \cos(\theta) \end{bmatrix} \begin{bmatrix} i_\alpha \\ i_\beta \end{bmatrix} \tag{4.10}$$

Which are similar formulae shown in Chapter 3.

The next step is to convert the output of the speed controller into a current-based value that will be usable in the current loop. Once again, the formulae shown in Chapter Two will be used. For this conversion, the formula is as follows:

$$T_e = \frac{3}{2} p \frac{L_m}{L_r} \lambda_r i_q \tag{4.11}$$

This can be manipulated to ensure that i_q is the subject of the formula, such that the formulae are as follows.

$$i_q = \frac{2}{3p} \frac{L_r}{L_m \lambda_r} T_e \tag{4.12}$$

where *p* is the number of pole pairs, L_r is the total inductance of the rotor, L_m is the mutual inductance of the motor, and T_e is the electromagnetic torque of the motor, which in this case is the value that is the output of the speed controller. Finally, λ_r is the rotor flux of the motor.

This is calculated using the following equation.

$$\lambda_r = \frac{L_m}{(1 + s\tau_r)} i_d \tag{4.13}$$

Which is in the form of a transfer function, with $\tau_r = \frac{L_r}{r_r}$, which is the inductance of the rotor divided by the resistance of the rotor.

This, of course, needs to be discretised as it will be implemented in a discrete-type system, so the initial transfer function, with all the parameters introduced, becomes the following.

$$\lambda_r = \frac{0.2428}{\left(1 + s\frac{0.01257}{2.12}\right)} i_d \tag{4.14}$$

And using the zero-order hold conversion to discretise this, it becomes the following.

$$\lambda_r = \frac{0.0004092}{z - 0.9983} \tag{4.15}$$

With T_s being the sampling time used. Both the simulations and the real-world tests will be 1×10^{-5}s, or 100,000 samples per second. This provides a flux value that can then be used in the calculation that enables the use of the FOC. The final thing that is needed is the calculation of theta, which is required to perform the transformation that takes the d-q axis values and transforms them into the axis values that are needed to perform space vector PWM. This is difficult, and calculating the exact values needs to consider the slip that the machine is experiencing.

For this to be done, the slip speed needs to be calculated, and this is done using the following formula:

$$\omega_{slip} = \frac{L_m}{\tau_r} \frac{i_q}{\lambda_r} \tag{4.16}$$

Which cannot be calculated using the above formulae. This slip speed is the speed of the rotating reference frame minus the speed of the rotation of the rotor. Since an encoder is being used to capture the speed of the rotor, it can then be used to calculate the rotational field speed using the formula shown below:

$$\omega = \omega_{slip} - \omega_r \tag{4.17}$$

In our case, it is not important for this, but for ω_r this needs to be from mechanical to electrical, which considers the number of pole pairs of the motor. For this case, the mechanical and electrical degrees will be the same since there is only one pole pair, but the formula to calculate this can be shown below:

$$\omega_{r\ (\ electrical)} = p \cdot \omega_{r\ (mechanical)} \tag{4.18}$$

where the $\omega_{r\ (mechanical)}$ is the measured speed of the rotor from the encoder. And the $\omega_{r\ (\ electrical)}$ is the value that is used in Equation 4.17.

Since this ω value is a rad/s value, it needs to be integrated to get an angle or θ value. This can then be used in the inverse Park's transformation formula, which was shown earlier in the chapter.

For the current loop controllers, the following values were used: P = 50 and I = 0.5. For the speed controller, the same values of the speed controller were used in the V/Hz closed-loop configuration, with the values of P = 2 and I = 0.05.

A simulation of the speed and torque of this system can be shown below with the same inputs as the V/Hz closed-loop configuration. The speed setpoint is 0 until t = 1s, then it goes to 3000 rpm. The load torque is 0 until t = 3s, where it changes to 0.8N.m. The speed and torque response of the control system is shown below.

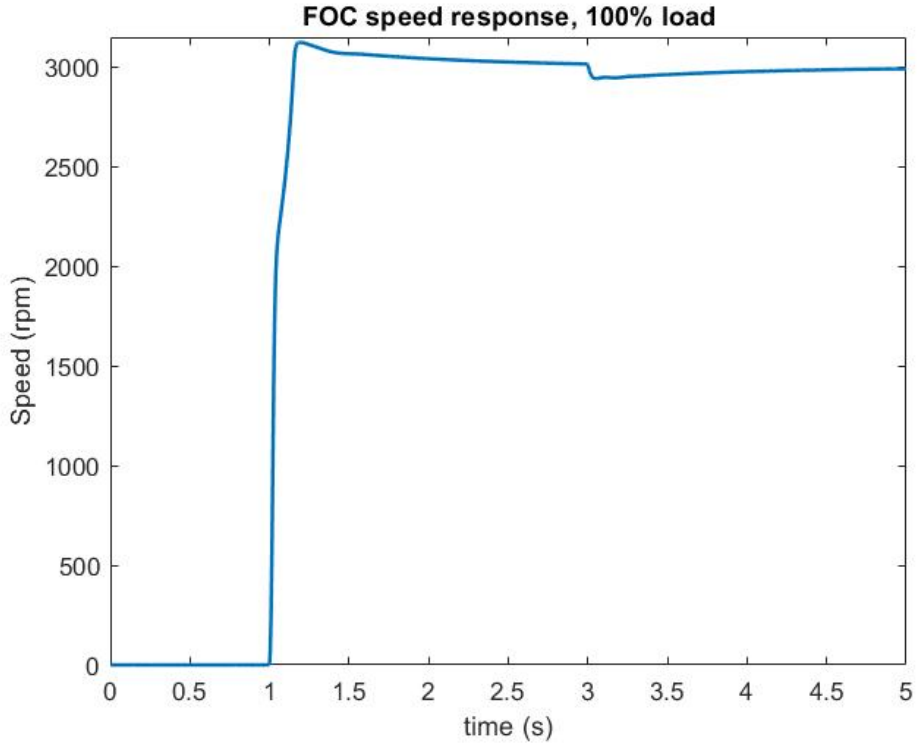

Figure 4.11: Speed response of the simulation of FOC controlled induction motor.

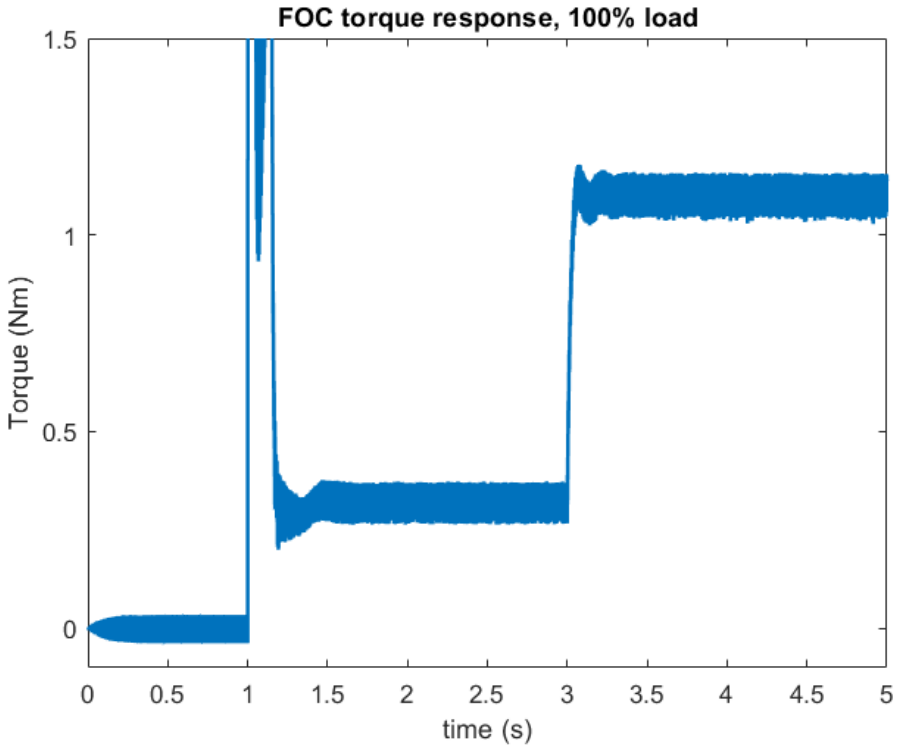

Figure 4.12: Torque response of simulation of FOC controlled Induction Motor.

As can be seen from Figures 4.11 and 4.12, the FOC algorithm can get the motor to closely match the desired speed, which the user desires, in this case, 3000 rpm. There is a discrepancy once additional torque is introduced at t = 3s; however, the key factor is that it is stable at a transient speed and does settle to the set point eventually, to the desired setpoint and can maintain that transient speed. This is important as the tests will be conducted at a constant speed and therefore frequency on the system.

The torque response is less important, as this is not a strict requirement. What this does show is that the FOC does settle at an inherent torque value, which is to be expected, but it does increase when the torque is introduced at t=3s. This is important as it shows that the current configuration of the algorithm can deal with load being introduced without making the system unstable, and therefore suitable to conduct the tests. There is a discrepancy in the torque due to the inherent additional electromagnetic torque that comes with spinning the rotor, but other than that, it is matched well in terms of the desired changes on the system.

The same simulations were run with a torque load of 0.2Nm, as this is what the experiment will be conducted at. The results can be seen in Figures 4.13 and 4.14 below.

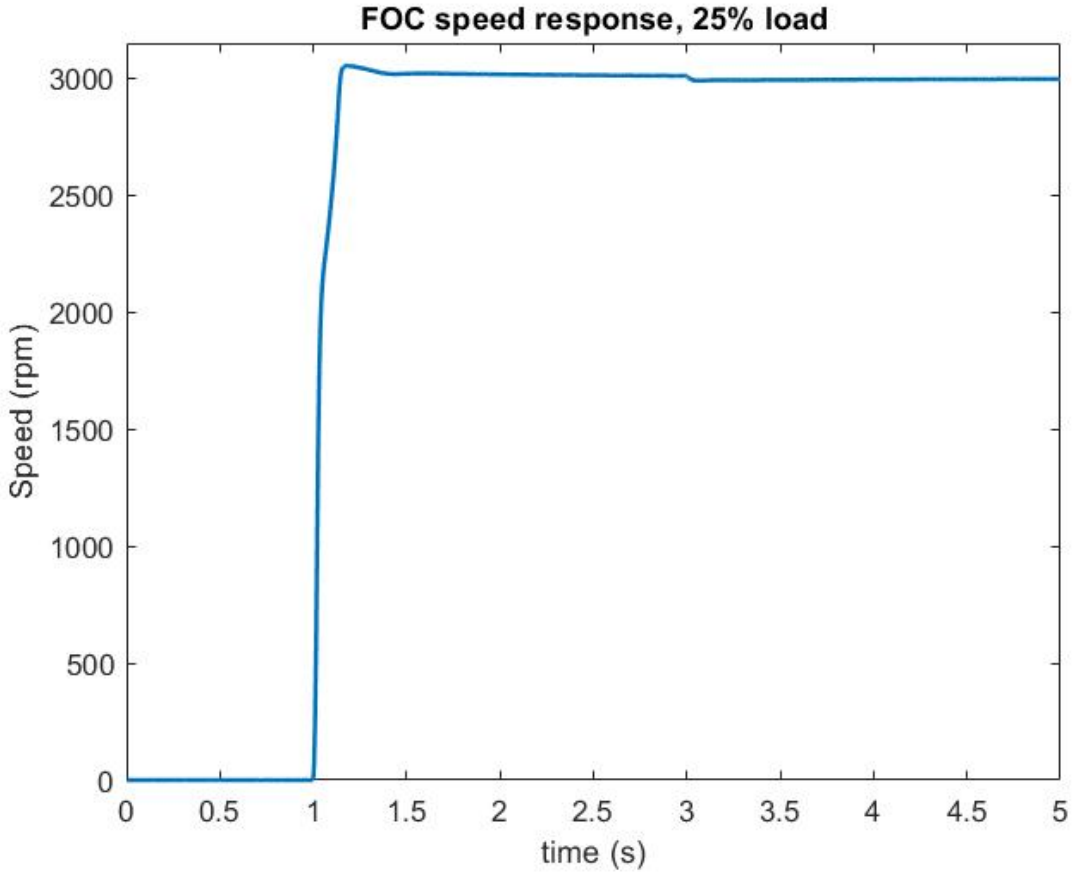

Figure 4.13: Speed response of FOC simulation at 25% load.

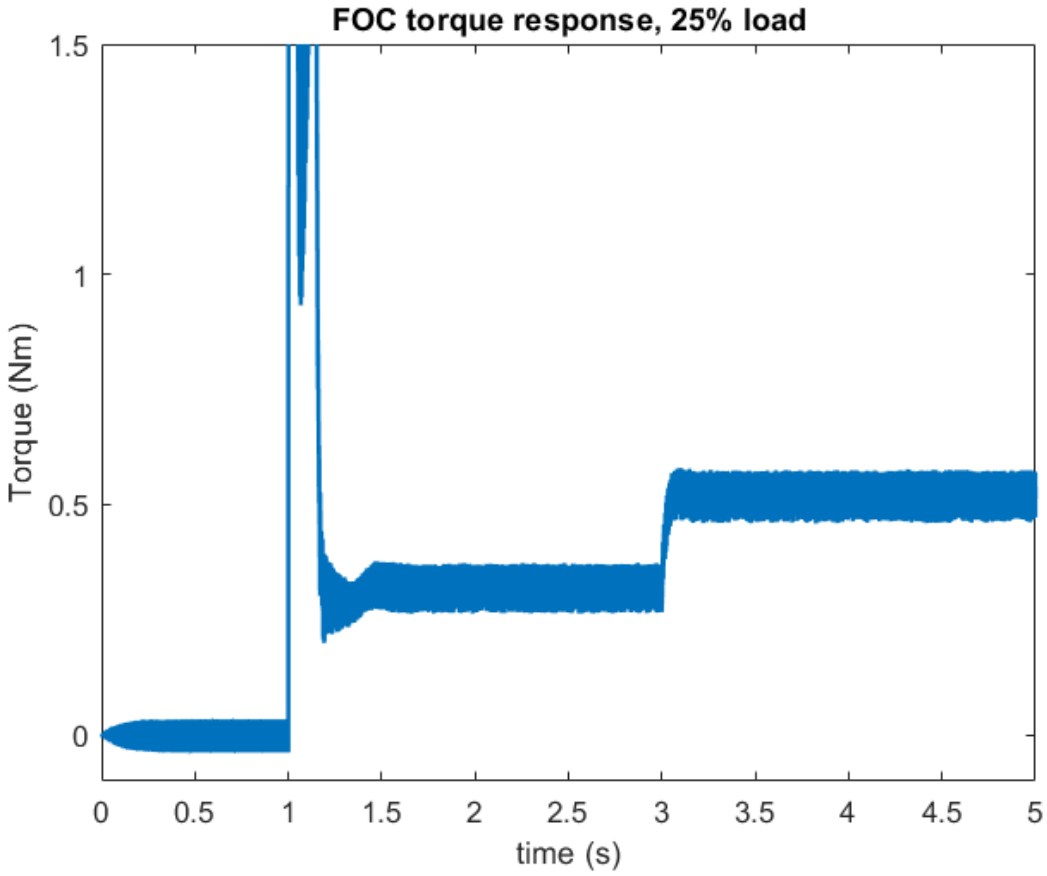

Figure 4.14: Torque response of FOC simulation, 25% load.

The lower load test follows the same patterns as the full load test, where there is a good initial speed response and settling at the desired speed, and finally a dip once the torque load is applied, before settling back to the desired speed. Ultimately, it is most important that the system behaves properly at transient conditions, which this configuration seems to do, and overall, the setup is satisfactory for our needs for this experiment and is what will be used in real-world experiments.

4.6 Conclusion

This chapter reviews the overall methodology and strategy used to experiment, collect the data and apply the various data analysis techniques that are needed throughout the experiment. The design methodology of the overall setup for the experiment was explored and verified using simulation tools. The design is analysed, and the final design has been decided based on the simulations done. The simulations provided useful insight into the control schemes as well as the filter design that would be used. Each control scheme behaved as expected, with all three being able to handle the desired load. The response time for both the FOC and V/Hz control schemes was fast enough (~2s), as well as proved stable when adding additional load. Since the focus of the study is to conduct research at the transition state, the control schemes are suitable for the study's focus. The filter design also provided valuable insight that even after following the desired questions, the filter performance needed additional tweaks due to the unsatisfactory THD on the motor line current. The design has now been finalised and deemed satisfactory for real-world tests. The testing equipment will be explored in the next chapter.

5 EXPERIMENTAL SETUP

5.1 INTRODUCTION

This chapter focuses on the details of the equipment used within the study as well as the methodology used to obtain the results from the experiment. The filter design used for the experimentation is also explored in this chapter.

5.2 TEST RIG

In this study, all tests were conducted using the SpectraQuest Machinery Fault Simulator in the Power Machines Laboratory at the University of Cape Town. This rig enables the simulation of various faults for a range of different industry applications, such as machines, pumps, and bearings.

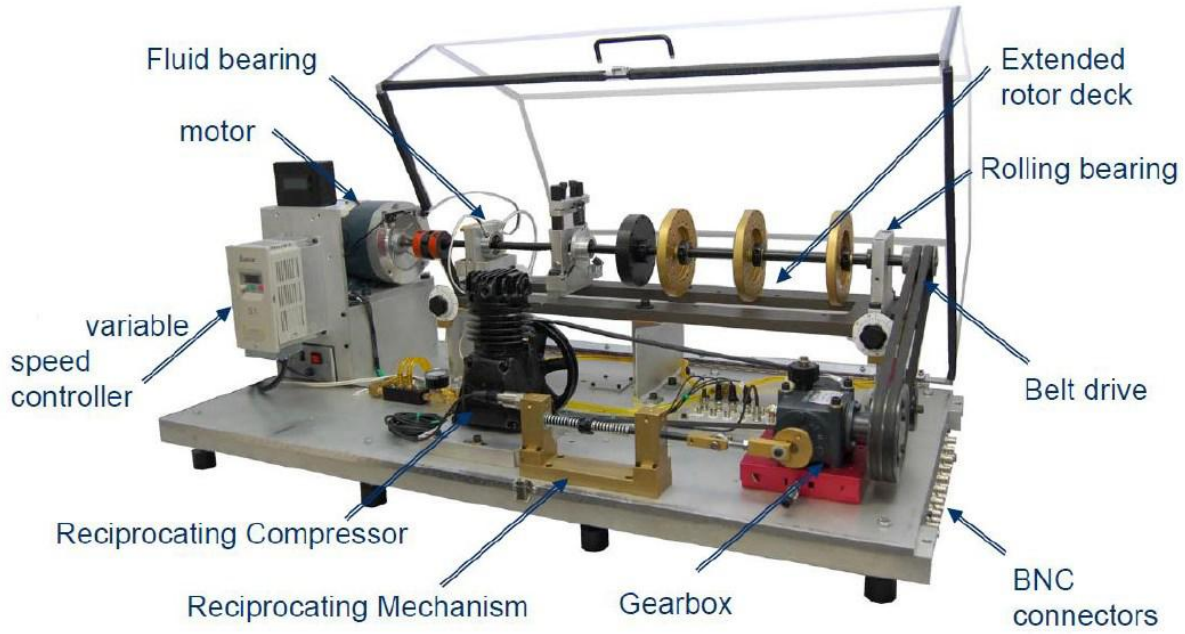

Figure 5.1: SpectraQuest machine fault simulator with its various pieces of equipment [96].

In conjunction with this rig, an electrical fault simulator and drive control panel were connected to allow for the selection of various scenarios such as:

- Grid vs inverter supply.
- Motor start/stop/emergency stop.
- Load selection – no load/ servo load/ resistive load.
- Servo start/stop.
- Servo Human Machine Interface.
- Fault Selection – inter-turn fault/phase loss/voltage unbalance.

The panel control layout can be seen in Figure 5.2 below.

Figure 5.2: Control Panel layout connected to the test rig.

A basic representation of the setup can be seen below in Figure 5.3.

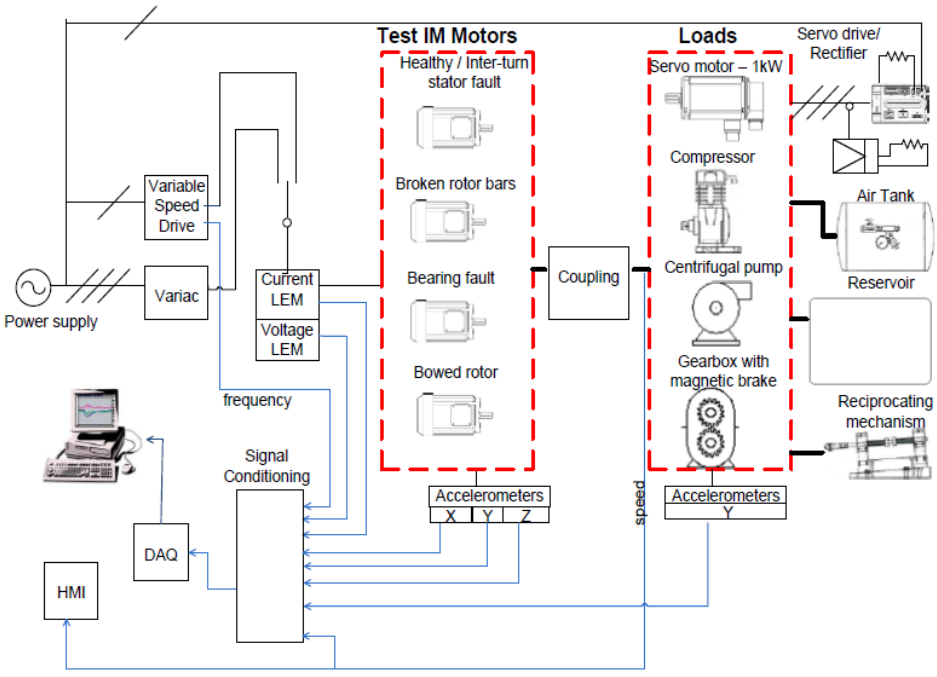

Figure 5.3: Basic overview for connection of overall setup used in this experiment [78].

5.2.1 Instrumentation

5.2.1.1 NI CompactDAQ system

To capture the data that was needed from this experiment, various instruments were used.

Firstly, to capture the data, such as current, voltage, shaft speed, shaft torque, etc., the National Instruments CompactDAQ system was used in conjunction with LabVIEW to capture the data.

This system allows for modular I/O devices such as the NI9215 differential analogue module. To be used. This model has four different inputs, each with a range, able to capture 100,000 samples per second at a resolution of sixteen bits. A picture of the module as well as the basic diagram of it, is shown below in Figure 5.4.

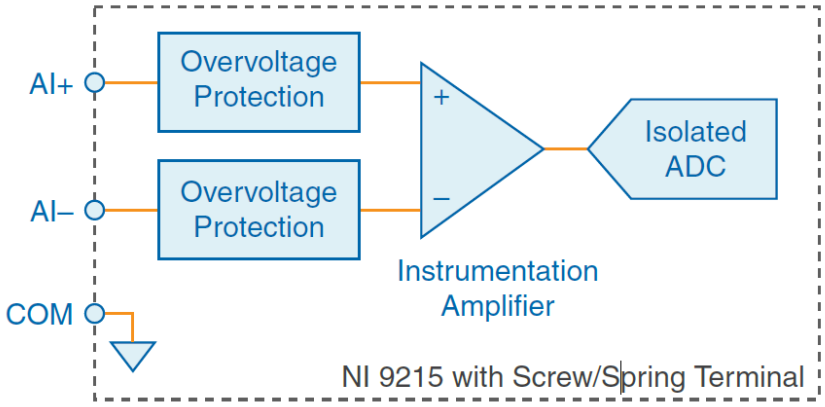

Figure 5.4: Diagram of ADC and picture of what the NI9215 module looks like [97].

The CompactDAQ system connects to a PC via a USB cable, and the data can be picked up using software such as LabVIEW to record the data, as well as the additional step of being able to visualise the data. Three NI9215 modules were used in this test setup to record the following data points:

- V_{ab} line-to-line voltage.
- V_{bc} line-to-line voltage.
- V_{ca} line-to-line voltage.
- Line current for phases A, B, and C.
- Shaft Torque.
- Shaft Speed.
- DC voltage of the inverter.
- DC current of the inverter.

The system was set up to record data for 10 seconds at a sampling rate of 100,000 samples per second, thus resulting in 1,000,000 samples of data per channel.

5.2.1.2 Voltage and Current Measurements

The three-phase voltage and DC voltage measurements were taken using LEM LV25-P Hall Effect voltage transducers mounted within the panel interface. Similarly, the system's currents were measured using LEM LA25-P Hall Effect current transducers. The outputs of these transducers are biased to a ±10V range and then passed through a low-pass frequency filter with a cutoff frequency of 12 kHz. Both current and voltage measurements were calibrated and linearised using the LabVIEW DAQ Assistant function to ensure accurate readings in volts and amperes, respectively.

5.2.1.3 Speed and Torque Measurements

The speed of the induction motor was measured using a 20-bit rotary incremental shaft encoder that was coupled to the servo drive on the test rig. Using the Servo's software, the encoder was set to output a maximum of 128,000 pulses per revolution, which would provide the highest resolution possible in aid of capturing the transient speed accurately during the tests. This speed signal was made available by outputting a 0- 8V analogue signal from the servo drive and sending it through the NI CompactDAQ system.

The torque was measured similarly, by utilising a Lorenz DR-2112 Torque Transducer, which had an analogue output of 0 - 10V, where the LabView DAQ assistant once again was able to convert the analogue system into the correct and usable values of N·m. This measurement was needed as it was used to capture how loaded the machine was for the different tests and scenarios.

5.2.2 Motor Control

In this test, V/Hz open and closed-loop control, as well as field orientation control (FOC), were implemented on the various induction machines. To do this, the dSpace CP1104 connector panel, in conjunction with the ControlDesk software, implements the control as well as takes in the needed measurements to complete the software in the loop system needed to conduct this experiment. A picture of the connector panel is shown below in Figure 5.5.

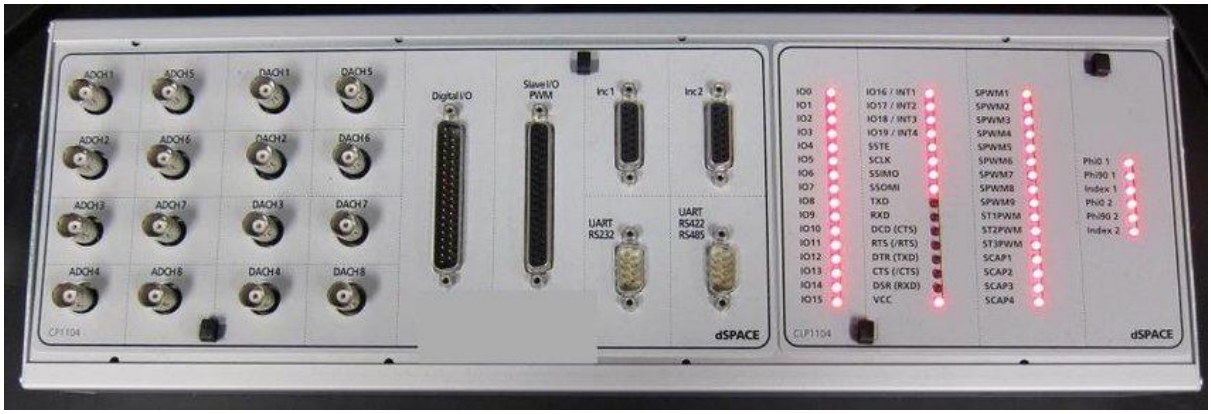

Figure 5.5: dSpace CP1104 connector panel with its various connector options [98].

This connector panel was used to measure the following:

- V_{ab} line-to-line voltage.
- V_{bc} line-to-line voltage.
- V_{ca} line-to-line voltage.
- Line current for phases A, B and C.
- V_{dc} DC voltage of the inverter.
- i_{dc} DC current of the inverter.
- Shaft Speed.

Mostly, this was daisy-chained from the LEM modules that were mentioned earlier, except for the shaft speed. Since the connector panel had the input for an RS422 encoder, an RLS MR22IC magnetic encoder was attached to the end of the shaft of the motors and sent straight to the CP1104 panel. This enabled real-time capturing of the speed and position of the shaft, which was necessary to implement the control schemes on the motor. This encoder used 2048 pulses per revolution.

The CP1104 was also needed as it was used to send the PWM signals to the inverter system that was being used to control the motor appropriately. This PWM signal had an output of either 0 or 5V. The Control Desk software was used in conjunction with a Simulink file where all the coding for the control schemes was done, and ControlDesk was used in the same way LabVIEW was, to visually represent data in real-time of the test rig.

The control system that was implemented was explained previously in Chapter 4.

5.2.3 Data Processing

All data processing was done by using MATLAB 2018a. Programs were coded to import the data captured by the LabVIEW software and then apply the processing techniques discussed in Chapter 3.

5.3 MOTORS

The SpectraQuest test rig is supplied with several motors with intentional faults and/or defects to the induction motor, as well as a healthy motor to provide a baseline. All motors are three-phase, class B, in star configuration, and have identical ratings, which can be represented in Tables 5.1 and 5.2 below.

Table 5-1: Motor specifications used on the test rig [99].

Induction motor Specifications	Value
Rated Power (W)	250
Frequency (Hz)	50
Number of Poles	2
Phase Voltage (V)	190
No Load Current (A)	0.7
Full Load Current (A)	1.85
Locked Rotor Torque (N.m)	4.06
Insulation class	F3

Table 5-2: Measured motor parameters of the healthy motor and the motor with 3 broken rotor bars.

Parameter	Value	
	Healthy Motor	Broken Rotor Bar
Stator Resistance, R_s	4.24Ω	5.17Ω
Stator Leakage Reactance, X_{ls}	3.95Ω	2.98Ω
Rotor Resistance, R_r	2.12Ω	4.12Ω
Rotor Leakage Reactance, X_{lr}	3.95Ω	4.12Ω
Magnetising Reactance, L_m	76.27Ω	78.21Ω
Moment of Inertia, J	0.0016797 kgm^2	0.0018219 kgm^2
Friction Coefficient, B	0.0010356 $Nm.s$	0.0011263 $Nm.s$

Results were obtained by conducting several experiments, such as the no-load test, locked rotor tests, DC tests and spin-down tests were carried out to determine the parameters of this machine. All the reactances were measured using a 50Hz frequency, as if in operation, thus the rotor, stator and mutual inductance can be calculated using these values.

The motors that are to be used in this study are outlined below.

5.3.1 Broken Rotor Bar

The motor, which is known to have a broken rotor bar fault, consists of 34 rotor bars, with 3 adjacent bars deliberately broken by the test rig manufacturer.

5.3.2 Inter-turn Fault

The motor that has the known inter-turn fault has its phase winding intentionally tapped so that either 0, 2 or 4 windings can be shorted to use a desired amount of severity of the fault when assessing the motor. This motor also serves as the basis for the healthy / control motor for this test, as if the windings are not intentionally shorted, it remains in normal working condition.

5.4 Motor Supplies and Loads

5.4.1 Supplies

5.4.1.1 Grid-connected supply

There are two supplies available within this test rig. The grid supply is supplied through a variac to the motor, which enables the startup of the motor to be gentle. This supply is fed

through an isolator and then through the variac and is of 50 Hz frequency, as is the standard in South Africa, where this test took place.

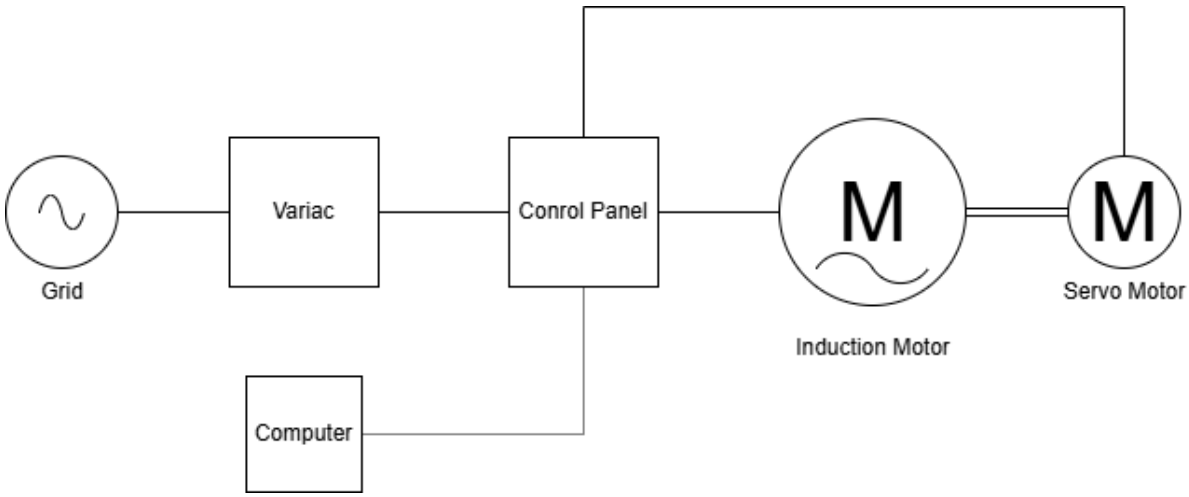

Figure 5.6: Block diagram showing the general setup for the connection of the grid-connected motor tests.

As shown above in Figure 5.6, the main supply is sourced from the grid connections in the laboratory where the experiments were conducted. The grid power is passed through a variac, which allows for controlled output voltage to the induction motor. This setup facilitates a gradual motor startup and provides flexibility in adjusting the voltage levels supplied to the motor. The variac is connected to a control panel, which in turn is linked to the motor. The details of the control panel will be discussed in the next chapter. Additionally, the control panel is connected to a servo motor, enabling variable loads. A data acquisition computer is then connected to the control panel's data acquisition equipment to collect data during the experiments.

5.4.1.2 Inverter Connected Motor

The inverter supply is first fed through the same variac, then through a rectifier, and then onto the SiC 3-phase inverter development kit from Taraz Technologies, which is then fed through a filter and onto the machine. The inverter is controlled through the dSpace connector panel as described earlier in this chapter. This allows the motor to be controlled through V/Hz and FOC schemes for multiple types of comparisons. The filter design and specifications can be found later in this Chapter.

The initial connection setup is the same, with the grid supplying power to a variac. However, to use an inverter, the supply is then fed through a rectifier before entering the inverter. The inverter is controlled through the dSpace controller, which allows for the implementation of various control schemes. The output of the inverter is then passed through a filter to clean up the voltage signals before being connected to the control panel and motor, maintaining the

same connection as in the grid-connected setup. A diagram of the connection can be seen in Figure 5.7 below.

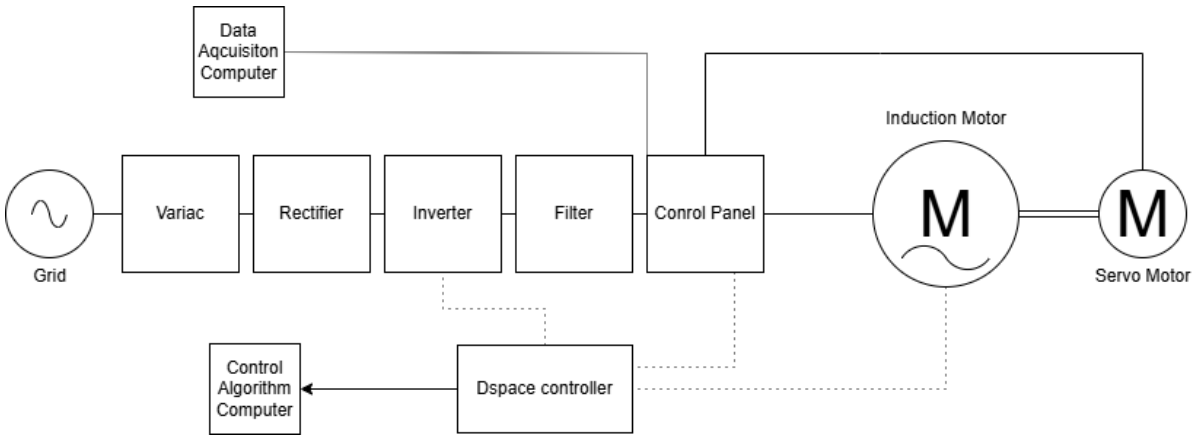

Figure 5.7: Block diagram showing the general setup for the connection of the inverter-connected motor tests.

The inverter serves as the central point where the control can affect the rest of the system. The specific inverter was chosen as it could manage high switching frequencies, up to 50 kHz, which would be a key aspect of the experiment. This is due to the higher switching frequency being useful in both playing a role in filter design, which will be explored below, as well as ensuring that when using the fault diagnostic techniques, there is not the presence of significant noise too close to the analysed harmonics.

The grid-connected rectification stage introduces additional harmonic content, most notably the 5th-order harmonic, which appears on the DC voltage of the rectifier. However, its magnitude was measured at approximately 2% of the fundamental grid frequency, which is sufficiently low to be considered negligible for the purposes of this analysis. Nevertheless, to ensure a conservative approach, the contribution of the rectifier was excluded when assessing the influence of potential motor faults. The DC voltage was observed to be smooth and stable, remaining within 5% of its average value throughout operation. While the setup does not fully replicate the conditions of a real electric vehicle (EV), it serves as a sufficiently accurate emulation platform for the development and evaluation of EV fault diagnostic techniques. The inverter stage offers access points for measurement of both DC bus voltage and current, enabling valuable data acquisition for diagnostic purposes. These signals are interfaced with the dSPACE controller, which is responsible for implementing the system's control algorithms.

5.4.2 Loads

The servo motor on the SpectraQuest test rig was used to simulate a load within this experiment. The servo is selected to apply a load through the HMI of the servo on the control panel of the test rig, where a load can be applied to the motor at a precise percentage of the servo's max torque. The energy generated by the servo is dissipated in the drive by raising its bus voltage or through an external 1 kW resistor that is located within the control panel. The list of servo parameters that have been configured can be found in the appendix.

The servo was applied at two distinct levels: for no load, it was left off and for 25% load of the motor. The values for the torque levels can be shown in Table 5.3 below.

Table 5-3: Torque values associated with % of loads.

Load Level	Torque (N.m)
0%	0
25%	0.2

The torque levels above fall into a $\pm$ 10% across all the tests that were conducted.

5.5 TEST BENCH SET UP

5.5.1 Variables for Experiment

To conduct the various tests required for this study, four configurations were implemented in the experimental setup. This subsection outlines the two main connection methods used: the grid-connected method and the inverter-connected method. The constant parameters for each test, where applicable, are summarised in Table 5.4 below.

Table 5-4: Constant Variables for the Tests

Parameter	Value
DC bus Voltage	320V
Motor Voltage (line-to-line RMS)	190V
Sampling Frequency	100kHz
Switching Frequency	10kHz

5.6 CONTROL CONDITIONS

The test rig from SpectraQuest, along with the supplied motors, features alignment slots that allow for quick motor changes. However, after each motor swap, the alignment was verified using a clock gauge to ensure consistent setup conditions across all tests.

To reach a steady-state temperature, each motor was run for 10 minutes at full load in a grid-connected scenario. This ensured that the tests were conducted under similar conditions for each motor and that any temperature effects on the results were minimised, as the motors reached a transient state.

The electrical supply was sourced from the laboratory mains and was checked for balance when connected directly to the motor and through the inverter. In both cases, the voltage was balanced.

5.7 CONCLUSION

This chapter reviews all the hardware and software that were used within the experimental process for this study. It also includes all the essential data for the values of items such as the motors being used and the load levels being used throughout the experiments.

6 RESULTS AND DISCUSSION

6.1 INTRODUCTION

This chapter presents the results obtained from the experiments described in the previous chapter. It covers two types of faults under two different supply conditions, with the inverter supply incorporating three distinct control strategies. Each experiment's results are analysed and discussed in detail, followed by a summary at the end of the subsection.

All results were gathered using the testing rig that was set up as per chapters 4 and 5. The tests were conducted under steady-state conditions. The data collected from the various tests were imported into MATLAB, where appropriate analysis and signal processing techniques were applied to facilitate comparison and draw meaningful conclusions. The detailed results are presented below.

6.2 GRID-CONNECTED MOTOR TESTS

6.2.1 Inter-turn Fault Analysis

6.2.1.1 Motor Current Signature Analysis

The Motor Current Signature Analysis (MCSA) method for detecting inter-turn faults has been thoroughly described earlier in this study. This method was applied to both a healthy motor and a motor with a known inter-turn fault. The tests were conducted at 0% and 25%, where the loads are shown in Table 5.3. The expected fault frequencies were calculated using Equation 3.2 and analysed with the healthy motor data as the control reference. Throughout the test, identifying distinct peaks proved challenging; however, a broad range of peaks were analysed, with $n = 1, k = 1, 3, 5$.

This test was run as per the described procedure. The following results will be shown for the maximum loaded machines, with a comparison of the spectra of the healthy motor vs. the shorted motor shown.

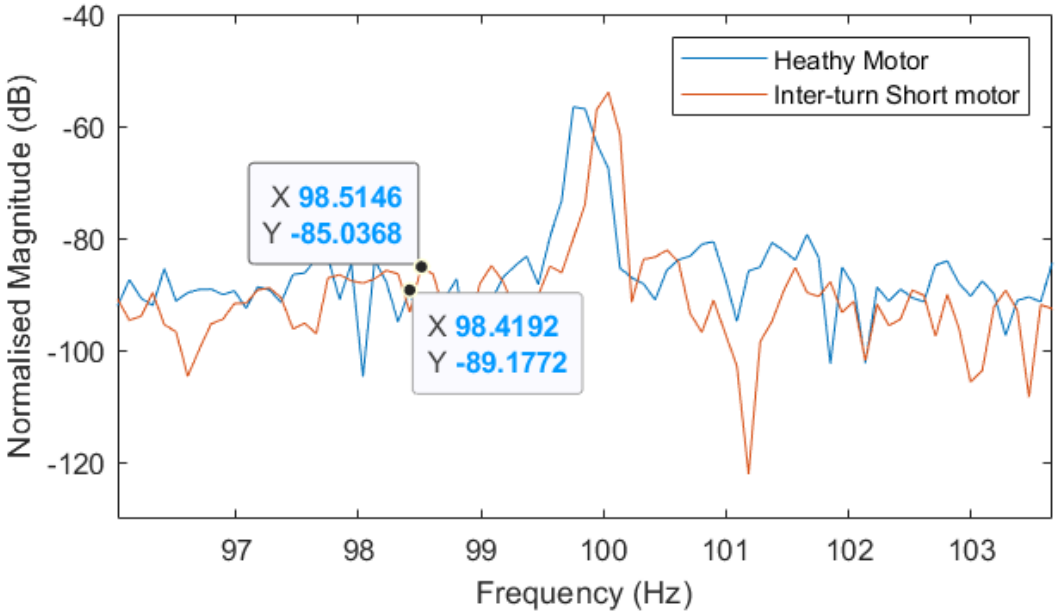

Figure 6.1: n = 1, k = 1 for grid-fed induction motor, with healthy vs inter-turn short motor spectrum.

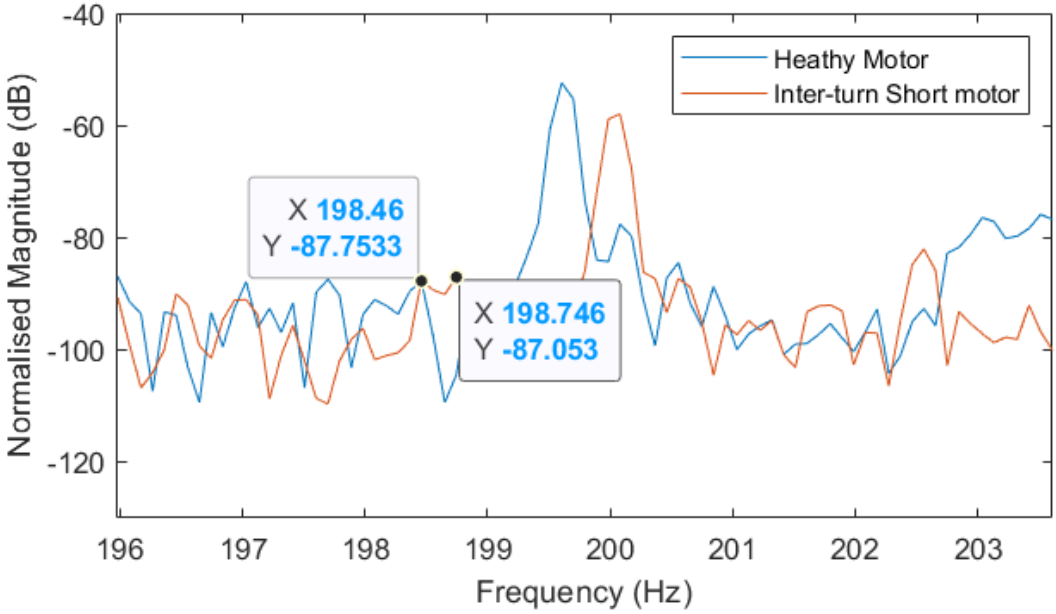

Figure 6.2: n = 1, k = 3 for grid-fed induction motor, with healthy vs inter-turn short motor spectrum.

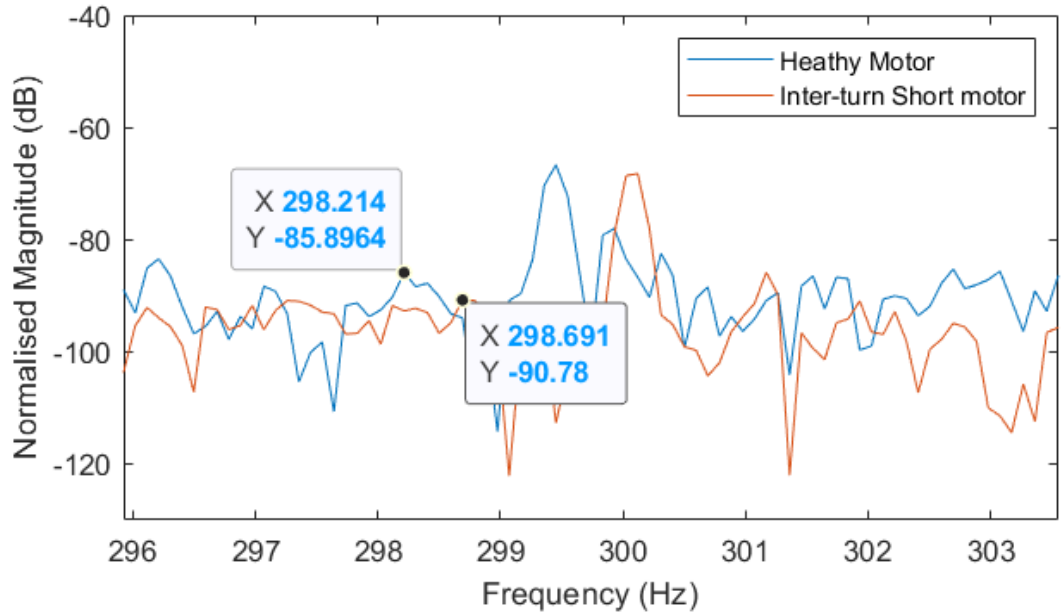

Figure 6.3: n = 1, k = 5 for grid-fed induction motor, with healthy vs inter-turn short motor spectrum.

As shown in Figures 6.1, 6.2 and 6.3 above, clearly identifying the fault harmonic proves to be quite challenging, even in the ideal scenario of a clean grid supply with 25% load on the motor. This does make sense since MCSA usually needs to be conducted at the max torque of the machine; however, this presents a concern for the inverter-fed tests, where more noise is expected on the system. These results will be presented below. The results from the above tests are not conclusive. For $n = 1$ and $k = 1$ a noticeable difference of 4.1404dB was observed; however, for k = 3, the difference is negligible, and for k = 5, the healthy motor exhibited a higher magnitude for the calculated fault harmonic than in the faulted condition. A clearer, tabular view of these results is provided below. The observed differences in peak

frequencies are attributed to slight variations in grid frequency. The healthy motor test was conducted with a fundamental frequency of 49.88 Hz, while the inter-turn fault test had a fundamental frequency of 49.97 Hz. All fault harmonics were within 0.2 Hz of the calculated value from the formula.

Table 6-1: Grid fed motor, 25% load healthy vs inter-turn fault MCSA results.

25% Load	Healthy		Inter-turn short		Difference
	Frequency (Hz)	Magnitude (dB)	Frequency (Hz)	Magnitude (dB)	
n = 1, k = 3	98.4192	-89.1772	98.5146	-85.0368	4.1404
n = 1, k = 3	198.46	-87.7533	198.746	-87.053	0.7003
n = 1, k = 5	298.214	-85.8964	298.691	-90.78	-4.8836

Tests were done for different loading percentages, but these will be found in the appendix; however, the overall effectiveness of the method will take these measurements into account.

6.2.1.2 Park's Vector Approach

The Park's Vector Approach (PVA) method for fault detection of inter-turn faults has been thoroughly described earlier in this study. This method has been applied to both a healthy motor and a motor with a known inter-turn fault under the same test conditions as those used for the Motor Current Signature Analysis (MCSA). These tests aim to provide a clearer indication of when a fault is present in the motor across various loading conditions.

The procedure followed in this test was consistent with that of the previous method, with the same data used for analysis. However, a different signal processing technique was employed. In this case, the stator current of the motor was transformed into the d-q plane, and a plot of these values was generated. The results of this analysis are presented below.

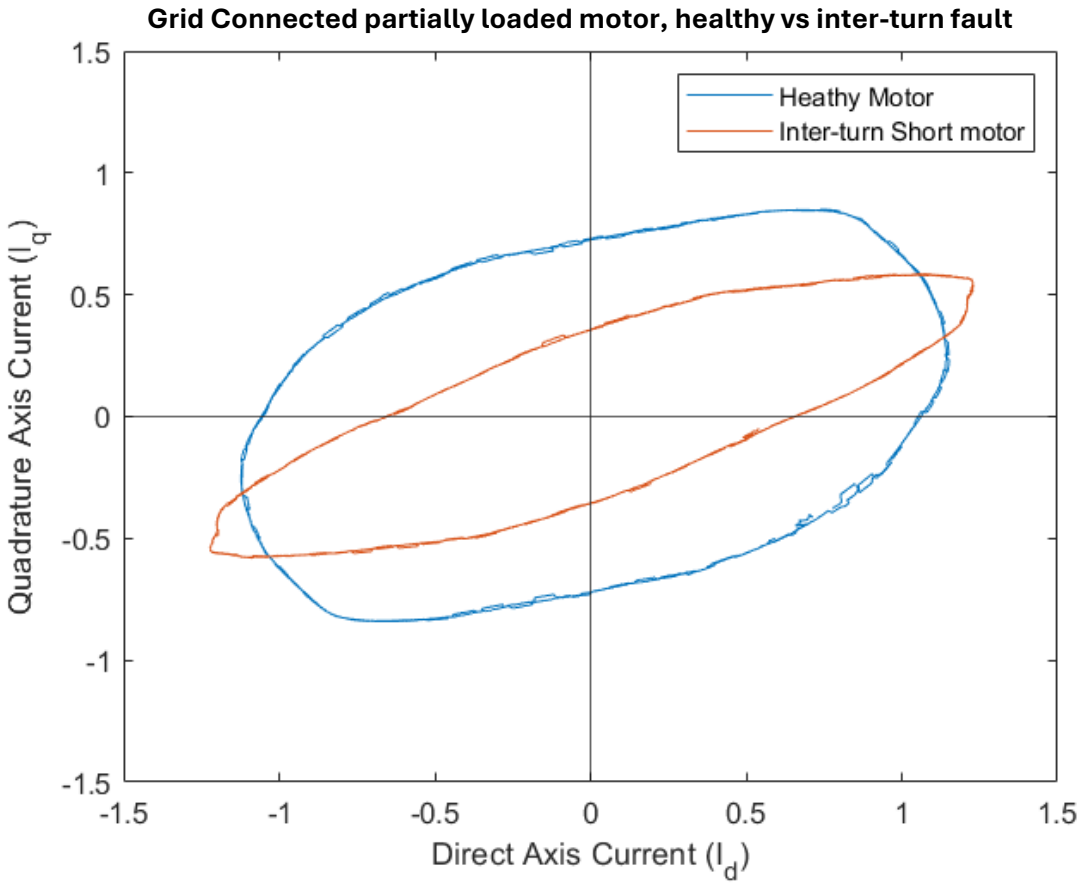

Figure 6.4: Normalised Park's Vector D-Q plot of grid-connected induction motor, healthy vs inter-turn short comparison.

Figure 6.4 clearly shows the presence of a fault, as the inter-turn short d-q plot is significantly different. The healthy motor plot is not perfectly circular speaks to the degree of unbalance already within the system, both on the supply and the motor side. The analysis needs to be taken from the healthy motor as a base, and with this in mind, the damaged motor has a slightly greater diameter, but moreover, it has a much less "circular" shape compared to the healthy motor. This will be the same throughout the thesis. It is important to note that these plots were generated from 1 period, i.e., 0.02s worth of data capture, due to the sheer size of data capture, as well as from t = 0 until t = 0.02s for all the following plots that will be discussed. A comparison from a different time of data capture will be shown below, and finally, over a broader timeframe to show that there is no significant difference, and thus the choice for a desired way of presentation of the data is clear and not swayed to highlight the faults.

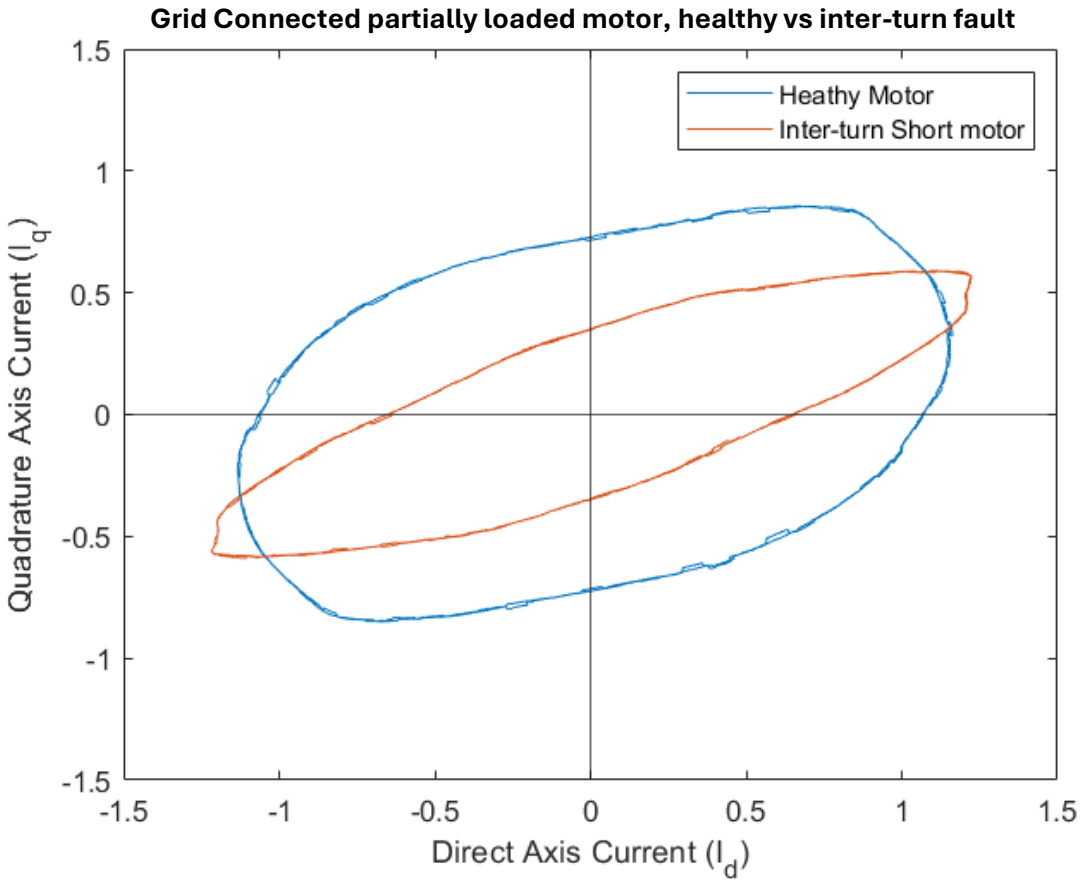

Figure 6.5: Normalised Park's Vector D-Q plot of grid-connected induction motor, healthy vs inter-turn short comparison. Different data period.

As can be seen from Figure 6.5, a completely different period produces an incredibly similar result. The plot over 10 periods is shown below in Figure 6.6.

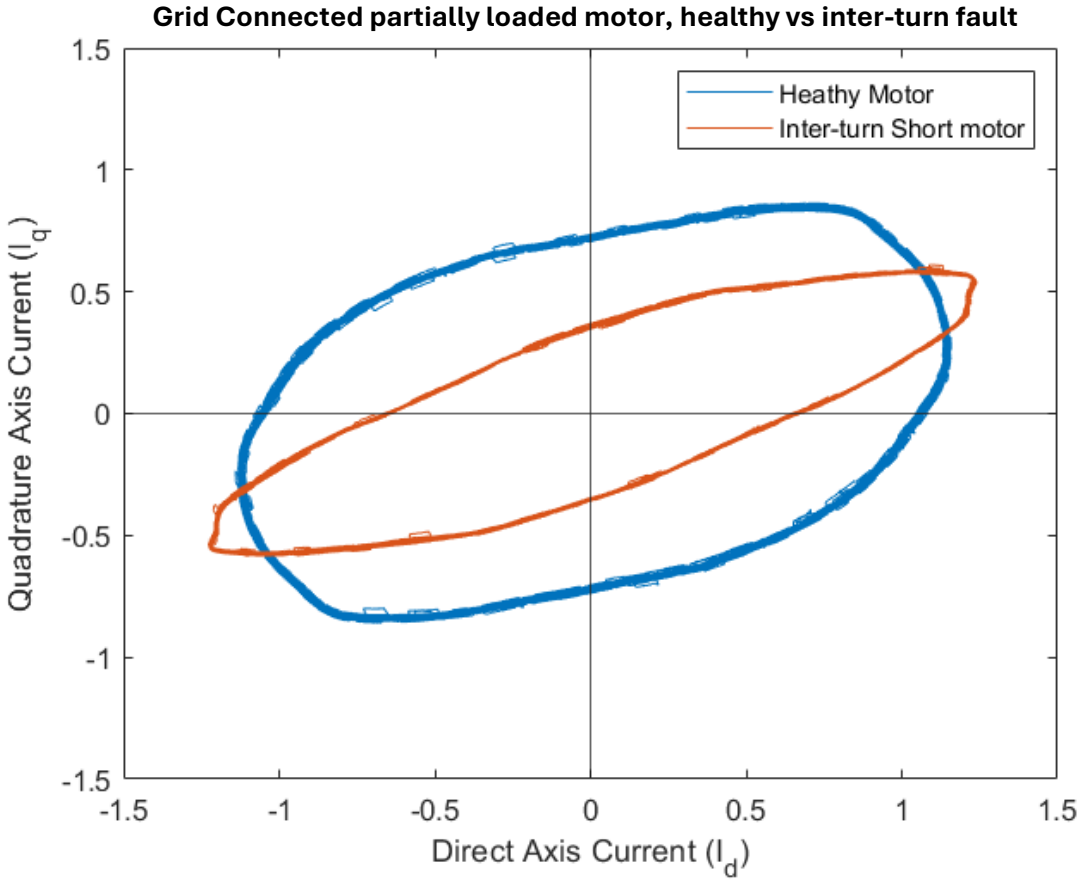

Figure 6.6: Normalised Park's Vector D-Q plot of grid-connected induction motor, healthy vs inter-turn short comparison. Plotted over 10 periods.

A similar comment can be made for the Park's vector approach plot over ten periods (0.2 seconds) shown in Figure 6.6. No significant differences other than appearing thicker. However, this is caused by the noise spikes that can be seen in the two earlier plots. This is due to some noise that was captured on the current data from the data-capturing system of the test rig.

This test does show that you can visually see the presence of a fault through Park's vector approach; however, it needs to be shown over various scenarios, which will be done throughout the chapter.

6.2.1.3 Extended Park's Vector Approach

This method aims to build upon the foundations of the previous method and provide a quantifiable number of harmonics to indicate the presence of a fault. The principal harmonic of interest is the harmonic present at twice the fundamental frequency. This test and method were applied to the same set of data as the previous two tests, and the results are as follows.

In the grid-supplied motor, the Extended Park's Vector Approach (EPVA) was applied to both a healthy motor and a motor with a known inter-turn short fault. The magnitude of the second harmonic (twice the fundamental frequency) of the Park's vector was measured and compared across the two conditions. All results were normalised against the DC component value of the

Park's vector, and thus, all values are presented per unit (p.u.). The results are shown below in Table 6.2.

Table 6-2: Table of Extended Park's Vector Approach measurements for grid connected motor, healthy vs inter-turn short.

Grid partial load, no Fault.		**Grid partial load, inter-turn short.**		**Difference (p.u.)**
Frequency (Hz)	99.8	**Frequency (Hz)**	100	
Magnitude (p.u.)	0.243083734	**Magnitude (p.u.)**	0.518173946	0.275090212
Grid no load, no fault.		**Grid no load, inter-turn short**		
Frequency (Hz)	99.8	**Frequency (Hz)**	100.2	
Magnitude (p.u.)	0.256757555	**Magnitude (p.u.)**	0.392291528	0.135533973

As shown in Table 6.2, the introduction of the fault leads to an increase in the magnitude at twice the fundamental frequency of the Park's vector across both levels of load in the comparison. The most significant increase is observed in the fully loaded test, with a magnitude increase of 0.2751 p.u., which is the largest observed across the different load conditions.

This increase in magnitude provides valuable insight into the detection of an inter-turn short within the motor. The clear differentiation between the healthy motor and the faulty motor, especially under partially loaded conditions, demonstrates that Park's Vector Approach is sensitive to the presence of this type of fault. This result is important because it indicates that even under higher load conditions, which might complicate fault detection in some methods, the Park's vector can still effectively highlight the presence of inter-turn faults.

Thus, this analysis reinforces the utility of Park's vector method as a promising tool for detecting faults such as inter-turn shorts, even in challenging operating conditions like partially loaded conditions.

6.2.2 Broken Rotor Bar Faults

6.2.2.1 Motor Current Signature Analysis

Motor Current Signature Analysis is applied in much the same way compared to when finding an inter-turn fault. The formula differs as it reveals that these harmonics should be present around the fundamental harmonic of the system, as is shown in Equation 3.4. The results are as follows.

This test was conducted as per the mentioned procedure. All results shown below will be of the 100% loaded machine, as was the case for MCSA in the previous section. The result for this test is shown below with a particular focus on $k = 1$.

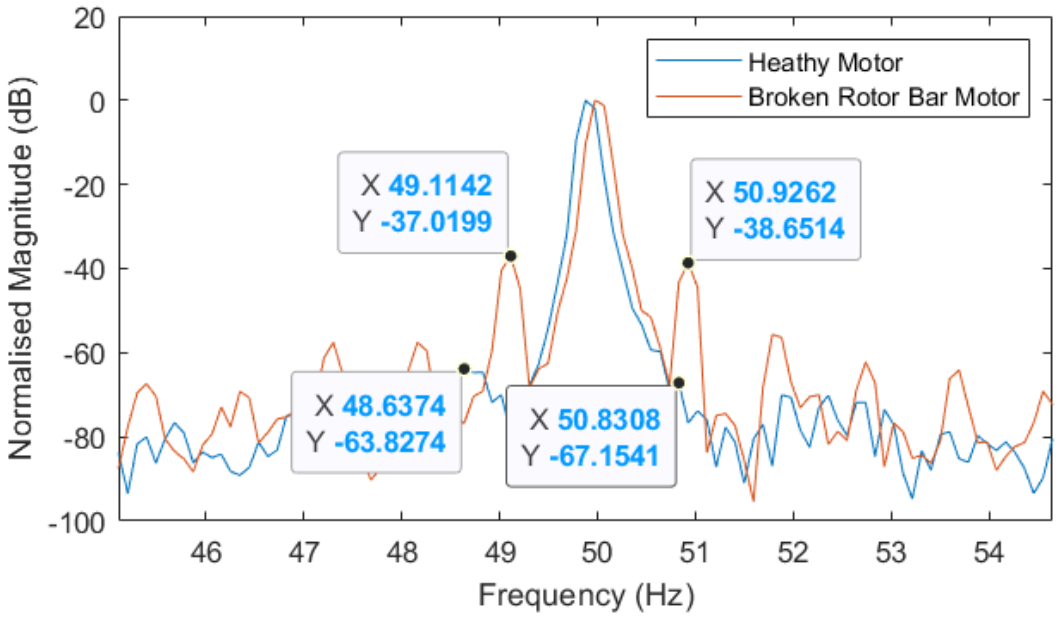

Figure 6.7: Frequency spectrum of line current, healthy motor vs broken rotor bar, k = 1.

The analysis in Figure 6.7 clearly shows significant differences in the broken rotor bar harmonics. This is particularly important due to the low load at which this test is conducted, so the differences being clear show the strength of the MCSA for broken rotor bars. The lower sideband exhibited an increase of 26.8075 dB, while the upper sideband showed a 28.5027 dB increase, both providing convincing evidence of the presence of a broken rotor bar. These results highlight how the harmonics related to the fault stand out, as noted in the appendix, where additional tests are included.

Regarding the harmonic position discrepancy, it is important to consider that the calculated harmonic locations were off by approximately 2 Hz. This difference could be attributed to variations in motor speed, as broken rotor bars can introduce oscillations in both the speed and torque. Since the synchronous speed is calculated as an average over the transient period, such oscillations could cause small shifts in the observed frequencies, leading to the noted 2 Hz deviation from the expected results. However, the overall spectral pattern remains consistent, which suggests that the method effectively identifies the fault despite these minor discrepancies.

6.2.2.2 Park's Vector Approach

The Park's vector approach is applied, with 1 cycle of data worth being presented on the plots that will be shown below. The results of the Park's Vector approach in detecting the broken rotor bar fault will now be presented.

The Park's vector approach was calculated and implemented in the same way as outlined by the experimental procedure, and the results are as follows.

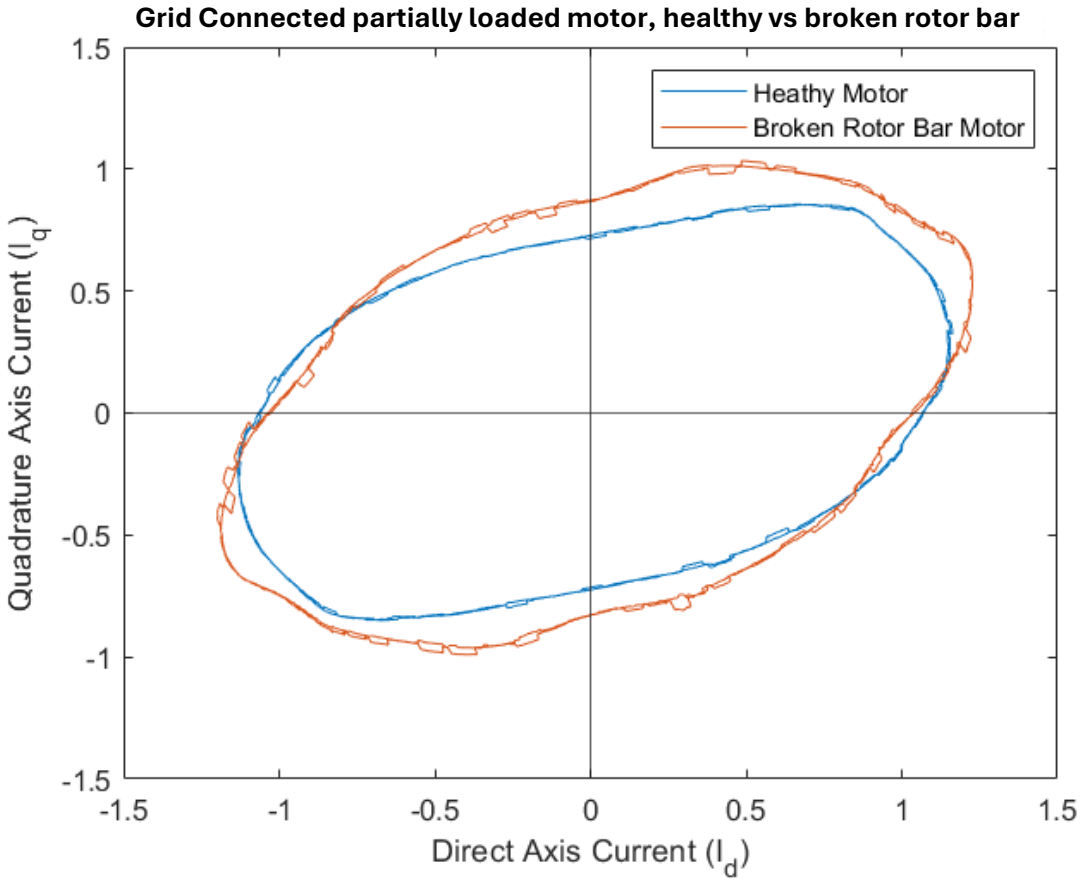

Figure 6.8: D-Q plot of broken rotor bar vs healthy motor, grid supplied, 1 cycle.

As can be observed in Figure 6.8, the overall shape of the healthy vs. the broken rotor bar motor is not significantly different, with the broken rotor bar having a slightly larger semi-major axis compared to the healthy motor. However, the real interest is observing the "thickness" of the d-q plot, as was discussed in Chapter 3 of this study, which can be observed over several cycles. This can be better observed below in Figure 6.9.

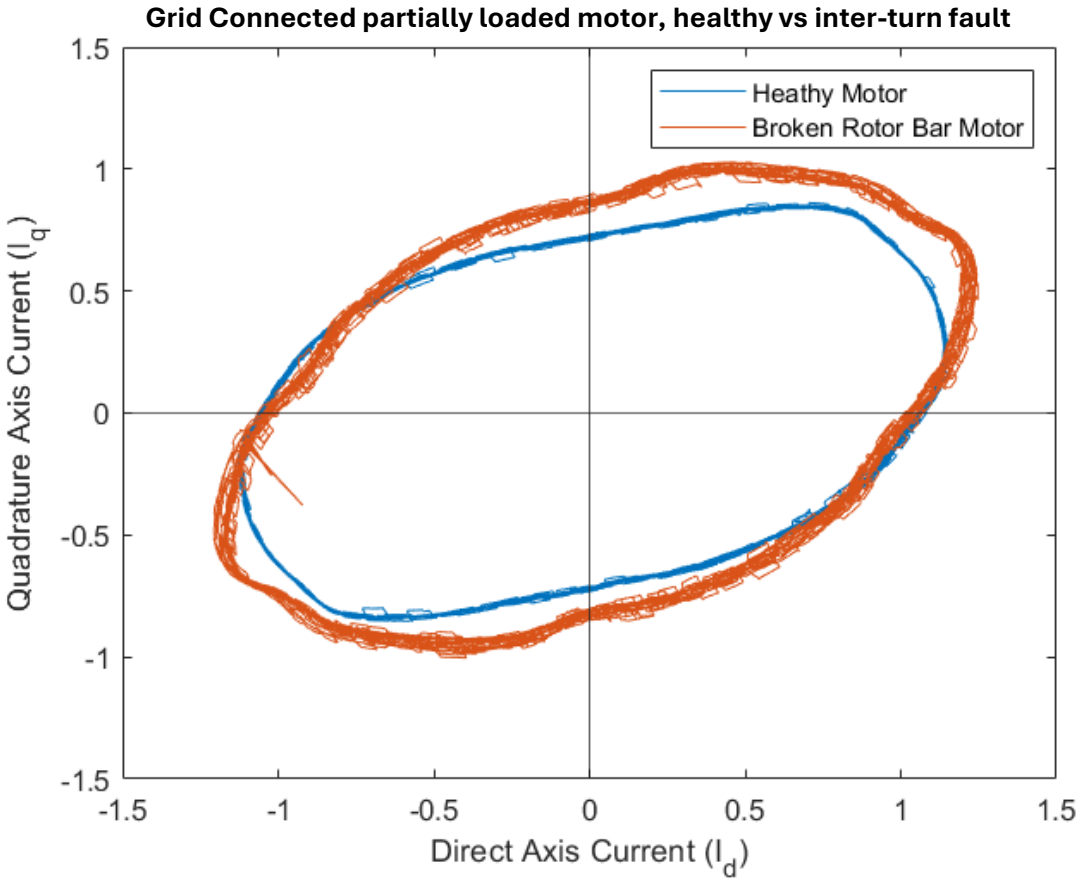

Figure 6.9: D-Q plot of healthy motor vs broken rotor bar, grid supplied, 10 cycles.

Although not immediately observable in Figure 6.9, once data from ten cycles are included within the D-Q plot (i.e., 0.2s worth of data captured), the thickness of the broken rotor bar plot does increase comparably to the healthy motor test.

As seen in the analysis, the overall thickness of the Park's Vector plot, measured from the innermost radius to the outermost radius at a specific point, is significantly greater in the case of a broken rotor bar fault compared to the healthy motor. The increased thickness, which is approximately twice that of the healthy motor, aligns with findings from the literature. However, this difference is not immediately obvious in the initial plots, due to the complexity of the fault and its interaction with the system's behaviour.

The situation improves when the graph is plotted using data from ten cycles, which helps in smoothing out transient effects and providing a clearer view of the fault signature. This longer data window allows for a more stable and recognisable pattern that distinguishes the broken rotor bar fault from other potential faults or normal operations.

As a result, this method proves to be a useful visual tool for detecting the presence of a broken rotor bar fault, and a 10-cycle timeframe will be adopted for the remainder of the tests. This approach not only improves clarity but also ensures a more reliable and accurate identification of faults within the system.

6.2.2.3 Extended Park's Vector Approach

As was done for the inter-turn fault case, the extended Park's vector approach is applied to the broken rotor bar data and analysis derived from it. The same method of application is used as in the previous test. The results are as follows.

For a grid-connected motor, the comparison of a healthy motor to a motor with broken rotor bars is made. As the mathematics within Chapter 3 shows, there is no expected increase of twice the fundamental harmonic of the Park's vector. The results of the test are shown below in Table 6.3.

Table 6-3: Extended Park's Vector Approach tests, grid supplied healthy motor vs broken rotor bar under various load conditions.

Grid partial load, no fault		**Grid partial load, broken rotor bar**		**Difference (p.u.)**
Frequency (Hz)	99.8	**Frequency (Hz)**	100	
Magnitude (p.u.)	0.243083734	**Magnitude (p.u.)**	0.23272	-0.010363845
Grid no load, no fault		**Grid no load, broken rotor bar**		
Frequency (Hz)	99.8	**Frequency (Hz)**	100	
Magnitude (p.u.)	0.256757555	**Magnitude (p.u.)**	0.209671	-0.047086513

As shown in Table 6.3, the harmonic present at twice the fundamental frequency exhibits a lower magnitude in the case of the motor with broken rotor bars, though the difference is small, with the largest difference being 0.0471 p.u. Less than in the healthy motor. This small variation indicates that the broken rotor bar fault may not significantly alter the harmonic magnitude under certain conditions.

What is particularly noteworthy is the trend observed as the load level increases from no load to partially loaded. In these cases, the difference in harmonic magnitude between the healthy and faulted motor decreases. This suggests that under partial load conditions, the presence of a broken rotor bar might be harder to detect, potentially leading to false negatives in fault detection. This could be an important consideration for real-world applications, as partially loaded motors are common in electric vehicle operating conditions, and relying solely on this method could result in not detecting faults in such scenarios.

The findings highlight the importance of considering load conditions when using this approach for fault detection, and further refinements to the method may be necessary to improve detection accuracy, especially under varying load levels.

6.2.3 Summary of grid-connected Motor Tests

Overall, the three methods used to analyse the two faults are applied to the grid-connected motor, and initially, it does show promise. The MCSA technique does not seem particularly adept at detecting the inter-turn fault on the motor at this load for the motor; however, for the broken rotor bar, it works significantly better. It is important to note that the technique is not the same, but does fall under the same category.

What does seem more promising is the Park's Vector Approach. In both fault cases, the visual representation of the fault is quite evident, with the "skewness" of the plot shown in the inter-turn fault case and the thickness increase of the plot being evident in the broken rotor bar case. This does provide a good stepping stone and a quick visual representation that something may be wrong with the motor, and a starting point for a deeper investigation to be done on the motors.

The extended Park's Vector Approach did provide some meaningful results, especially in the case of the inter-turn fault, where an increase as great as 0.275 p.u. in the magnitude of the fault harmonic that is located at twice the fundamental frequency of the system. This is significant as even at lower loads, this fault is still present, and is likely to increase in presence at higher loads. This does provide a numeric indication of the presence of a fault. The same case cannot be made for the broken rotor bar case. In all test cases, the broken rotor bar harmonic was lower in magnitude than the normal motor. This does not discount the validity of the Extended Park's Vector Approach but rather highlights the strength of the strategy in determining specific faults.

6.3 V/HZ OPEN-LOOP TESTS

6.3.1 Stator inter-turn Fault tests

This subsection shall cover the experiments focusing on the comparison between a healthy motor and a motor that has four windings shorted on its stator. Results have been captured from an inverter-fed machine implementing a V/Hz open-loop control scheme and run at two loading levels. The results are as follows.

6.3.1.1 Motor Current Signature Analysis

With the inter-turn short motor, the same test was run by being supplied by an inverter, controlled by an open-loop V/Hz control method. This was run at 50 Hz fundamental frequency. The same procedure was followed as the grid-connected tests, and thus, the ruggedness of the MCSA method for detecting inter-turn faults is assessed. The results are as follows.

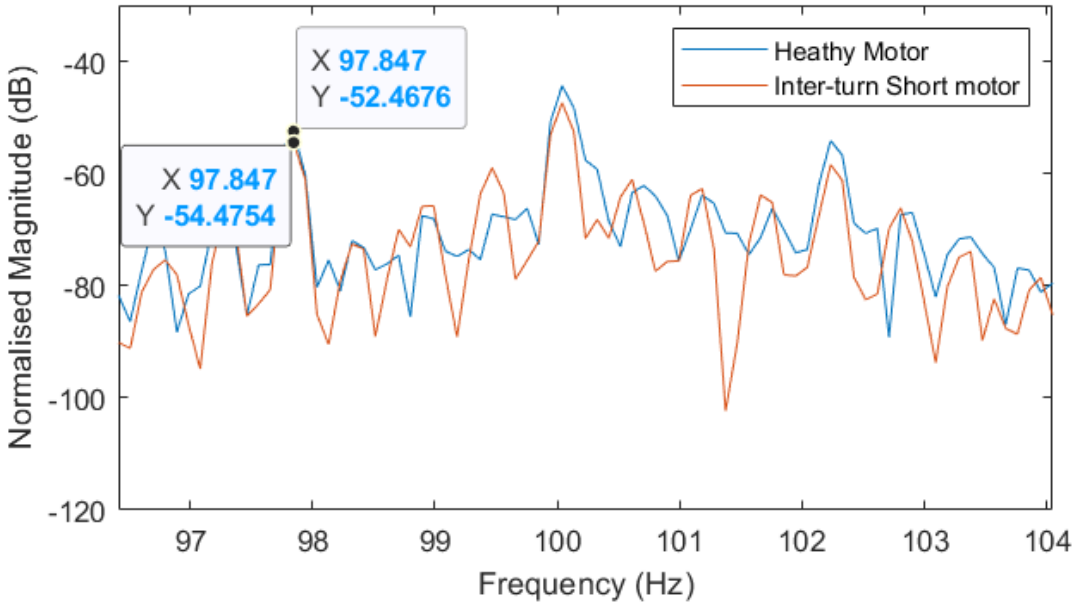

Figure 6.10: n=1, k=1 for V/Hz open-loop fed induction motor, healthy vs inter-turn short frequency spectrum.

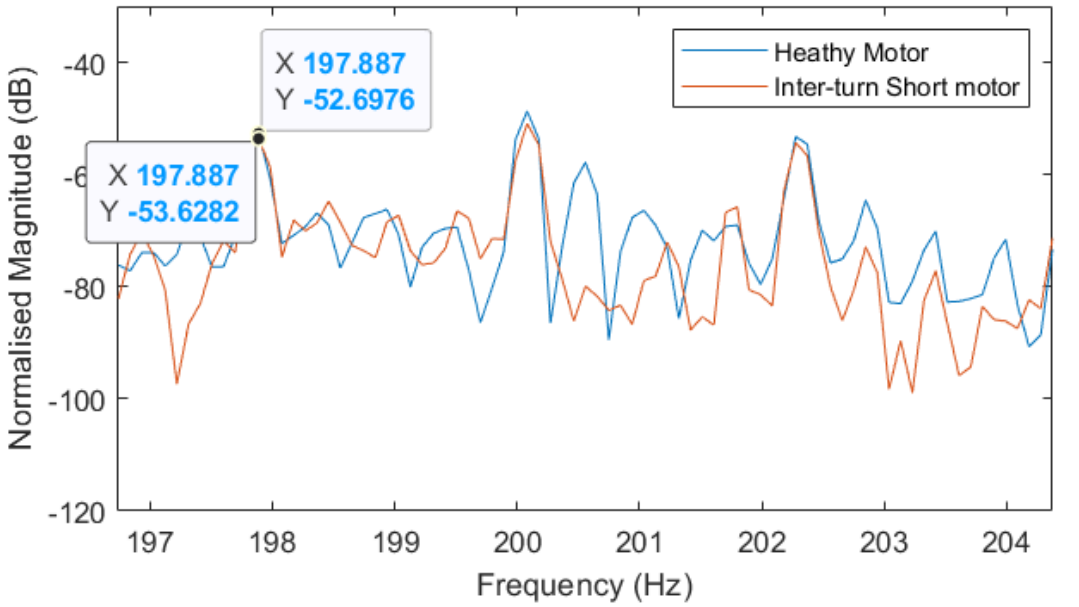

Figure 6.11: n=1, k=3 for V/Hz open-loop fed induction motor, healthy vs inter-turn short frequency spectrum.

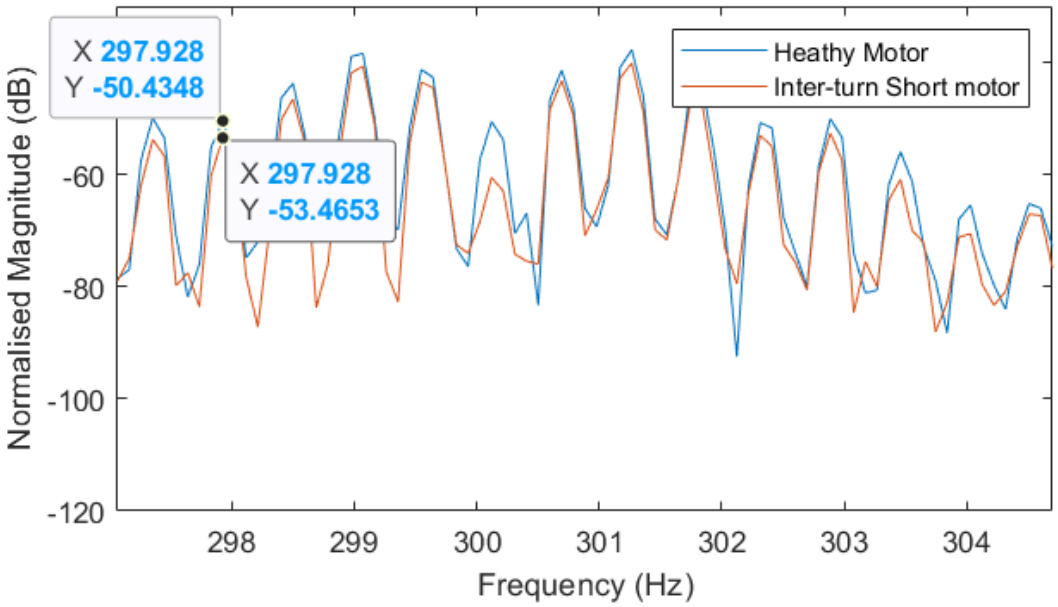

Figure 6.12: n=1, k=5 for V/Hz open-loop fed induction motor, healthy vs inter-turn short frequency spectrum.

As can be seen in Figures 6.10, 6.11 and 6.12 above, there is no obvious distinction between the two tests, i.e., healthy vs. inter-turn short motor. The frequencies are also significantly closer together as the frequency was controlled through an inverter; thus, the variation seen in the grid connected test is no longer occurring. Once again, the test proves inconclusive, as in both cases the healthy motor has a greater magnitude compared to the faulty motor, in addition to there being no clear fault peaks to choose from, mostly due to the additional noise that is automatically present when a switch-mode converter is used. Additionally, the low load at which the test was conducted adds additional inconclusiveness, as the lower current magnitude could hamper this method's effectiveness. This does not discredit the use of MCSA in inter-turn short findings, but does illuminate the potential limitations that this method has concerning its range of use cases. The MCSA technique was used as a benchmark for the following chosen tests and does provide a stepping stone for where the following tests may improve upon. However, in both the case of a partially loaded grid-fed and inverter-fed machine, it does provide an inconclusive result. A table of the results can be shown below in Table 6.4.

Table 6-4: Inverter fed V/Hz open-loop controlled, 25% load healthy vs inter-turn fault MCSA results.

25% Load	Healthy		Inter-turn short		Difference
	Frequency (Hz)	Magnitude (dB)	Frequency (Hz)	Magnitude (dB)	
n = 1, k = 3	97.847	-52.4676	97.847	-54.4754	-2.0078
n = 1, k = 3	197.887	-52.6976	197.887	-53.6282	-0.9306
n = 1, k = 5	297.928	-50.4348	297.928	-53.4653	-3.0305

The results for this case had a variation of 2.6703 Hz maximum from the calculated values, which is a significantly broader spectrum compared to the grid-fed results, once again highlighting how once connected to an inverter, the spectrum is significantly more filled with additional harmonics, and thus harder to find clear fault peaks within it.

Figure 6.12 is particularly interesting, as the spectrum of both motors is very closely matched, almost identical in fact. This does help illuminate that once significant additional noise is placed within the system, detection methods do have a higher requirement for robustness to aid in the process of detecting the fault.

6.3.1.2 Park's Vector Approach

In the same way that the data was processed and presented in the previous chapter, it will be presented from now on.

The same test was run, but through an inverter-connected motor that was being controlled by an open-loop V/Hz scheme. The results from the Park's vector approach are as follows.

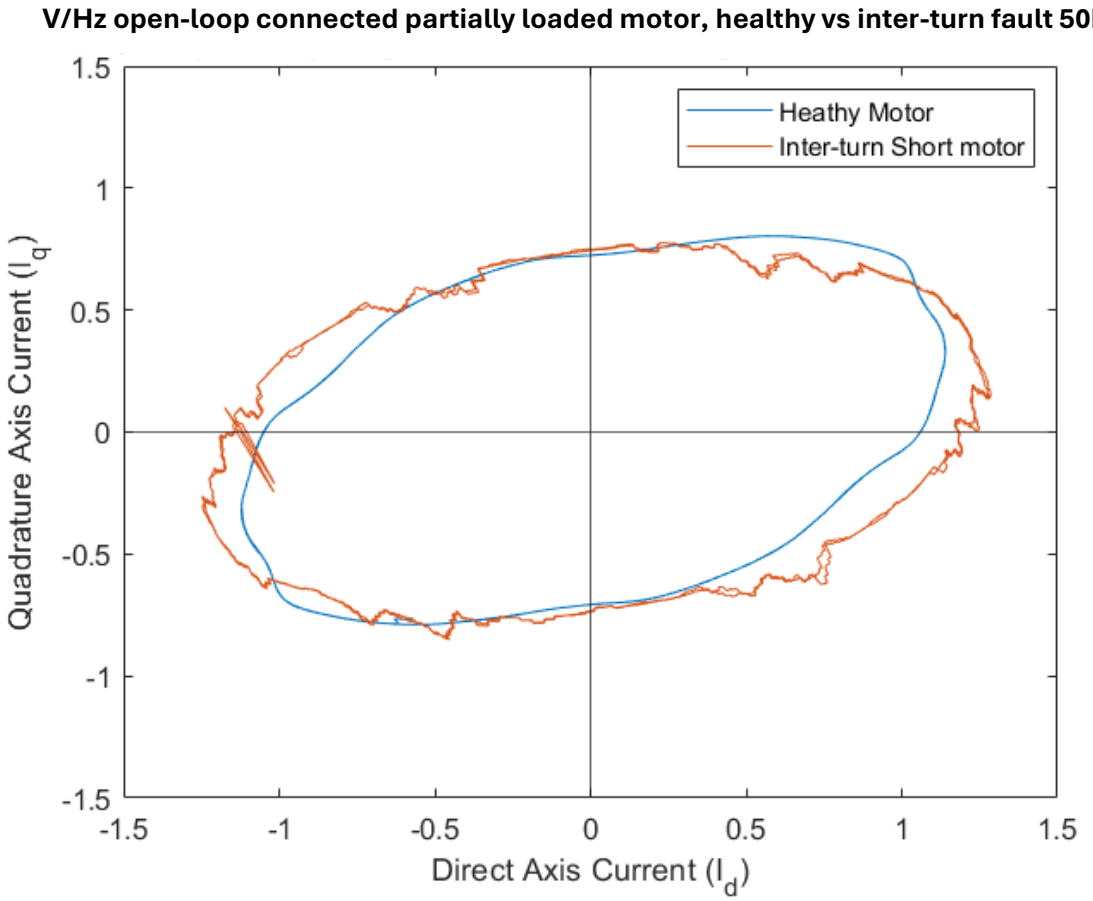

Figure 6.13: Normalised Park's Vector D-Q plot of inverter connected induction motor, healthy vs inter-turn short comparison.

As can be seen in Figure 6.13, there is a visual difference between the two ellipse shapes, with a definite added tilt on the plot of the inter-turn short motor. This result is not as significantly clear as the grid-connected motor, which may be because the inverter-connected motor was less unbalanced than the grid-connected motor, possibly due to the nature of how it was connected to the inverter. However, this does provide a useful metric to show that a range of imbalances can be detected through this method.

Both baseline tests from above show that this method can detect the presence of the inter-turn short fault. With both having the same level of fault severity, how the motor was connected provided various levels of imbalance under the same load and fault conditions. However, in both cases, the presence of the fault was able to be detected.

This does provide a useful visual and basic approach; however, the next method can help quantify the severity of the fault once it is present in a clearer metric.

6.3.1.3 Extended Park's Vector Approach

The same test and method are being applied to data captured from an inverter-connected, V/Hz open-loop controlled motor. This was done to determine the robustness of the method. The results are as follows.

Table 6-5: Table of Extended Park's Vector Approach measurements for V/Hz open-loop inverter connected motor, healthy vs inter-turn short.

V/Hz Open-loop, partial load, no fault		**V/Hz open-loop, partial load, inter-turn short**		**Difference (p.u.)**
Frequency (Hz)	100	**Frequency (Hz)**	100	
Magnitude (p.u.)	0.110613842	**Magnitude (p.u.)**	0.18433319	0.073719349
V/Hz open-loop, no load, no fault		**V/Hz open-loop, no load, inter-turn short**		
Frequency (Hz)	100	**Frequency (Hz)**	100	
Magnitude (p.u.)	0.11160173	**Magnitude (p.u.)**	0.176938363	0.065336633

As shown in Table 6.5, the same trend observed in the grid-connected tests is also evident in the inverter-fed tests, where the increase in load correlates with an increase in the magnitude of the "faulted" harmonic. Although the difference in magnitude is not as significant as in the grid-connected tests, there is still a measurable increase in the per-unit (p.u.) values, which could aid in the detection of the fault.

What is particularly noteworthy is that the increase in load does not appear to significantly affect the fault-free (healthy) tests, where the harmonic remains stable. In contrast, the faulted motor shows a notable increase in the magnitude of the faulted harmonic, with a difference of up to 0.0737 p.u., which is significant enough to be considered a reliable indicator of the inter-turn fault.

The smaller differences in comparison to the grid-connected tests are due to the presence of some control in the inverter-fed setup. One of the key differences is that, unlike in the grid-connected case, where there was a deviation of about 0.4 Hz in the frequency of the second harmonic across all tests, the inverter-fed tests maintained a consistent frequency at twice the fundamental frequency. This consistency reduces the impact of external variations in frequency, which may explain why the difference in harmonic magnitudes is less pronounced but still significant enough to detect the fault.

This reinforces the effectiveness of the test in detecting inter-turn faults under both grid-connected and inverter-fed conditions, although the consistency offered by the inverter-controlled setup appears to reduce the variation in harmonic frequencies, leading to smaller magnitude differences between healthy and faulted conditions. Nonetheless, this method still offers a valuable diagnostic tool for identifying faults in electric motors. Even at lower load torque.

6.3.1.4 DC Bus tests

The core focus of this study is on the detection of the inter-turn fault by analysing the frequency spectrum of the DC bus current of the powertrain. This, for obvious reasons, can only be within the inverter-connected scenarios, and that is what will be presented below.

As was found within the literature, the presence of the inter-turn fault should increase the magnitude of the harmonic at twice the fundamental frequency on the DC bus current. The DC bus current was analysed around this harmonic, and the results are as follows.

With the inverter set to run at 50 Hz with a V/Hz open-loop control scheme, the DC bus was analysed and compared against a healthy motor and a motor with a known inter-turn fault. All harmonics have been normalised against the DC component of the current. The ripple factor of the DC bus was also used as a metric in aid of detecting the presence of the fault. The results of this analysis are shown below.

Table 6-6: DC Bus analysis of V/Hz open-loop inverter connected motor: healthy vs inter-turn short.

V/Hz open-loop, no load, no fault		**V/Hz open-loop, no load, inter-turn short**		**Difference (p.u.)**	**Difference (faulted / healthy)**
Frequency (Hz)	100	**Frequency (Hz)**	100		
Magnitude (p.u.)	0.03331718	**Magnitude (p.u.)**	0.15105633	0.117739149	4.533886992
Ripple Factor	0.45047894	**Ripple Factor**	0.88340887	0.432929931	1.961043664
V/Hz open-loop, partial load, no fault		**V/Hz open-loop, partial load, inter-turn short**			
Frequency (Hz)	100	**Frequency (Hz)**	100		
Magnitude (p.u.)	0.01332265	**Magnitude (p.u.)**	0.11500937	0.101686716	8.632619336
Ripple Factor	0.67101362	**Ripple Factor**	1.08380458	0.412790958	1.61517523

As observed in Table 6.6, the presence of the fault is detectable using this method, as both load cases show a significant increase in the harmonic at twice the fundamental frequency. The largest difference is seen at 8.63 times higher once the fault is introduced, indicating a clear fault signature in the motor's behaviour. This is particularly significant as this test is not conducted at max load torque of the machine, so it stands to reason that in that case, the increase would be more significant.

Interestingly, the overall magnitude in per-unit (p.u.) does decline as the load increases, which may seem counterintuitive at first. This decrease is primarily due to the increase in the DC component as the load rises. The DC component increases more significantly than the harmonic at twice the fundamental frequency, leading to a reduction in the p.u. magnitude of the harmonic. Despite this, the difference between the healthy and faulty cases remains significant, providing a reliable fault detection indicator.

Furthermore, the ripple factor provides additional valuable insight. The ripple factor tends to increase in all load cases, with the increase being almost double in two cases and about 1.6 times higher in the partially loaded test. This increase in the ripple factor suggests that there are more harmonics present on the DC bus of the inverter when the fault is present. This provides further evidence that the fault is influencing the harmonic content in the system, and the ripple factor is a useful metric for detecting faults, particularly in inverter-fed systems.

In conclusion, despite the counterintuitive decline in p.u. magnitude with increasing load, both the harmonic analysis at twice the fundamental frequency and the ripple factor indicate the presence of a fault. This method, in combination with ripple factor monitoring, provides a robust approach to detecting faults in motors, especially in inverter-fed systems.

6.3.2 Broken Rotor Bar Fault Tests

This subsection focuses on the analysis and detection of a broken rotor bar within an induction motor. The same techniques that were used above will be used in the following section, with the same methods of signal processing and analysis applied to them. The results are as follows.

6.3.2.1 MCSA

The same method and harmonics are being used and focused on in this test compared to the previous one. The results shown below can highlight the differences in the grid supplied versus the V/Hz open-loop inverter supplied tests.

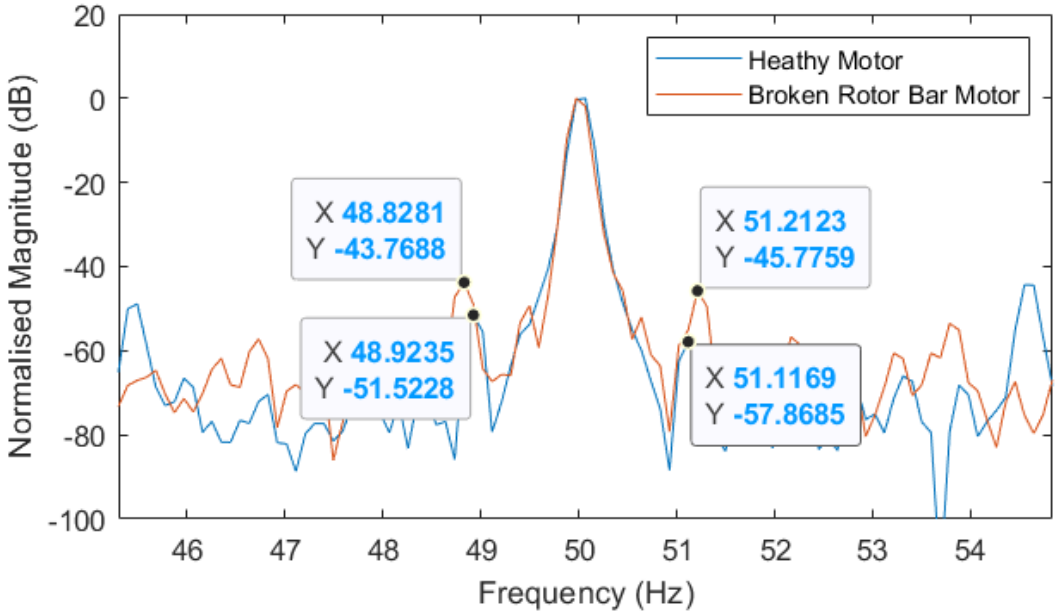

Figure 6.14: Healthy motor vs broken rotor bar motor, V/Hz open-loop inverter supplied, k = 1.

The harmonics are easily noticeable for the broken rotor bar test, as seen in Figure 6.14. The upper sideband has a 12.0926 dB increase, and the lower sideband has a 7.7540 dB increase in the broken rotor bar motor measurements. Once again, the supply from the inverter results in a noisier frequency spectrum, with more harmonic peaks in the healthy motor measurement compared to the grid-supplied experiments.

There was also a difference of 4.1 Hz in some cases of the calculated values, and once again, it is believed to be due to the speed ripple that can occur during the presence of broken bars; however, once observing the frequency spectrum, it becomes trivial as to where the harmonics are present throughout the spectrum.

These tests do show that the detection of a broken rotor bar is possible, even when supplied with an inverter. Although the differences between the healthy and faulty motors are smaller compared to the grid-connected experiments, there is still a noticeable increase in the magnitude of the faulted harmonics. This smaller difference can be attributed to the fact that there is a basic element of control inherent in the V/Hz open-loop, although nothing complex or even robust, but still enough to see a significant difference between the two experiments, with the harmonics in the grid-connected test with an increased magnitude level of at least 7dB in the broken rotor bar tests. The small difference can also be attributed to the higher magnitude level of the healthy motor harmonics, most likely due to the added noise of the inverter; thus, an increase appears smaller as the baseline magnitude has increased, at least 7 dB in one case of the healthy motor grid supplied versus inverter-supplied tests.

Overall, the MCSA technique is proving more adept at detecting the presence of a broken rotor bar compared to an inter-turn short in this set of experiments.

6.3.2.2 Park's Vector Approach

The same technique is applied to the V/Hz open-loop inverter supplied motor, and the comparison is made between the healthy and broken rotor bar motors. The results are shown below in Figure 6.15.

V/Hz open-loop connected partially loaded motor, healthy vs broken rotor bar 50Hz

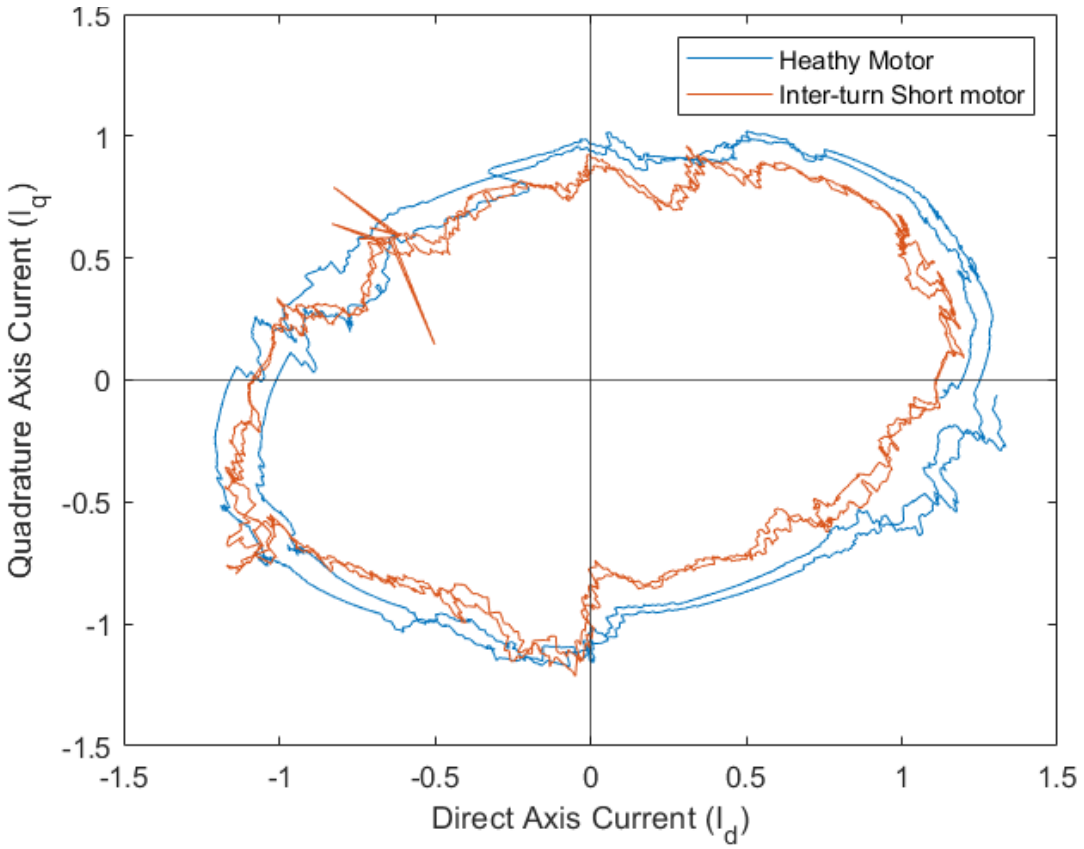

Figure 6.15: Normalised D-Q plot of broken rotor bar vs healthy motor, V/Hz open-loop inverter supplied, 1 cycle.

As was the case for the grid supplied, remarkably similar observations can be made for the V/Hz inverter supplied tests. There is no meaningful change in the plot that is immediately observable, other than the healthy plot seeming less “consistent” with its ellipsoid shape; thus, further investigation into additional data is required. The D-Q plot with ten cycles worth of data is shown below.

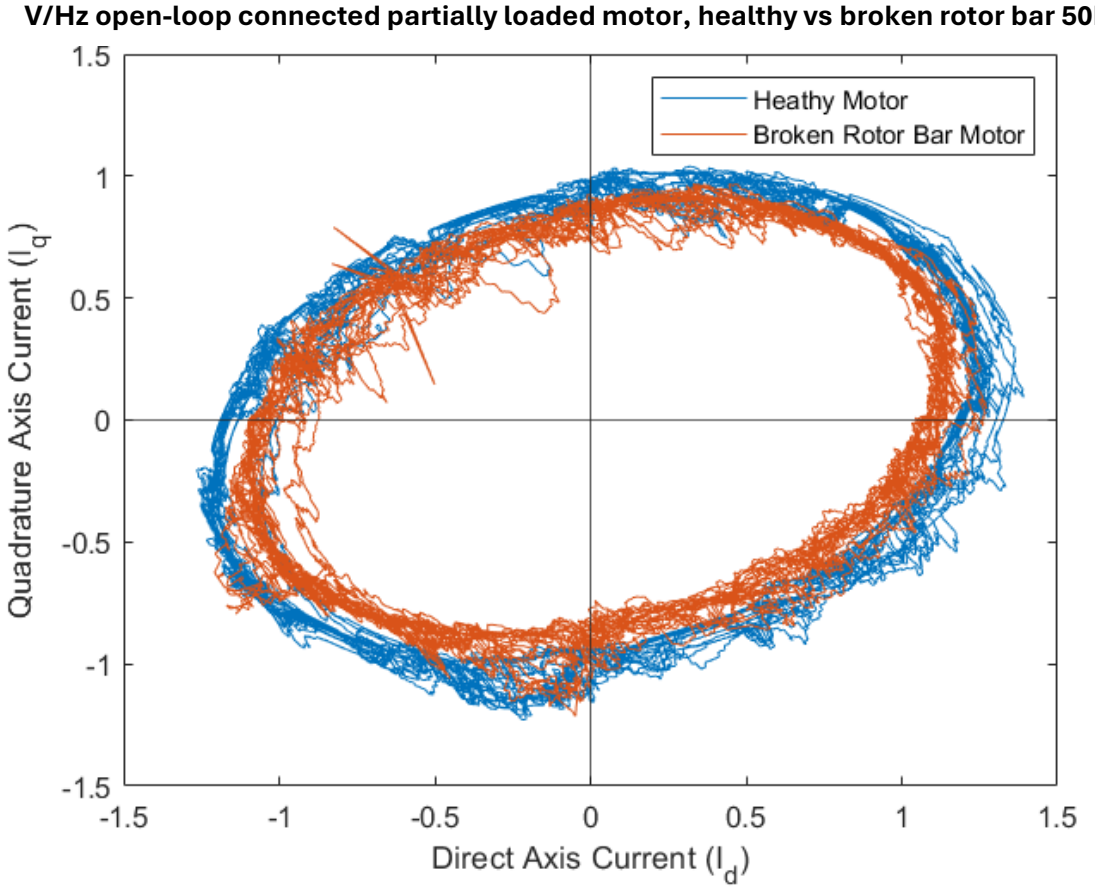

Figure 6.16: Normalised D-Q plot of broken rotor bar vs healthy motor, V/Hz open-loop inverter supplied, 10 cycles.

In Figure 6.16, the observations are the opposite of what was made in the grid-supplied broken rotor bar section. The thickness of the plot of the broken rotor bar has increased, but so has the healthy motor bar baseline. This does indicate that the additional noise generated through an inverter-supplied system is hampering the effectiveness of this method in determining a broken rotor bar fault. It is inconclusive as the thickness seems to be the same in some sections of both plots; however, in some spots, the faulted graph is thicker than the healthy one and vice versa. Once again, this does provide somewhat of a nice visual representation that a fault may be present within the motor; however, given that there is no numerical evidence to measure, but rather an overall plot shape to follow, it remains a useful stepping stone in classifying the fault, rather than being an outright detection method for a broken rotor bar fault.

6.3.2.3 Extended Park's Vector Approach

As above, the same test is applied to V/Hz open-loop controlled inverter-supplied motors. The results for the extended Park's vector approach are shown in Table 6.7 below.

Table 6-7: Extended Park's Vector Approach tests, V/Hz open-loop supplied healthy motor vs broken rotor bar under various load conditions.

V/Hz open-loop partial load, no fault.		V/Hz open-loop partial load, broken rotor bar.		Difference (p.u.)
Frequency (Hz)	100	**Frequency (Hz)**	100	
Magnitude (p.u.)	0.11160173	**Magnitude (p.u.)**	0.162442087	0.050840358
V/Hz open-loop no load, no fault.		**V V/Hz open-loop partial load, broken rotor bar.**		
Frequency (Hz)	100	**Frequency (Hz)**	100	
Magnitude (p.u.)	0.110613842	**Magnitude (p.u.)**	0.160370145	0.049756303

The data presented in Table 6.7 provides valuable insight, although it reveals some limitations when using the Extended Park's Vector Approach (EPVA) for detecting broken rotor bars. In all cases, there is an increase in the magnitude of the harmonic when the broken rotor bar is present, even if only marginally. However, like the grid-supplied tests, the change in harmonic magnitude from the healthy motor to the motor with the broken rotor bar is not significant enough to identify the fault. The largest increase in magnitude observed is 0.051 p.u., which is small.

Based on these findings, the current application of the EPVA, focusing on this harmonic, does not appear to provide a definitive method for detecting broken rotor bars, particularly in lower load conditions. This suggests that further refinement of the method or the incorporation of additional parameters may be necessary to improve the sensitivity and reliability of fault detection using the EPVA.

6.3.2.4 DC Bus tests

As for the inter-turn fault tests, the DC bus will be analysed at twice the fundamental frequency to analyse the change in magnitude of the harmonic in the healthy case versus the broken rotor bar case. This is only possible when connected to an inverter, as this is the time that the DC bus is available to monitor. The results of this analysis are below in Table 6.8.

Table 6-8: DC Bus analysis for V/Hz open-loop inverter supplied motor, healthy vs broken rotor bar.

V/Hz open-loop no load, no fault.		V/Hz open-loop no load, broken rotor bar.		Difference
Frequency (Hz)	100	**Frequency (Hz)**	100	
Magnitude (p.u.)	0.033317179	**Magnitude (p.u.)**	0.033337763	2.0584E-05
Ripple Factor	0.450478941	**Ripple Factor**	0.518110848	0.067631907
V/Hz open-loop partial load, no fault.		**V/Hz open-loop partial load, broken rotor bar.**		
Frequency (Hz)	100	**Frequency (Hz)**	100	
Magnitude (p.u.)	0.013322649	**Magnitude (p.u.)**	0.015472262	0.002149613
Ripple Factor	0.671013622	**Ripple Factor**	0.699597281	0.028583659

As can be observed in Table 6.8 above, the results are not as significant as compared to the inter-turn short results. The difference in the magnitude of the harmonic at twice the fundamental frequency is negligible in both cases, with the no-load case being almost identical and the same up until the fourth decimal point. Overall, it seems that the harmonic analysis, especially focusing on the harmonic at twice the fundamental frequency, is not a viable option for detecting a broken rotor bar fault on the powertrain. This is further backed up by the fact that the ripple factor does not significantly increase in the presence of the fault either.

There is a slight increase in the ripple factor for the lower load tests; however, not nearly as significant as the inter-turn fault on the DC bus. This is indicative that there is not a significant increase in the number of harmonics that are present on the DC bus when there is a broken rotor bar fault present in the motor.

This does make sense with the literature, as a broken rotor bar does not induce an unbalance as the inter-turn short does, but rather a speed and torque ripple into the system, which, seemingly, has no significant increase in the harmonics present on the DC bus of an electric vehicle powertrain.

6.3.3 Summary of V/Hz open-loop tests

As can be seen from the tests, the MCSA technique does not seem to be able to detect an inter-turn fault; in this case, it seems even more indiscernible due to the additional noise that is presented through the inverter-connected system. The MCSA technique does seem to be able to better detect a broken rotor bar, as was shown; however, it does seem less so compared to the grid-connected case, as was shown in the earlier chapter. Due to the MCSA technique's limitations in its ability to detect the inter-turn fault, for the remaining chapters, this will not be shown in the main body of this study. This is suspected due to the low torque load level as well as additional noise presented by the inverter connection. The results can be seen in the appendix, but do follow similar patterns as shown in the first two sections of the results.

The Park's Vector Approach can again visually show the presence of both faults. In the inter-turn faults, the graph is more skewed in the case of the faulted motor; although it is not significant, it is still easily noticeable and once again provides a useful visual indication that the fault is present. In the case of the broken rotor bar, the thickness of the graph does increase; although a larger time sample was used in the broken rotor bar case, the thickness of the plot in the broken rotor bar case is significantly thicker than the graph in the healthy case. This technique, once again, is proving to be a useful visual indicator as well as a stepping stone to indicate that further analysis should be employed to understand the presence and severity of a fault, even when connected to an inverter supply.

The extended Park's Vector Approach once again provides comparable results as was the case in the grid-connected results. For the inter-turn fault, there was an increase in magnitude as big as 0.0737 p.u. of the analysed harmonic; this is less than the grid-connected case but is still a significant increase on the harmonic. For the broken rotor bar case, there is still an overall increase in the analysed harmonic, but only as large as 0.0508 p.u., which is not as significant as the inter-turn fault but still significant enough that it is worth analysing and taking note of. This does provide better results compared to the grid-connected tests and does indicate that the extended Park's vector approach may be adept at identifying multiple fault cases, as opposed to what was shown in the grid-connected results.

The additional technique applied to the V/Hz open-loop case was the DC bus analysis, in which the second fundamental component is analysed in the DC bus current of the supply. In

the inter-turn fault case, it provided substantial results. There was an increase in the analysed harmonic as significant as 0.1219 p.u., as well as an increase in the ripple factor of the DC bus across both load tests. This is not the same case in the broken rotor bar tests. This technique relies on the introduction of an imbalance in the system through the inter-turn fault to have an increase in the analysed harmonic, which is not the case for the broken rotor bar. There are inconclusive differences in the healthy vs. broken rotor bar cases; in one of the load tests, it is smaller in the case of the broken rotor bar. The same case can be said for the ripple factor; although there is an increase, it is not as significant as the inter-turn fault proved to be. Again, this does not disprove the technique's ability but rather highlights the faults in which the technique is better at detecting. Overall, the DC bus analysis provides some useful insight into the changes on the DC bus that can occur when a fault appears on the motor, especially considering this is not occurring at max torque load.

6.4 V/Hz CLOSED-LOOP TESTS

The chosen techniques were applied to the same set of tests, although with a V/Hz closed-loop controlled inverter supply. The results are as follows.

6.4.1 Inter-turn Fault Analysis

6.4.1.1 Park's Vector Approach

The Park's vector approach was applied to the data, and the resulting DQ plot is shown below in Figure 6.17.

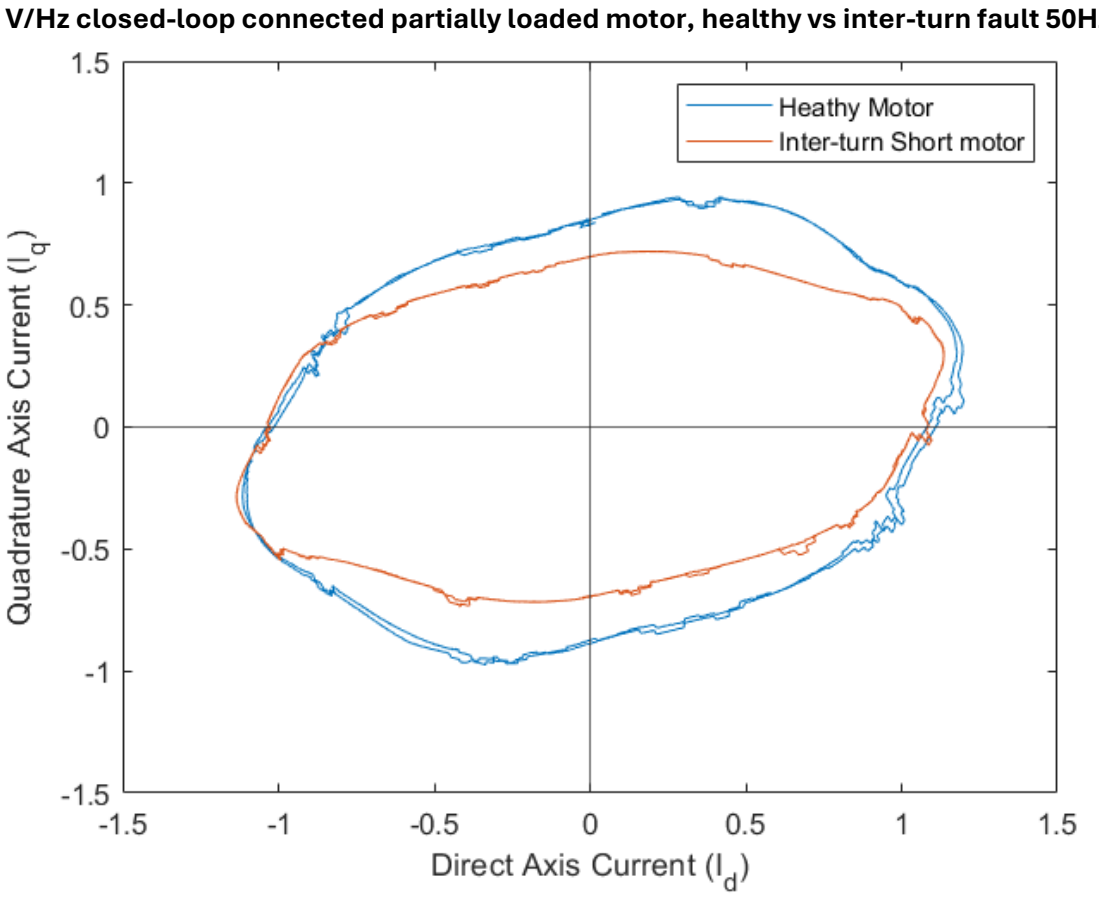

Figure 6.17: Normalised DQ plot of V/Hz closed-loop inverter supplied motor, healthy vs inter-turn fault.

The DQ plot shown in Figure 6.17 for the inter-turn fault shows a trend like previous results, where the semi-major axis of the healthy motor is larger compared to the motor with the inter-turn fault, though the difference is small. Despite this, it is not immediately obvious to the eye.

However, a more noticeable characteristic is the shape of the inter-turn fault DQ plot, which tends to be more elliptical compared to the healthy motor plot. This clear difference becomes evident when visually comparing the two, indicating the presence of a fault.

This observation aligns with the trends seen in both the inverter and grid-supplied tests, where the method successfully identifies the presence of a fault. Despite the subtle nature of the

differences in some cases, the change in shape and the clear visual distinction in the DQ plot make this method useful for detecting inter-turn faults in induction motors.

6.4.1.2 Extended Park's Vector Approach

The extended Park's vector approach has been applied, and the results are shown below in Table 6.9.

Table 6-9: Extended Park's Vector Approach results for V/Hz closed-loop inverter supplied motors, healthy vs inter-turn fault.

V/Hz closed-loop, no load, no fault 50Hz.		**V/Hz closed-loop, no load, inter-turn fault 50Hz.**		**Difference (p.u.)**
Frequency (Hz)	100	**Frequency (Hz)**	100	
Magnitude (p.u.)	0.16465213	**Magnitude (p.u.)**	0.27125391	0.106601775
V/Hz closed-loop, partial load, no fault 50Hz.		**V/Hz closed-loop, partial load, inter-turn fault 50Hz.**		
Frequency (Hz)	100	**Frequency (Hz)**	100	
Magnitude (p.u.)	0.1628958	**Magnitude (p.u.)**	0.25652209	0.093626289

The results in Table 6.9 show a clear increase in the harmonic present at twice the fundamental frequency. The increase is consistent across both load conditions, with values ranging from 0.0936 p.u. to 0.107 p.u. This indicates a noticeable change in the harmonic, which could be used to detect the presence of a fault.

This consistent and stable response at higher speeds highlights the potential of this method for fault detection, particularly in scenarios with varying load conditions. The ability to identify fault characteristics despite the increased load variations further strengthens the reliability of the approach for real-world applications.

6.4.1.3 DC Bus

The DC bus current and voltage were analysed for this closed-loop control algorithm, and the results are shown in Table 6.10 below.

Table 6-10: DC Bus analysis for V/Hz closed-loop inverter supplied motor, healthy vs inter-turn fault.

V/Hz closed-loop, no load, no fault.		**V/Hz closed-loop, no load, inter-turn fault.**		**Difference (p.u.)**	**Difference (faulted / healthy)**
Frequency (Hz)	100.3	**Frequency (Hz)**	100		
Magnitude	0.0127351	**Magnitude**	0.237648808	0.224914	18.66093
Ripple Factor	0.43107816	**Ripple Factor**	0.936507585	0.505429	2.172477
V/Hz closed-loop, partial load, no fault.		**V/Hz closed-loop, partial load, inter-turn fault.**			
Frequency (Hz)	100.3	**Frequency (Hz)**	100		
Magnitude	0.0163855	**Magnitude**	0.180802239	0.164417	11.03428
Ripple Factor	0.650555434	**Ripple Factor**	1.100907527	0.450352	1.692258

The results from Table 6.10 provide convincing evidence of the presence of the fault, as the harmonic at twice the fundamental frequency shows a noticeable increase. The increase ranges from a minimum of 0.164 p.u. to a maximum of 0.225 p.u., which is a notable change. Considering this increase accounts for up to 22.5% of the DC component of the current, the presence of a broken rotor bar leads to a marked alteration in the harmonic pattern.

Furthermore, the ripple factor shows consistent trends across all load conditions, similarly increasing in the presence of the fault. This increase in ripple factor further supports the detection of the fault and may also provide insight into the severity of the fault, as larger ripple factors often correlate with more severe disruptions in the motor's operation.

The analysis of the DC bus once again proves to be the most effective method for both detecting the fault and assessing its severity. The consistent behaviour of the DC bus signals in the presence of the broken rotor bar fault makes this technique a reliable approach for fault detection and offers valuable information for evaluating the health of the motor.

6.4.2 Broken Rotor Bar Fault

6.4.2.1 Park's Vector Analysis

The Park's Vector Approach was applied to the data gathered in a V/Hz closed-loop configuration, and the results are as follows in Figure 6.18.

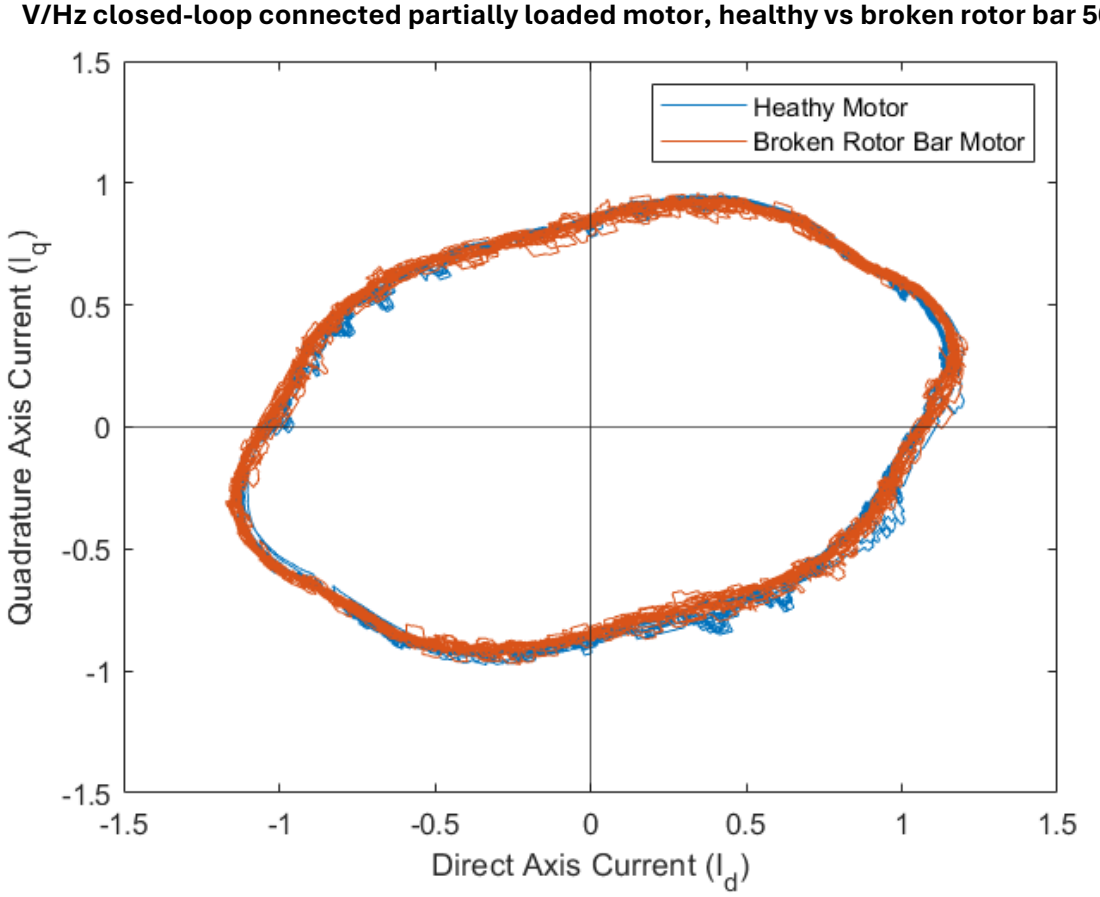

Figure 6.18: Normalised D-Q plot of broken rotor bar vs healthy motor, V/Hz closed-loop inverter supplied, 10 cycles.

As can be immediately noticed in Figure 6.18, there is no significant difference between the two plots. The thickness of the two plots is extremely similar in most places around the graphs as well. This does not provide conclusive proof that there is a fault, as the two graphs are significantly identical; however, this could be the case, as the closed-loop system is managing the effect of the presence of a fault in a more substantial way than was seen in the previous two test scenarios.

Overall, this does not seem to provide a clear visual test in which a fault can be detected and indicates some limitations with this method's efficacy in detecting various faults. This does seem to insinuate that the more advanced control scheme is better adept at managing the presence of the fault, as this plot is less noisy than the V/Hz open-loop tests as well and is more similar. Overall, this does provide a nice visual representation of the "health" of the motor, although it is not a particularly strong indicator of the presence of a broken rotor bar.

6.4.2.2 Extended Park's Vector Approach

The Extended Park's Vector Approach was applied to a V/Hz closed-loop connected system, and the results are as follows.

Table 6-11: Extended Park's Vector Approach results for V/Hz closed-loop inverter supplied motors, healthy broken rotor bar fault.

V/Hz closed-loop, no load, no fault.		**V/Hz closed-loop, no load, broken rotor bar.**		**Difference (p.u.)**
Frequency (Hz)	100	**Frequency (Hz)**	100	
Magnitude (p.u.)	0.164652134	**Magnitude (p.u.)**	0.164940094	0.00028796
V/Hz closed-loop, partial load, no fault.		**V/Hz closed-loop, partial load, broken rotor bar.**		
Frequency (Hz)	100	**Frequency (Hz)**	100	
Magnitude (p.u.)	0.162895801	**Magnitude (p.u.)**	0.167467667	0.004571867

As shown in Table 6.11 above, the Extended Park's Vector Approach (EPVA) does not seem to provide conclusive evidence that a fault is present within the motor in all cases. The partially loaded motor case only exhibits a minor increase in the magnitude of the faulted harmonic of 0.00457 p.u., which is not significant enough to confidently confirm the presence of a fault. Additionally, the results across different load cases are mixed, indicating variability in the method's effectiveness.

This starkly contrasts with the results for the inter-turn fault, which showed a much more substantial increase in magnitude in the same load conditions. The significant difference underscores the strengths of this technique for detecting inter-turn faults as opposed to broken rotor bars.

What is particularly intriguing is that the maximum magnitude increase is almost ten times less in the V/Hz closed-loop case compared to the open-loop case. This suggests that the complexity of the control scheme might either mask the fault or allow the system to manage better the irregularities caused by the fault.

6.4.2.3 DC bus analysis

The DC bus voltage and current were analysed in the V/Hz closed-loop tests and the results are as follows.

Table 6-12: DC Bus analysis for V/Hz closed-loop inverter supplied motor, healthy vs broken rotor bar fault.

V/Hz closed-loop, no load, no fault.		**V/Hz closed-loop, no load, broken rotor bar.**		**Difference (p.u.)**	**Difference (Faulted/Healthy)**
Frequency (Hz)	100	**Frequency (Hz)**	100		
Magnitude (p.u)	0.025699512	**Magnitude (p.u)**	0.003305454	-0.022394	0.128619316
Ripple Factor	0.439701764	**Ripple Factor**	0.43107816	-0.008624	0.980387607
V/Hz closed-loop, partial load, no fault.		**V/Hz closed-loop, partial load, broken rotor bar.**			
Frequency (Hz)	100	**Frequency (Hz)**	100		
Magnitude (p.u)	0.007010159	**Magnitude (p.u)**	0.006948682	-6.15E-05	0.991230298
Ripple Factor	0.647070236	**Ripple Factor**	0.650555434	0.003485	1.00538612

As can be seen from Table 6.12 above, the DC bus analysis was unable to provide substantial, if any, that there was a broken rotor bar fault within the motor. In all cases the difference in magnitude of the fault harmonic was less in the presence of the broken rotor bar than they were in the healthy case, except for the partially loaded motor, the ripple factor of the DC bus voltage as well. This indicates that the presence of the broken rotor bar does not contribute to additional harmonics on the Voltage of the DC bus, at least not in a significant way.

This does follow a similar trend compared to the V/Hz open-loop tests where there are slight differences in the healthy vs faulted case but does seem to be more extreme in the closed-loop as there is no increase in the magnitude of the harmonic at all. This again follows the trend of the more complex the control schemes the less the fault can be detected through these methods.

This does show how the DC bus analysis has been used is that it is better suited for the inter-turn short than the broken rotor bar fault.

6.4.3 Summary of V/HZ closed-loop Analysis

The Park's Vector approach was able to show a change in the shape of the d-q plot when the motor had an inter-turn fault; however, this effect was smaller compared to the grid and V/Hz open-loop tests. When the healthy vs inter-turn fault graphs are overlayed, the difference is noticeable, although nothing drastic, but would prove difficult if looked at in a solitary fashion. This does provide a useful visual representation of the fault's presence, but requires a comparison to the healthy test to be noticed. The same cannot be said for the broken rotor bar test, as the two plots look almost identical. Even when overlayed together, it is extremely difficult to tell the difference between the graphs. As there was an increase in the thickness of the plots in both cases, this does indicate that there is an increase in noise on the system, but also that the presence of the fault is minimised or dealt with more capably with the increased complexity of a closed-loop control algorithm. Once again, the Park's Vector Approach seems

to be better able to detect the inter-turn fault, and the added complexity of the control scheme does prove a challenging task for the approach to detect a broken rotor bar.

The Extended Park's Vector approach was revealed to be a strong method for detecting an inter-turn fault once again. With a consistent increase of 0.09 – 0.1 p.u. magnitude increase from the fault case to the healthy case; this indicates that there is around a 10% maximum value increase on the fault harmonic that is being analysed using this method. This is higher compared to the V/Hz open-loop tests, despite having a higher baseline from the healthy motor. Although the increase is greater, which is not initially intuitive, the difference is only 0.035 p.u., which may just be a variance based on the test cases or due to the closed-loop configuration amplifying the harmonics found within the system. Overall, it still shows the Extended Park's Vector Approach is a strong technique that can be used for determining the presence of an inter-turn fault in a wide array of supply schemes. For the broken rotor bar tests, however, the test proved inconclusive. The biggest difference in magnitude in the fault harmonic that was being analysed was 0.00457 p.u., which is around 20 times smaller than the inter-turn fault results. Across the tests, the partially loaded motor produced a result that had a larger harmonic in the healthy case compared to the faulted case, and the no-load case was 20 times smaller than the partially loaded case. This was significantly smaller than the open-loop test results, with it being of around 10 times smaller in magnitude difference. This, along with the Park's Vector Approach, does seem to indicate that the closed-loop can deal with the broken rotor bar in such a way that detecting it is much more difficult using this control algorithm. However, as a standalone case for detecting a broken rotor bar, the Extended Park's Vector Approach needs to have a bit more experimentation for the exact harmonic in which to focus with this method, as it does not seem to provide the same significant results focus on the harmonic at twice the fundamental frequency as the inter-turn fault tests suggest.

The DC bus analysis for the inter-turn fault tests provided a sturdy base on which to determine the presence of the inter-turn fault on the motor. With a minimum increase of 10 times the baseline healthy magnitude of the harmonic that was being analysed, as well as a 1.69 times increase in the ripple factor of the DC bus voltage, there is a significant increase in the harmonics on the DC bus once there is an inter-turn fault present within the system. This is again an increase compared to the open-loop tests, where the largest increase was found on the partial load test, being an 8.63 times increase in the fault harmonic. This does seem to align with the extended Park's Vector Approach results, which does seem to indicate that the closed-loop control scheme can be improved upon with its controller values, but also that the closed-loop nature of the control scheme can amplify the effect on the DC bus that the inter-turn fault may have on the system. This analysis will be continued in the FOC section below, further expanded upon. The broken rotor bar tests did not provide comparable results. Once again, the results are inconclusive, as in all cases, there was a decrease in the magnitude of the harmonic at twice the fundamental frequency on the DC bus. There was a significant decrease in the magnitude of the harmonic, especially in the no-load case, where it decreased by almost 87%. This does seem to show once again that the closed-loop is much better at handling and/or hiding the presence of the broken rotor bar within the system, at the very least at the harmonics that are being analysed. Overall, the DC bus tests provided some valuable insight and highlighted the strength of the ability to determine an imbalance on the drivetrain in the presence of an inter-turn fault on the motor.

6.5 Field Orientation Control Tests

The chosen techniques were applied to the same set of tests, although with FOC FOC-controlled inverter supply. The results are as follows.

6.5.1 Inter-turn Fault Analysis

6.5.1.1 Park's Vector Approach

The Park's Vector approach was applied to the data gathered in the FOC tests and the results are shown below.

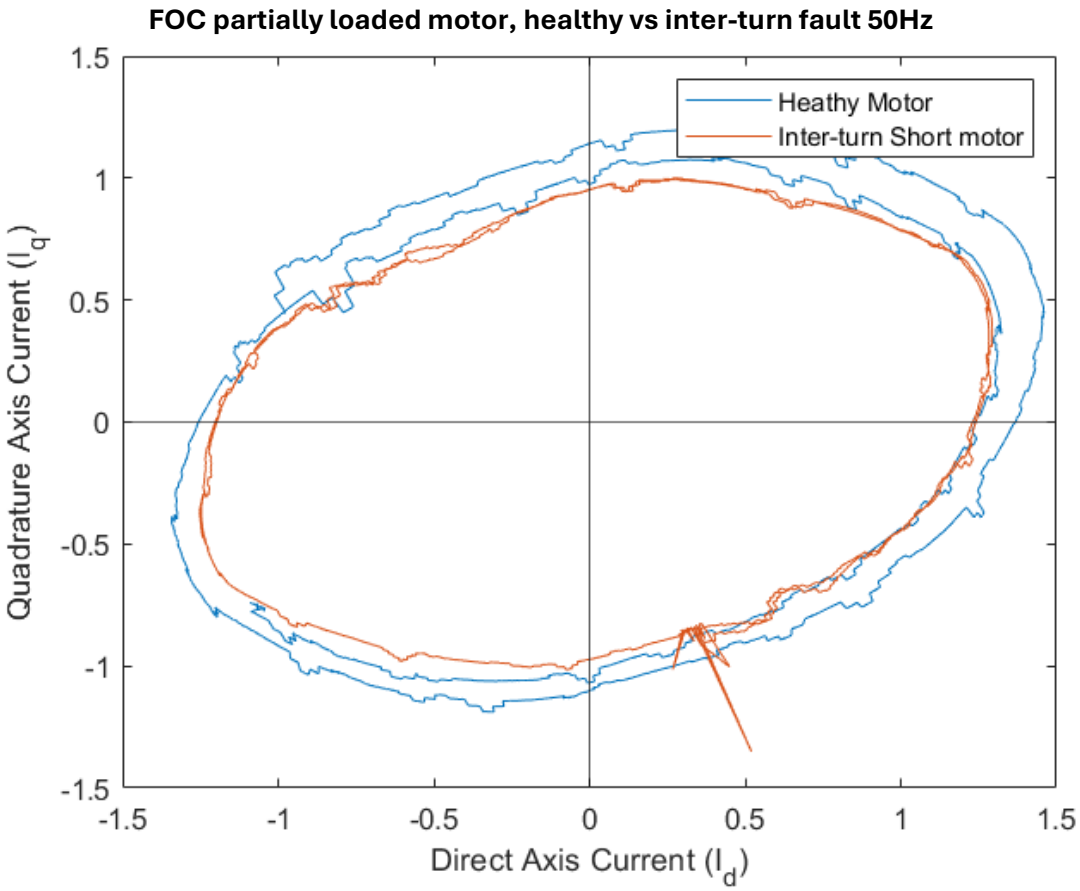

Figure 6.19: Normalised D-Q plot of FOC controlled inverter supplied motors, healthy vs inter-turn fault.

The shape of the plot in Figure 6.19 indicates that the healthy motor case has a larger semi-major axis than the inter-turn fault plot. However, this observation does not provide a clear indication of the presence of the fault within the system. The difference between the two plots is marginal, and in some cases, the semi-major axis appears to decrease once the fault is introduced.

This suggests that the Park's Vector Approach may not be sensitive enough to detect inter-turn faults based solely on the semi-major axis change, at least within the range of the fault severity evaluated. The small magnitude of the change may make it difficult to distinguish from normal operating fluctuations, particularly in the presence of noise or other system

irregularities. Further refinement of the method or alternative diagnostic techniques might be necessary for more reliable fault detection in these scenarios.

6.5.1.2 Extended Park's Vector Approach

Table 6-13: Extended Park's Vector Approach data for FOC controlled inverter supplied motor, healthy vs inter-turn fault.

FOC no load, no fault, 50Hz.		**FOC no load, inter-turn fault, 50Hz.**		**Difference (p.u.)**
Frequency (Hz)	87.1	**Frequency (Hz)**	86.1	
Magnitude (p.u.)	0.0716956	**Magnitude (p.u.)**	0.110293	0.0385974
FOC partial load, no fault, 50Hz.		**FOC partial load, inter-turn fault, 50Hz.**		
Frequency (Hz)	88	**Frequency (Hz)**	88	
Magnitude (p.u.)	0.0883102	**Magnitude (p.u.)**	0.158677177	0.070366977

The difference between the faulted and healthy cases is indeed the smallest on average, but the results still show a positive increase in the magnitude of the harmonic. This indicates that while the Extended Park's Vector Approach (EPVA) may not show substantial changes in the presence of the fault, it still provides valuable insight into detecting the fault within the system.

The minor increase in magnitude observed in the more complex control schemes, like the closed-loop controls, suggests that these systems may be more adept at compensating for imbalances such as those caused by inter-turn faults. This could indicate that the fault's impact is masked by the control system's ability to stabilize the motor, thereby making the fault harder to detect through this method.

Overall, the EPVA shows promise as a fault detection tool, especially when used with simpler control schemes, though its sensitivity may decrease with more advanced control techniques that help mitigate imbalances. This suggests that while the method is useful, it might require adjustments or complementary diagnostic tools to better detect faults under complex control strategies.

6.5.1.3 DC Bus

Table 6-14: DC bus analysis of FOC controlled inverter supplied motor, healthy vs inter-turn fault.

FOC no load, no fault, 50Hz.		FOC no load, inter-turn fault, 50Hz.		Difference (p.u.)	Difference (Faulted / healthy)
Frequency (Hz)	87.1	**Frequency (Hz)**	86.1		
Magnitude	0.027397547	**Magnitude**	0.04417927	0.016781723	1.612526486
Ripple Factor	0.405743957	**Ripple Factor**	0.414293834	0.008549877	1.0210721
FOC partial load, no fault, 50Hz.		**FOC partial load, inter-turn fault, 50Hz.**			
Frequency (Hz)	88	**Frequency (Hz)**	88		
Magnitude	0.021791625	**Magnitude**	0.021880092	8.8467E-05	1.00405968
Ripple Factor	0.546407183	**Ripple Factor**	0.699090999	0.152683816	1.2794323

The DC bus analysis for the Field-Oriented Control (FOC) supply running at 50Hz does indeed present inconclusive results. The observed decrease in the magnitude of the DC harmonic with increasing load is due to the DC component increasing at a faster rate than the fault-related harmonic, which could be masking the fault's signature.

The ripple factor, however, increases across the two load conditions, which suggests some fault-related behaviour, even though the differences are small. This trend aligns with expectations given the complexity of the control scheme, where the system's ability to adapt and compensate for irregularities reduces the visibility of faults.

Interestingly, the no-load condition still shows a significant increase in the fault harmonic (1.6 times higher than the baseline), indicating that at lower loads, the system may be more sensitive to faults. However, as load increases, this sensitivity diminishes, due to the compensating effect of the control scheme and the higher DC component.

Overall, while the FOC system's complexity seems to mask the fault to some extent, the use of DC bus current and voltage analysis holds promise. The results warrant further investigation, especially considering the potential for this method to provide valuable insights into fault detection and severity assessment in more complex control systems. Further research could refine this approach and improve its sensitivity to faults, particularly in high-load and high-control complexity scenarios.

6.5.2 Broken Rotor Bar Tests

6.5.2.1 Park's Vector Approach

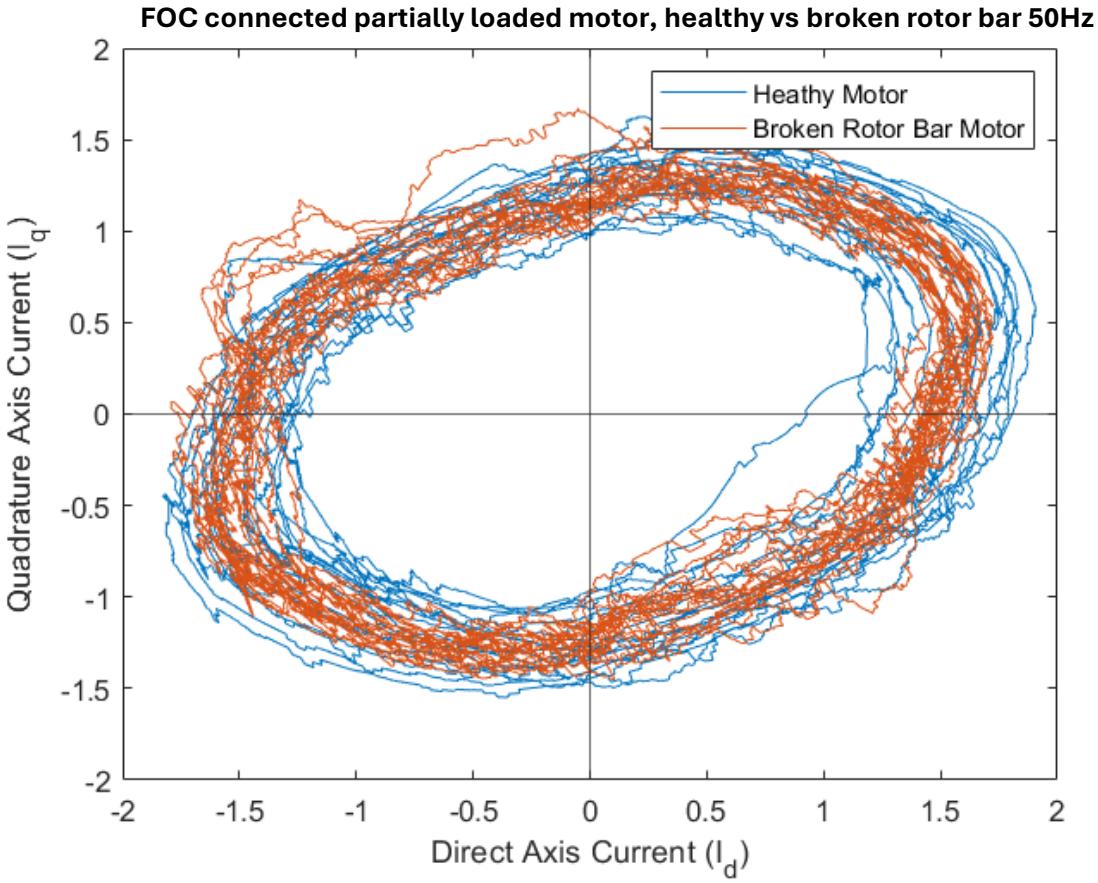

Figure 6.20: Park's Vector Approach of FOC controlled inverter supplied induction motor. Healthy vs Broken Rotor Bar, 10 cycles.

The Park's Vector approach was applied to a FOC-controlled, inverter-supplied system connected to an induction motor, and the results are in Figure 6.20 above. The two plots do seem to be similar; however, the broken rotor bar case seems to have a more concentrated circumference compared to the healthy test. However, the "thickness" of the edges of the plots seems to be similar to each other, with no other indication of the fault being present. The overall noisiness of the plot does seem to indicate that the control scheme was not running with stable magnitudes of the three-phase currents, as the variation in the plots seems to indicate but does seem to show that due to the similarities, that can handle the presence of the fault without major issues within the systems. This follows a similar trend to the V/Hz closed-loop test. Overall, no conclusion can be drawn from this technique, and further investigation would be needed to determine the presence of a broken rotor bar within the motor.

6.5.2.2 Extended Park's Vector Approach

Table 6-15: Extended Park's Vector Approach data for FOC controlled inverter supplied motor, healthy vs broken rotor bar fault.

FOC, no load, no fault.		**FOC, no load, broken rotor bar.**		**Difference (p.u.)**
Frequency (Hz)	87.1	**Frequency (Hz)**	85.3	
Magnitude (p.u.)	0.071695601	**Magnitude (p.u.)**	0.120133844	0.048438
FOC, partial load, no fault.		**FOC, partial load, broken rotor bar.**		
Frequency (Hz)	88	**Frequency (Hz)**	87.3	
Magnitude (p.u.)	0.088310217	**Magnitude (p.u.)**	0.166680001	0.07837

The application of the Extended Park's Vector Approach (EPVA) in the FOC tests, as shown in Table 6.15, indicates a clear detection of the fault, albeit with smaller differences in magnitude compared to the inter-turn fault tests. The smallest observed difference was 0.0484 p.u., still significant enough to suggest the presence of a fault, especially in comparison to the inconclusive results from the V/Hz tests.

What stands out from these results is that, unlike the V/Hz tests, the EPVA method can detect an increase in the harmonic across both load scenarios, signalling the presence of a fault. This is particularly notable because the expected trend for more complex control strategies (like FOC) is that they would mask fault-related signatures, making the detection of faults harder. Contrary to this expectation, the EPVA method showed the largest increases in harmonic magnitude across all tests conducted in this study, pointing to a stronger detection capability in FOC systems.

This result challenges the intuition that more complex control systems obscure faults, and it warrants further investigation. Understanding why the EPVA method performs better in detecting faults under FOC conditions, especially broken rotor bars, could help improve the robustness of fault detection methods for motors using advanced control strategies. The study suggests that the EPVA method has potential, but further research is needed to refine its application and to make it more dependable across varying test conditions and fault types.

6.5.2.3 DC Bus

Table 6-16: DC bus analysis of FOC controlled inverter supplied motor, healthy vs broken bar fault.

FOC, no load, no fault.		FOC, no load, broken rotor bar.		Difference (p.u.)	Difference (Faulted/ Healthy)
Frequency (Hz)	87	**Frequency (Hz)**	85.2		
Magnitude (p.u.)	0.026297477	**Magnitude (p.u.)**	0.017413396	-0.00888408	0.662169856
Ripple Factor	0.405743957	**Ripple Factor**	0.327448902	-0.078295055	0.807033342
FOC, partial load, no fault.		**FOC, partial load, broken rotor bar.**			
Frequency (Hz)	88.2	**Frequency (Hz)**	87.4		
Magnitude (p.u.)	0.012822203	**Magnitude (p.u.)**	0.005708643	-0.00711356	0.445215442
Ripple Factor	0.546407183	**Ripple Factor**	0.540115877	-0.006291306	0.988486047

The DC bus analysis results appear inconclusive, as they do not provide straightforward evidence of a broken rotor bar fault. While there are minor differences in the magnitude of the fault harmonic, the trend is inconsistent across the different load cases. In both load scenarios, the harmonic magnitude decreases, which aligns with similar findings in the V/Hz tests. Additionally, the Ripple Factor of the DC bus also decreases in both cases, further complicating the detection of faults.

A particularly intriguing observation is that for the partially loaded motor, the Ripple Factor in the broken rotor bar case is closer to that of the healthy motor, suggesting that the fault's signature becomes more difficult to detect at higher loads.

The DC bus analysis does not conclusively indicate the presence of a broken rotor bar fault. The minor and inconsistent changes in harmonic magnitude, combined with the lack of a clear pattern in the Ripple Factor, suggest that this method is not suitable for reliable fault detection in the context of broken rotor bars under varying load conditions. Further research and alternative techniques may be needed to improve fault detection in systems with advanced control strategies, such as FOC.

6.5.3 Summary of FOC Results

The Park's Vector approach for the FOC test was inconclusive for both faults, the inter-turn fault and the broken rotor bar fault. For the inter-turn fault, there were slight differences in the overall shape of the graph, although are largely similar from the fault case compared to the healthy case, even though their semi-major axis is slightly different, there is not enough of a visual difference to definitively state that there is indeed an inter-turn fault present. This is due to the complex FOC algorithm and its ability to deal with the imbalance presented by the fault. For the Broken rotor bar case, the same can be said as was for the inter-turn fault. However, in this case, the graphs are almost indiscernible from each other. The graphs are indeed a lot "noisier" visually, and this is the case in the V/Hz closed-loop test as well. This tends to show that the closed-loop control schemes can implement some "instability" in the magnitude of the three-phase current of the system. This just means that the steady-state operation of the control scheme can be improved and could be a factor in the shape of the plot shown from the test. Overall, the Park's Vector approach did provide a visual aid in the "health" of the system, but was not valuable in determining the presence of either fault in this test case.

The extended Park's Vector Approach, however, did provide some substantial results, especially when it came to the inner-turn fault. There was an increase in the magnitude of the harmonic by 0.03 p.u. to 0.103 p.u. across the different load tests. This indicates that the fault harmonic is increasing by 3% - 10% of the value of the largest harmonic of the Park's Vector. This is a significant additional harmonic component that is present in the system in the presence of the inter-turn fault. These tests for the FOC-controlled system do, on average, show a smaller increase compared to the V/Hz closed and open loop tests, which is to be expected from the higher complexity of the FOC control scheme. This does indicate that the more "advanced" control scheme can better manage the imbalance that is introduced into the system through the inter-turn fault. For the broken rotor bar tests, there was an increase in the magnitude of the harmonic across both load tests, from 0.0484 to 0.0998 p.u. being the smallest and largest increase, respectively. This is larger than the smallest increase from the inter-turn fault but smaller than the largest increase from the same tests. However, if the same logic were applied to the inter-turn faults, these results would indicate that there is a fault present in the system, but from the data gathered in this study, it would lean towards being an inter-turn fault. This does provide an interesting set of data, as this was not the case for any of the other tests of different supplies and control schemes. This may indicate that the FOC was not tuned properly and, as such, is not able to conceal the fault in such a way that the harmonic increase caused by the fault was less detectable, or that this could be an outlier, and more sets of data would be needed to conclude. Overall, the Extended Park's vector approach was a valuable tool for determining the presence of an inter-turn fault through the significant increase in analysed harmonic and provided an outlier set of data for the broken rotor bar tests, which would indicate that there would be a fault present, but more data would be required to conclude this technique.

The DC bus analysis again provided evidence that a fault was present in the case of the inter-turn fault. This test, however, provided the lowest increases across all other inter-turn fault DC bus analyses in terms of the increase of the magnitude of the fault harmonic compared to the other tests. This was expected as it does seem that the higher complexity of the control scheme can better manage the imbalance imposed through the presence of the inter-turn fault and would be able to not have as significant an effect on the system. This sentiment is echoed through the Extended Park's Vector technique results across all the different test cases as well. There was an increase of 8.8467E-05 p.u. as the minimum increase and 0.0168 p.u. Increase by a maximum. This represents a 1.004 and 1.61 times increase in the magnitude of the harmonic on the DC bus. What was interesting about this data set was that the higher the load, the lower the increase in the magnitude of the harmonic became. This can be due to the DC component increasing at a faster rate than the other harmonics throughout the system, or that this set of results would be an outlier, and more sets of data need to be collected to be conclusive. The ripple factor of the DC bus follows the opposite trend, as the higher the load, the higher the increase of the Ripple factor becomes, with an increase of 1.02 times larger at no load to 1.27 times at partial load. This does indicate that although the magnitude of the harmonic at partial load may not increase more than at no-load, there is a definite increase in overall harmonics present on the DC bus; they may just not be concentrated at the harmonic of twice the fundamental frequency when a FOC control algorithm is being used.

For the Broken rotor bar, it provides inconclusive evidence that there was a fault present. In all cases, there was a decrease in harmonics present on the DC bus of the system, and if there was an increase in the magnitude of the harmonic, it was only ever 0.002357 p.u. at its greatest. In most cases, however, the magnitude did decrease. Although there was a decrease it was never greater than 0.0088 p.u., which is about half the magnitude of the greatest increase in the inter-turn fault tests. This does seem to echo the sentiment that the FOC just seems to manage the presence of the faults, and there is not as significant a change in the

ripple factor nor the magnitude of the analysed harmonic once a fault is present within the system.

6.6 SUMMARY OF RESULTS

Four techniques were applied to the data to detect and analyse the presence of a fault in an electric vehicle powertrain. MCSA, Park's Vector Approach, Extended Park's Vector Approach, and DC bus analysis.

The MCSA technique worked incredibly well in identifying the fault in the case of the motor with a broken rotor bar, but was not effective when analysing it in the case of a motor with an inter-turn fault. This does not discount the validity of the use of the technique as it is a common and well-known technique but rather shows that in certain conditions, such as a low torque load, it can have difficulty in aiding a user in detecting a fault within a motor system It particularly struggled once the supply was coming from an inverter, as the additional noise on the system made it impossible to detect the fault harmonics as deemed by the MCSA formulae for the inter-turn fault. For the broken rotor bar, however, it provided a clear analysis and the formula that was used pointed in the correct direction as to the location of the fault harmonics presented by a broken rotor bar.

The Park's Vector approach was used and initially provided valuable visual insight into the presence of an inter-turn fault, especially in the grid-connected motor scenario. However, as the different control schemes were applied to the inverter-supplied motor, as well as for the broken rotor bar, it became difficult to differentiate between the two cases, i.e. healthy vs faulted motor. Also, when applied to the broken rotor bar, the analysis becomes less conclusive and clear; however, a difference in the shape of the plots is indeed noticeable. It can be used as a nice visual aid in determining the "health" of the system, but it provides no numerical comparison to delve deeper into the analysis. Overall, a helpful technique that can serve as a starting point and a computationally uncomplicated way for trying to identify a fault in a system.

The Extended Park's vector approach was applied and utilised, and for the inter-turn short cases, provided helpful numerical evidence that there was indeed a presence of a fault in the system. In all load cases and control schemes, there was an increase in the analysed harmonic, which provides evidence that there was a fault within the system. As the complexity of the control scheme increased, the difference in magnitudes decreased, as the control schemes were better suited to deal with imbalances within the system in which an inter-turn fault may be introduced. The FOC algorithm was able to deal with the imbalance present the best and thus had the lowest differences between the magnitudes. Overall, it proved to be a useful analysis technique that does show the presence of a fault quite well. In terms of the broken rotor bar, it proved inconclusive. Since the broken rotor bar does not introduce imbalance to the system as an inter-turn fault, this approach is not suited to detecting a broken rotor bar fault. Therefore, it does have its limitations in its range of faults that it can analyse; however, further research can be focused on utilising that technique but focusing on different harmonic components to detect and analyse the broken rotor bar fault.

Finally, the DC bus analysis, which serves as the primary focus of this study, was used. For the inter-turn fault, as was the case for the extended Park's vector approach, it proved extremely useful in proving the presence of the fault within the system. Moreover, it shows that the fault can propagate its way through the entire powertrain up until the DC bus of the system. A key insight, especially with regard to electric vehicle powertrains. In all tests with at

least 2 load conditions, there was an increase in the faulted harmonic, sometimes even up to 20 times the size compared to the healthy case. The FOC control scheme does however prove the biggest challenge to this technique, as it does provide a significantly lower difference in magnitude for the DC bus harmonic, which does pose a challenge for the electric vehicle application, however, this does still provide an increase in the harmonic, and ultimately still shows that the fault can propagate its way through the powertrain and add additional harmonic stress on the DC bus of the system. Considering that these tests were conducted at a low torque load (~25% of max torque), there could still be an increase in the presence of the fault harmonic at higher loads on the motor; thus, the technique does show good promise, especially in higher load cases.

7 CONCLUSIONS AND RECOMMENDATIONS

7.1 CONCLUSIONS

In this dissertation, the impact of inter-turn faults and broken rotor bar faults on an electric vehicle powertrain was analysed using various techniques. After reviewing the literature on the field of condition monitoring and analysis techniques, an experimental methodology was developed, and tests were conducted on motors with stator and rotor faults. All the tests were conducted in steady state, using either grid or inverter supplies and various control schemes on the inverter supplies. The induction motor was loaded using a servo motor, and then the techniques explored were applied to the data captured in the tests, with analysis being conducted on each set of data.

The primary fault that was investigated was the inter-turn fault with varying supply methods. Firstly, the MCSA technique was applied to data, but it did not prove very adept at being able to identify the fault harmonics at either grid-connected or inverter-connected supply scenarios. Following that, Park's Vector approach, extended Park's vector approach and DC bus analysis were applied (where applicable).

The additional analysis on top of the MCSA technique provided much more insight and was able to identify the fault much more conclusively. The Park's vector approach on the grid-connected supply, as well as the basic V/Hz open-loop supply, was able to conclusively identify the presence of a fault. However, once varying fundamental frequencies were applied and the different control strategies were used, the results started becoming more inconclusive. Specifically, as the control strategies became more complex, the results were harder to pick out conclusive evidence of a fault that was present. The extended Park's Vector approach was significantly better. The technique was able to show an increase in the fault harmonics in all cases and for all load variations of the tests. The increase in the magnitude of the fault harmonic tended to decrease as the control scheme complexity increased. Finally, the DC bus analysis was applied to all inverter-supplied sets of data and provided the most intriguing results. In all cases, there was a significant increase in the fault harmonic in the presence of the inter-turn fault, sometimes increasing to up to twenty times the magnitude of the healthy motor baseline. This did follow the same trend as the extended Park's vector approach in that the increases in the magnitude of fault harmonic did decrease as the complexity of the control strategy increased. However, the DC bus analysis did show conclusively that the presence of the inter-turn fault can and does propagate its way through the powertrain and has a significant presence on the DC bus. This shows how a fault on the motor can put a strain on the DC bus in the presence of a low-order frequency harmonic, which means that additional heat needs to be dealt with on the DC bus of the powertrain.

The second fault that was analysed was the broken rotor bar fault. The same techniques were applied to the inter-turn fault, but with opposite results. The MCSA proved very conclusive in its ability to determine the presence of the fault harmonics even when connected to an inverter. However, the remaining methods did not provide conclusive proof that the harmonic was able to propagate its way through onto the DC bus of the system. The Park's vector approach did provide a picture of a change, however, nowhere near as clear compared to the inter-turn short test. The extended Park's vector approach and DC bus analysis provide inconclusive evidence of the fault. This is because the two techniques rely on there being an imbalance within the system as the negative sequence component of the system current seems to

present itself on the DC bus and within the Park's Vector; however, this was not the case for the broken rotor bar.

The extensive range of supplies and load variations proved that a single technique is not a one-size-fits-all when detecting a fault and monitoring how it propagates its way through the system, with certain techniques better suited to specific supplies and faults. What is evident, is that the DC bus analysis is a viable option for monitoring the presence of a fault in terms of the inter-turn fault and shows that even if a fault on the motor occurs, protection is required on the DC bus so that the additional harmonics and therefore heat present on the system, does not cause damage to the components on the DC bus.

7.2 RECOMMENDATIONS

Several recommendations can be made depending on the avenue of research that would be desired to be reviewed. Since the focus of this study is the analysis of electric vehicles, the use of a battery supply inverter would be recommended to see the long-term implications of the battery in the presence of the inter-turn fault. This would also provide a pure DC bus rather than a grid-rectified DC bus, matching up closer to real-world applications of EVs. Secondly, multiple iterations of each test scenario would be recommended to be captured, as there were a few outlier points of data that would not hamper the conclusions drawn if multiple sets of data were to be used. The DC bus analysis could also be further investigated for how it could be used to detect a series of faults, and not just the inter-turn fault. Looking at different harmonic components and how these relate to the fault could be useful and therefore lead to the DC bus analysis proving to be a more robust technique in terms of determining the overall health of the powertrain.

Additionally, the waveform of the voltages can be looked at in more detail, especially in the inverter-fed scenarios. Increased filtering, especially on the voltage waveforms, could aid in the effectiveness of the methods that were used in this paper, especially on the MCSA techniques. Therefore, an interesting avenue that can be expanded upon is the proper conditions in which these techniques are being used.

Another suggestion would be to apply a wider range of torque loads to analyse how a further increase in torque affects the DC bus analysis. This would also benefit the other techniques to see the effectiveness throughout the different control schemes as well.

Finally, further investigation should be focused on different switching schemes and different control schemes, with a focus on different types of FOC schemes. This would provide a broader view on how these techniques can be applied to various different control schemes that are used within electric vehicles, and help provide a more comprehensive overview on how robust the techniques are on a wider range of variables as it relates to Electric vehicle topologies.

8 LIST OF REFERENCES

[1] Advantage Converting, "Why Battery Protection Matters In Electric Vehicles," *Advantage Converting*, [Online]. Available: https://advantageconverting.com/ev-battery-design-considerations/.

[2] Y. -C. Lee and W. -H. Hsu, "The study of EV data collection and analysis based on Taiwan i-EV pilot project," *2013 World Electric Vehicle Symposium and Exhibition (EVS27)*, Barcelona, Spain, 2013, pp. 1-7, doi: 10.1109/EVS.2013.6914756.

[3] C. Gong and Y. Hu, "A new method for the dispersal of high-voltage energy stored in EV powertrains," *Research Features*, Mar. 2023. [Online]. Available: https://researchfeatures.com/new-method-dispersal-high-voltage-energy-stored-powertrains/

[4] M. M. Rehman and W. G. Morsi, "Comparative Economic Analysis of Conventional and Plug-in Battery Electric Vehicles in Canada," 2022 IEEE Electrical Power and Energy Conference (EPEC), Victoria, BC, Canada, 2022, pp. 218-223, doi: 10.1109/EPEC56903.2022.10000170.

[5] B. Frieske, M. Kloetzke and F. Mauser, "Trends in vehicle concept and key technology development for hybrid and battery electric vehicles," *2013 World Electric Vehicle Symposium and Exhibition (EVS27)*, Barcelona, Spain, 2013, pp. 1-12, doi: 10.1109/EVS.2013.6914783.

[6] M. Drif and A. J. M. Cardoso, "Stator Fault Diagnostics in Squirrel Cage Three-Phase Induction Motor Drives Using the Instantaneous Active and Reactive Power Signature Analyses," in IEEE Transactions on Industrial Informatics, vol. 10, no. 2, pp. 1348-1360, May 2014, doi: 10.1109/TII.2014.2307013

[7] A. Moradi, J. Yaghoobi, F. Zare and D. Kumar, "Analysis of 0–9 kHz Current Harmonics in a Three-Phase Power Converter Under Unbalanced-Load Conditions," in *IEEE Access*, vol. 9, pp. 161862-161876, 2021, doi: 10.1109/ACCESS.2021.3131304.

[8] J. Zhao *et al.*, "Battery fault diagnosis and failure prognosis for electric vehicles using spatio-temporal transformer networks," *Applied Energy*, vol. 352, 2023, Art. no. 121949. [Online]. Available: https://doi.org/10.1016/j.apenergy.2023.121949

[9] J. Wang, S. Zhang, and X. Hu, "A Fault Diagnosis Method for Lithium-Ion Battery Packs Using Improved RBF Neural Network," *Frontiers in Energy Research*, vol. 9, Aug. 2021. [Online]. Available: https://doi.org/10.3389/fenrg.2021.702139

[10] M. B. Kaleem, Y. Zhou, F. Jiang, Z. Liu, and H. Li, "Fault detection for Li-ion batteries of electric vehicles with segmented regression method," *Scientific Reports*, vol. 14, Dec. 2024, Art. no. 31922. [Online]. Available: https://doi.org/10.1038/s41598-024-82960-0

[11] X. Pei, W. Zhou and Y. Kang, "Analysis and Calculation of DC-Link Current and Voltage Ripples for Three-Phase Inverter With Unbalanced Load," in *IEEE Transactions on Power Electronics*, vol. 30, no. 10, pp. 5401-5412, Oct. 2015, doi: 10.1109/TPEL.2014.2375353.

[12] N. Bhole and S. Ghodke, "Motor Current Signature Analysis for Fault Detection of Induction Machine–A Review," *2021 4th Biennial International Conference on Nascent Technologies in Engineering (ICNTE)*, NaviMumbai, India, 2021, pp. 1-6, doi: 10.1109/ICNTE51185.2021.9487715.

[13] S. Ben Salem, W. Touti, K. Bacha and A. Chaari, "Induction motor mechanical fault identification using Park's vector approach," *2013 International Conference on Electrical*

Engineering and Software Applications, Hammamet, Tunisia, 2013, pp. 1-6, doi: 10.1109/ICEESA.2013.6578381.

[14] H. Nejjari and M. E. H. Benbouzid, "Monitoring and diagnosis of induction motors electrical faults using a current Park's vector pattern learning approach," in *IEEE Transactions on Industry Applications*, vol. 36, no. 3, pp. 730-735, May-June 2000

[15] S. M. A. Cruz and A. J. M. Cardoso, "Stator winding fault diagnosis in three-phase synchronous and asynchronous motors, by the extended Park's vector approach," in *IEEE Transactions on Industry Applications*, vol. 37, no. 5, pp. 1227-1233, Sept.-Oct. 2001, doi: 10.1109/28.952496.

[16] "Introduction to the Fourier Transform," Swarthmore College, Linear Physical Systems Analysis (LPSA), [Online]. Available: https://lpsa.swarthmore.edu/Fourier/Xforms/FXformIntro.html. [Accessed: May 11, 2024].

[17] S. K. Gundewar and P. V. Kane, "Condition Monitoring and Fault Diagnosis of Induction Motor in Electric Vehicle," in *Machines, Mechanism and Robotics*, Lecture Notes in Mechanical Engineering, Singapore: Springer, 2021, pp. 531–539, doi: 10.1007/978-981-16-0550-5_53.

[18] A. S. Alsharif, H. M. El-Shimy, M. A. Abdelwahab, and M. M. Eissa, "Fault Detection and Diagnosis of the Electric Motor Drive and Battery System in Electric Vehicles," *Machines*, vol. 11, no. 7, p. 713, 2023, doi: 10.3390/machines11070713.

[19] Ghassemi, Alireza & Chakraborty Banerjee, Parama & Hollenkamp, Anthony & Zhang, Zhe & Bahrani, Behrooz. (2020). Effects of alternating current on Li-ion battery performance: Monitoring degradative processes with in-situ characterization techniques. Applied Energy. 284. 116192. 10.1016/j.apenergy.2020.116192.

[20] Juang, Larry & Kollmeyer, Phil & Anders, Adam & Jahns, Thomas & Lorenz, Robert & Gao, Dawei. (2017). Investigation of the influence of superimposed AC current on lithium-ion battery aging using statistical design of experiments. Journal of Energy Storage. 11. 93-103. 10.1016/j.est.2017.02.005.

[21] P. Albrecht, J. Appiarius and D. K. Sharma, ASSESSMENT OF RELIABILITY OF MOTORS IN UTILITY APPLICATIONS - UPDATED, EPRI /IEEE, 1986.

[22] A. Sharma, S. Chatterji and L. Mathew, "A Novel Park's Vector Approach for Investigation of Incipient Stator Fault Using MCSA in Three-Phase Induction Motors," *2017 International Conference on Innovations in Control, Communication and Information Systems (ICICCI)*, Greater Noida, India, 2017, pp. 1-5, doi: 10.1109/ICICCIS.2017.8660892.

[23] V. Kulkarni, S. Singh and P. S. Jamwal, "Optimized Field Oriented Control for Induction Motor Driven Electric Vehicles," 2022 IEEE 2nd International Conference on Sustainable Energy and Future Electric Transportation (SeFeT), Hyderabad, India, 2022, pp. 1-6, doi: 10.1109/SeFeT55524.2022.9909017.

[24] P. Lumyong and P. Sarikprueck, "A Study on Induction Motor Efficiency Improvement for Implementing in Electric Vehicle," 2018 21st International Conference on Electrical Machines and Systems (ICEMS), Jeju, Korea (South), 2018, pp. 616-619, doi: 10.23919/ICEMS.2018.8549478.

[25] P. C. Senn, Principles of Electric Machines and Power Electronics, John Wiley and Sons, 1996.

[26] B. Amin, Induction Motors: Analysis and Torque Control, Springer-Verlag Berlin Heidelberg, 2001.

[27] LNCT Group of Colleges, "Induction Motor," RGPV, Bhopal, India, [Online]. Available: https://www.rgpv.ac.in/campus/EE/Induction%20Motor.pdf. [Accessed: 12 July, 2024].

[28] EPRI, "Electric Motor Predictive and Preventive," EPRI, 1992.

[29] B. Frieske, M. Kloetzke and F. Mauser, "Trends in vehicle concept and key technology development for hybrid and battery electric vehicles," *2013 World Electric Vehicle Symposium and Exhibition (EVS27)*, Barcelona, Spain, 2013, pp. 1-12, doi: 10.1109/EVS.2013.6914783.

[30] "Control Scheme and Controller Design for Induction Motor Drives," *Tennessee Technological University*, [Online]. Available: https://www.tntech.edu/engineering/pdf/cesr/ojo/asuri/Chapter5.pdf. [Accessed: June 17, 2024].

[31] MathWorks, "Induction Machine Scalar Control," *Simscape Electrical*, 2017. [Online]. Available: https://nl.mathworks.com/help/sps/ref/inductionmachinescalarcontrol.html. [Accessed: May 8, 2024].

[32] M. Kutija, D. Sumina and I. Čolović, "A current limiting technique for V/f controlled induction machines," *2014 16th International Power Electronics and Motion Control Conference and Exposition*, Antalya, Turkey, 2014, pp. 1001-1004, doi: 10.1109/EPEPEMC.2014.6980639.

[33] K. B. Hunasikatti, R. L. Naik and B. V. Hiremath, "Implementation of FPGA Based Closed Loop V/f Speed Control of Induction Motor Employed for Industrial Applications," *2018 Second International Conference on Advances in Electronics, Computers and Communications (ICAECC)*, Bangalore, India, 2018, pp. 1-6, doi: 10.1109/ICAECC.2018.8479518.

[34] V. Kulkarni, S. Singh and P. S. Jamwal, "Optimized Field Oriented Control for Induction Motor Driven Electric Vehicles," *2022 IEEE 2nd International Conference on Sustainable Energy and Future Electric Transportation (SeFeT)*, Hyderabad, India, 2022, pp. 1-6, doi: 10.1109/SeFeT55524.2022.9909017.

[35] Texas Instruments, "Field Oriented Control of 3-Phase AC-Motors," Application Report BPRA073, Feb. 1998. [Online]. Available: https://www.ti.com/lit/an/bpra073/bpra073.pdf. [Accessed: April 13, 2024].

[36] University of Cape Town, "EEE4123C – Notes 1 – Reference Frame Transformations," Department of Electrical Engineering, [Online]. Available: https://vula.uct.ac.za/access/content/group/de6c2f6a-27b9-4754-aa9c-3103e2dccac1/02.%20Notes/EEE4123C%20-%20Notes%201%20-%20Reference%20Frame%20Transformations.pdf. [Accessed: March 22, 2024].

[37] S. Jadhav, "Impact of faults on the efficiency of squirrel cage induction motor," *2017 International Conference on Nascent Technologies in Engineering (ICNTE)*, Vashi, India, 2017, pp. 1-6, doi: 10.1109/ICNTE.2017.7947971.

[38] M. Drif and A. J. M. Cardoso, "Stator Fault Diagnostics in Squirrel Cage Three-Phase Induction Motor Drives Using the Instantaneous Active and Reactive Power Signature Analyses," in *IEEE Transactions on Industrial Informatics*, vol. 10, no. 2, pp. 1348-1360, May 2014

[39] Valtierra-Rodriguez M, Rivera-Guillen JR, Basurto-Hurtado JA, De-Santiago-Perez JJ, Granados-Lieberman D, Amezquita-Sanchez JP. Convolutional Neural Network and Motor Current Signature Analysis during the Transient State for Detection of Broken Rotor Bars in Induction Motors. *Sensors*. 2020; 20(13):3721. https://doi.org/10.3390/s20133721

[40] M. Drif and A. J. M. Cardoso, "The Use of the Instantaneous-Reactive-Power Signature Analysis for Rotor-Cage-Fault Diagnostics in Three-Phase Induction Motors," *IEEE TRANSACTIONS ON INDUSTRIAL ELECTRONICS,* vol. 56, no. 11, pp. 4606-4614, 2009.

[41] S. S. Duvvuri, S. KP, S. D. K. Varma, S. Gogula, V. S. B. C. Duvvury and V. S. N. N. Raju, "Broken Rotor Bar Fault in 3-Φ Squirrel-Cage Induction Motors: A Critical Observations," *2023 International Conference on Power, Instrumentation, Control and Computing (PICC)*, Thrissur, India, 2023, pp. 1-6, doi: 10.1109/PICC57976.2023.10142469.

[42] A. Bellini, F. Filippetti, C. Tassoni and G. -A. Capolino, "Advances in Diagnostic Techniques for Induction Machines," in *IEEE Transactions on Industrial Electronics*, vol. 55, no. 12, pp. 4109-4126, Dec. 2008, doi: 10.1109/TIE.2008.2007527.

[43] P. V. J. Rodrıguez, M. Negrea and A. Arkkio, "A simplified scheme for induction motor condition monitoring," *Science Direct - Mechanical Systems and Signal Processing,* vol. 22, p. 1216–1236, 2008.

[44] A. V. J. S. Praneeth and S. S. Williamson, "Algorithm for prediction and control of induction motor stator interturn faults in electric vehicles," *2017 IEEE Transportation Electrification Conference and Expo (ITEC)*, Chicago, IL, USA, 2017, pp. 130-134, doi: 10.1109/ITEC.2017.7993259.

[45] B. Corne, B. Vervisch, C. Debruyne, J. Knockaert and J. Desmet, "Comparing MCSA with vibration analysis in order to detect bearing faults — A case study," *2015 IEEE International Electric Machines & Drives Conference (IEMDC)*, Coeur d'Alene, ID, USA, 2015, pp. 1366-1372, doi: 10.1109/IEMDC.2015.7409240.

[46] J. C. Roura and J. L. R. Martinez, "Transient Analysis and Motor Fault Detection using the Wavelet Transform", *InTech*, pp. 43-60, 2011.

[47] M. W. Abitha and V. Rajini, "Park's vector approach for online fault diagnosis of induction motor," *2013 International Conference on Information Communication and Embedded Systems (ICICES)*, Chennai, India, 2013, pp. 1123-1129, doi: 10.1109/ICICES.2013.6508332.

[48] H. Song, H. Gao, F. Peng and B. Xu, "Positive and Negative Sequence Components Separation Control Method for PV Inverters Based on Second-order Generalized Integrator," *2022 4th International Conference on Smart Power & Internet Energy Systems (SPIES)*, Beijing, China, 2022, pp. 537-542, doi: 10.1109/SPIES55999.2022.10082063.

[49] M. D. de Castro e Silva, A. L. Ferreira Filho and C. C. Abada, "Evaluation of the effect of the zero and negative sequence components on the current and temperature of a three phase induction motor," *2016 17th International Conference on Harmonics and Quality of Power (ICHQP)*, Belo Horizonte, Brazil, 2016, pp. 937-942, doi: 10.1109/ICHQP.2016.7783396.

[50] J. Sottile and J. L. Kohler, "An on-line method to detect incipient failure of turn insulation in random-wound motors," in *IEEE Transactions on Energy Conversion*, vol. 8, no. 4, pp. 762-768, Dec. 1993, doi: 10.1109/60.260992.

[51] J. L. Kohler, J. Sottile and F. C. Trutt, "Alternatives for assessing the electrical integrity of induction motors," in *IEEE Transactions on Industry Applications*, vol. 28, no. 5, pp. 1109-1117, Sept.-Oct. 1992, doi: 10.1109/28.158836.

[52] N. Mohan, T. Undeland and W. Robins, Power Electronics, Wiley, 2003.

[53] D. G. Holmes and T. A. Lipo, Pulse Width Modulation for Power Converters: Principles and Practice, Hoboken, NJ, USA:Wiley, 2003.

[54] B. P. McGrath and D. G. Holmes, "A General Analytical Method for Calculating Inverter DC-Link Current Harmonics," in *IEEE Transactions on Industry Applications*, vol. 45, no. 5, pp. 1851-1859, Sept.-oct. 2009, doi: 10.1109/TIA.2009.2027556.

[55] K. Nishizawa, J. -I. Itoh, A. Odaka, A. Toba and H. Umida, "Current Harmonic Reduction Based on Space Vector PWM for DC-Link Capacitors in Three-Phase VSIs Operating Over a Wide Range of Power Factor," in *IEEE Transactions on Power Electronics*, vol. 34, no. 5, pp. 4853-4867, May 2019, doi: 10.1109/TPEL.2018.2859763.

[56] Lalit Kumar, Shailendra Jain, ”Electric propulsion system for electric vehicular technology: A review”, in *Renewable and Sustainable Energy Reviews*, Volume 29,2014,Pages 924-940,ISSN 1364-0321, https://doi.org/10.1016/j.rser.2013.09.014.

[57] Saldarriaga, Sergio & López-Lezama, Jesús & Ríos, Carlos & Jaramillo, Alejandro. (2022). Effects of the Incorporation of Electric Vehicles on Protection Coordination in Microgrids. World Electric Vehicle Journal. 13. 163. 10.3390/wevj13090163.

[58] G. Amar, G. Ismail and B. Riad, "Suitability of Electric Motors and Conventional Control Techniques for Electric Vehicle Applications," *2022 International Conference of Advanced Technology in Electronic and Electrical Engineering (ICATEEE)*, M'sila, Algeria, 2022, pp. 1-6, doi: 10.1109/ICATEEE57445.2022.10093716.

[59] Abhisek Karki, Sudip Phuyal, Daniel Tuladhar and Subarna Basnet, Status of Pure Electric Vehicle Power Train Technology and Future Prospects, 2020.

[60] Z. Jinwen and Q. Yumei, "Research on motor control of new energy electric vehicle," *2023 IEEE 3rd International Conference on Electronic Technology, Communication and Information (ICETCI)*, Changchun, China, 2023, pp. 637-640, doi: 10.1109/ICETCI57876.2023.10176454.

[61] C. Sagert, B. Rolle, M. Walter and O. Sawodny, "Current and Voltage Harmonics in the Powertrain of Electric Vehicles," in *IEEE Transactions on Vehicular Technology*, vol. 69, no. 10, pp. 10736-10749, Oct. 2020, doi: 10.1109/TVT.2020.3008385.

[62] K. Uddin, A. D. Moore, A. Barai and J. Marco, "The effects of high frequency current ripple on electric vehicle battery performance", *Appl. Energy*, vol. 178, pp. 142-154, Sep. 2016.

[63] H. Wang and F. Blaabjerg, "Reliability of Capacitors for DC-Link Applications in Power Electronic Converters—An Overview," in IEEE Transactions on Industry Applications, vol. 50, no. 5, pp. 3569-3578, Sept.-Oct. 2014, doi: 10.1109/TIA.2014.2308357.

[64] P. Tian, C. A. Platero, F. Blázquez and J. M. Guerrero, "Ground Fault Location System for Powertrain of Electric Vehicles," *2019 IEEE 12th International Symposium on Diagnostics for Electrical Machines, Power Electronics and Drives (SDEMPED)*, Toulouse, France, 2019, pp. 488-492, doi: 10.1109/DEMPED.2019.8864859.

[65] S. Nouphengdy, S. Pathoumvanh, P. Indahak and K. Southisombath, "The investigated on Harmonic Monitoring for the Inverter Applications by using Microprocessor," *2019 5th*

International Conference on Engineering, Applied Sciences and Technology (ICEAST), Luang Prabang, Laos, 2019, pp. 1-4, doi: 10.1109/ICEAST.2019.8802556.

[66] Y. Feng, G. Konstantinou, B. Hredzak, J. Fletcher and K. Sun, "Topologies for Reduction of Second Harmonic Ripple in Battery Energy Storage Systems," *2019 IEEE 10th International Symposium on Power Electronics for Distributed Generation Systems (PEDG)*, Xi'an, China, 2019, pp. 414-419, doi: 10.1109/PEDG.2019.8807611.

[67] H. Wen, W. Xiao and Xuhui Wen, "Comparative evaluation of DC-link capacitors for electric vehicle application," *2012 IEEE International Symposium on Industrial Electronics*, Hangzhou, China, 2012, pp. 1472-1477, doi: 10.1109/ISIE.2012.6237308.

[68] D. Cittanti *et al*., "Analysis and Design of a High Power Density Full-Ceramic 900 V DC-Link Capacitor for a 550 kVA Electric Vehicle Drive Inverter," *2022 International Power Electronics Conference (IPEC-Himeji 2022- ECCE Asia)*, Himeji, Japan, 2022, pp. 1144-1151, doi: 10.23919/IPEC-Himeji2022-ECCE53331.2022.9807220.

[69] S. Barcellona and L. Piegari, "Battery aging due to 100 Hz current Ripple of power converters," *The 9th Renewable Power Generation Conference (RPG Dublin Online 2021)*, Online Conference, 2021, pp. 301-305, doi: 10.1049/icp.2021.1410.

[70] J. Biľanský, T. Merva, J. Ivan, A. Marcinek and M. Lacko, "Cyclic Tester of Battery Cells for Electric Vehicles," *2021 IEEE International Workshop of Electronics, Control, Measurement, Signals and their application to Mechatronics (ECMSM)*, Liberec, Czech Republic, 2021, pp. 1-7, doi: 10.1109/ECMSM51310.2021.9468858.

[71] "Battery university [online] 2020", *Whats the Best Battery?*, [online] Available: https://batteryuniversity.com/learn/archive/whats_the_best_battery.

[72] A. V. Grishin, A. R. Asoyan, A. A. Solntsev, V. V. Guly and O. V. Fediushkina, "Ensuring the Operation of Electric Bus Batteries in the Optimal Temperature Range," *2022 Intelligent Technologies and Electronic Devices in Vehicle and Road Transport Complex (TIRVED)*, Moscow, Russian Federation, 2022, pp. 1-4, doi: 10.1109/TIRVED56496.2022.9965484.

[73] L. Timilsina, P. R. Badr, P. H. Hoang, G. Ozkan, B. Papari and C. S. Edrington, "Battery Degradation in Electric and Hybrid Electric Vehicles: A Survey Study," in *IEEE Access*, vol. 11, pp. 42431-42462, 2023, doi: 10.1109/ACCESS.2023.3271287.

[74] A. Ghassemi, P. C. Banerjee, Z. Zhang, A. Hollenkamp and B. Bahrani, "Aging Effects of Twice Line Frequency Ripple on Lithium Iron Phosphate (LiFePO4) Batteries," *2019 21st European Conference on Power Electronics and Applications (EPE '19 ECCE Europe)*, Genova, Italy, 2019, pp. P.1-P.9, doi: 10.23919/EPE.2019.8915538.

[75] F. Ruecker, I. Bremer and D. U. Sauer, "Development and analysis of a charging algorithm for electric vehicle fleets extending battery lifetime," *2016 IEEE Transportation Electrification Conference and Expo, Asia-Pacific (ITEC Asia-Pacific)*, Busan, Korea (South), 2016, pp. 029-033, doi: 10.1109/ITEC-AP.2016.7512917.

[76] C. Liu, J. Wang, K. Colombage, C. Gould, B. Sen and D. Stone, "Current ripple reduction in 4kW LLC resonant converter based battery charger for electric vehicles," *2015 IEEE Energy Conversion Congress and Exposition (ECCE)*, Montreal, QC, Canada, 2015, pp. 6014-6021, doi: 10.1109/ECCE.2015.7310503.

[77] Miljković, Dubravko. (2015). Brief Review of Motor Current Signature Analysis. CrSNDT Journal. 5. 14-26.

[78] Hameed, Armughan et al. “A Park’s vector approach using process monitoring statistics of principal component analysis for machine fault detection.” *2016 International Conference on Emerging Technologies (ICET)* (2016): 1-5.

[79] BSI Standards Publication, "BS ISO 20958:2013 - Condition monitoring and diagnostics of machine systems — Electrical signature analysis of three-phase induction motors," BSI/ ISO, 2013.

[80] Ince, Turker. (2019). Real-time broken rotor bar fault detection and classification by shallow 1D convolutional neural networks. Electrical Engineering. 101. 10.1007/s00202-019-00808-7.

[81] D. M. Sonje, P. Kundu and A. Chowdhury, "Detection and discrimination of simultaneous stator inter-turn and broken rotor bar faults in induction motor," *2015 International Conference on Condition Assessment Techniques in Electrical Systems (CATCON)*, Bangalore, India, 2015, pp. 133-138, doi: 10.1109/CATCON.2015.7449522.

[82] A. Aboubou, M. Sahraoui, S. E. Zouzou, H. Razik and A. Rezzoug, "Broken bars and/or end rings detection in three-phase induction motors by the extended Park’s vector approach," *9th IEEE International Power Electronics Congress, 2004. CIEP 2004*, Celaya, Mexico, 2004, pp. 128-133, doi: 10.1109/CIEP.2004.1437564.

[83] "Discrete Fourier Transform - Frequencies," Statlect, 2021. [Online]. Available: https://www.statlect.com/matrix-algebra/discrete-Fourier-transform-frequencies. [Accessed: May 12, 2024].

[84] A. Sapena-Bañó, M. Pineda-Sanchez, R. Puche-Panadero, J. Martinez-Roman and D. Matić, "Fault diagnosis of rotating electrical machines in transient regime using a single stator currents FFT", *IEEE Trans. Instrum. Meas.*, vol. 64, no. 11, pp. 3137-3146, Nov. 2015

[85] "Spectral leakage and windowing," *Digital Signals Theory*, Brian McFee, [Online]. Available: https://brianmcfee.net/dstbook-site/content/ch06-dft-properties/Leakage.html. [Accessed: May 12, 2024].

[86] "Understanding FFTs and Windowing," National Instruments, Instrument Fundamentals Series, Feb. 1998. [Online]. Available: https://download.ni.com/evaluation/pxi/Understanding%20FFTs%20and%20Windowing.pdf. [Accessed: May 12, 2024].

[87] "Zero Padding," National Instruments, [Online]. Available: https://www.ni.com/docs/en-US/bundle/labwindows-cvi/page/advancedanalysisconcepts/lvac_zero_padding.html. [Accessed: May 13, 2024].

[88] "Amplitude Estimation and Zero Padding," MathWorks, [Online]. Available: https://nl.mathworks.com/help/signal/ug/amplitude-estimation-and-zero-padding.html. [Accessed: May 14, 2024].

[89] Saïd-Romdhane, Marwa & Naouar, M.W. & Slama-Belkhodja, Ilhem & Monmasson, E.. (2015). Simple and systematic LCL filter design for three-phase grid-connected power converters. Mathematics and Computers in Simulation. 130. 10.1016/j.matcom.2015.09.011.

[90] P. Mishra and R. Maheshwari, "Design, Analysis, and Impacts of Sinusoidal LC Filter on Pulsewidth Modulated Inverter Fed-Induction Motor Drive," in IEEE Transactions on Industrial Electronics, vol. 67, no. 4, pp. 2678-2688, April 2020, doi: 10.1109/TIE.2019.2913824.

[91] B. Frieske, M. Kloetzke and F. Mauser, "Trends in vehicle concept and key technology development for hybrid and battery electric vehicles," *2013 World Electric Vehicle Symposium and Exhibition (EVS27)*, Barcelona, Spain, 2013, pp. 1-12, doi: 10.1109/EVS.2013.6914783.

[92] "Electric Car Energy Consumption," *EV Database*, [Online]. Available: https://ev-database.org/cheatsheet/energy-consumption-electric-car. [Accessed: 01 Jan 2025].

[93] M. Pastura and M. Zigliotto, "Overview and Challenges of Fault Detection Methods in Electrical Motors for EV Applications," 2024 International Conference on Electrical Machines (ICEM), Torino, Italy, 2024, pp. 1-7, doi: 10.1109/ICEM60801.2024.10700355.

[94] D. Liu, A. Varatharajan, A. Goldsmith, C. Kong, L. K. Sigatapu and Y. Wang, "Broken-bar Fault Detection by Injecting a Frequency Modulated Continuous Wave Signal," *2023 IEEE International Electric Machines & Drives Conference (IEMDC)*, San Francisco, CA, USA, 2023, pp. 1-6, doi: 10.1109/IEMDC55163.2023.10239083.

[95] T. Garcia-Calva, D. Morinigo-Sotelo, V. Fernandez-Cavero, and R. Romero-Troncoso, "Early detection of faults in induction motors—A review," *Energies*, vol. 15, no. 21, p. 7855, 2022. [Online]. Available: https://doi.org/10.3390/en15217855

[96] M. Dlamini, "DEVELOPMENT OF AN INDUCTION MOTOR CONDITION MONITORING TEST RIG AND FAULT DETECTION STRATEGIES," University of Cape Town, Cape Town, 2014.

[97] National Instruments, "NI 9215 Datasheet," National Instruments.

[98] Sotoodeh, Pedram. (2014). A single-phase multi-level D-STATCOM inverter using modular multi-level converter (MMC) topology for renewable energy sources.

[99] SpectraQuest Inc, "User Operating Manual for Machinery Fault Simulator," SpectraQuest Inc.

[100] "SPM-VFD 3-Phase Inverter Power Module," Taraz Technologies, [Online]. Available: https://www.taraztechnologies.com/Downloads/Datasheets/SPM-VFD.pdf. [Accessed: December 5, 2024].

9 APPENDIX

9.1 REMAINING GRID SUPPLIED RESULTS

9.1.1 Inter-turn Fault

9.1.1.1 MCSA

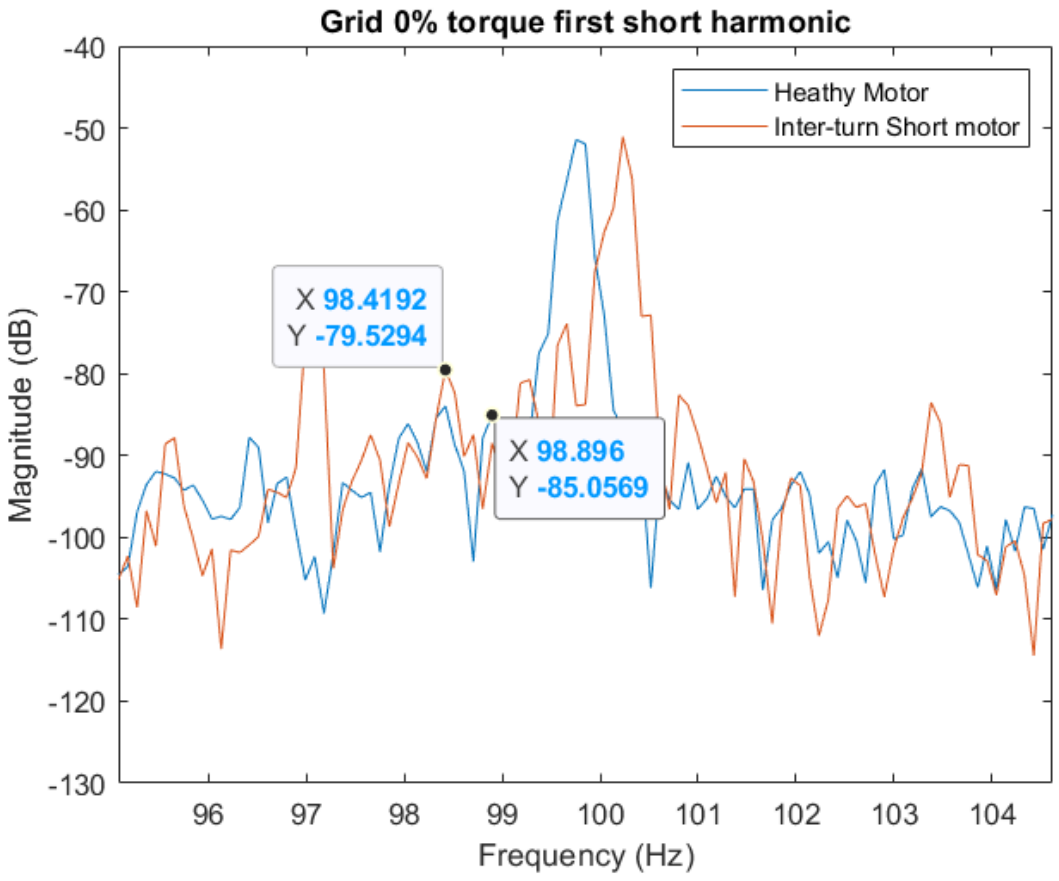

Appendix Figure 1: n=1, k=1 for grid fed induction motor, healthy vs inter-turn short frequency spectrum, no load.

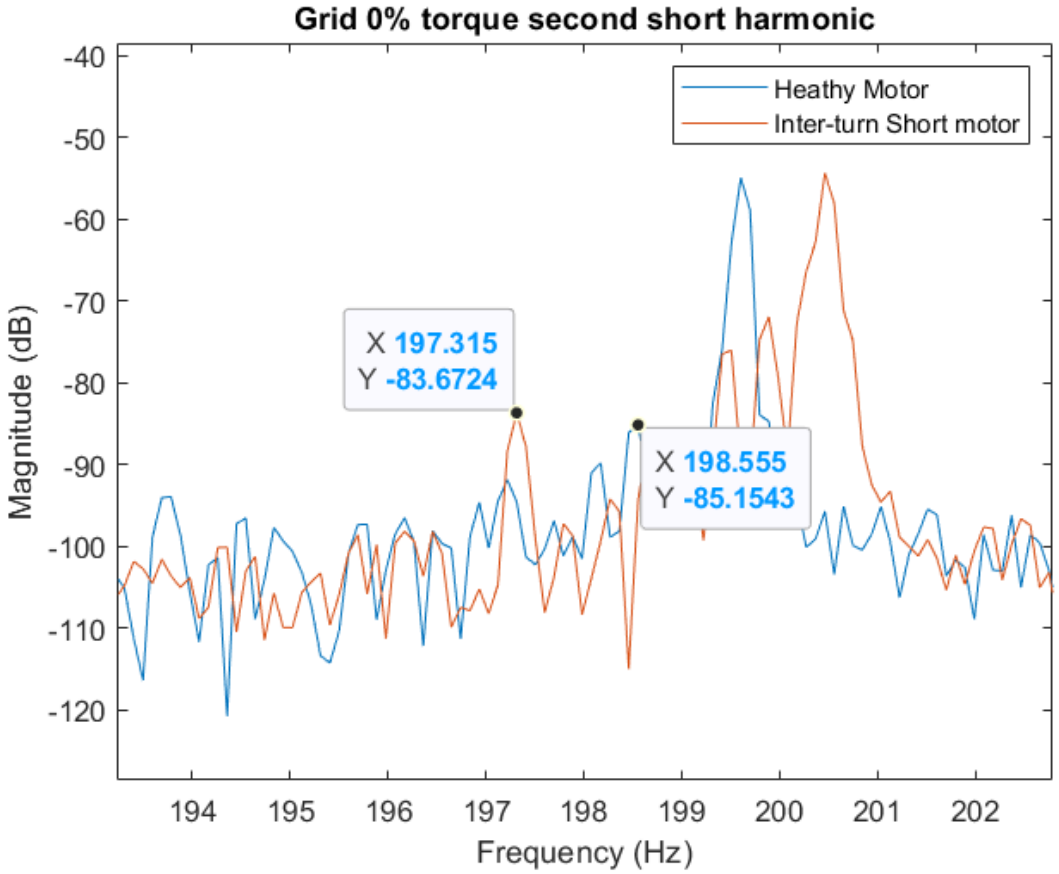

Appendix Figure 2: n=1, k=3 for grid fed induction motor, healthy vs inter-turn short frequency spectrum, no load.

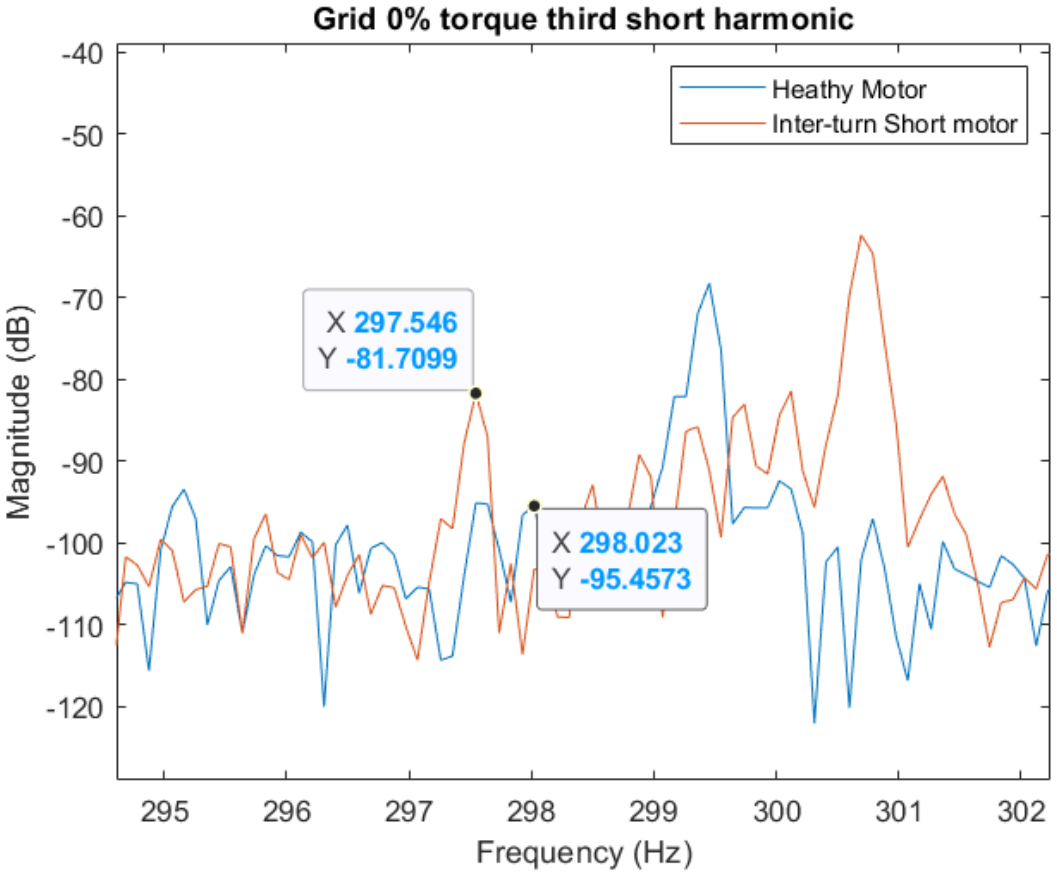

Appendix Figure 3: n=1, k=5 for grid fed induction motor, healthy vs inter-turn short frequency spectrum, no load.

9.1.1.2 Park's Vector Approach

9.1.1.2.1 No load

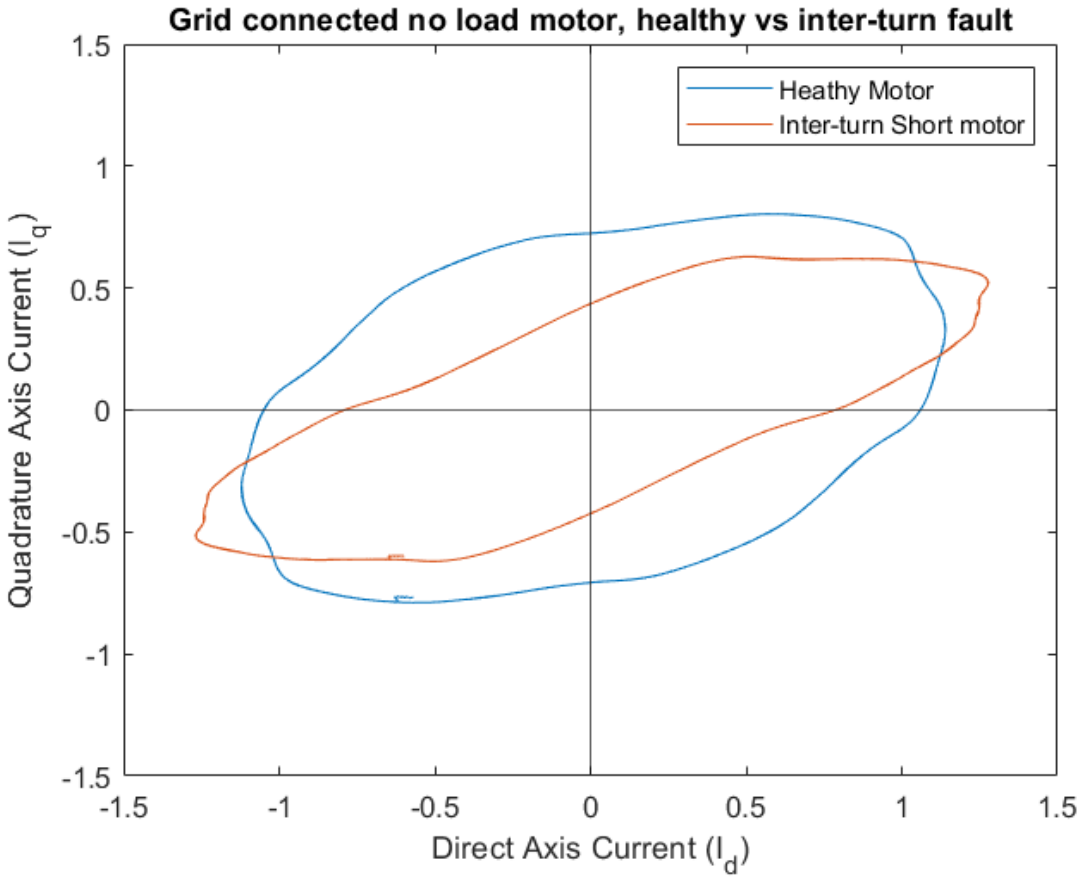

Appendix Figure 4: Normalised D-Q plot of grid supplied motor, healthy vs inter-turn motor, no load.

9.1.2 Broken Rotor Bar

9.1.2.1 MCSA

9.1.2.1.1 No Load

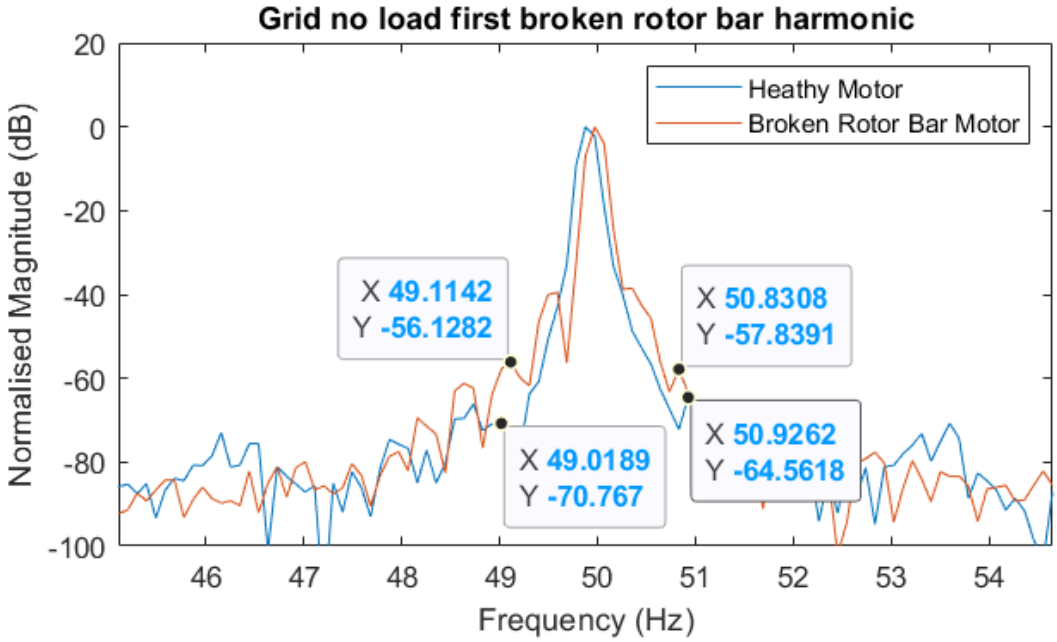

Appendix Figure 5: Frequency spectrum of grid supplied line current , healthy motor vs broken rotor bar, k = 1, no load.

9.1.2.2 Park's Vector Approach

9.1.2.2.1 No Load

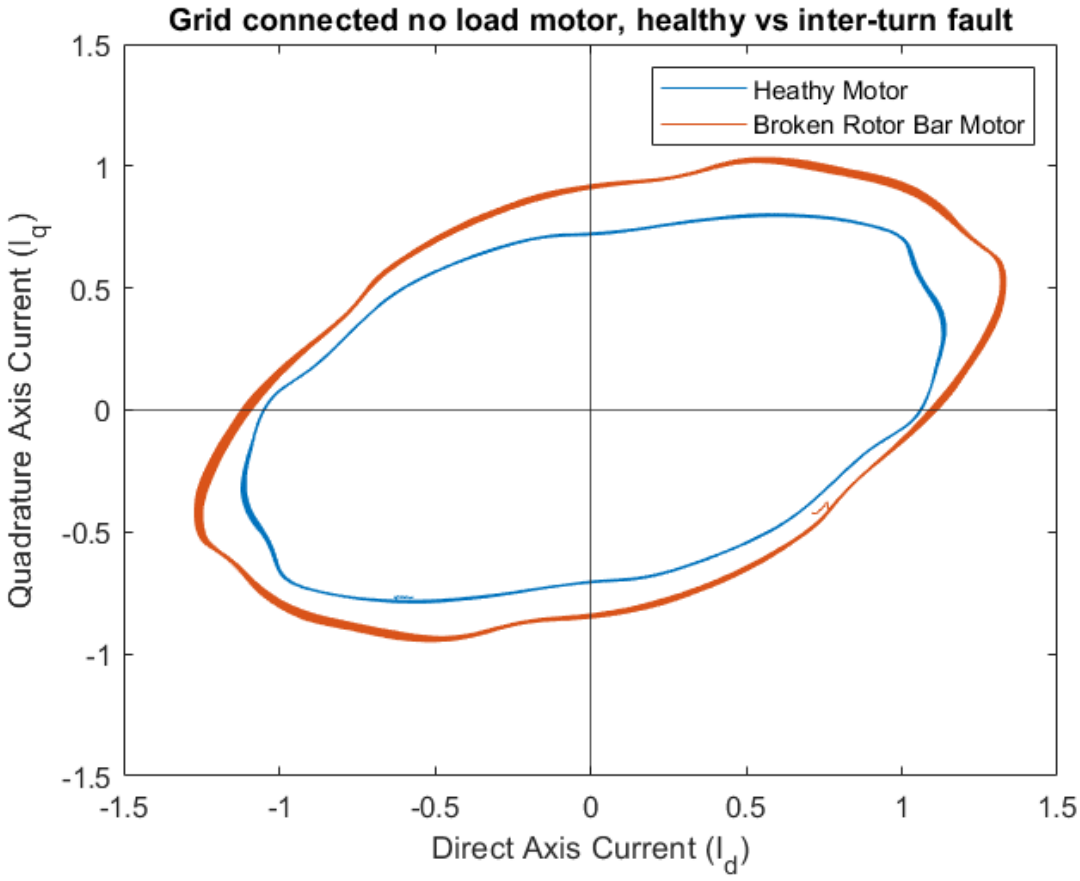

Appendix Figure 6: Normalised D-Q plot of grid supplied motor, healthy vs broken rotor bar, 10 cycles, no load.

9.2 V/Hz OPEN-LOOP 50Hz RESULTS

9.2.1 Inter-turn Faults

9.2.1.1 MCSA

9.2.1.1.1 No Load

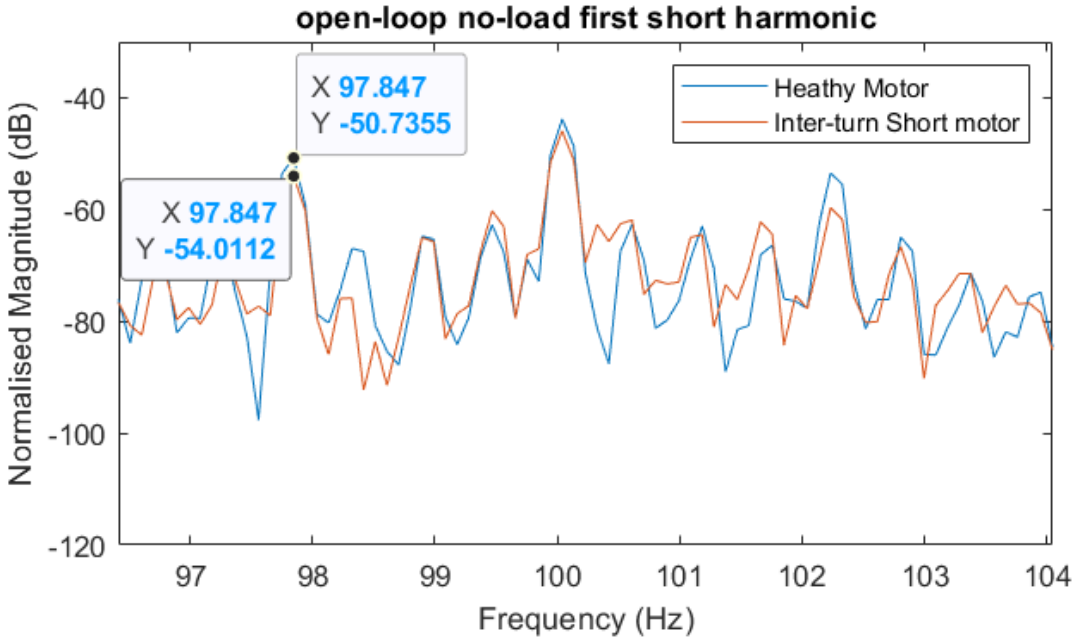

Appendix Figure 7: n=1, k=1 for V/Hz open-loop fed induction motor, healthy vs inter-turn short frequency spectrum, no load.

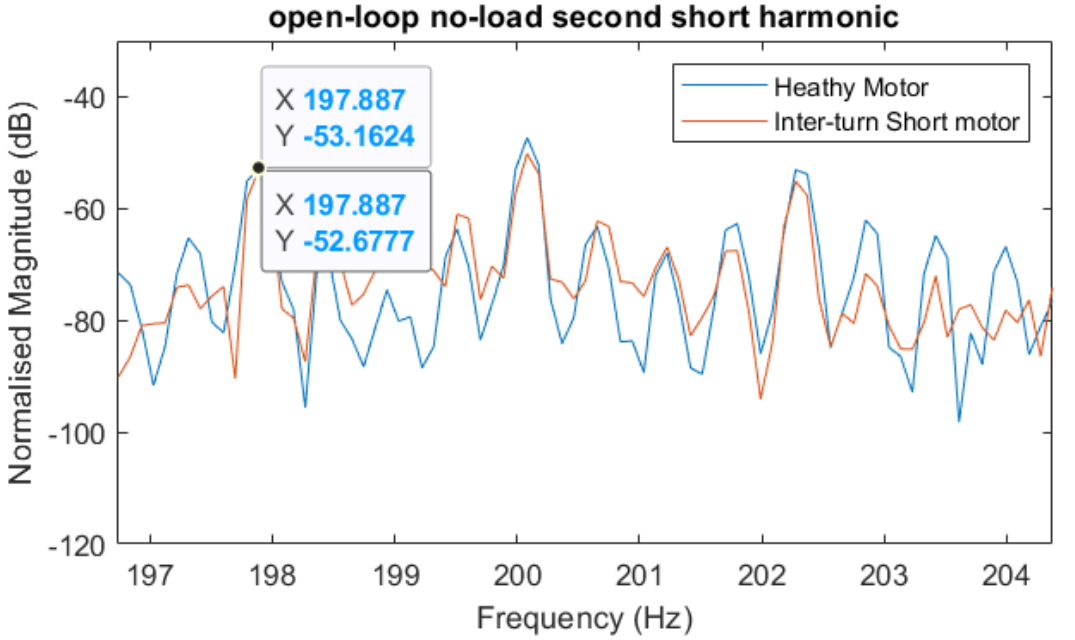

Appendix Figure 8: n=1, k=3 for V/Hz open-loop fed induction motor, healthy vs inter-turn short frequency spectrum, no load.

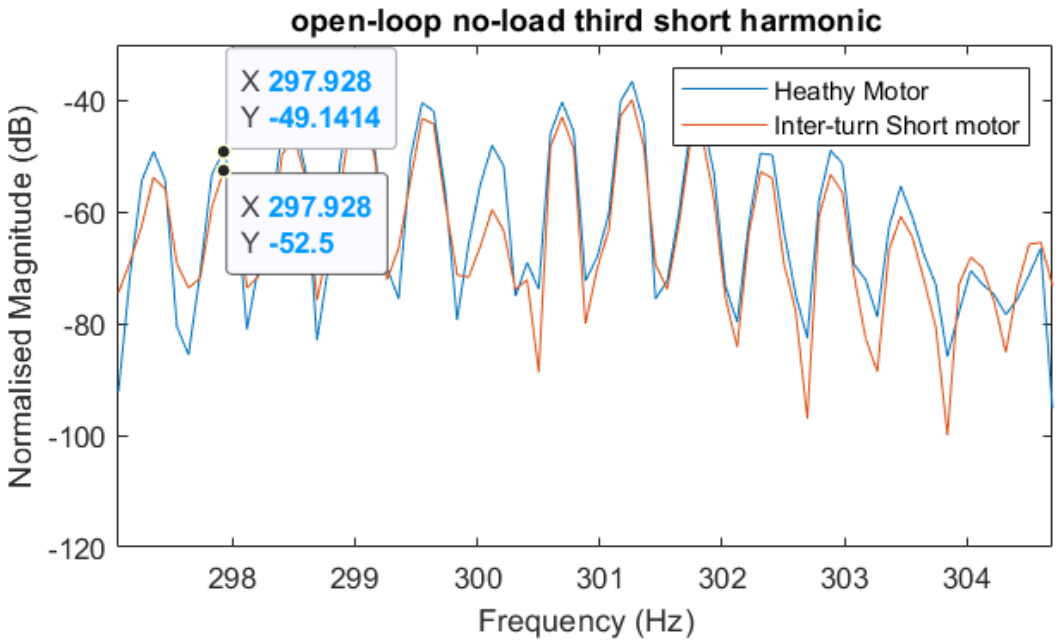

Appendix Figure 9: n=1, k=5 for V/Hz open-loop fed induction motor, healthy vs inter-turn short frequency spectrum, no load.

9.2.1.2 Park's Vector Approach

9.2.1.2.1 No Load

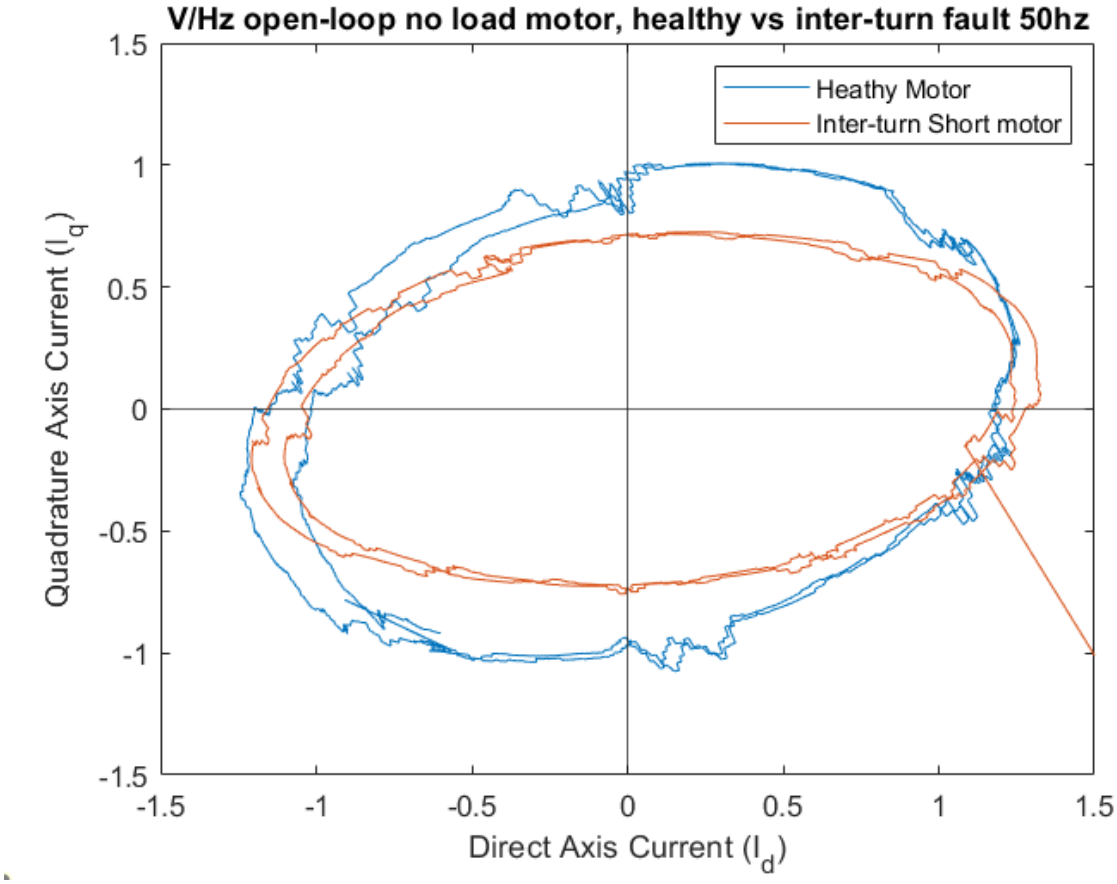

Appendix Figure 10: Normalised D-Q plot of grid-supplied motor, healthy vs inter-turn fault, no load.

9.2.2 Broken Rotor Bar

9.2.2.1 MCSA

9.2.2.1.1 No Load

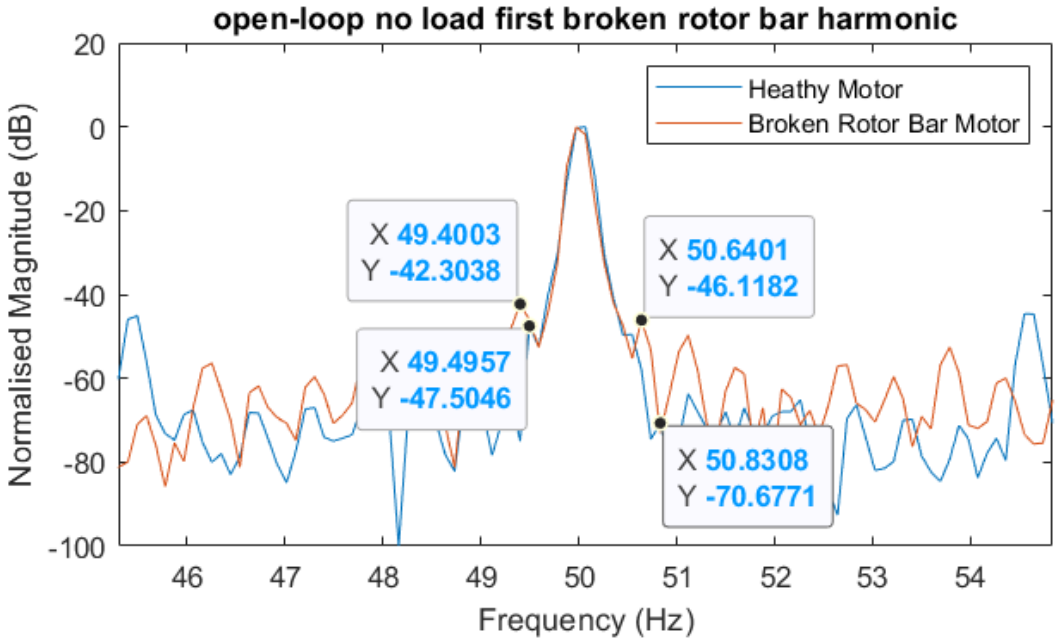

Appendix Figure 11: Frequency spectrum of line current, healthy motor vs broken rotor bar, k = 1, no load.

9.2.2.2 Park's Vector Approach

9.2.2.2.1 No Load

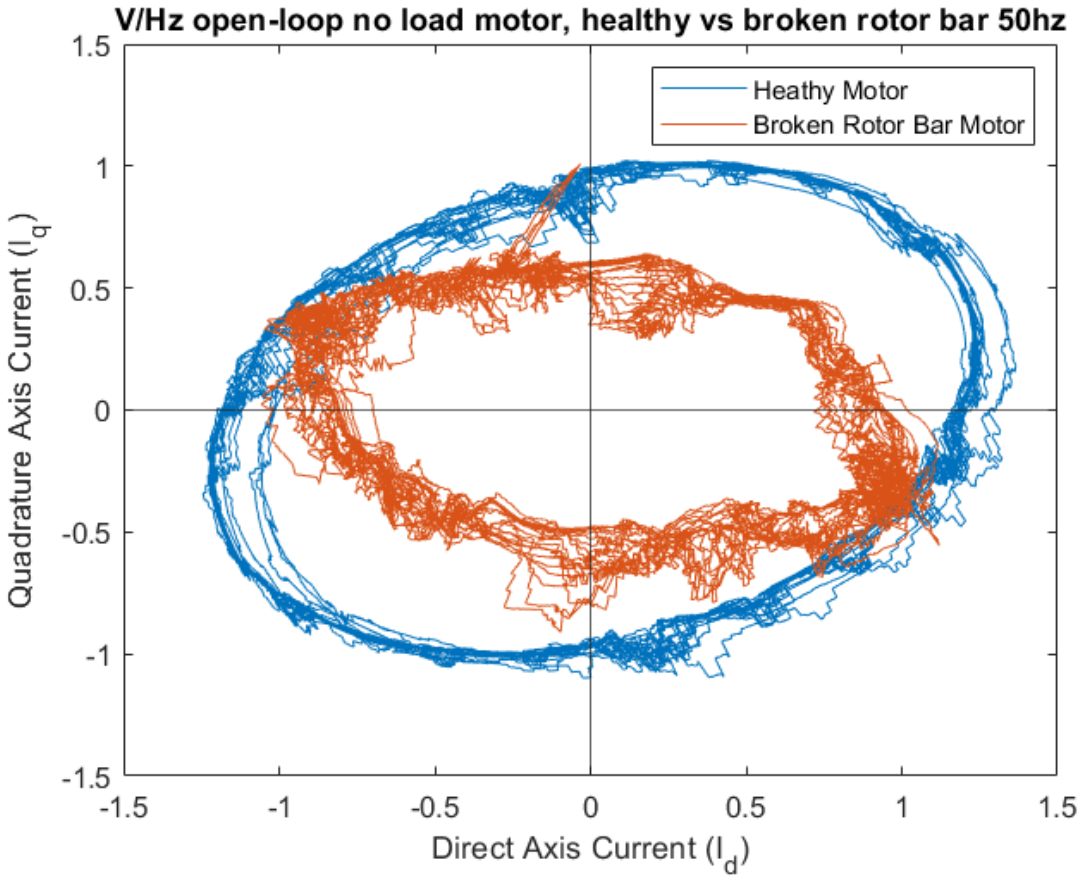

Appendix Figure 12: Normalised D-Q plot of grid-supplied motor, healthy vs broken rotor bar, no load, 10 cycles.

9.3 V/Hz OPEN-LOOP 25Hz RESULTS

9.3.1 Inter-turn fault

9.3.1.1 MCSA

9.3.1.1.1 Partial Load

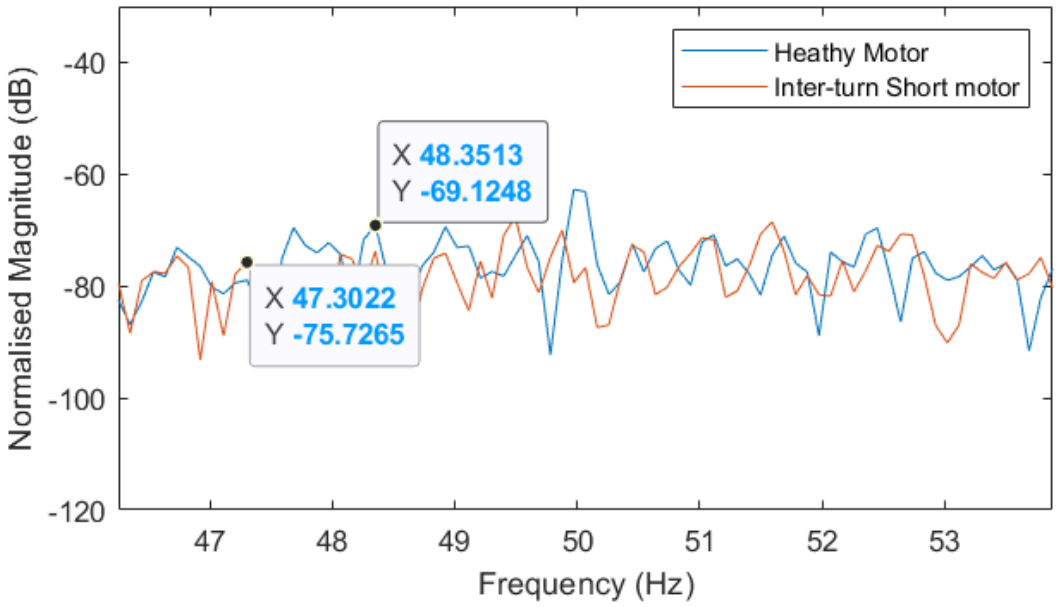

Appendix Figure 13: n=1, k=1 for V/Hz open-loop fed induction motor, healthy vs inter-turn short frequency spectrum, partial load, 25Hz.

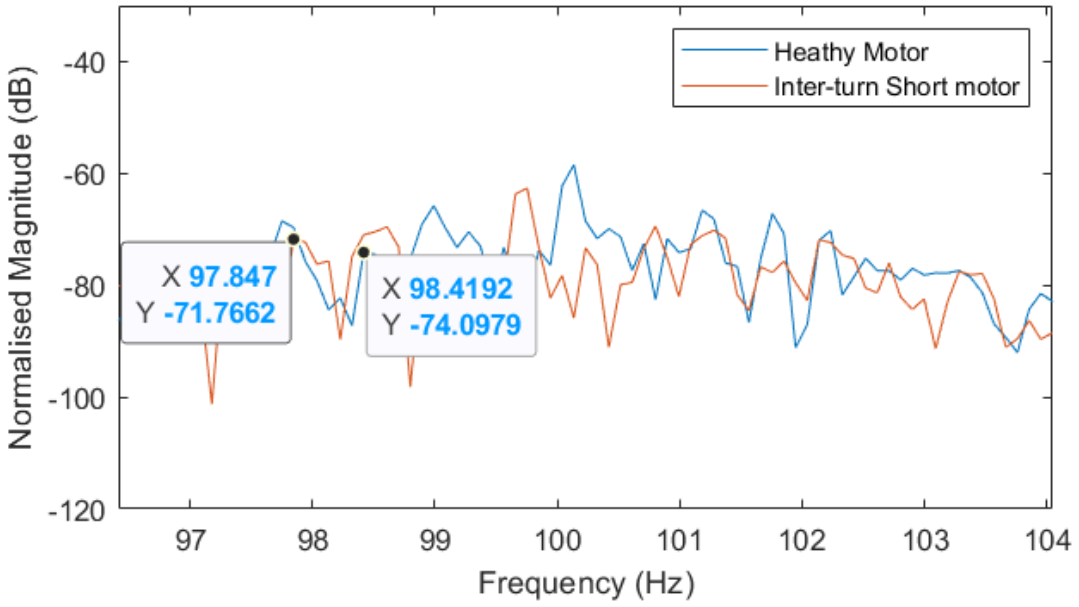

Appendix Figure 14: n=1, k=3 for V/Hz open-loop fed induction motor, healthy vs inter-turn short frequency spectrum, partial load, 25Hz.

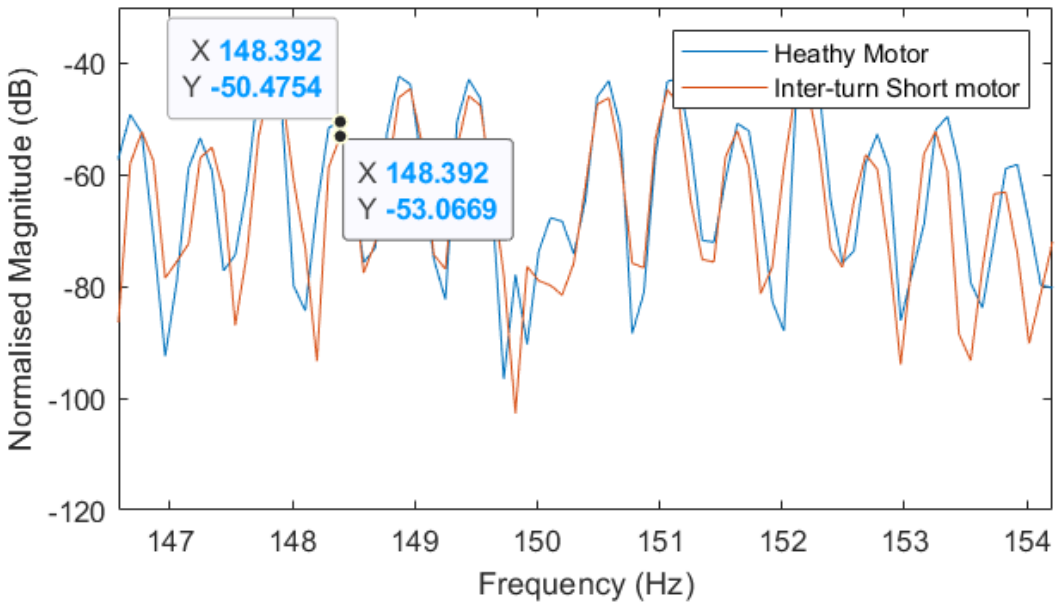

Appendix Figure 15: n=1, k=5 for V/Hz open-loop fed induction motor, healthy vs inter-turn short frequency spectrum, partial load, 25Hz.

9.3.1.1.2 No Load

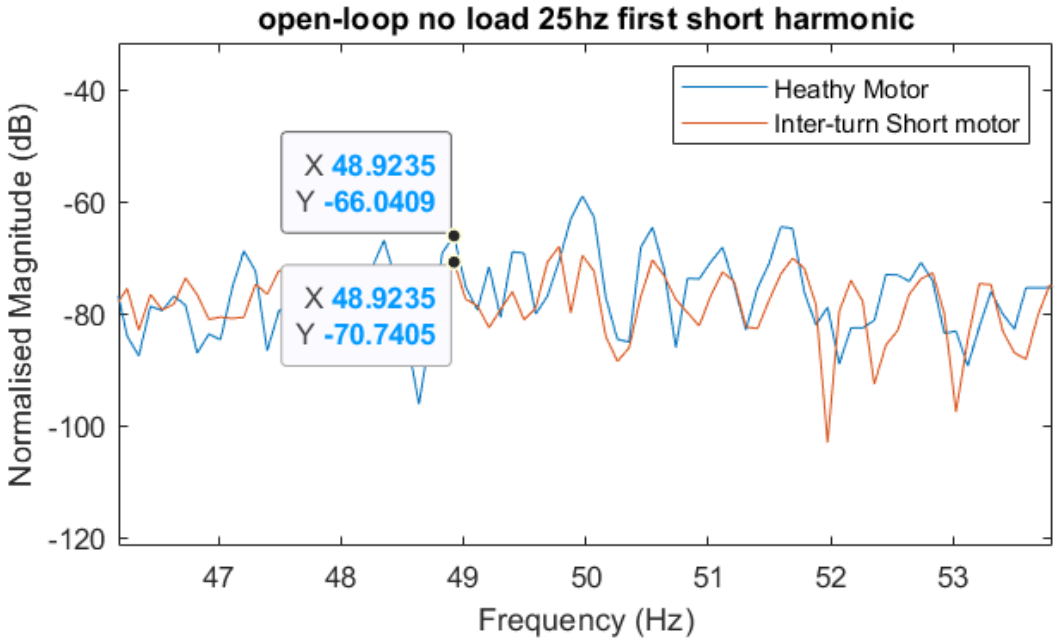

Appendix Figure 16: n=1, k=1 for V/Hz open-loop fed induction motor, healthy vs inter-turn short frequency spectrum, no load, 25Hz.

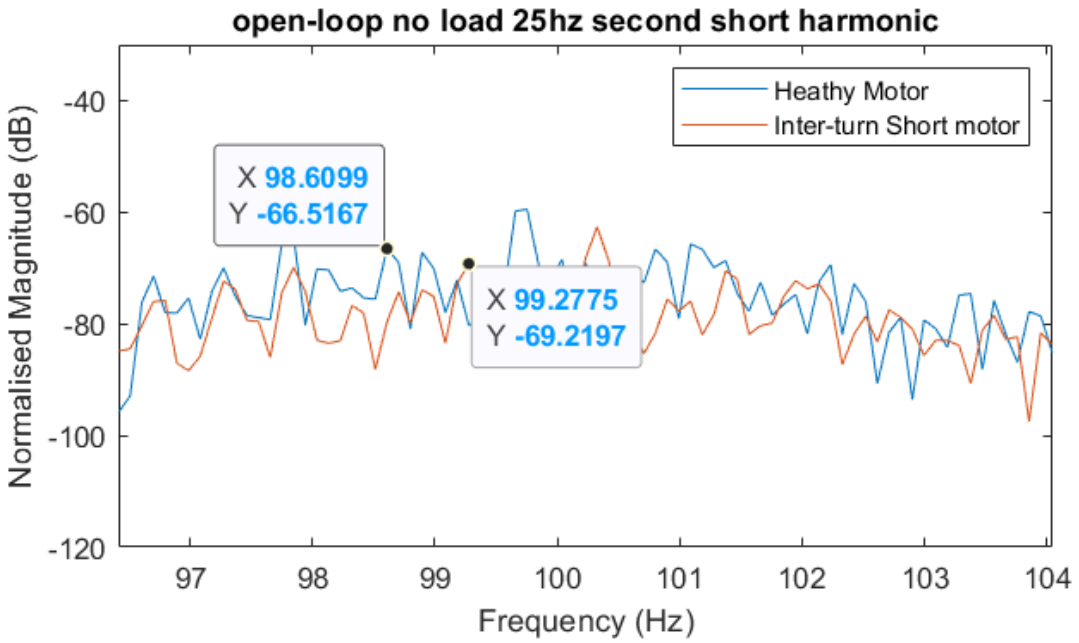

Appendix Figure 17: n=1, k=3 for V/Hz open-loop fed induction motor, healthy vs inter-turn short frequency spectrum, no load, 25Hz.

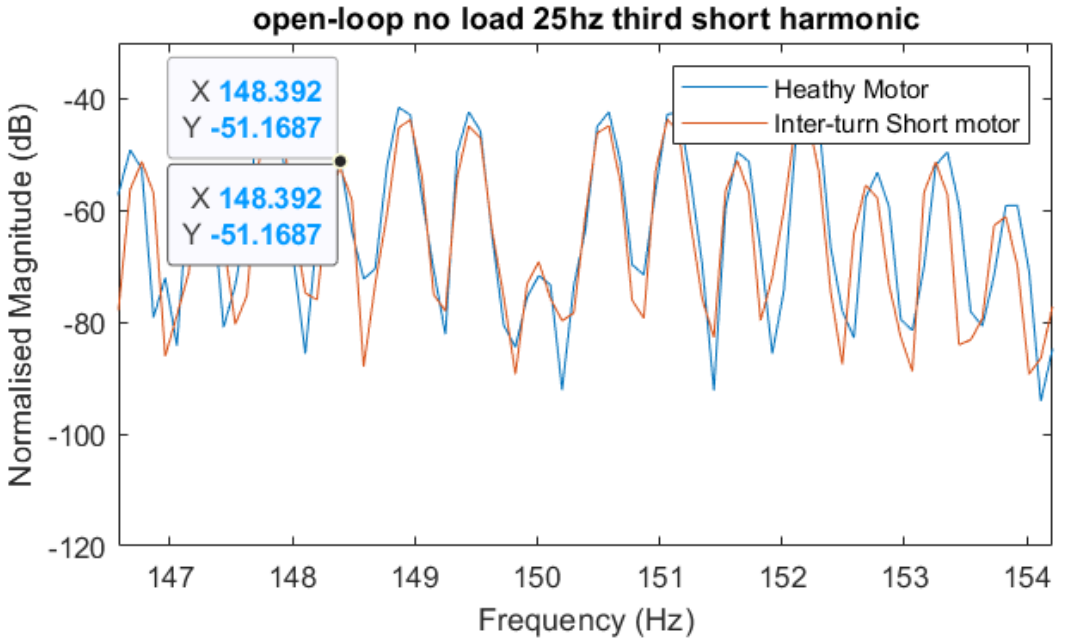

Appendix Figure 18: n=1, k=5 for V/Hz open-loop fed induction motor, healthy vs inter-turn short frequency spectrum, no load, 25Hz.

9.3.1.2 Park's Vector Approach

9.3.1.2.1 Partial load

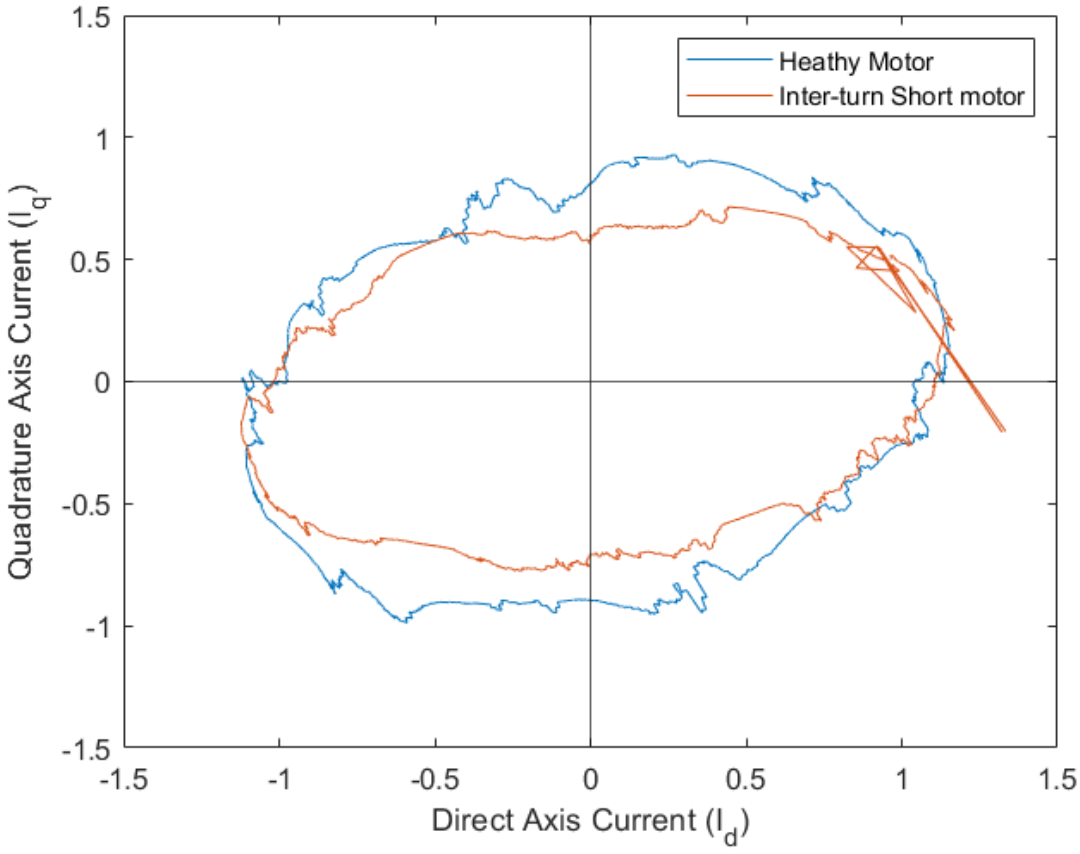

Appendix Figure 19: Normalised D-Q plot of V/Hz open-loop supplied motor, healthy vs inter-turn fault, partial load, 25Hz.

9.3.1.2.2 No Load

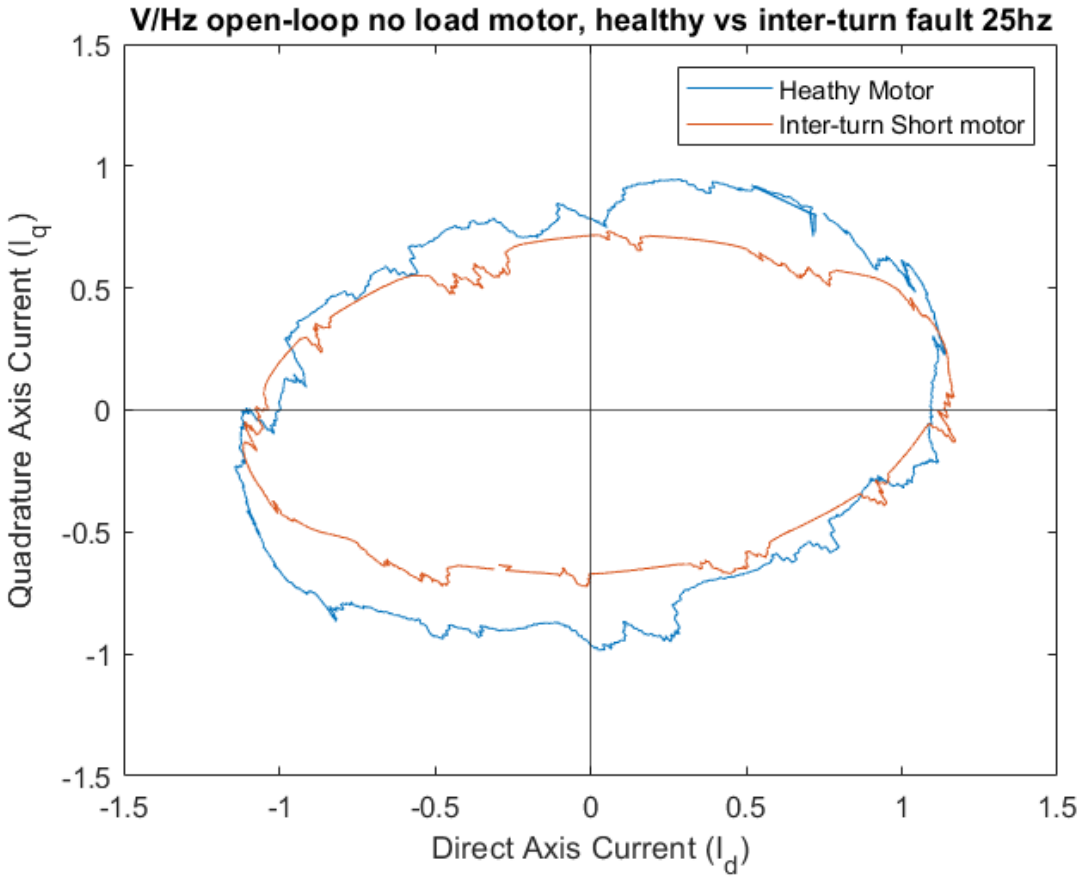

Appendix Figure 20: Normalised D-Q plot of V/Hz open-loop supplied motor, healthy vs inter-turn fault, no load, 25Hz.

9.3.1.3 Extended Park's Vector Approach

Appendix Table 1: Table of Extended Park's Vector Approach for V/Hz open-loop, 25Hz supplied motor, healthy vs inter-turn short, 25Hz.

V/Hz open-loop, no fault, no load, 25Hz.		**V/Hz open-loop, inter-turn short, no load, 25Hz.**		**Difference (p.u.)**
Frequency (Hz)	50	**Frequency (Hz)**	50	
Magnitude (p.u.)	0.16751786	**Magnitude (p.u.)**	0.247863107	0.080345247
V/Hz open-loop, no fault, partial load, 25Hz.		**V/Hz open-loop, inter-turn short, partial load, 25Hz.**		
Frequency (Hz)	50	**Frequency (Hz)**	50	
Magnitude (p.u.)	0.164483021	**Magnitude (p.u.)**	0.247721235	0.083238215

9.3.1.4 DC Bus Analysis

Appendix Table 2: Table of DC bus analysis of V/Hz open-loop 25Hz supply, healthy vs inter-turn short.

V/Hz open-loop, no fault, no load, 25Hz.		**V/Hz open-loop, inter-turn short, no load, 25Hz.**		**Difference (p.u.)**	**Difference (faulted / healthy)**
Frequency (Hz)	50	**Frequency (Hz)**	50		
Magnitude (p.u.)	0.034015707	**Magnitude (p.u.)**	0.152405595	0.118389887	4.480447608
Ripple Factor	0.273628371	**Ripple Factor**	0.445826753	0.172198382	1.629314795
V/Hz open-loop, no fault, partial load, 25Hz.		**V/Hz open-loop, inter-turn short, partiall load, 25Hz.**			
Frequency (Hz)	50	**Frequency (Hz)**	50		
Magnitude (p.u.)	0.023379276	**Magnitude (p.u.)**	0.113534379	0.090155104	4.856197459
Ripple Factor	0.366643448	**Ripple Factor**	0.545514723	0.178871275	1.487861644

9.3.2 Broken Rotor Bar

9.3.2.1 MCSA

9.3.2.1.1 Partial load

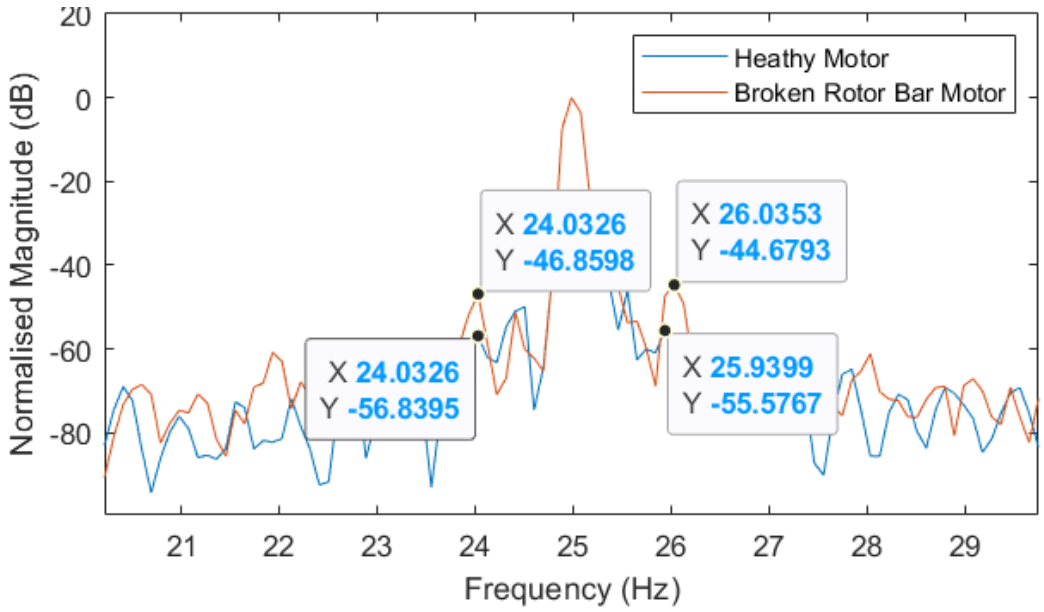

Appendix Figure 21: Frequency spectrum of line current from V/Hz open-loop supplied induction motor, healthy motor vs broken rotor bar, k = 1, partial load, 25Hz.

9.3.2.1.2 No Load

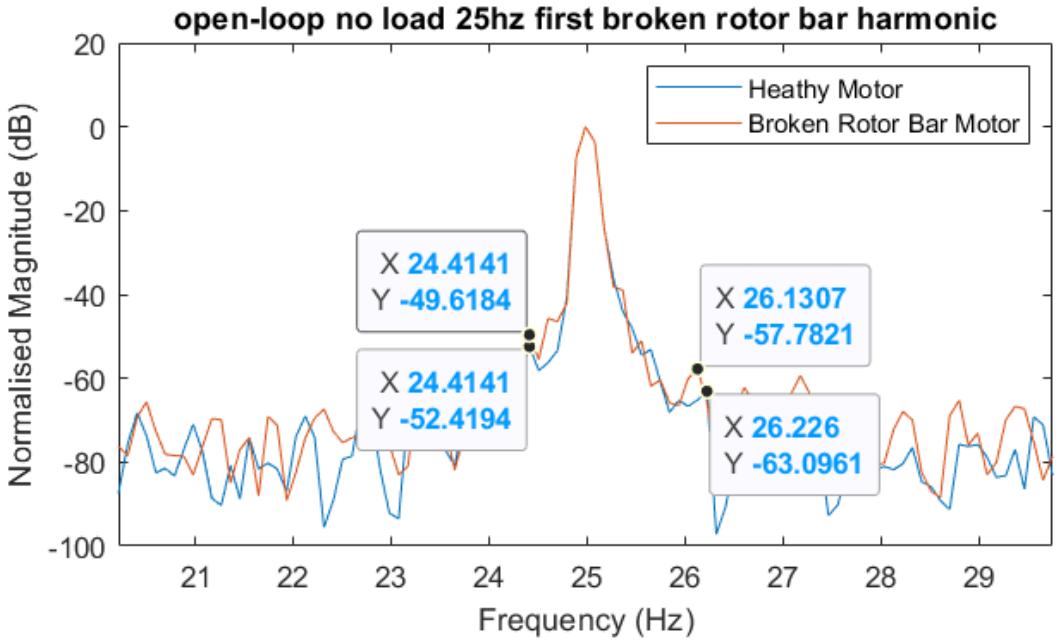

Appendix Figure 22: Frequency spectrum of line current from V/Hz open-loop supplied induction motor, healthy motor vs broken rotor bar, k = 1, no load, 25Hz.

9.3.2.2 Park's Vector Approach

9.3.2.2.1 Partial Load

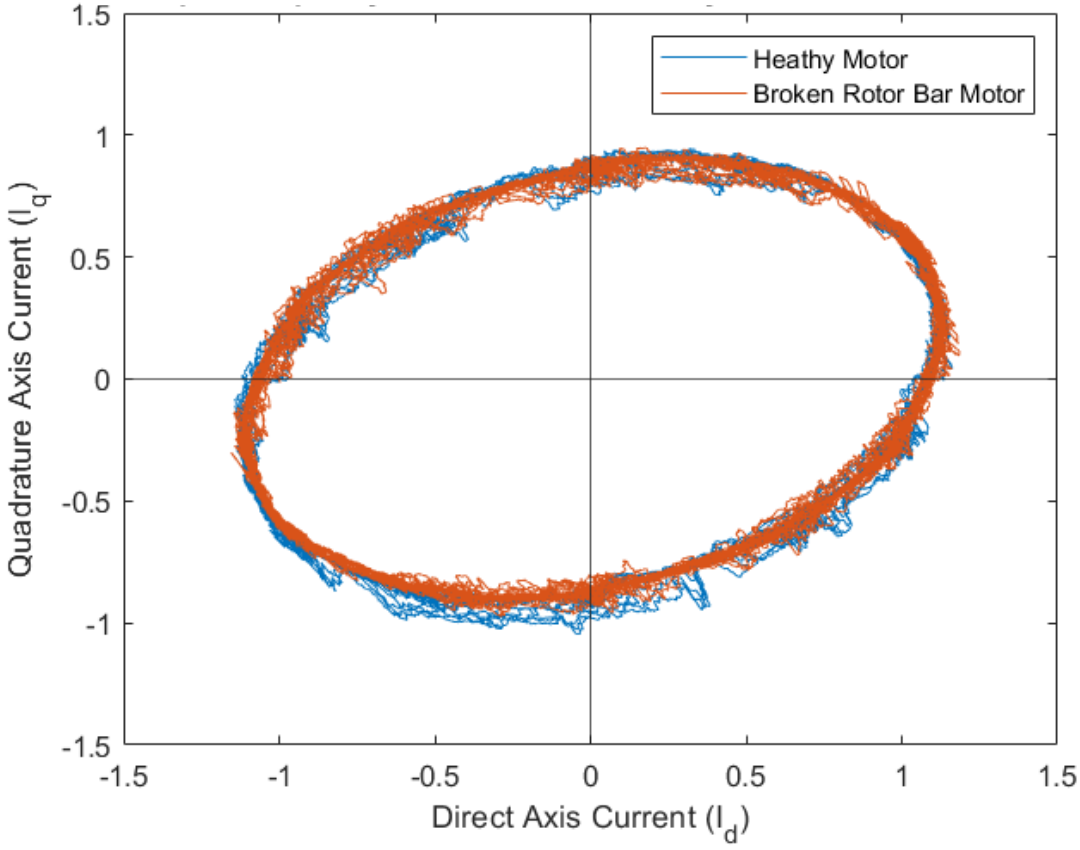

Appendix Figure 23: Normalised D-Q plot from V/Hz open-loop supplied induction motor, healthy motor vs broken rotor bar, partial load, 25Hz.

9.3.2.2.2 No Load

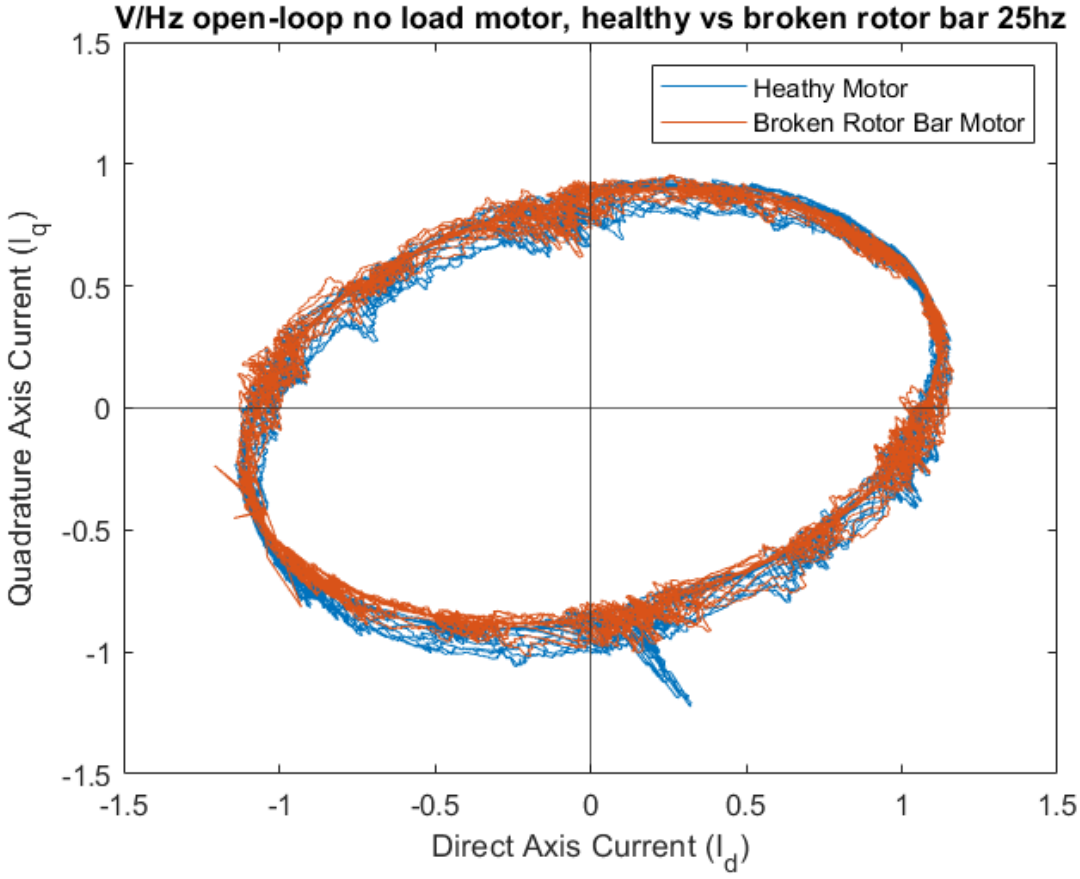

Appendix Figure 24: Normalised D-Q plot from V/Hz open-loop supplied induction motor, healthy motor vs broken rotor bar, no load, 25Hz.

9.3.2.3 Extended Park's Vector Approach

Appendix Table 3: Extended Park's Vector approach results, V/Hz open-loop, 25Hz.

V/Hz no load, no fault, 25Hz.		**V/Hz no load, broken rotor bar, 25Hz.**		
Frequency	50	**Frequency**	50	
Magnitude	0.164483021	**Magnitude**	0.164329362	-0.000153658
V/Hz partial load, no fault, 25Hz.		**V/Hz partial load, broken rotor bar, 25Hz.**		Difference (p.u.)
Frequency	50	**Frequency**	50	
Magnitude	0.16751786	**Magnitude**	0.165128047	-0.002389813

9.3.2.4 DC Bus Analysis

Appendix Table 4: DC Bus analysis results, V/Hz open-loop, 25Hz.

V/Hz no load, no fault, 25Hz.		V/Hz no load, broken rotor bar, 25Hz.		Difference (p.u.)	Difference (Faulted / Healthy)
Frequency	50	**Frequency**	50		
Magnitude	0.034015707	**Magnitude**	0.010453121	-0.023562587	0.307302763
Ripple Factor	0.273628371	**Ripple Factor**	0.285387422	0.011759051	1.04297453
V/Hz partial load, no fault, 25Hz.		**V/Hz partial load, broken rotor bar, 25Hz.**			
Frequency	50	**Frequency**	50		
Magnitude	0.023379276	**Magnitude**	0.006855186	-0.01652409	0.293216359
Ripple Factor	0.366643448	**Ripple Factor**	0.365308263	-0.001335184	0.996358357

9.4 V/Hz CLOSED-LOOP 50Hz RESULTS

9.4.1 Inter-turn Fault

9.4.1.1 MCSA

9.4.1.1.1 Partial load

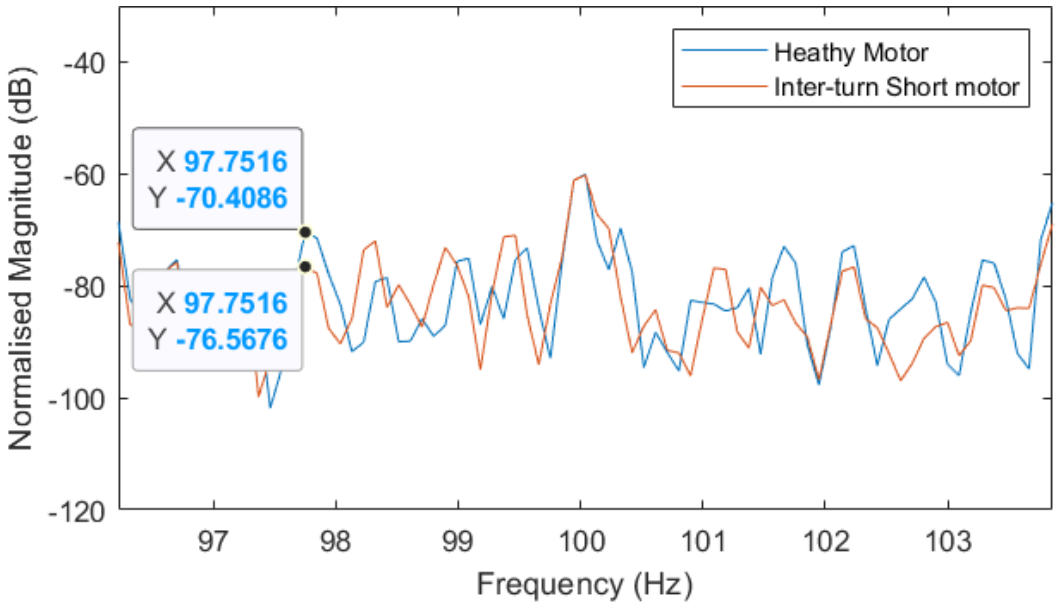

Appendix Figure 25: n=1, k=1 for V/Hz closed-loop fed induction motor, healthy vs inter-turn short frequency spectrum, partial load, 50Hz.

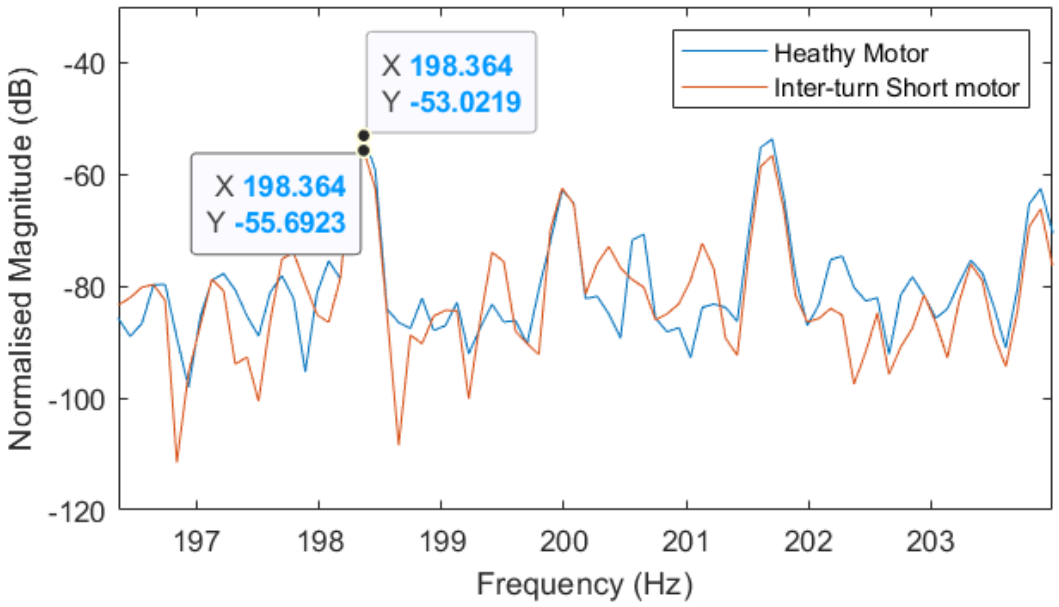

Appendix Figure 26: n=1, k=3 for V/Hz closed-loop fed induction motor, healthy vs inter-turn short frequency spectrum, partial load, 50Hz.

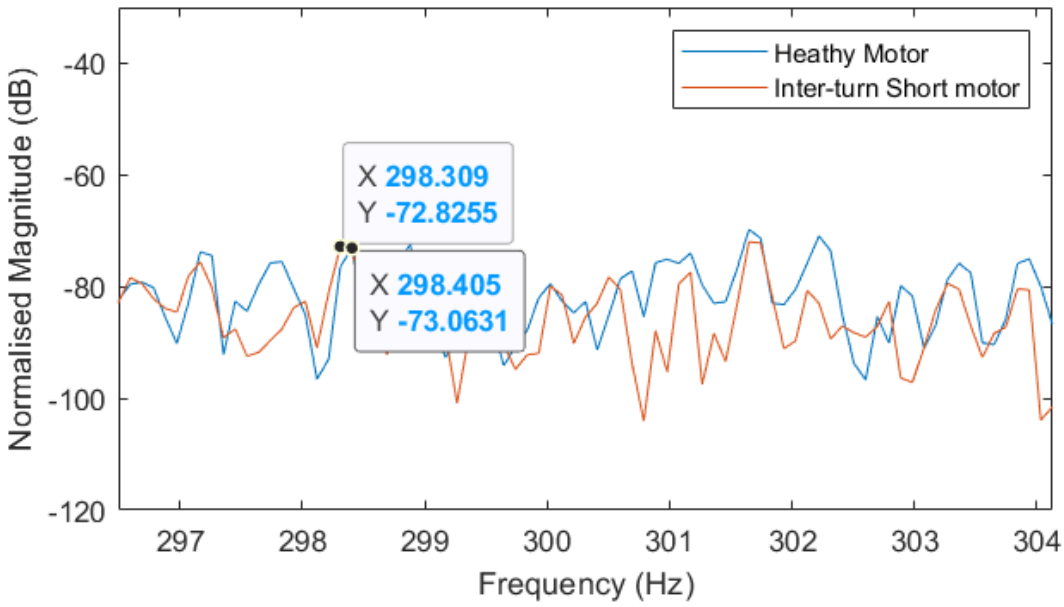

Appendix Figure 27: n=1, k=5 for V/Hz closed-loop fed induction motor, healthy vs inter-turn short frequency spectrum, partial load, 50Hz.

9.4.1.1.2 No load

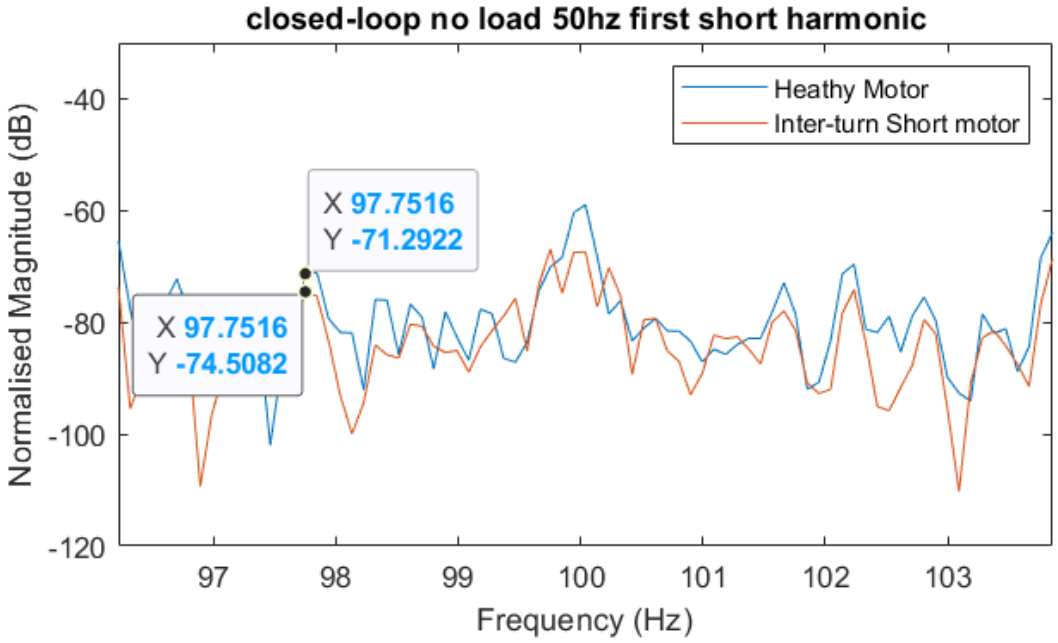

Appendix Figure 28: n=1, k=1 for V/Hz closed-loop fed induction motor, healthy vs inter-turn short frequency spectrum, no load, 50Hz.

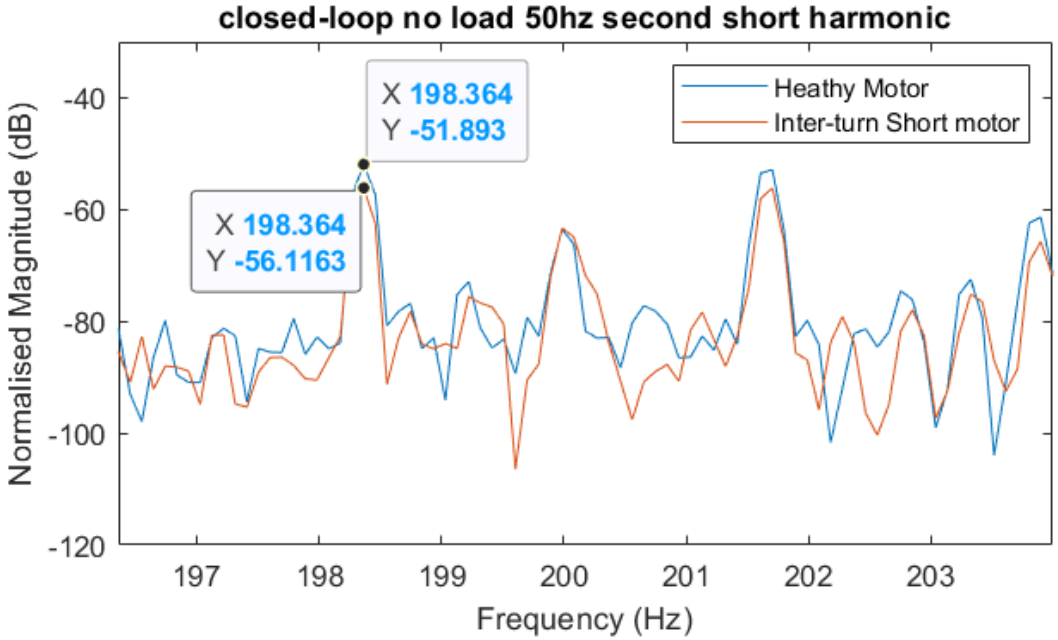

Appendix Figure 29: n=1, k=3 for V/Hz closed-loop fed induction motor, healthy vs inter-turn short frequency spectrum, no load, 50Hz.

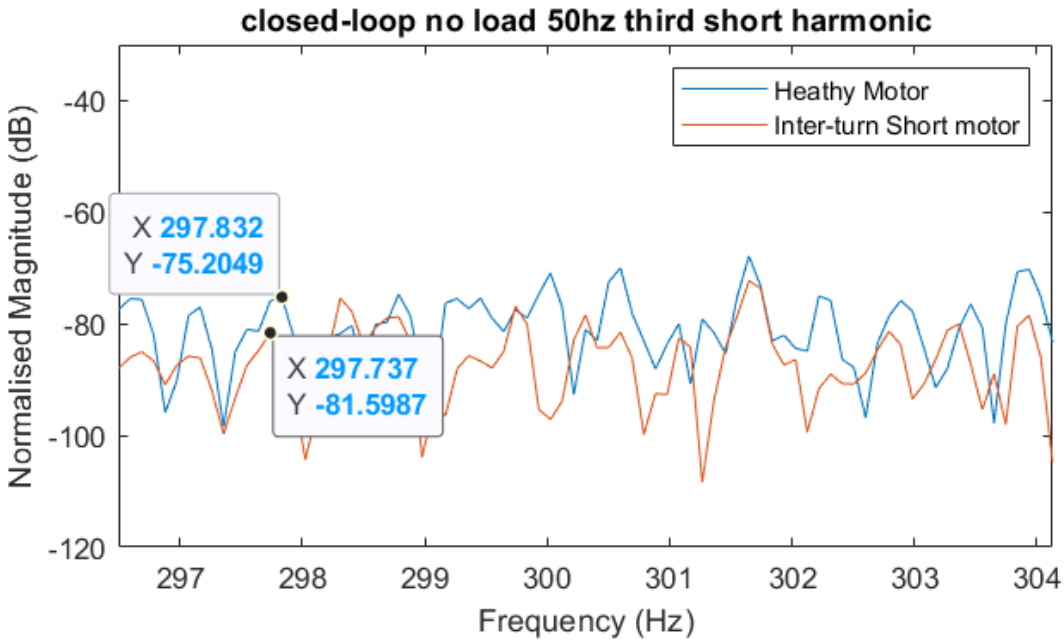

Appendix Figure 30: n=1, k=5 for V/Hz closed-loop fed induction motor, healthy vs inter-turn short frequency spectrum, no load, 50Hz.

9.4.1.2 Park's Vector Approach

9.4.1.2.1 No Load

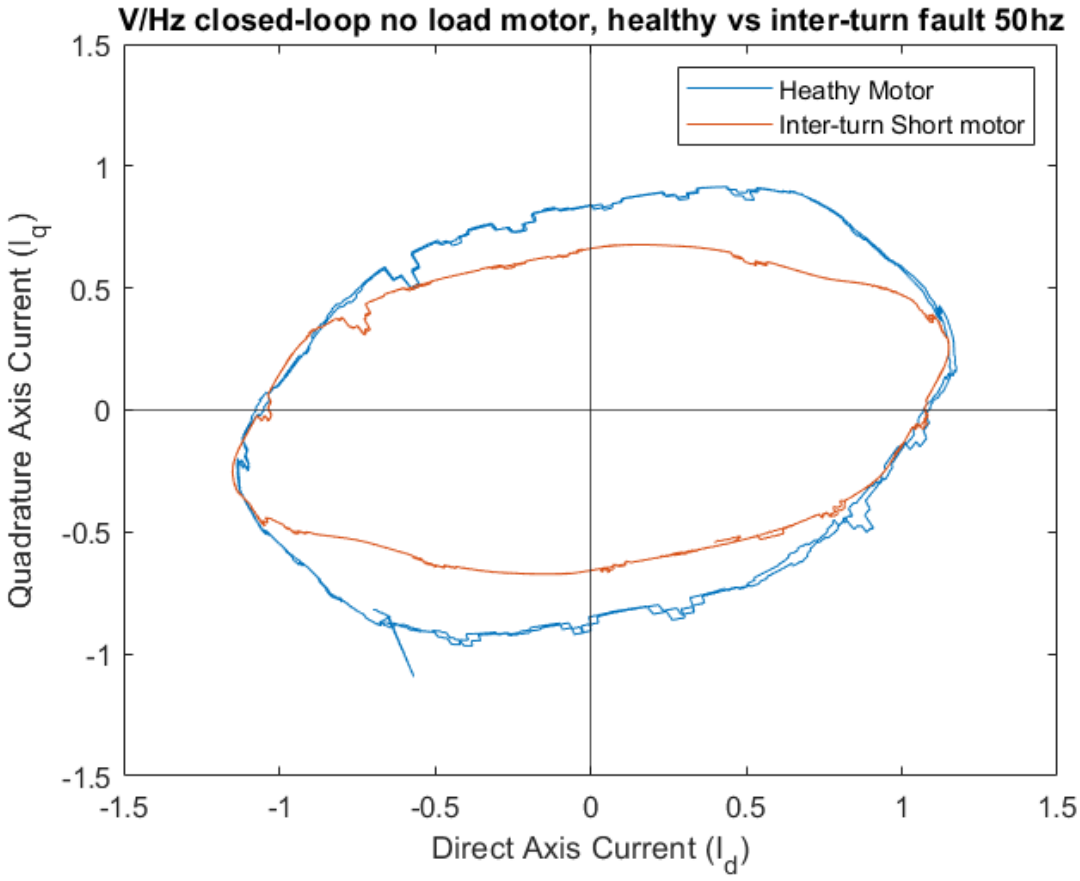

Appendix Figure 31: Normalised D-Q plot of V/Hz closed-loop fed induction motor, healthy vs inter-turn fault, no load.

9.4.2 Broken Rotor Bar

9.4.2.1 MCSA

9.4.2.1.1 Partial load

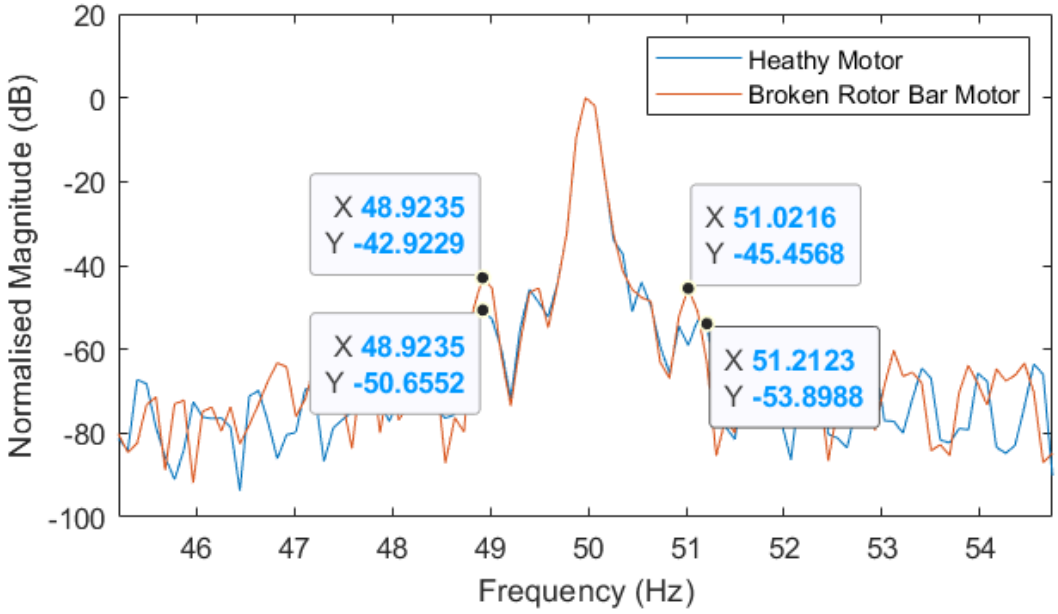

Appendix Figure 32: Frequency spectrum of line current from V/Hz closed-loop supplied induction motor, healthy motor vs broken rotor bar, k = 1, partial load, 50Hz.

9.4.2.1.2 No load

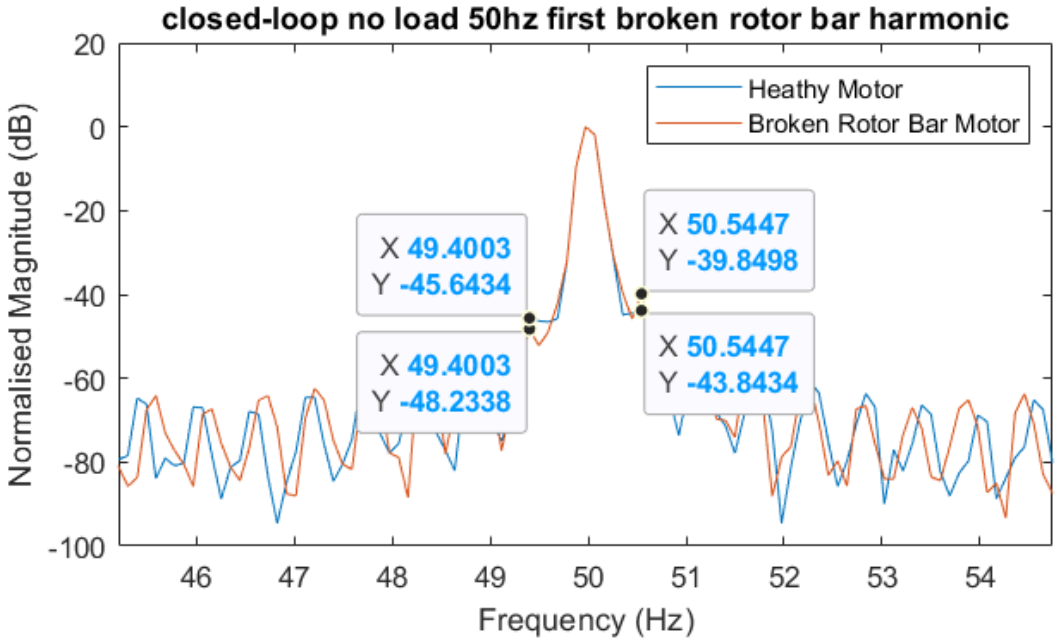

Appendix Figure 33: Frequency spectrum of line current from V/Hz closed-loop supplied induction motor, healthy motor vs broken rotor bar, k = 1, no load, 50Hz.

9.4.2.2 Park's Vector Approach

9.4.2.2.1 No Load

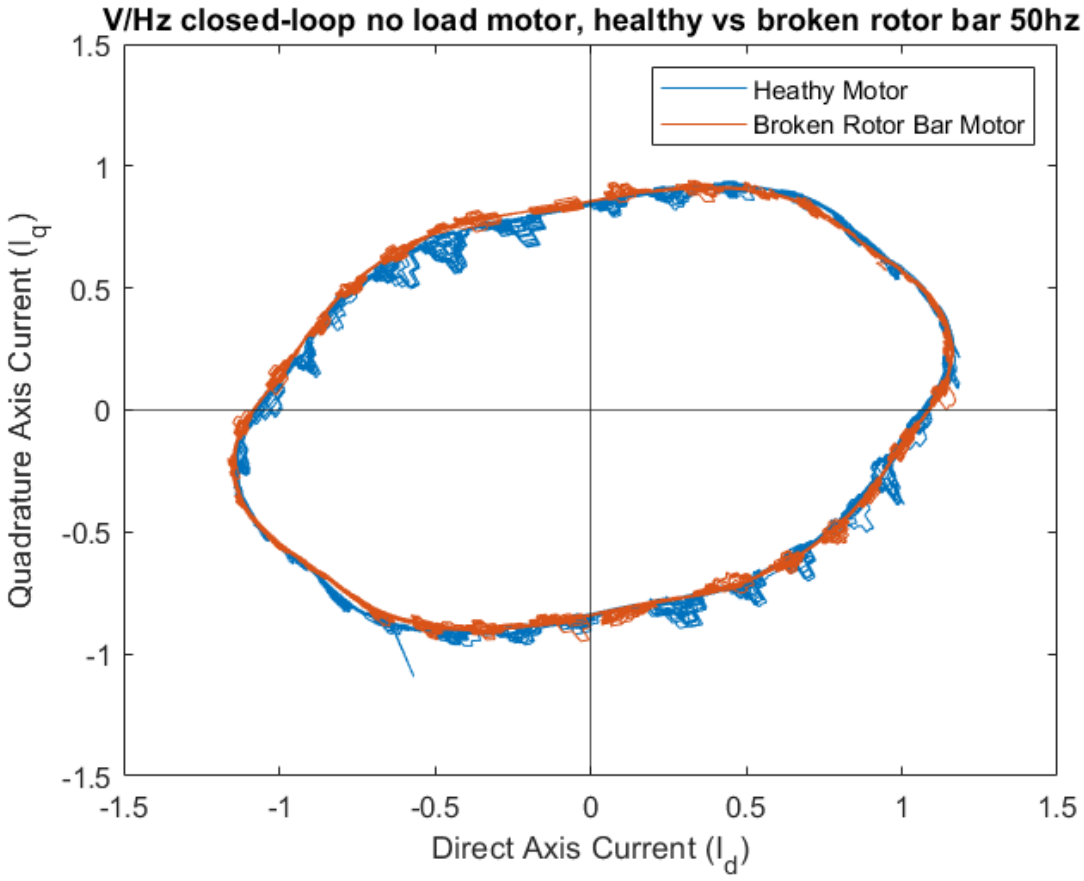

Appendix Figure 34: Normalised D-Q plot of V/Hz closed-loop supplied motor, healthy vs broken rotor bar, no load, 50Hz.

9.5 V/Hz CLOSED-LOOP 25Hz RESULTS

9.5.1 Inter-turn Fault

9.5.1.1 MCSA

9.5.1.1.1 Partial load

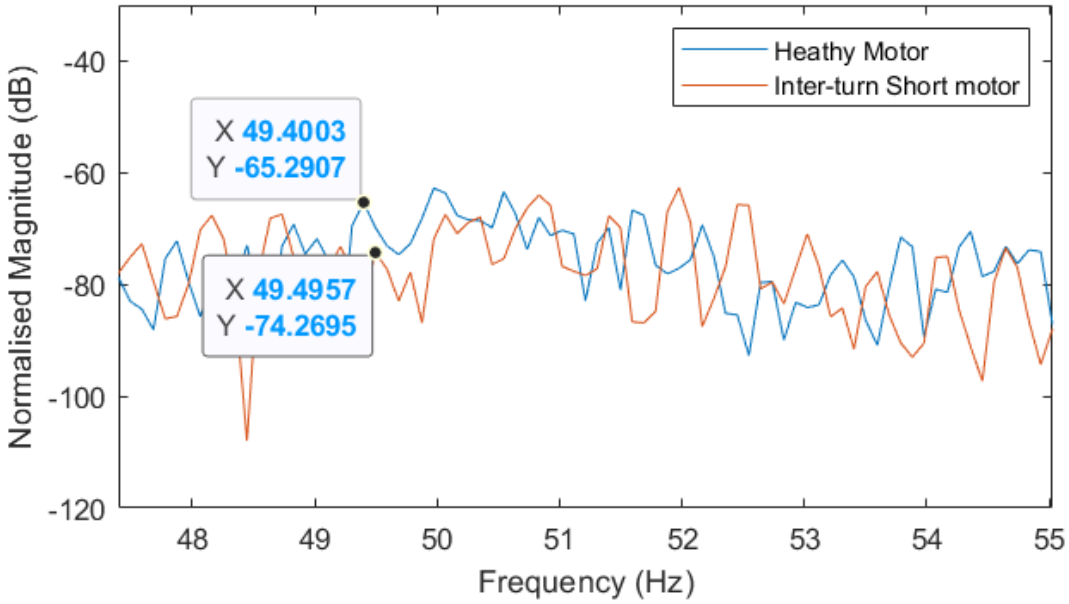

Appendix Figure 35: n=1, k=1 for V/Hz closed-loop fed induction motor, healthy vs inter-turn short frequency spectrum, full load, 25Hz.

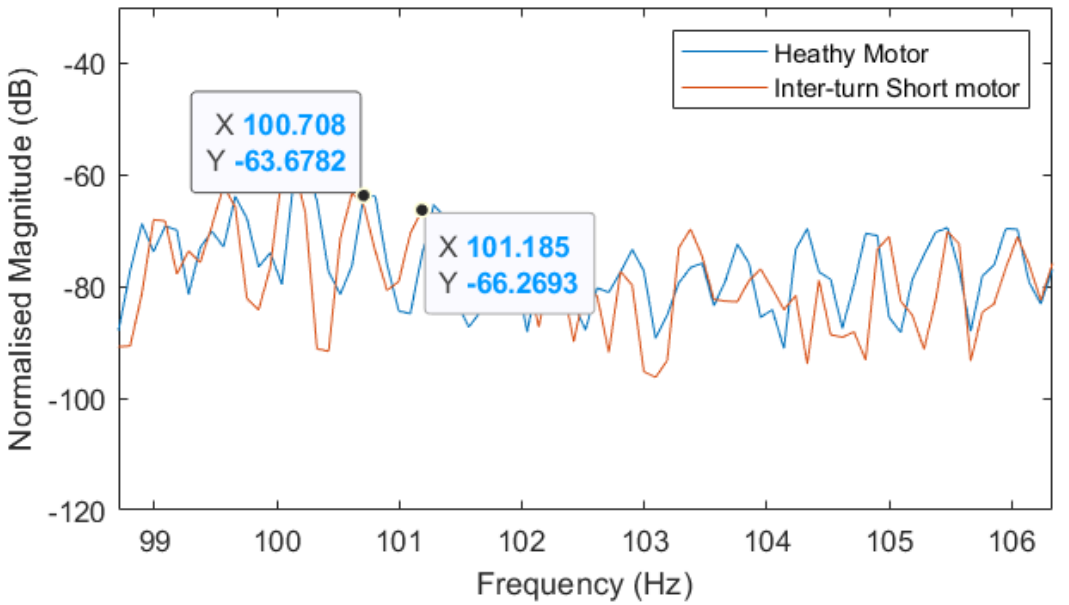

Appendix Figure 36: n=1, k=3 for V/Hz closed-loop fed induction motor, healthy vs inter-turn short frequency spectrum, full load, 25Hz.

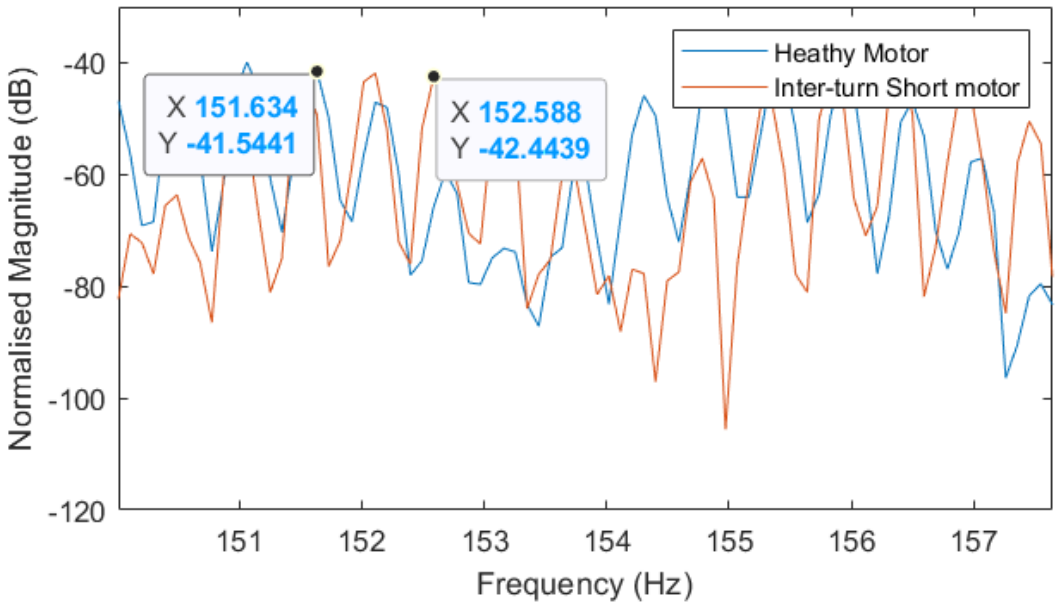

Appendix Figure 37: n=1, k=5 for V/Hz closed-loop fed induction motor, healthy vs inter-turn short frequency spectrum, full load, 25Hz.

9.5.1.1.2 No load

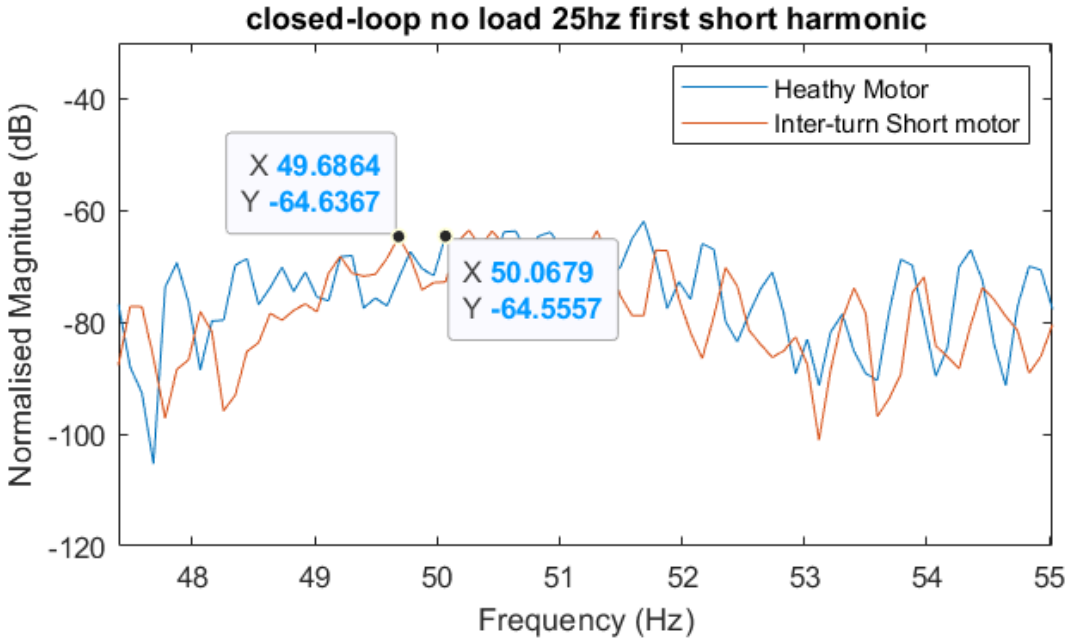

Appendix Figure 38: n=1, k=1 for V/Hz closed-loop fed induction motor, healthy vs inter-turn short frequency spectrum, no load, 25Hz.

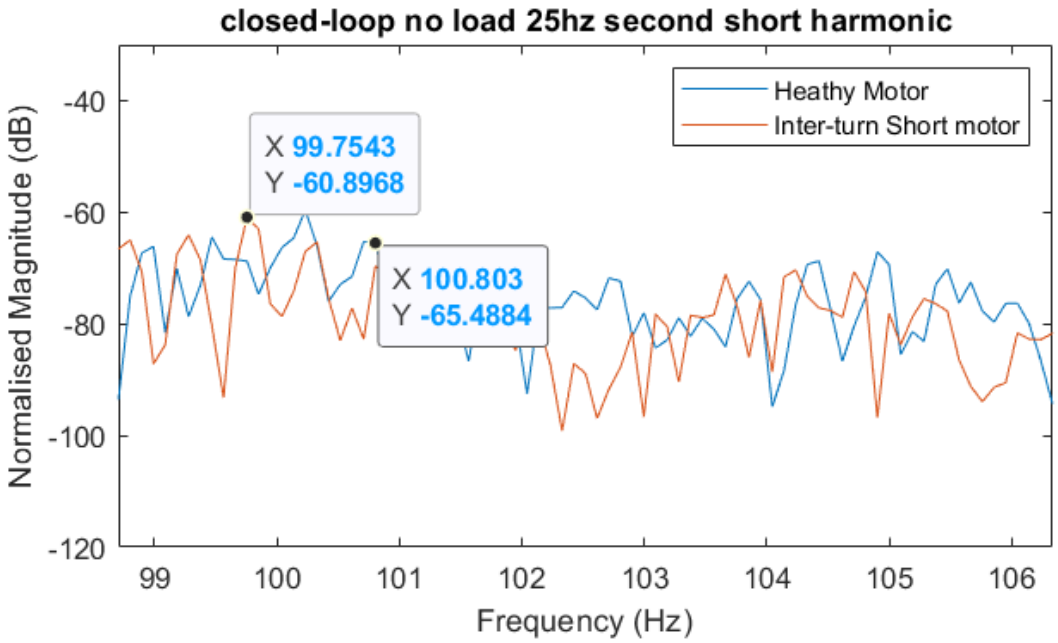

Appendix Figure 39: n=1, k=3 for V/Hz closed-loop fed induction motor, healthy vs inter-turn short frequency spectrum, no load, 25Hz.

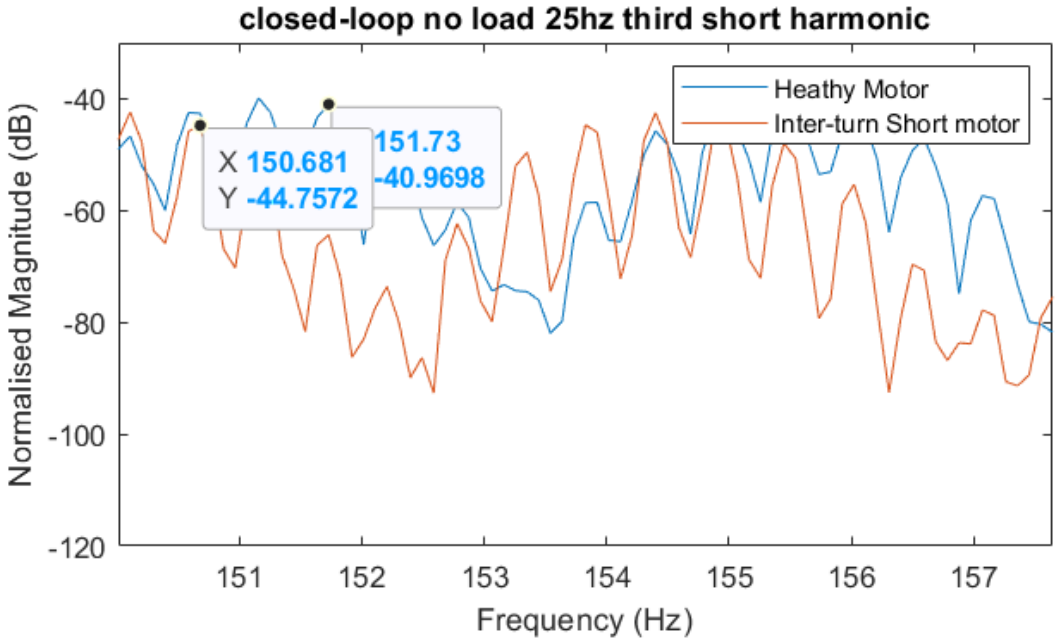

Appendix Figure 40: n=1, k=5 for V/Hz closed-loop fed induction motor, healthy vs inter-turn short frequency spectrum, no load, 25Hz.

9.5.1.2 Park's Vector Approach

9.5.1.2.1 Partial Load

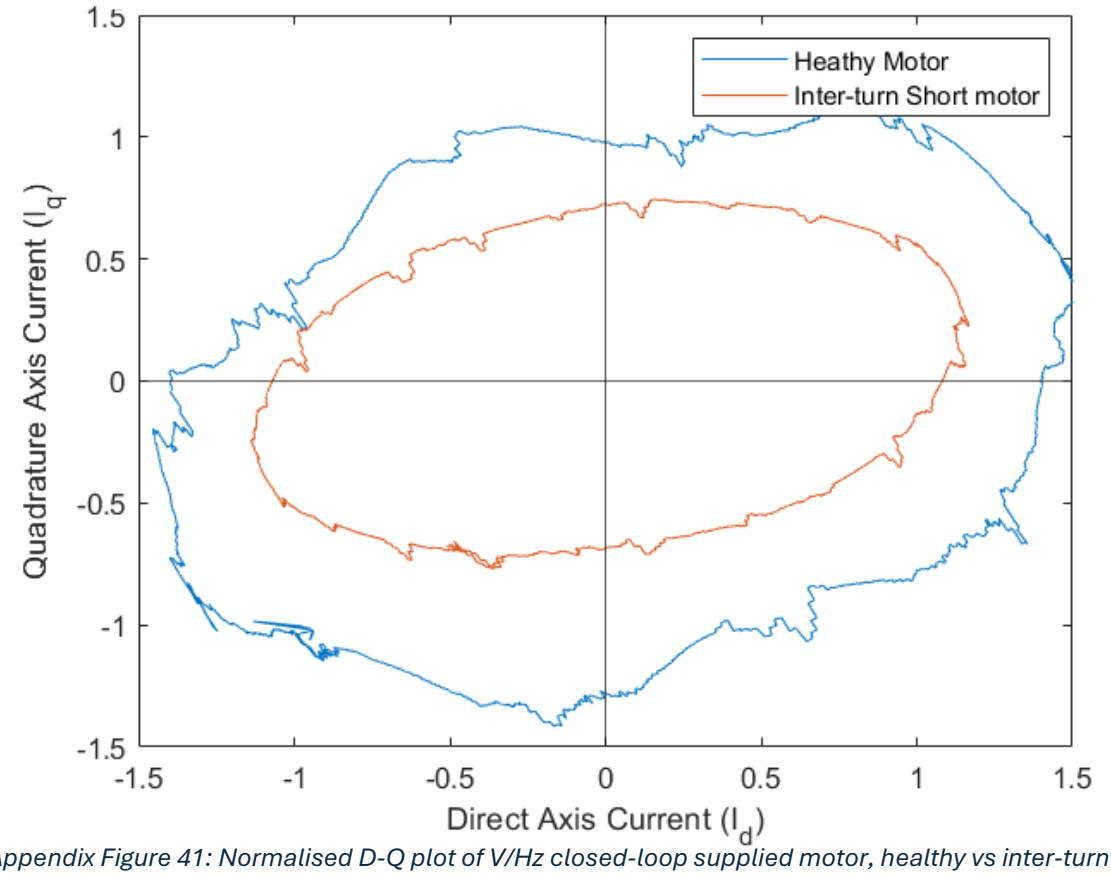

Appendix Figure 41: Normalised D-Q plot of V/Hz closed-loop supplied motor, healthy vs inter-turn fault, partial load, 25Hz.

9.5.1.2.2 No Load

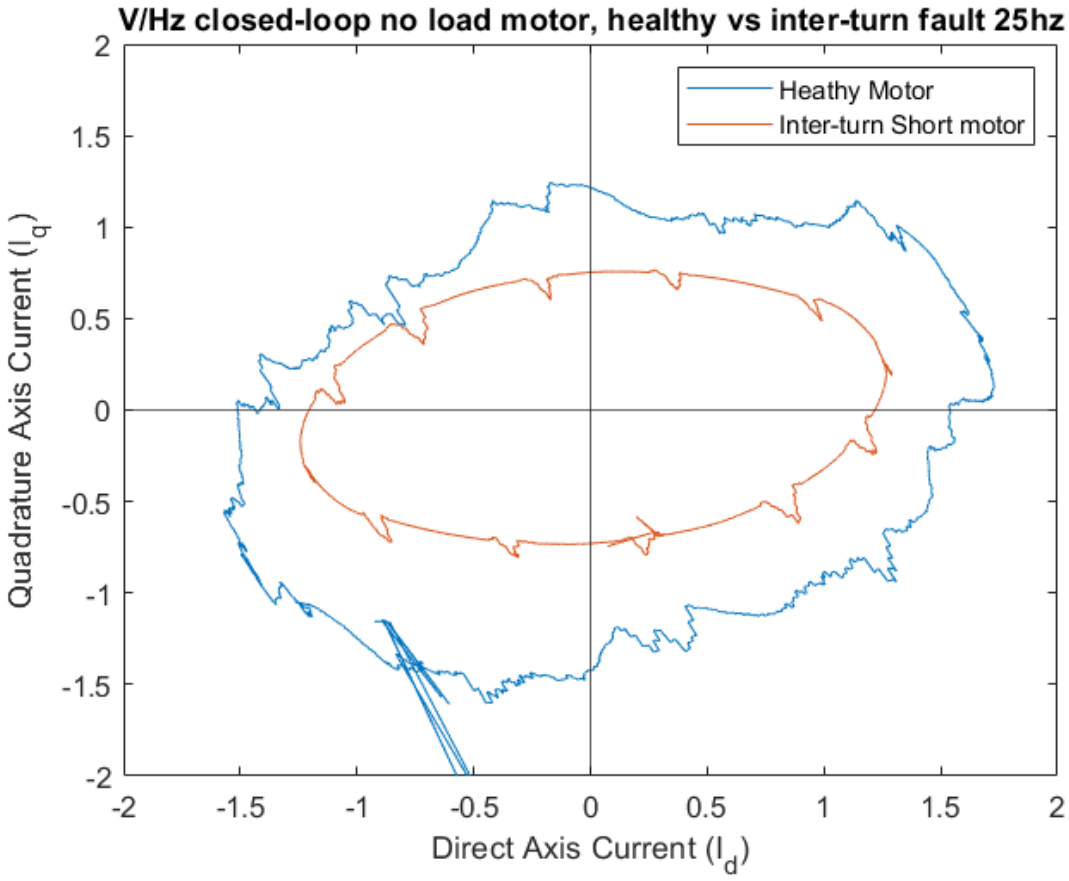

Appendix Figure 42: Normalised D-Q plot of V/Hz closed-loop supplied motor, healthy vs inter-turn fault, no load, 25Hz.

9.5.1.3 Extended Park's Vector Approach

The extended Park's Vector approach was applied, and the results are shown below.

Appendix Table 5: Extended Park's Vector Approach V/Hz closed-loop inverter supplied motor 25Hz, healthy vs inter-turn fault.

V/Hz closed-loop, no load, no fault 25Hz.		**V/Hz closed-loop, no load, inter-turn fault 25Hz.**		**Difference (p.u.)**
Frequency (Hz)	51.2	**Frequency (Hz)**	50.8	
Magnitude (p.u.)	0.043332939	**Magnitude (p.u.)**	0.170834494	0.127501555
V/Hz closed-loop, partial load, no fault 25Hz.		**V/Hz closed-loop, partial load, inter-turn fault 25Hz.**		
Frequency (Hz)	51	**Frequency (Hz)**	51.4	
Magnitude (p.u.)	0.045561759	**Magnitude (p.u.)**	0.248434323	0.202872564

9.5.1.4 DC Bus analysis

Appendix Table 6: Extended Park's Vector Approach V/Hz closed-loop inverter supplied motor 25Hz, healthy vs inter-turn fault.

V/Hz closed-loop, no load, no fault, 25Hz.		V/Hz closed-loop, no load, inter-turn fault, 25Hz.		Difference (p.u.)	Difference (faulted / healthy)
Frequency	51.1	**Frequency**	50.8		
Magnitude	0.0117816	**Magnitude**	0.099145164	0.087364	8.415255
Ripple Factor	0.281076206	**Ripple Factor**	0.406571498	0.125495	1.446481
V/Hz closed-loop, partial load, no fault, 25Hz.		**V/Hz closed-loop, partial load, inter-turn fault, 25Hz.**			
Frequency	51.1	**Frequency**	51.4		
Magnitude	0.0129085	**Magnitude**	0.104125944	0.091217	8.066463
Ripple Factor	0.372063142	**Ripple Factor**	0.503587823	0.131525	1.353501

9.5.2 Broken Rotor Bar

9.5.2.1 MCSA

9.5.2.1.1 Partial load

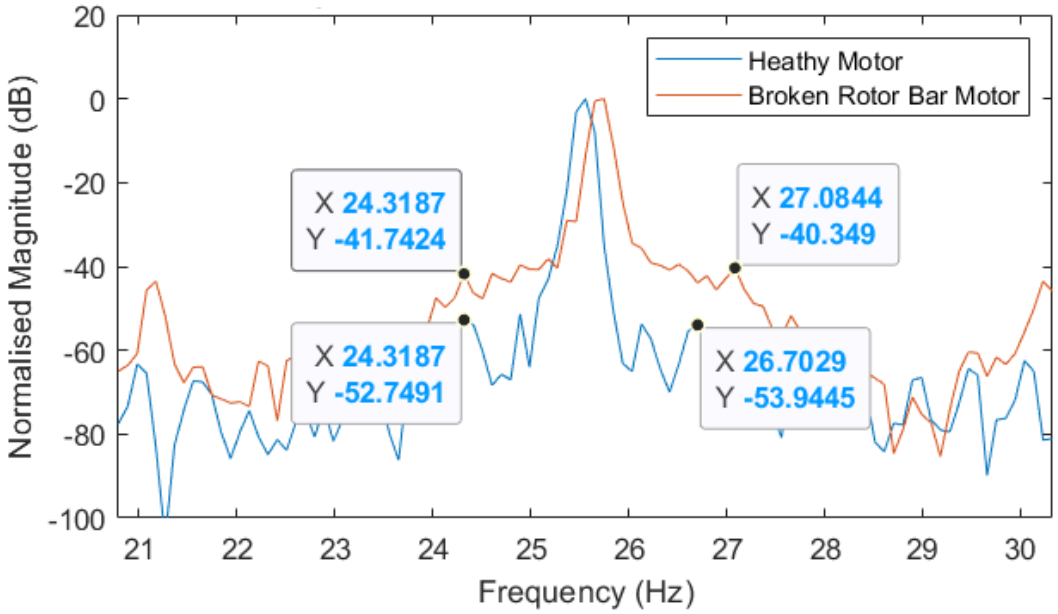

Appendix Figure 43: Frequency spectrum of line current from V/Hz closed-loop supplied induction motor, healthy motor vs broken rotor bar, k = 1, partial load, 25Hz.

9.5.2.1.2 No load

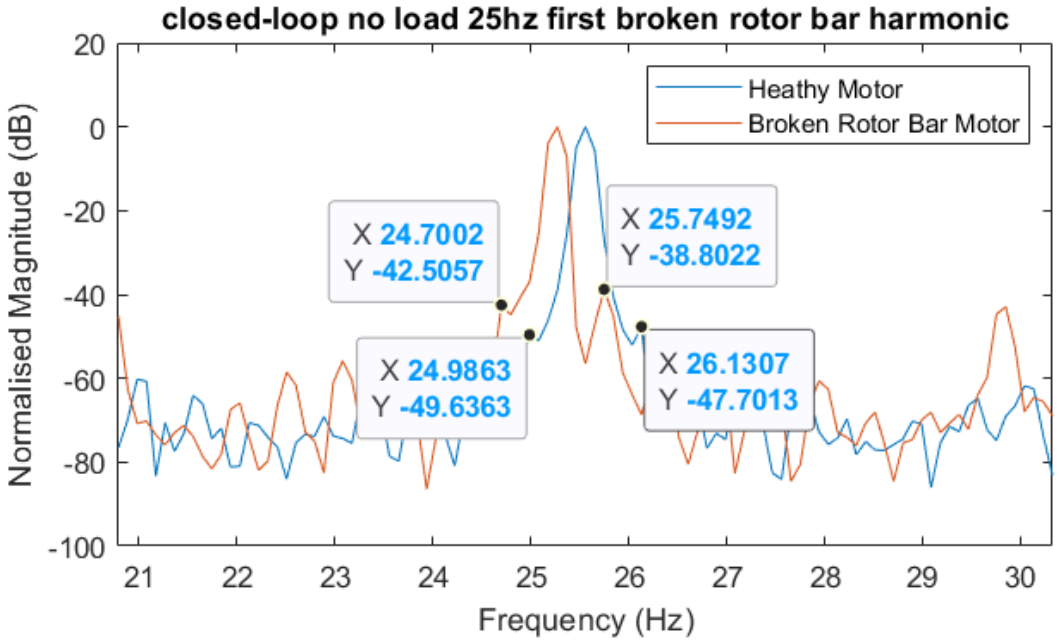

Appendix Figure 44: Frequency spectrum of line current from V/Hz closed-loop supplied induction motor, healthy motor vs broken rotor bar, k = 1, no load, 25Hz.

9.5.2.2 Park's Vector Approach

9.5.2.2.1 Partial Load

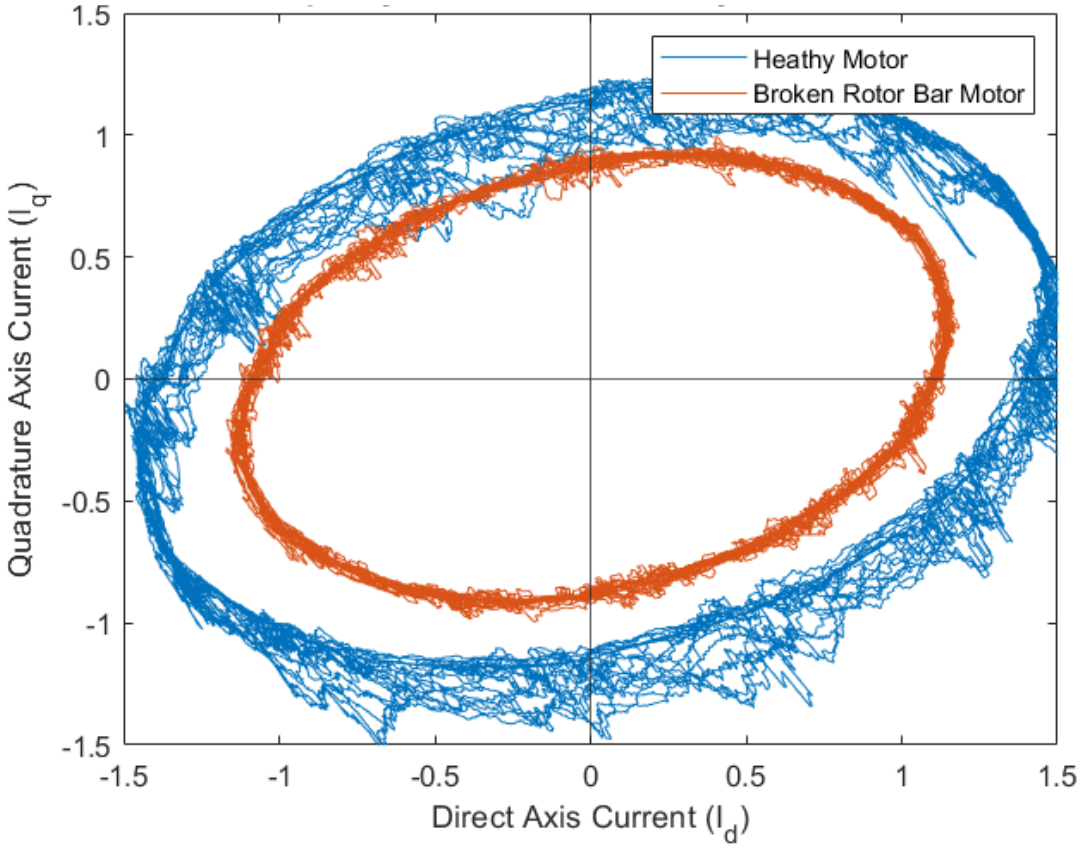

Appendix Figure 45: Normalised D-Q plot of V/Hz closed-loop supplied motor, healthy vs broken rotor bar, partial load, 25Hz.

9.5.2.2.2 No Load

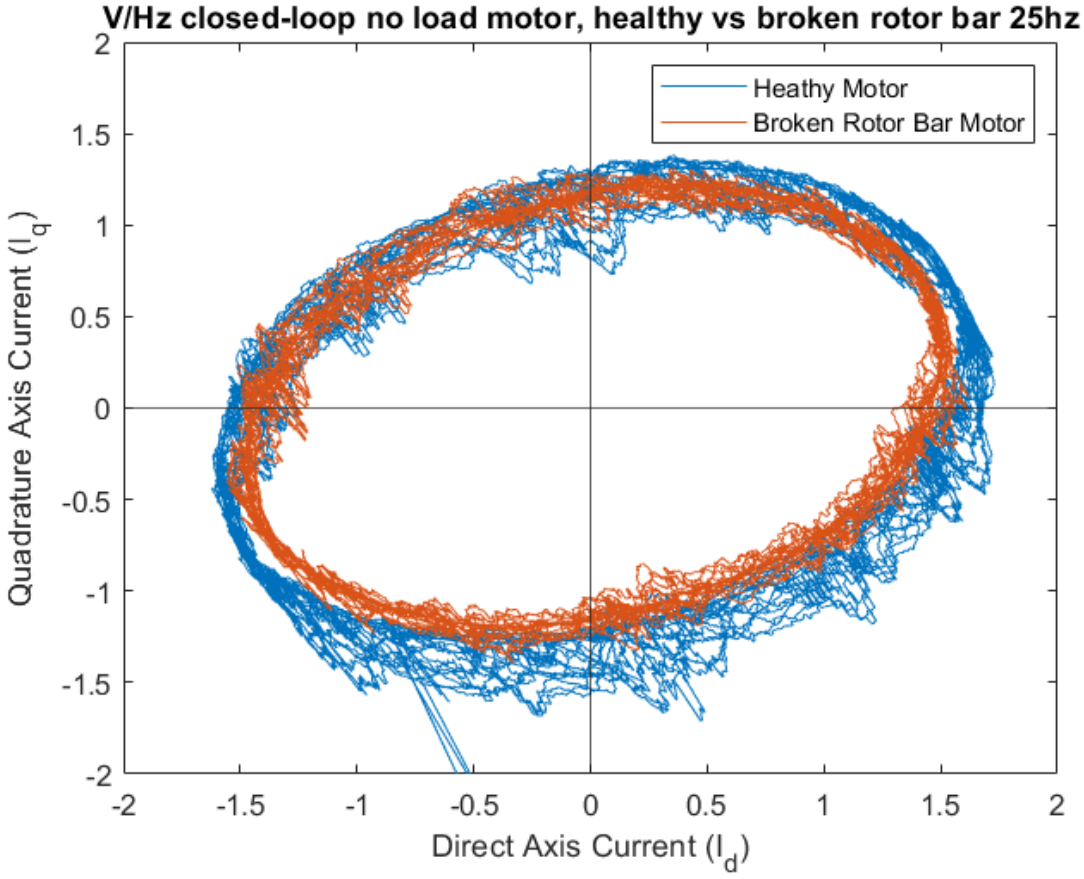

Appendix Figure 46: Normalised D-Q plot of V/Hz closed-loop supplied motor, healthy vs broken rotor bar, no load, 25Hz.

9.5.2.3 Extended Park's Vector Approach

Appendix Table 7: Extended Park's Vector Approach results, V/Hz closed-loop supplied motor, 25Hz.

V/Hz closed-loop, no load, no fault, 25Hz.		**V/Hz closed-loop, no load, broken rotor bar, 25Hz.**		**Difference**
Frequency (Hz)	51.1	**Frequency (Hz)**	50.5	
Magnitude (p.u.)	0.152219162	**Magnitude (p.u.)**	0.156089627	0.003870465
V/Hz closed-loop, partial load, no fault, 25Hz.		**V/Hz closed-loop, partial load, broken rotor bar, 25Hz.**		
Frequency (Hz)	51.1	**Frequency (Hz)**	51.4	
Magnitude (p.u.)	0.15437997	**Magnitude (p.u.)**	0.159470132	0.005090162

9.5.2.4 DC Bus analysis

Appendix Table 8: DC Bus analysis results, V/Hz closed-loop, 25Hz.

V/Hz closed-loop, no load, no fault, 25Hz.		V/Hz closed-loop, no load, broken rotor bar, 25Hz.		Difference	Difference (Faulted/Healthy)
Frequency (Hz)	51.2	**Frequency (Hz)**	50.6		
Magnitude (p.u)	0.003394463	**Magnitude (p.u)**	0.004265353	0.000871	1.256561896
Ripple Factor	0.281076206	**Ripple Factor**	0.278472333	-0.002604	0.990736058
V/Hz closed-loop, partial load, no fault, 25Hz.		**V/Hz closed-loop, partial load, broken rotor bar, 25Hz.**			
Frequency (Hz)	51	**Frequency (Hz)**	51.4		
Magnitude (p.u)	0.005440189	**Magnitude (p.u)**	0.009584003	0.004144	1.761703943
Ripple Factor	0.372063142	**Ripple Factor**	0.369185623	-0.002878	0.992266045

9.6 FOC 50Hz Results

9.6.1 Inter-turn Fault

9.6.1.1 MCSA

9.6.1.1.1 Partial load

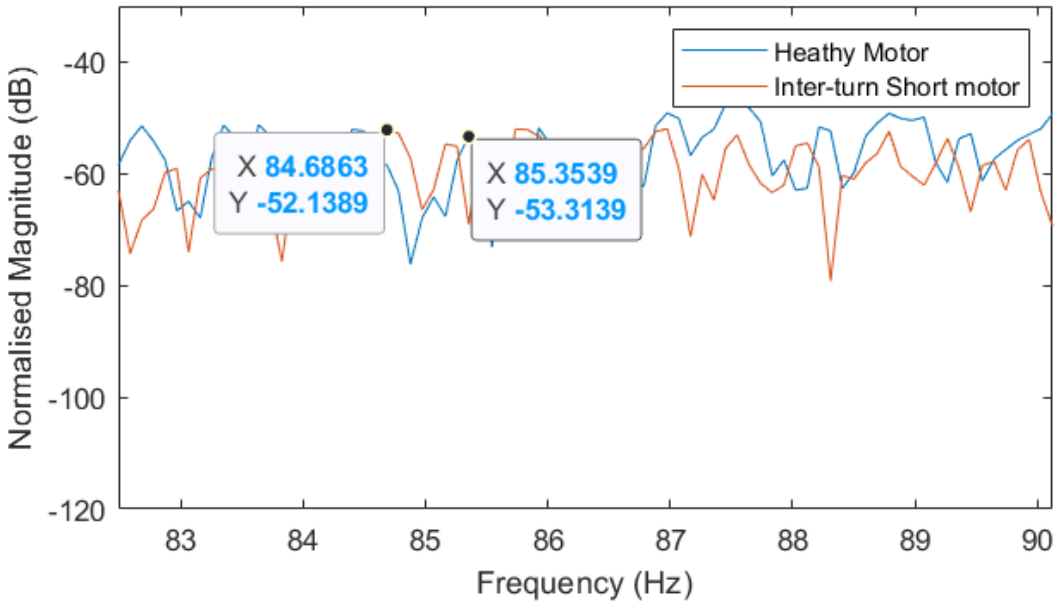

Appendix Figure 47: n=1, k=1 for FOC fed induction motor, healthy vs inter-turn short frequency spectrum, partial load, 50Hz.

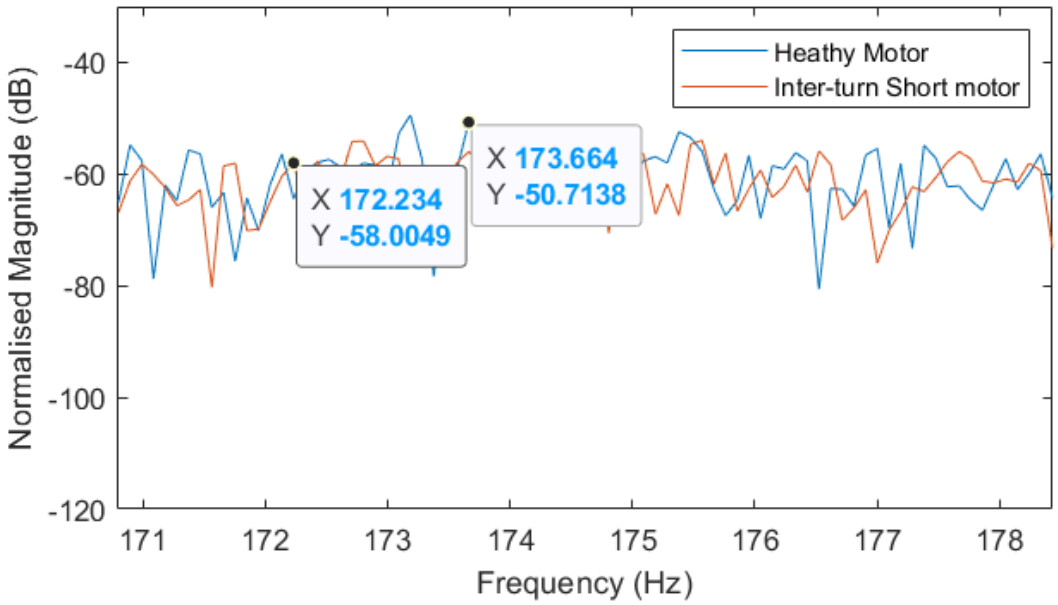

Appendix Figure 48: n=1, k=3 for FOC fed induction motor, healthy vs inter-turn short frequency spectrum, partial load, 50Hz.

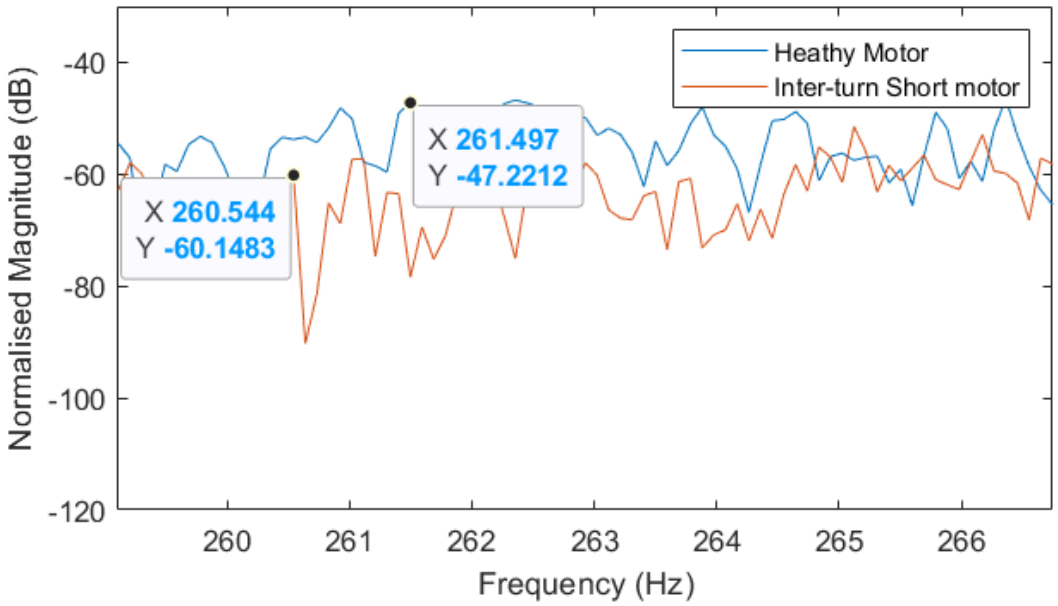

Appendix Figure 49: n=1, k=5 for FOC fed induction motor, healthy vs inter-turn short frequency spectrum, partial load, 50Hz.

9.6.1.1.2 No load

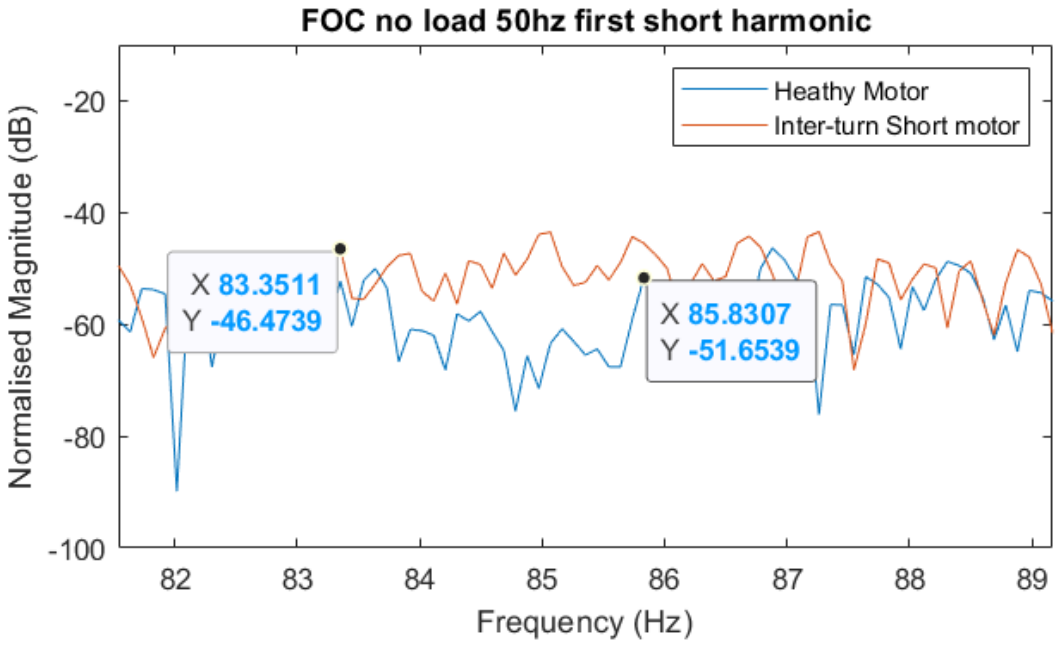

Appendix Figure 50: n=1, k=1 for FOC fed induction motor, healthy vs inter-turn short frequency spectrum, no load, 50Hz.

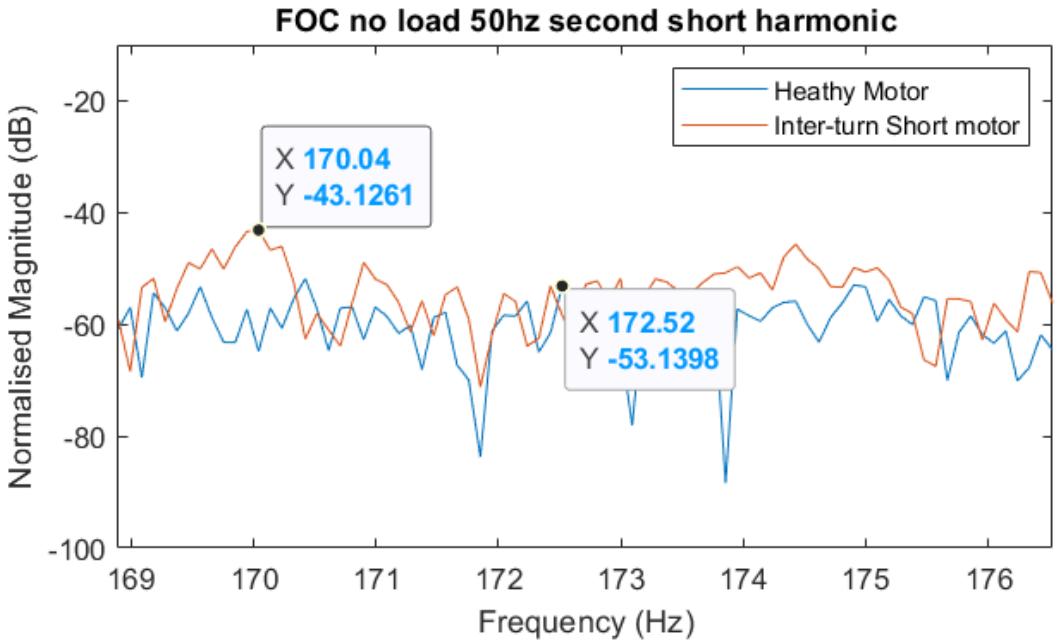

Appendix Figure 51: n=1, k=3 for FOC fed induction motor, healthy vs inter-turn short frequency spectrum, no load, 50Hz.

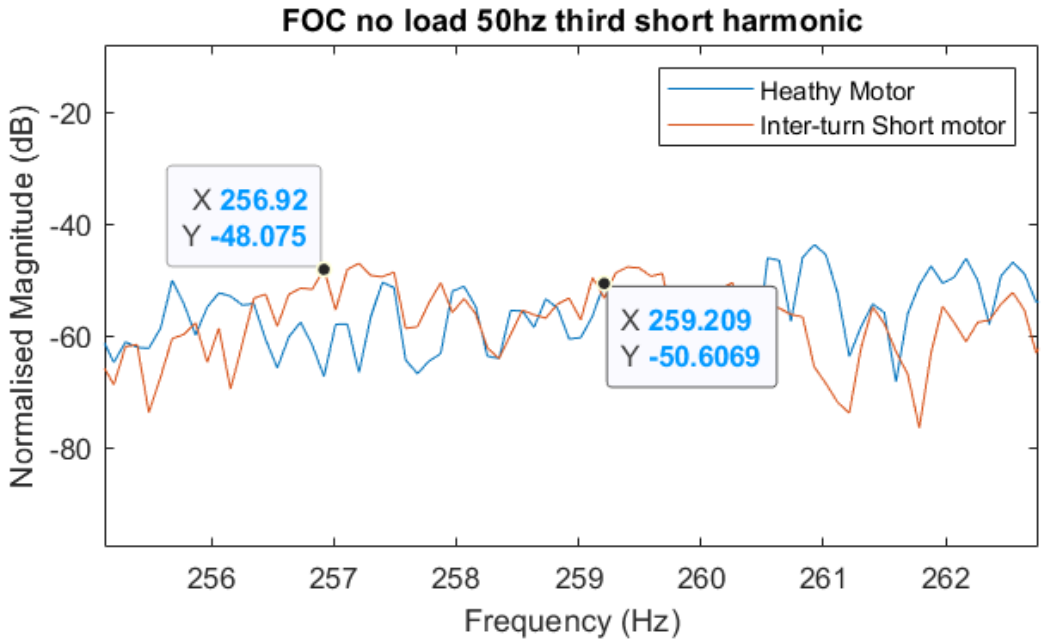

Appendix Figure 52: n=1, k=5 for FOC fed induction motor, healthy vs inter-turn short frequency spectrum, no load, 50Hz.

9.6.1.2 Park's Vector Approach

9.6.1.2.1 No Load

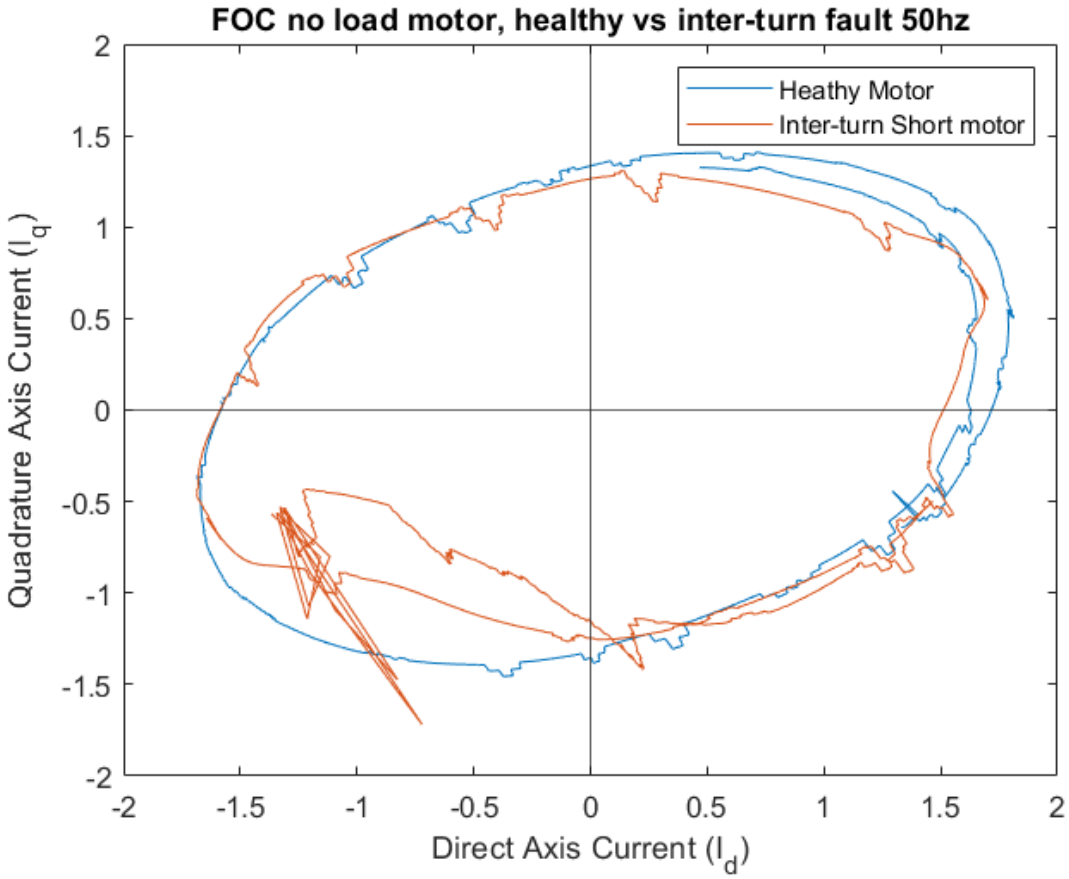

Appendix Figure 53: Normalised D-Q plot of V/Hz closed-loop supplied motor, healthy vs inter-turn fault, no load, 50Hz.

9.6.2 Broken Rotor Bar

9.6.2.1 MCSA

9.6.2.1.1 Partial load

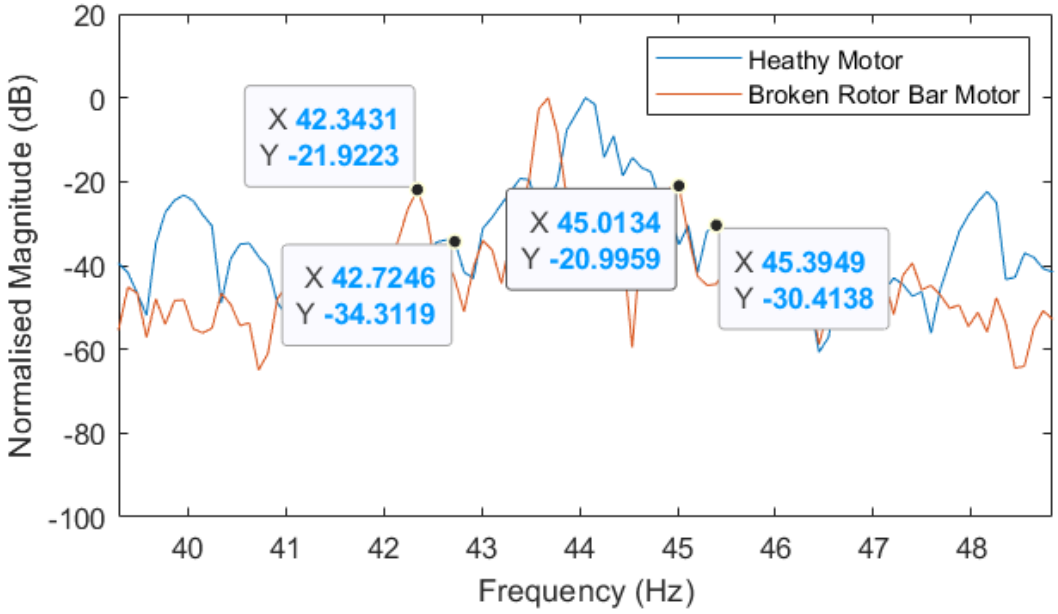

Appendix Figure 54: Frequency spectrum of line current from FOC supplied induction motor, healthy motor vs broken rotor bar, k = 1, partial load, 50Hz.

9.6.2.1.2 No load

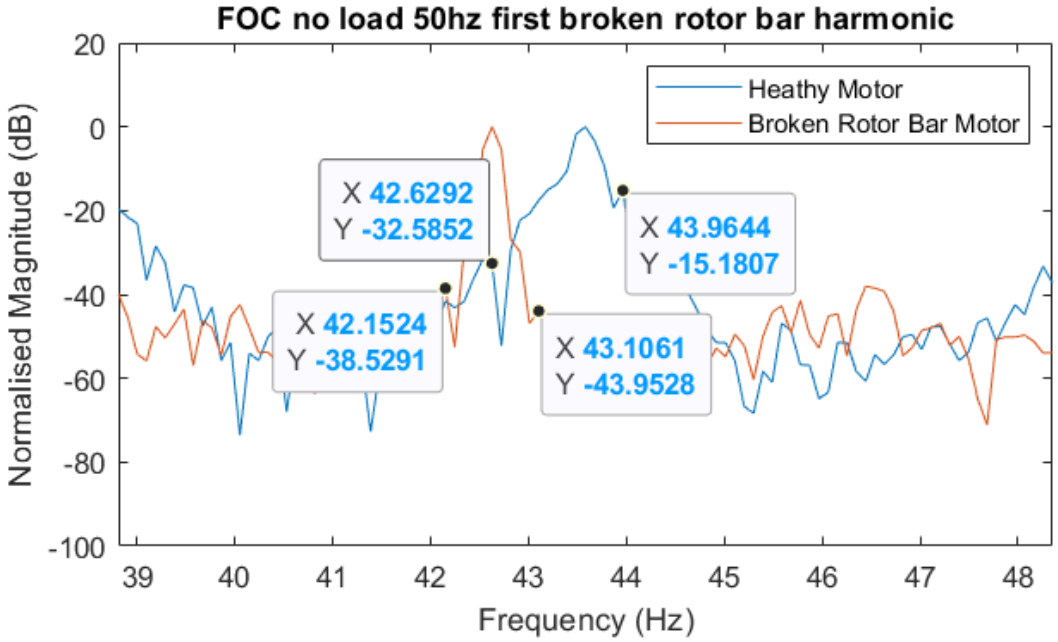

Appendix Figure 55: Frequency spectrum of line current from FOC supplied induction motor, healthy motor vs broken rotor bar, k = 1, no load, 50Hz.

9.6.2.2 Park's Vector Approach

9.6.2.2.1 No Load

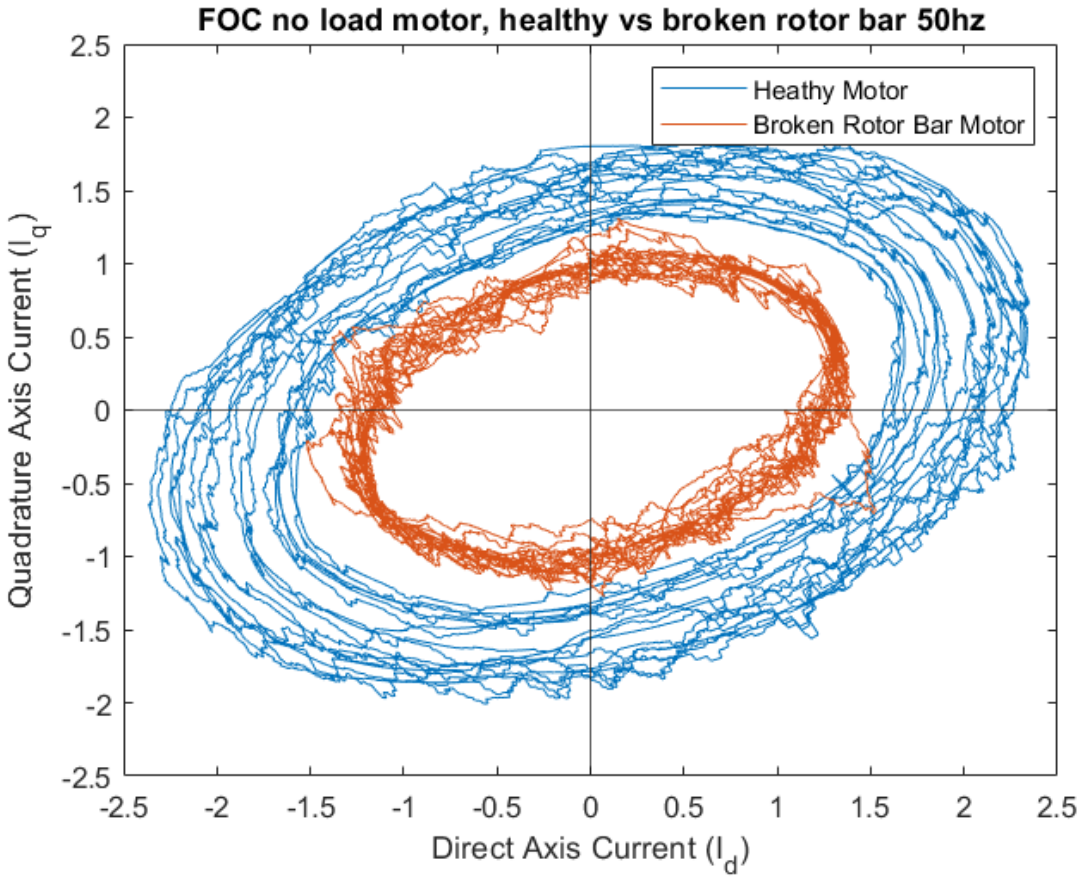

Appendix Figure 56: Normalised D-Q plot of FOC supplied motor, healthy vs broken rotor bar, no load, 50Hz.

9.7 FOC 25Hz Results

9.7.1 Inter-turn Fault

9.7.1.1 MCSA

9.7.1.1.1 Partial load

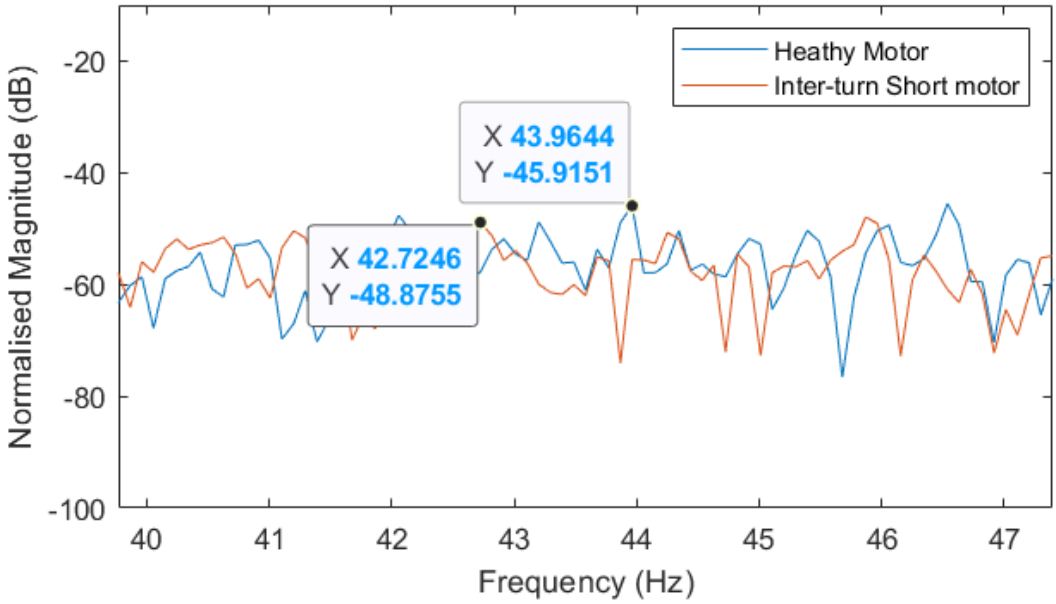

Appendix Figure 57: n=1, k=1 for FOC fed induction motor, healthy vs inter-turn short frequency spectrum, partial load, 25Hz.

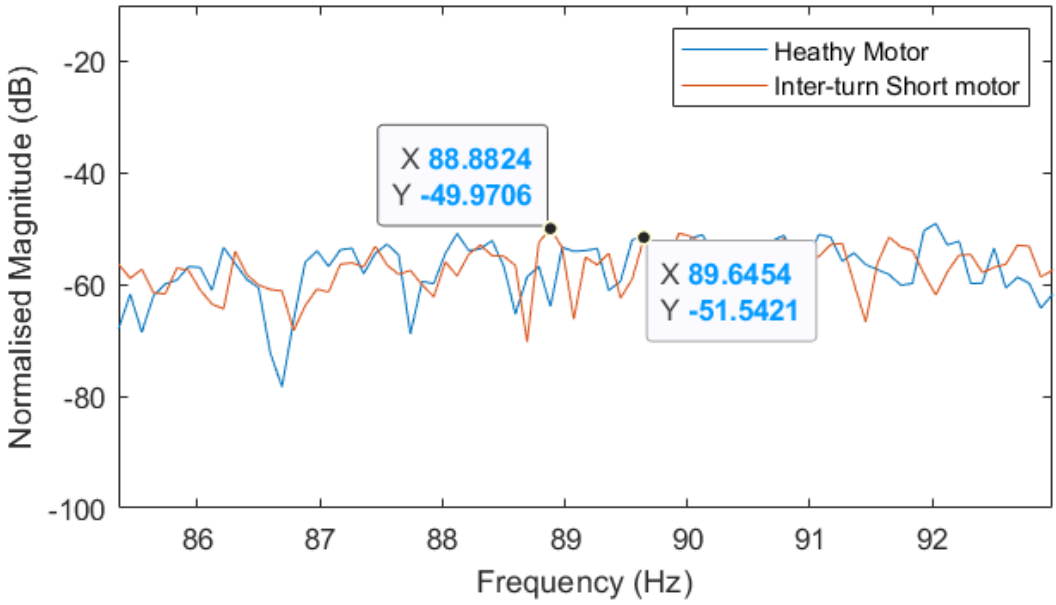

Appendix Figure 58: n=1, k=3 for FOC fed induction motor, healthy vs inter-turn short frequency spectrum, partial load, 25Hz.

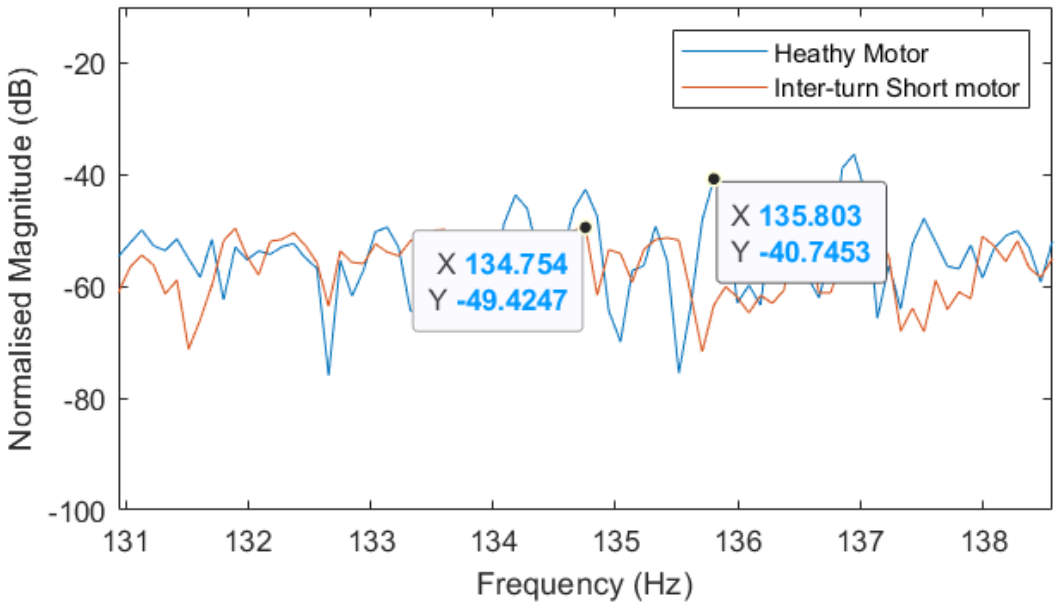

Appendix Figure 59: n=1, k=5 for FOC fed induction motor, healthy vs inter-turn short frequency spectrum, partial load, 25Hz.

9.7.1.1.2 No load

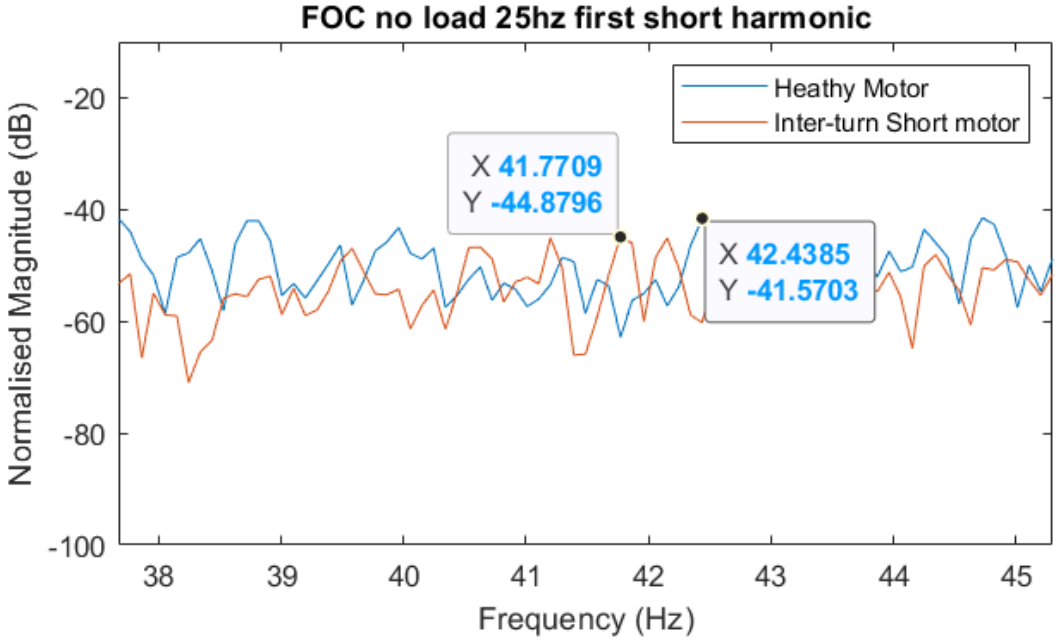

Appendix Figure 60: n=1, k=1 for FOC fed induction motor, healthy vs inter-turn short frequency spectrum, no load, 25Hz.

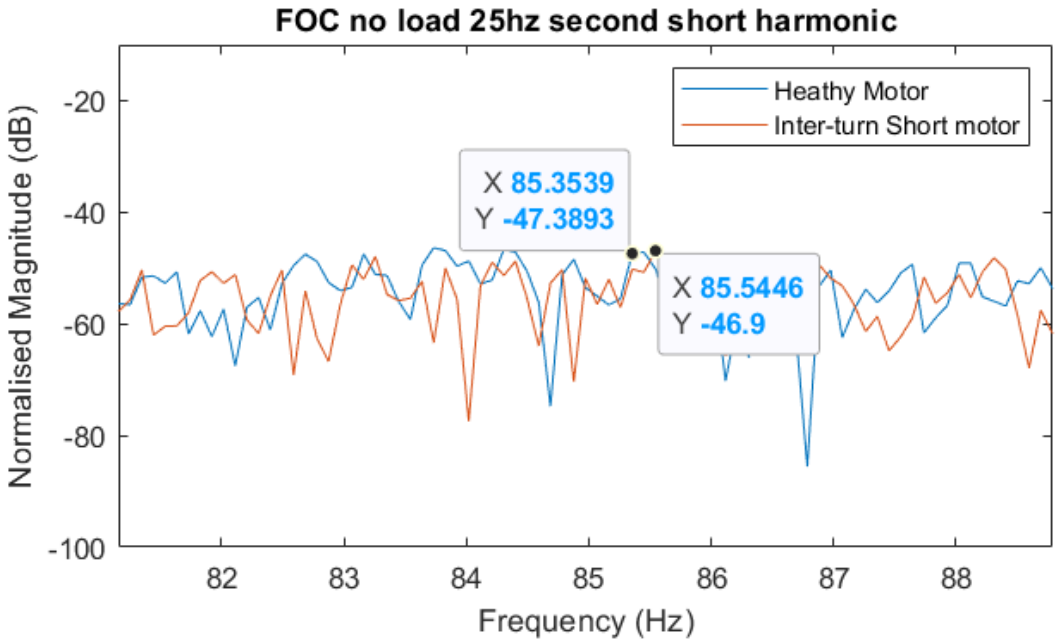

Appendix Figure 61: n=1, k=3 for FOC fed induction motor, healthy vs inter-turn short frequency spectrum, no load, 25Hz.

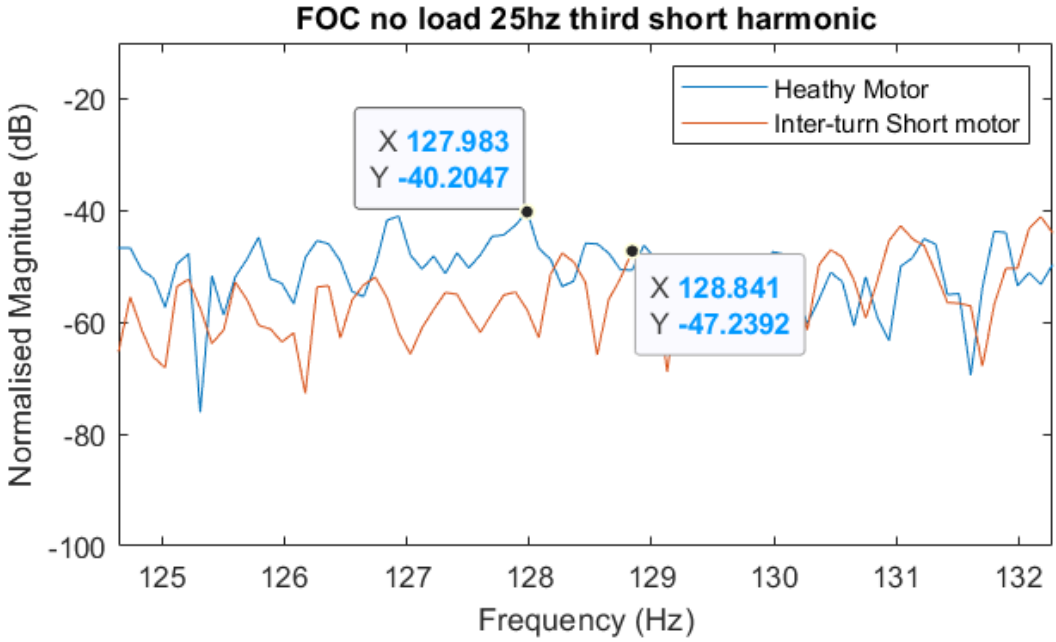

Appendix Figure 62: n=1, k=5 for FOC fed induction motor, healthy vs inter-turn short frequency spectrum, no load, 25Hz.

9.7.1.2 Park's Vector Approach

9.7.1.2.1 Partial Load

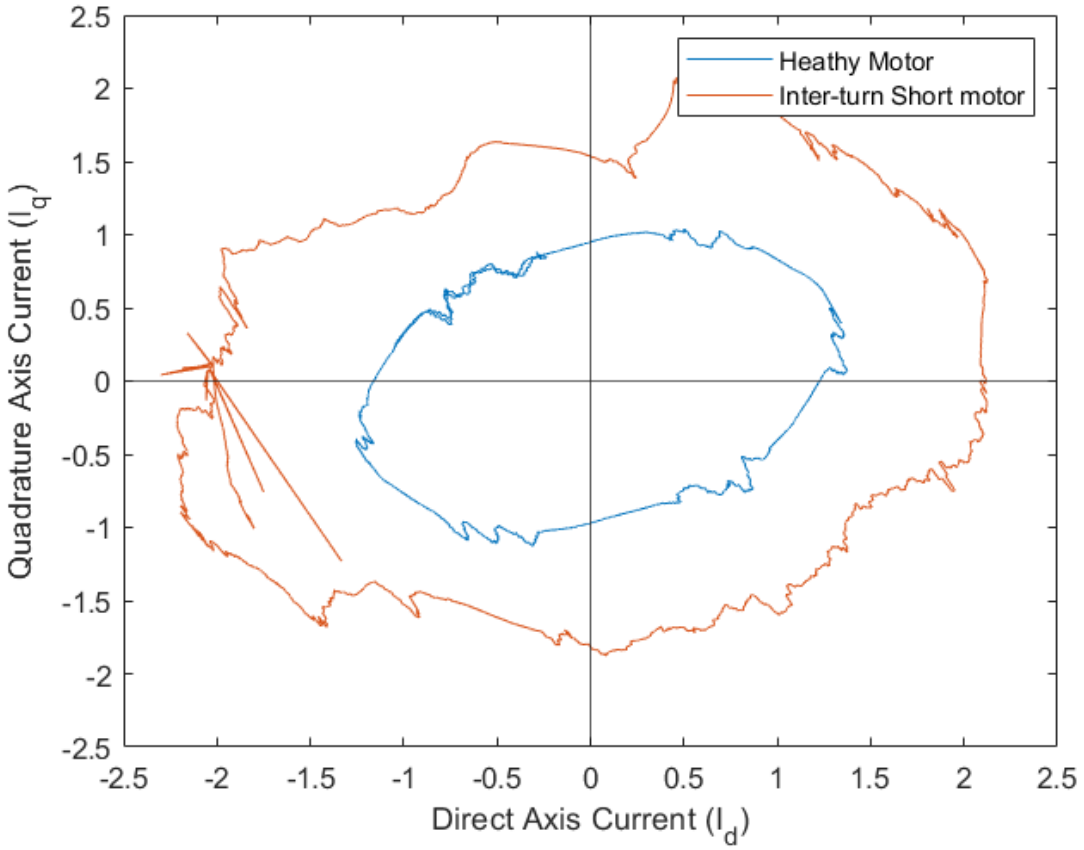

Appendix Figure 63: Normalised DQ plot of FOC inverter supplied motors, healthy vs inter-turn fault, partial load, 25Hz.

9.7.1.2.2 No Load

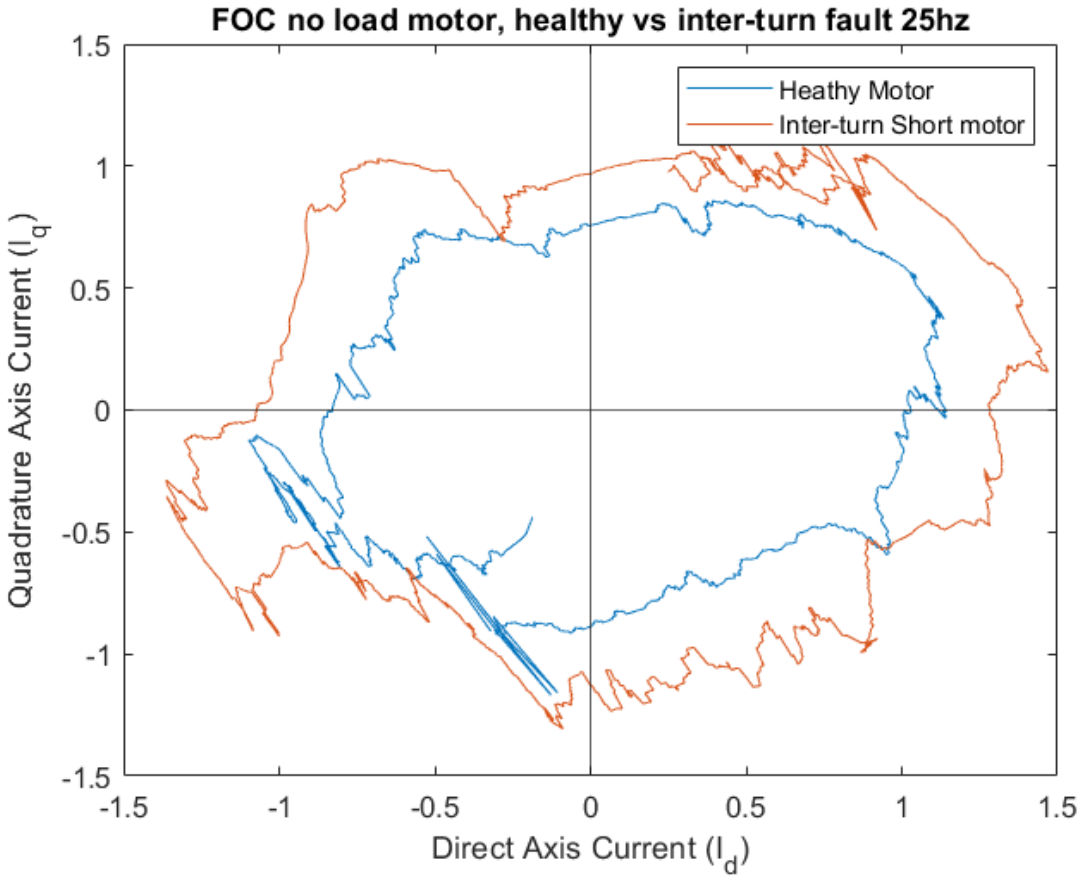

Appendix Figure 64: Normalised DQ plot of FOC inverter supplied motors, healthy vs inter-turn fault, no load, 25Hz.

9.7.1.3 Extended Park's Vector Approach

Appendix Table 9: Extended Park's Vector Approach data for FOC controlled inverter supplied motor, healthy vs inter-turn fault, 25Hz.

FOC no load, no fault, 25Hz.		**FOC no load, inter-turn fault, 25Hz.**		**Difference (p.u.)**
Frequency (Hz)	43.2	**Frequency (Hz)**	43.9	
Magnitude (p.u.)	0.153029637	**Magnitude (p.u.)**	0.126086	-0.026943637
FOC partial load, no fault, 25Hz.		**FOC partial load, inter-turn fault, 25Hz.**		
Frequency (Hz)	45.5	**Frequency (Hz)**	46.9	
Magnitude (p.u.)	0.133471	**Magnitude (p.u.)**	0.0937016	-0.0397694

9.7.1.4 DC Bus analysis

Appendix Table 10: DC bus analysis of FOC controlled inverter supplied motor, healthy vs inter-turn fault, 25Hz.

FOC no load, no fault, 25Hz.		FOC no load, inter-turn fault, 25Hz.		Difference (p.u.)	Difference (Faulted / healthy)
Frequency	43.2	**Frequency**	43.3		
Magnitude	0.029705615	**Magnitude**	0.03302707	0.003321454	1.111812332
Ripple Factor	0.230566983	**Ripple Factor**	0.264714956	0.034147973	1.14810435
FOC partial load, no fault, 25Hz.		**FOC partial load, inter-turn fault, 25Hz.**			
Frequency	45.5	**Frequency**	45.3		
Magnitude	0.019913086	**Magnitude**	0.015211357	-0.004701729	0.763887478
Ripple Factor	0.338581214	**Ripple Factor**	0.476043508	0.137462294	1.405995042

9.7.2 Broken Rotor Bar

9.7.2.1 MCSA

9.7.2.1.1 Partial load

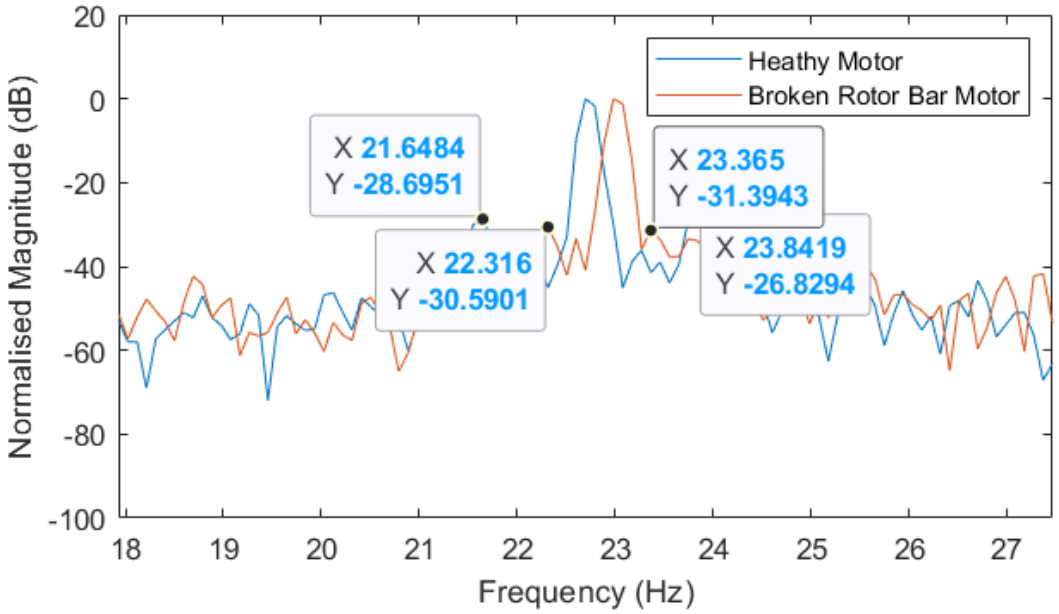

Appendix Figure 65: Frequency spectrum of line current from FOC supplied induction motor, healthy motor vs broken rotor bar, k = 1, partial load, 25Hz.

9.7.2.1.2 No load

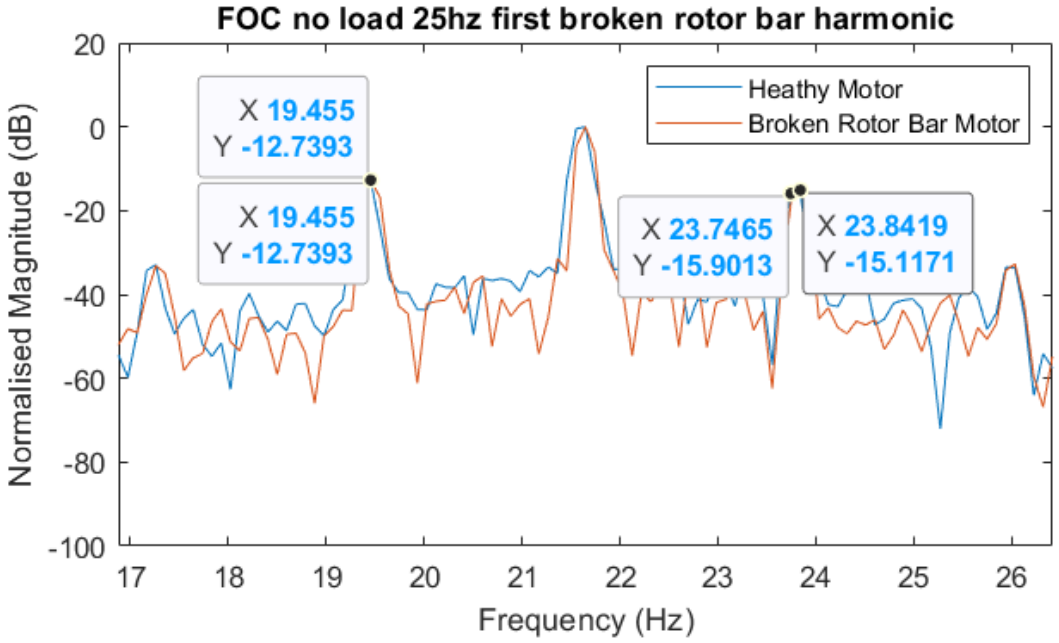

Appendix Figure 66: Frequency spectrum of line current from FOC supplied induction motor, healthy motor vs broken rotor bar, k = 1, no load, 25Hz.

9.7.2.2 Park's Vector Approach

9.7.2.2.1 Partial Load

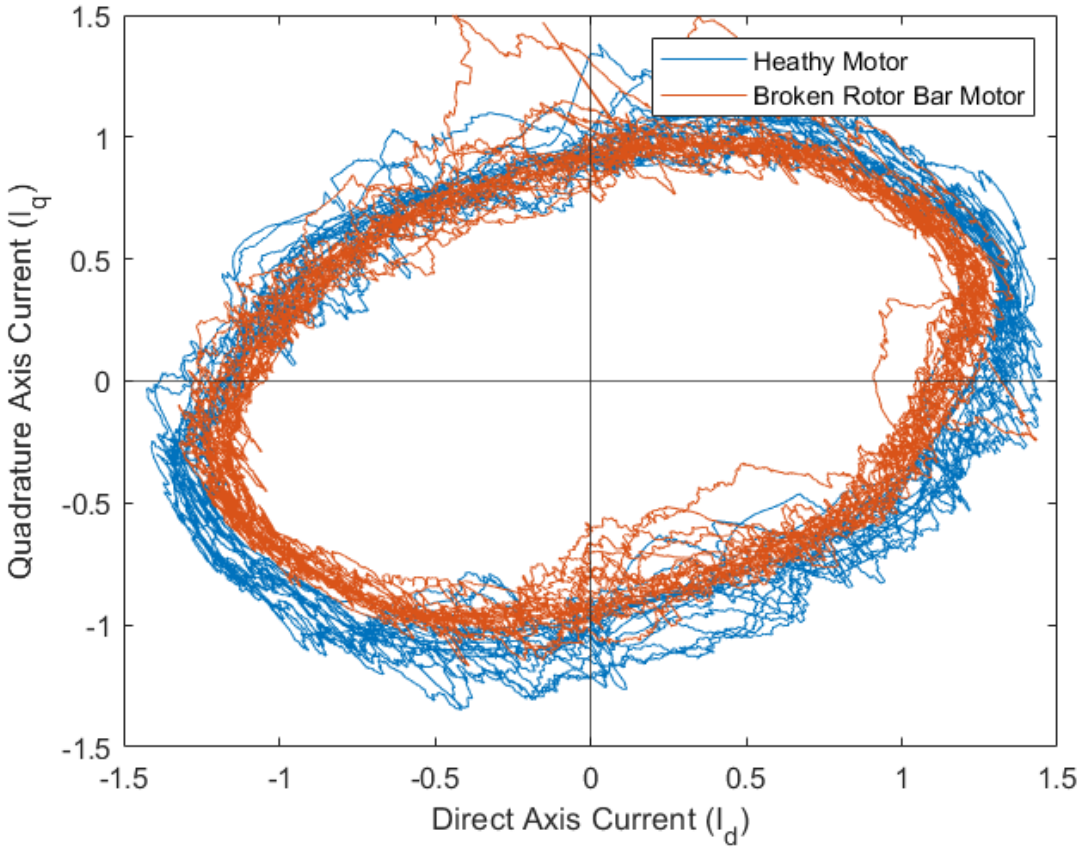

Appendix Figure 67: Normalised D-Q plot of FOC supplied motor, healthy vs broken rotor bar, partial load, 25Hz.

9.7.2.2.2 No Load

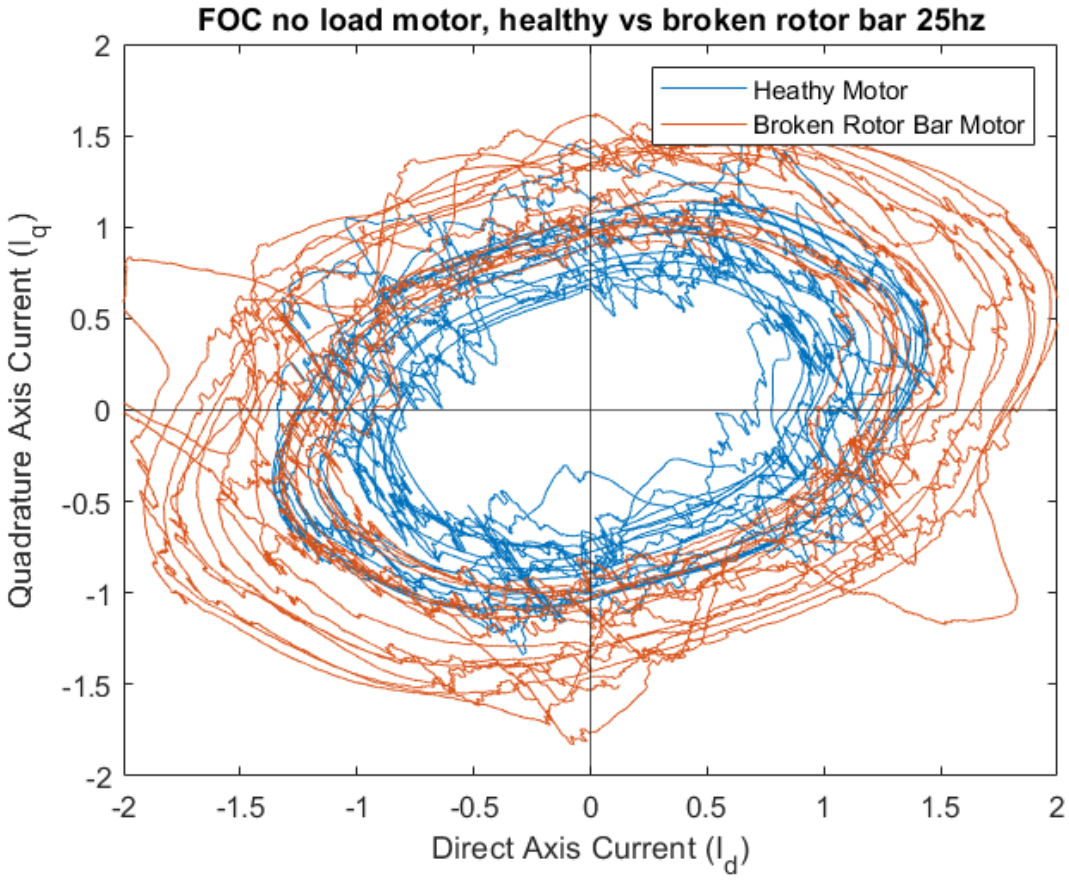

Appendix Figure 68: Normalised D-Q plot of FOC supplied motor, healthy vs broken rotor bar, no load, 25Hz.

9.7.2.3 Extended Park's Vector Approach

Appendix Table 11: Extended Park's Vector Approach results, FOC supplied motor, healthy vs broken rotor bar, 25Hz.

FOC, no load, no fault, 25Hz.		**FOC, no load, broken rotor bar, 25Hz.**		**Difference (p.u.)**
Frequency (Hz)	43.2	**Frequency (Hz)**	43.3	
Magnitude (p.u.)	0.153029637	**Magnitude (p.u.)**	0.146145166	-0.006884
FOC, partial load, no fault, 25Hz.		**FOC, partial load, broken rotor bar, 25Hz.**		
Frequency (Hz)	45.5	**Frequency (Hz)**	46	
Magnitude (p.u.)	0.133471107	**Magnitude (p.u.)**	0.138391832	0.004921

9.7.2.4 DC Bus analysis

Appendix Table 12: DC bus analysis of FOC controlled inverter supplied motor, healthy vs broken rotor bar, 25Hz.

FOC, no load, no fault, 25Hz.		**FOC, no load, broken rotor bar, 25Hz.**		**Difference (p.u.)**	**Difference (Faulted/ Healthy)**
Frequency (Hz)	43.2	**Frequency (Hz)**	43.2		
Magnitude (p.u.)	0.029705615	**Magnitude (p.u.)**	0.007001743	-0.022703873	0.235704354
Ripple Factor	0.230566983	**Ripple Factor**	0.229122852	-0.001444131	0.99373661
FOC, partial load, no fault, 25Hz.		**FOC, partial load, broken rotor bar, 25Hz.**			
Frequency (Hz)	45.4	**Frequency (Hz)**	46		
Magnitude (p.u.)	0.011560634	**Magnitude (p.u.)**	0.020425446	0.008864813	1.766810275
Ripple Factor	0.338581214	**Ripple Factor**	0.332454074	-0.006127139	0.981903487

9.8 HARDWARE INFORMATION

9.8.1 Inverter Model and Specifications

Appendix Table 13: Inverter specifications of the inverter used in this experiment. The SiC model was used for this study. [100]

Parameter	Test Condition	MOSFET	IGBT	SiC	Unit
DC Input Voltage		600	600	600	Vdc
AC Input Voltage	Single or three phase	420	420	420	Vac
Over-Voltage Protection	Clamping Voltage	735	735	735	Vdc
Output Current	@ 2kHz, TA 25C, DC Input	6.7	7.5	9.5	Arms
Output Power	@ 2kHz, 25C, 600V DC Input	4.4	5	6.1	kW
Output Power	@ 2kHz, 25C, 420V AC Input	2.9	3	3.1	kW
Overload Capacity	@ 2kHz, 25C, 10s	100	100	100	%
Switching Frequency	Max.	100	30	200	kHz
Short Circuit Withstand Time	Max.	0	10	10	µs

9.8.2 Servo Motor Parameters

Appendix Table 14: Critical parameters for the Servo motor used in this study [96].

Parameter (P)	Description	Parameter setting
P1-01	Control Mode and output direction	0 x 000A
P1-02	Speed and torque limit setting	0 x 0000
P1 -04	Analogue Monitor output portion 1 (MON1)	100

P1 -05	Analogue Monitor output portion 2 (MON2)	100
P1-52	Regenerative resistor value	20
P1-53	Regenerative resistor capacity	1000
P1-72	Full-closed Loop Resolution (for CN5 terminal)	128000